Constraining cosmological models with cosmic microwave background fluctuations from the late universe

by

Tommaso Giannantonio

The thesis is submitted in partial fulfilment of the requirements for the award of the degree of
Doctor of Philosophy
of the
University of Portsmouth

September, 2008

Copyright

Declaration

Whilst registered as a candidate for the above degree, I have not been registered for any other research award. The results and conclusions embodied in this thesis are the work of the named candidate and have not been submitted for any other academic award.

Abstract

In this thesis we discuss how late time anisotropies in the cosmic microwave background (CMB), such as the integrated Sachs-Wolfe effect (ISW), can be detected and used to constrain cosmology, and in particular to investigate the nature of dark energy and modified gravity theories. We present the state-of-the-art measurement of this phenomenon together with some of its applications. We also discuss how cosmic reionisation can be studied with a similar technique.

After an introduction describing the main points of the work, we review the current standard model of cosmology, describing the dark energy problem and some of its possible solutions. We then review the theory of cosmological perturbations as a method to study the evolution of inhomogeneities. Afterwards, we present the CMB anisotropies and its physical primary and secondary sources, which include the ISW effect and cosmic reionisation. The ISW consists of the production of some small additional anisotropies on the CMB due to the time evolution of the gravitational potentials, and is interesting because in the standard model it can only be produced if the Universe undergoes a transition to a curvature or dark energy phase. A direct measurement of this effect is challenging, because the signal is combined with the primary CMB anisotropies, whose amplitude is bigger. However, since the ISW signal has been originated at late times, we can extract it by correlating the total CMB anisotropies with a tracer of the large scale structure, such as a galaxy catalogue.

Most of the following is dedicated to this effect. We first describe the ISW measurement as obtained by cross-correlating the CMB maps from WMAP with a catalogue of quasars from the Sloan Digital Sky Survey (SDSS); we obtain a positive correlation at the 2σ level. The analysis is then extended to a collection of six different catalogues, which bring the total significance of the measurement up to $\sim 4.5\sigma$ and is the current state-of-the-art in the field. We also analyse other phenomena which can produce a correlation between the CMB and the large scale structure of the Universe, such as cosmic reionisation. We will see that this is an important foreground for the ISW measurements at high redshift and, at the same time, an interesting tool to study the history of reionisation. We then present how the ISW data may be used to distinguish between standard general relativity and some different models, such as the DGP theory, before concluding and presenting some ongoing and future projects.

Preface

The work of this thesis was carried out at the Institute of Cosmology & Gravitation, University of Portsmouth, United Kingdom.

The following chapters are based on published work:

- Chapter 4: *"A high redshift detection of the integrated Sachs-Wolfe effect"*
  by T. Giannantonio, R. G. Crittenden, R. C. Nichol, R. Scranton , G. T. Richards, A. D. Myers, R. J. Brunner, A. G. Gray, A. J. Connolly, D. P. Schneider,
  published in Phys. Rev. D **74**, 063520 (2006)

- Chapter 5: *"Combined analysis of the integrated Sachs-Wolfe effect and cosmological implications"*
  by T. Giannantonio, R. Scranton, R. G. Crittenden, R. C. Nichol, S. P. Boughn, A. D. Myers and G. T. Richards,
  published in Phys. Rev. D **77**, 123520 (2008)

- Chapter 6: *"The effect of reionization on the CMB-density correlation"*
  by T. Giannantonio and R. Crittenden,
  published in Mon. Not. Roy. Astron. Soc. **381**, 819 (2007)

- Chapter 7:*"Detectability of a phantom-like braneworld model with the integrated Sachs-Wolfe effect"*
  by T. Giannantonio, Y. S. Song and K. Koyama,
  published in Phys. Rev. D **78**, 044017 (2008).

Acknowledgements

First I would like to thank my supervisor Dr. Robert Crittenden for being always present and patient enough to answer my questions, willing to help me with suggestions and encouragement whenever I needed it.

Then, I am also very grateful to my second supervisor Prof. Bob Nichol for helping me often, and especially for communicating to me the greatest enthusiasm for research.

I am happy to repeat my acknowledgement to Dr. Alessandro Melchiorri for keeping an ongoing interest in my work and career, and for always giving me valuable suggestions about both.

I would also like to thank the University of Cape Town and Prof. Bruce Bassett for the generous hospitality during part of the writing of this thesis.

I am glad to thank all my collaborators, especially Prof. Steven Boughn, Dr. Kazuya Koyama, Dr. Hubert Lampeitl, Prof. Roy Maartens, Dr. Björn Malte Schäfer, Dr. Ryan Scranton, Dr. Yong-Seon Song and Dr. Jussi Väliviita and for their help and patience.

I will remain grateful to my officemate and friend Elisabetta Majerotto for putting up with me in comic and tragic circumstances, and for amusing me with interesting discussions in both cases. I am also grateful to Dr. Will Percival for thoughtfully tolerating the aforementioned discussions from the adjacent office.

I would like to greatly thank all my friends and colleagues at the ICG and elsewhere for being always nice and fun and helping me to enjoy the last three years, and especially: Antonio, Ben, Chiara, Chris B., Claudia, Domenico, Elena & Francesca, Fred, Jim, Lukas, Marina, Mat, Mehri, Prina, Silvia, my flatmates Fabio and Kelly, and Linda.

I finally thank my parents for the times they have been kind and supportive.

Portsmouth, 23rd August 2008

Table of Contents

Chapter 1

Introduction

The standard model of cosmology today, which is based on Einstein's general relativity and the Copernican principle, successfully describes observed physical phenomena over a wide range of scales and times. From the earliest times just after the big bang until the late time formation of galaxies, and from the scale of the solar system to the edge of our visible horizon, we are able to describe the observed phenomena with a consistent theory. New observations have been constantly performed over the past few decades, resulting often in a confirmation of theoretical forecasts, such as with the detection of the cosmic microwave background (CMB) anisotropies by the Nobel prize winning experiment COBE [Smoot, 2007]. However, the observations have on other occasions been in disagreement with the previously accepted theory, leading to the subsequent modification of the standard model. This was the case for the discovery of the late time acceleration of the Universe from the Hubble diagram of type Ia supernovae. This in turn led to the introduction of dark energy. A consequence of this, the standard model is now in agreement with the observations, however it still contains some features, such as dark energy and dark matter, whose existence is questionable and whose characteristics are yet unknown, lacking any direct evidence. For this reason it is of the highest importance for cosmology and the whole of physics to further investigate these components, in order to either understand their nature or otherwise disprove their existence. In this thesis we will focus on the dark energy problem and try to understand more about its characteristics and properties.

The cosmic microwave background (CMB) is an almost isotropic radiation originating at the epoch of recombination of the hydrogen atoms when the Universe was 300,000 years old. We know that the Universe was opaque before this epoch and then has been transparent, because the lack of free electrons prevents the photons from Compton scattering. Therefore this radiation represents an image of the Universe at that time, and its small fluctuations depend on the fluctuations of the physical fields, such as temperature, density and velocity, at recombination.

Indirect evidence for dark energy arises from the observation of the primary CMB anisotropies, combined with supernovae and other probes such as baryon acoustic oscillations (BAO) or galaxy cluster counts. Another possibility is to study the late time modifications of the CMB, which are produced in different ways depending on the cosmological model.

In fact, the CMB signal has been almost unchanged since recombination, but some small alterations arise due to several effects. If a fraction of the hydrogen in the Universe becomes ionised again at late times, the CMB photons will undergo Compton scattering again, smearing out a part of the primary anisotropies; reionisation may happen globally or locally around some sources. Different types of secondary anisotropy may be generated when the photons go through high density areas such as clusters of galaxies. In this case the high temperatures and velocities can be transfered to the photons, producing characteristic, frequency dependent anisotropies on small scales called thermal and kinetic Sunayev-Zel'dovich effect respectively.

Here we are mostly interested in yet another type of secondary anisotropies, due to the effect of the gravitational potentials on the streaming CMB photons. There will firstly be a correction on the temperature anisotropies proportional to the difference in the gravitational potential between the source at the last scattering surface and the observer; this is called the ordinary Sachs-Wolfe effect. In the following, we will focus on the effect that variations in the potential may have at the linear level along the line of sight of the photon, which is called the integrated Sachs-Wolfe (ISW) effect and was firstly described by Sachs and Wolfe [1967]. Smaller non-linear corrections can be formed at smaller scales, and are called Rees-Sciama effect. In a flat Universe dominated by matter only, the gravitational potentials are constant in time, and therefore this effect would not be produced. We may only observe this phenomenon in the case where other components are important, such as radiation at early times (thus producing early ISW) or curvature or dark energy at late times (late ISW). For this reason a measurement of this effect at late times would be an interesting and independent evidence for dark energy or, in general, a departure from a pure matter Universe. However, this remained a very theoretical possibility for many years, because for most models the ISW effect is only a small correction to the already small primary CMB anisotropies, and arises at late time on the largest scales, mostly due to cosmic variance.

This changed when Crittenden and Turok [1996] presented a new technique, which made it possible to extract this effect by cross-correlating the observed CMB map with some tracer of the matter density. The primary CMB anisotropies have been generated a long time ago, and therefore are completely uncorrelated from the large scale structure we observe; on the other hand, these structures were already formed coincident with the generation of the ISW effect. For this reason, the cross-correlation of the total CMB with some tracer of the large scale structure of the Universe will isolate the late ISW signal, allowing us to measure dark energy.

The first attempt to perform the measurement was done by Boughn et al. [1998], using the COBE data for the CMB and the HEAO map of the X-ray background, and later by Boughn and Crittenden [2002] correlating COBE with the NVSS catalogue of radio galaxies. In both cases it was possible to obtain only an upper limit on the amount of dark energy present in the Universe today, due to the fairly large uncertainties in the COBE data. However, these works laid out the procedure to perform the analysis of the cross-correlation in real space. When the first WMAP data were released for the CMB, it became possible to perform this measurement with higher precision: the first significant detection of a correlation between the CMB and the large scale structure due to the ISW effect has been described by Boughn and Crittenden [2004a], where a positive correlation was found between the same NVSS and HEAO data and the CMB, at a level compatible with the predictions from the ΛCDM model.

Several groups then repeated the analysis using the WMAP maps from the first, third and fifth years, correlating them with several tracers of the matter density at different redshifts and in different regions of the electromagnetic spectrum. The radio galaxies data from NVSS have been studied again in detail by Nolta et al. [2004] also finding consistent results. Some groups used shallow infrared observations from 2MASS [Afshordi et al., 2004, Rassat et al., 2007] obtaining only limited significance and finding a high level of contamination. Finally, several analysis have been carried out using visible surveys, such as APM and mostly SDSS [Fosalba et al., 2003, Scranton et al., 2003, Fosalba and Gaztanaga, 2004, Padmanabhan et al., 2005, Cabre et al., 2006]. These measurements span a range of redshift going from $z = 0.1$ to $z = 1.0$, and the level of significance of the detection is usually found to be around $2 - 3\sigma$, appearing generally compatible with the expectation from the ΛCDM model. It is interesting to highlight here a point: the ISW signal from a standard ΛCDM model is expected to vanish at redshifts $z > 2$ because the Universe is thought to be matter dominated at that stage. For this reason measurements of this effect at high redshifts are interesting since they are potentially capable of detecting departures from this model, as has been highlighted for example by Lue et al. [2004].

The main motivation behind the first project described in this thesis is the measurement of the ISW effect with the cross-correlation of the CMB data from WMAP and the QSO data from SDSS. This was first proposed in theory by Peiris and Spergel [2000], and made possible by the release of the SDSS data. In particular, we have used a catalogue of quasars originally obtained by Richards et al. [2004] from the first SDSS data release and then extended. This data set has been selected from the whole SDSS database with a neural network method which, after training on a limited subsample, is able to deliver a reliable set of $300,000$ quasars distributed around a median redshift $\bar{z} = 1.5$ with a limited contamination from other objects: the expected stellar contamination is around 5%.

It is worth noting here a technical point. The measurement of the cross-correlation between temperature and density can be described equivalently by the 2-point correlation function in real space, or by its cross power spectrum in the harmonic space, which is in theory equivalent to its Legendre transform. However the real world data are never covering the full sky, which makes dealing with the harmonic space more difficult. On the other hand, the real space approach presents the unwanted feature of having the contributions on different scales mixed. For these reasons, some groups have chosen the first approach, and others the latter. A third possible way to deal with this problem has been introduced by Vielva et al. [2004], McEwen et al. [2007a], and is a compromise between the two methods. These authors use a wavelet basis to expand the signal and recover constraints on the cosmological parameters, which are comparable with the other two methods.

We decided to do our analysis in real space, thus simplifying the understanding of the masks. Therefore, we have measured the cross-correlation between the CMB and the quasars as a 2-point angular correlation function, obtaining a positive detection, which is compatible with the prediction for a ΛCDM model but somewhat higher. To obtain this result, we have kept under control a wide range of possible systematics, such as dust extinction from our galaxy, poor seeing, sky brightness and point sources. We have also confirmed that the measurement is frequency independent, thus excluding any contamination from the Sunayev-Zel'dovich (SZ) effect, which would also produce a correlation.

Special attention has been devoted to the estimation of errors. In the literature, there are two established techniques to estimate errors in this case: the jack-knife (JK) method, in which we generate new random realisations of the data set by excluding some patches of it, and the Monte Carlo technique (MC), which consists of generating mock catalogues based on a theoretical model, as described in detail by Cabre et al. [2007]. The first method has the appealing feature of being completely model-independent, but is intrinsically ambiguous in the definition of how to perform the cuts, while the second is more stable, since we can generate as many random data sets as we want in this way. In this first analysis, we chose to use the MC technique, generating random temperature and density maps based on the ΛCDM model, and taking into account the expected correlations between them.

In this way, we have found that the significance of our detection is $\simeq 2\sigma$, and compatible with the prediction for the ΛCDM model but not with a pure dark matter theory. This represented at the time the highest redshift evidence for dark energy, confirming that the Universe still behaves like ΛCDM at a redshift $z = 1.5$. Nevertheless, this level of significance means that, while important to confirm the standard model, the constraining power of this data set is limited.

From a theoretical point of view, it has been known since the introduction of the cross-correlation technique [Crittenden and Turok, 1996] that the expected signal-to-noise ratio for this measurement is and will remain rather low, being limited to $< 8 - 10\,\sigma$ for a standard ΛCDM model for an ideal measurement spanning the entire redshift range of interest, $0 < z < 3$. In practice, real world surveys add some uncertainties, and especially they only feature a limited redshift range. Therefore, to maximise the signal and obtain more information about cosmology at different redshifts, it is useful to try and combine together the measurements obtained from several data sets. This has been first suggested by Afshordi [2004], Hu and Scranton [2004] in theory, and then implemented by Gaztanaga et al. [2006] and Corasaniti et al. [2005] with a collection of the results then available. These data have also been used by Cooray et al. [2005], Giannantonio and Melchiorri [2006] to constrain other cosmological models. These measurements have been obtained by different groups using sometimes different techniques for both the detection and the error estimation, and then the errors themselves are not independent. Since different catalogues overlap both in redshift and in sky coverage, we expect the measurements to be covariant. However, this earlier analysis accounted for the covariance between the data sets in a fairly arbitrary way, and it did not include the latest measurements, especially the quasars.

This is why we have decided to perform a combined analysis of the ISW effect with all the available data sets. For this purpose, we have collected the data from six catalogues of tracers of the large scale structure: the 2MASS infrared survey, the main galaxies, luminous red galaxies (LRG) and quasars from SDSS, and the aforementioned radio galaxies from NVSS and X-ray background from HEAO. These catalogues span a redshift range $0 < z < 2$ and are therefore able to cover most of the region in which we expect to find the late ISW signal. This project has been carried on as a generalisation of the quasar correlation; however, there are many problems we have to deal with when joining together the results obtained with several data sets. First, we reconsidered all the data set cuts and foreground masks for the catalogues in a consistent way, using their redshift distributions from the data where available or otherwise from models from previous literature. We then measured the density-density angular correlations between pairs of data sets, and their auto-correlations, obtaining results consistent with the ΛCDM model and the redshift distributions of each catalogue. At this point, we calculated the cross-correlation between each catalogue and the CMB, obtaining again results in agreement with the previous measurements and the best ΛCDM model from WMAP, although generally higher. Concerning the error estimation, we extended our analysis to account for three possibilities: the JK errors, obtained using two different cutting procedures, the MC errors from random CMB maps only (MC1), and finally the MC errors from both temperature and density random maps (MC2). For this last step, we developed a new technique which enabled us to generate random maps on the sky which include the correlations with all the other maps. The errors obtained in the three ways are sometimes significantly different; in particular, we found that the JK procedure tends to underestimate them. We chose the MC errors as our best estimation, and in this way we produced the full covariance matrix which, in conjunction with the observed angular correlations, can be used to test different models. We found a total significance of the measurement of 4.5σ.

The constraining power of the ISW data, while still not comparable with other more powerful techniques such as the supernovae, is now significantly increased. For example, if we choose a flat model with one free parameter Ω_m, we obtain from this dataset only the constraints $\Omega_m = 0.20^{+0.09}_{-0.07}$ at 1σ. We also explore other models, obtaining the likelihood contours for flat and curved ΛCDM and wCDM models, showing how the ISW results can be intersected with the constraints from other datasets, such as the CMB, the supernovae and the baryon acoustic oscillations (BAO) to obtain tighter constraints. One interesting feature in the curved case is that the ISW constraints present a degeneracy line in the $\Omega_m - \Omega_\Lambda$ plane which is different from the other data. This is because curvature can produce some late ISW too, which can thus balance the amount of dark energy.

During the final stages of this project a similar and complementary analysis appeared [Ho et al., 2008], performing the analysis of the cross-correlation in harmonic space for four catalogues, consisting of our dataset minus the X-ray background and the main galaxies from SDSS, and with a different dataset for the quasars. The amplitude of the signal measured in this work is higher, at the level of a 2σ excess above the best ΛCDM model. These authors performed the error estimation using the JK and MC1 techniques, finding a total significance of 3.7σ.

Having obtained a complete dataset for the measurement of the ISW effect at several redshifts we can now focus on its possible applications. First, we focus on the possible constraints on modified gravity theories. In fact we know that the phenomenology of acceleration, explained by a cosmological constant or dark energy in the current standard model, might instead be produced by some different more exotic theories of modified gravity.

Several theories of modified gravity have been developed in the past years, along many directions. A first possibility is to modify by hand the Einstein-Hilbert action for gravity, leading to the so-called $f(R)$ theories [Nojiri and Odintsov, 2008]. Another approach is to extend the dimensionality of the Universe by assuming that our observed 4D world is actually embedded in a higher dimensional reality: this is the case of the braneworld models [Maartens, 2004]. The DGP model of gravity, first described by Dvali et al. [2000] and extended by Deffayet [2001], is a particular braneworld theory which has the property of self-acceleration. In more detail, this theory assumes that the observable Universe is contained in a 4D brane where matter and radiation sit and where all forces are bound with the exception of gravity which, at certain scales, is allowed to leak into the outside 5D Minkowski bulk. The scale at which gravity assumes the 5D behaviour is called *critical radius* r_c. At smaller scales there is a transitional regime where the theory is equivalent to a scalar-tensor theory of gravity, and at small scales the standard general relativistic behaviour is recovered.

The evolution equations of this model have two different solutions: in the first branch, called self accelerating (SA), the Universe is spontaneously accelerating at scales (or times) greater than r_c. This means that, by choosing a critical radius comparable to the

Hubble radius today, we can explain the observed acceleration without the need for dark energy nor a cosmological constant; this theory has no extra parameters. From a theoretical point of view, it is known that this branch has a ghost, i.e. an intrinsic instability of the ground state, although its severity is still the argument of debate [Koyama, 2007]. The second, normal branch (NB) does not have such a feature, and therefore it requires an extra parameter, such as a tension of the brane, to act as a cosmological constant thus producing acceleration. This branch is interesting because it features an effective dark energy equation of state which is $w_{\rm eff} < -1$, which is not easily recovered from dark energy models, and therefore could explain the observations should a phantom value of w be observed in the future. This branch is not affected by any ghost problem.

Current observational constraints on this model have been performed looking at the background expansion history [Maartens and Majerotto, 2006, Lazkoz et al., 2006, Lazkoz and Majerotto, 2007], and generally show that the GR theory is favoured by the data, but not by a great margin. It is interesting to deepen the level of this analysis by looking not only at the background expansion, but also at the evolution of the perturbations in these theories, and the formation of structure. In particular, the late ISW effect is a useful probe to constrain structure formation, because of its dependence on the evolution of the gravitational potentials, which is a distinctive feature of these models: in the SA case, the potentials decay earlier than in GR, while in the NB they first increase and then begin to decay later. This reflects directly onto the ISW effect, which depends on the derivatives of the potentials .

As a first step towards a full likelihood analysis of both branches, we decided to first look at the NB. Indeed, in light of recent experiments such as the latest BAO results by Percival et al. [2007b], it seems possible that in the near future a phantom value of w will be found for the dark energy. We first reviewed the observational constraints on this model from the expansion history, using data from the supernovae, CMB shift parameter and the measurement of the Hubble constant. As expected, we found that these data do not favour the flat NB DGP model over GR; however we show that, if curvature is allowed, a rather wide region of the parameter space is still permitted.

This is why we decided to deepen the analysis, using the ISW database to perform a structure formation test. We calculated the projected 4D perturbation equations for this model to find the theoretical CMB, density, and cross power spectra. By comparing the results with our ISW data, we showed that models which are still allowed by the background tests can be ruled out at 2σ by the ISW data: the permitted parameter space region for this model, even in the general curved case, is significantly reduced and is getting very close to the limiting GR case.

While the late ISW effect and the presence of a correlation between the CMB and the density are strictly related, it is important to remember that there are other possible sources of this signal. Some of them act simply as foregrounds, such as the SZ effect, and can therefore be removed or kept under control. However, at higher redshifts there are other phenomena which we have to consider.

Cosmic magnification appears when a distribution of far sources is lensed and distorted by intervening objects. This has been studied in detail by LoVerde et al. [2007], where it is shown that this effect introduces a correction on the expected CMB-density correlations which, at redshifts $z > 2$, becomes significantly large, and therefore will have to be taken into account when performing high-redshift measurements. On the other hand, the lensing of the CMB has negligible effects on the cross-correlation measurements, since it mostly affects the small scales.

Here we decided to focus on another source of correlation at high redshift, namely cosmic reionisation. From current observations we know that in the recent history of the Universe the neutral hydrogen atoms became ionised once again, probably by action of the ignition of quasars or other sources. From the CMB we know that the optical depth to electron scattering of CMB photons is $\kappa_r \simeq 0.09$ which, assuming the Universe reionised instantly, would correspond to a redshift $z_r \simeq 11$. On the other hand, from the observation of spectra of distant quasars we learn that the Universe was fully ionised out to a redshift of $z'_r \simeq 6$. Precisely how the process went is currently matter of debate.

At reionisation a new peak in the CMB photons visibility function appears, meaning that Compton scattering becomes possible once more, even if not highly probable because of the low density at this stage. The ensuing effect on the CMB is a combination of a damping of the anisotropies on small scales, and the formation of additional secondary anisotropies, produced exactly in the same way as the primary did at the last scattering surface. The biggest contribution to these new anisotropies is due to a Doppler effect, which is due to the velocity of the scatterers. The interesting point is that these new anisotropies, though small, have the property of being correlated with the density distribution, since they originated at late times.

We studied this phenomenon in detail, showing how the CMB-density correlation produced by this secondary Doppler effect compares with the ISW effect; for a standard ΛCDM model, we showed that the two effects are comparable for redshifts $z > 2$, which is due to dark energy becoming negligible after that stage. We also show that the corrections due to reionisation on the expected cross-correlation signal are comparable with cosmic magnification, and therefore ought to be included when measuring correlations at high redshifts, or would otherwise bias the conclusions.

We finally explored the observability of the Doppler-density correlation in itself as a tool to understand the history of reionisation, highlighting how its evolution in redshift strongly depends on the behaviour of the visibility function. We found that a small but potentially observable signal-to-noise is present at medium redshifts $z \simeq 5$, which may be probed in future by data such as distant quasars, while a higher signal is probably present at higher redshifts, which will be accessible by the 21-cm radiation measurements [Alvarez et al., 2006].

This thesis is organised as follows: we begin with an introduction of the standard model of cosmology in Chapter 2, where we also review the dark energy problem. We then describe the physics of the CMB in Chapter 3, including the ISW effect. Chapter

4 presents the measurement of the cross-correlation between the CMB and the quasars from SDSS, while Chapter 5 extends this to the full data set of six galaxy catalogues. We then present in Chapter 6 the effect of reionisation on the CMB-density correlations, including the possibility of measuring the reionisation history with this technique. In Chapter 7 we present the possibility of constraining the normal branch of the DGP braneworld with our ISW data, before concluding in Chapter 8.

Chapter 2

The standard model of cosmology

In this chapter we will review the foundations of the standard model of cosmology which has emerged from Einstein's general relativity and a century of observations. We will follow the reviews by Frieman et al. [2008b], Peebles and Ratra [2003] and the classic books by Kolb and Turner [1988], Peebles [1994], Peacock [1999], Dodelson [2003], Weinberg [2008]. For relativity, see for example the book by Wald [1984]. We will follow the standard practice and set the speed of light to unity $c = 1$.

2.1 The Friedmann-Robertson-Walker cosmology

2.1.1 The basic picture

Modern cosmology was born as a consequence of Einstein's general relativity and its fundamental equation

$$G_{\mu\nu} = -\kappa T_{\mu\nu}, \tag{2.1}$$

which expresses the interaction of energy, described by $T_{\mu\nu}$, and geometry, given by $G_{\mu\nu}$. The constant is $\kappa \equiv 8\pi G$, where the G is Newton's gravitational constant.

The standard model of cosmology is based on a modern formulation of the Copernican principle, which states that the Universe is homogeneous and isotropic on large scales [Wu et al., 1998]; this is observationally verified at scales > 100 Mpc from the large scale distribution of galaxies (as observed for example by the Sloan digital sky survey (SDSS) [Yadav et al., 2005])[1] and even more accurately from observations of the cosmic microwave background (CMB), whose anisotropies are of the order of one part in 10^{-5}.

Under these conditions, the most general expression for the metric can be written in the Robertson-Walker form:

$$ds^2 \equiv g_{\mu\nu} dx^\mu dx^\nu = -dt^2 + a^2(t)\gamma_{ij} dx^i dx^j, \tag{2.2}$$

[1]This is however still matter of debate and opposed by some, e.g. see Labini et al. [2008] for possible hints of inhomogeneity and Copi et al. [2008] for a recent claim to possible anisotropy in the CMB. We briefly discuss the possibility of an inhomogeneous Universe in Section 2.3.4.

where the scaling factor $a(t)$ represents the expansion of the Universe and is assumed that today $a = 1$, and the spatial part of the metric can be written in spherical coordinates as

$$\gamma_{ij} dx^i dx^j = \frac{dr^2}{1 - Kr^2} + r^2 d\Omega^2. \tag{2.3}$$

Here K is the curvature parameter which can be 1, 0, -1 depending on the Universe being closed, flat or open respectively.

The comoving distances x are constant by definition. So physical distances d are related to them by the scale factor: $d = ax$, and similarly the comoving time is defined as $\tau \equiv t/a$. From the scale factor, we can define the Hubble parameter as $H(t) \equiv \dot{a}/a$, where the dot indicates a derivative with respect to the proper time t.

We have evidence of the expansion of the Universe and we can measure its velocity by observing the speed v at which galaxies move away from us. The expansion velocity of the Universe is then given by the Hubble law $v = \dot{d} = \dot{a}x \equiv H_0 d$ [Hubble, 1929], where H_0 is the Hubble constant today, which is measured to be $H_0 = (71 \pm 8)$ km/s/Mpc [Freedman et al., 2001]. This is often expressed in terms of the dimensionless quantity $h \equiv \frac{H_0}{100\text{km/s/Mpc}}$.

In order to solve the Einstein equation for this metric, we need to define the stress-energy tensor for the Universe $T^{\mu\nu}$. In the simplest approach, this is well approximated by a perfect fluid with density ρ, pressure P and velocity u^μ, as $T^{\mu\nu} = -Pg^{\mu\nu} + (P + \rho)u^\mu u^\nu$. In this case, the time-time component of the Einstein equation can be solved to obtain the Friedmann equation for the expansion rate H [Friedmann, 1924]:

$$H^2 \equiv \left(\frac{\dot{a}}{a}\right)^2 = \frac{\kappa}{3}\rho - \frac{K}{a^2}, \tag{2.4}$$

which describes the evolution of the Universe, while from the space-space components we can obtain

$$\ddot{a} = -\frac{\kappa}{6}(\rho + 3P)a, \tag{2.5}$$

which describes the acceleration.

It is easy to understand the qualitative behaviour of the expansion from Eq. (2.4). We can see that, if the density ρ is positive, the expansion can only stop if the Universe is closed ($K = 1$). Also we see that at any time t, if the density is equal to the critical value $\rho_{\text{crit}}(t) \equiv \frac{3H^2(t)}{\kappa}$ then the Universe is flat; it will be instead open or closed if the density is smaller or bigger than the critical value respectively. We can use this quantity to define the density parameter $\Omega(t) \equiv \rho(t)/\rho_{\text{crit}}(t)$, to obtain a simplified form of Eq. (2.4)

$$\Omega(t) = 1 - \frac{K}{a^2 H^2}, \tag{2.6}$$

which shows how in a curved Universe $\Omega(t) \neq 1$. From this observation, we can introduce by analogy a curvature density parameter $\Omega_k(t) \equiv 1 - \Omega(t)$. We can also see from Eq. (2.5) that, if $\rho + 3P > 0$, then $\ddot{a}/a \leq 0$, so the expansion must have started at

$a = 0$. Furthermore, if the Universe is closed and the expansion stops, then it will start collapsing back towards a singularity.

Energy conservation is expressed by the condition $T^{\mu\nu}_{;\mu} = 0$, which for a perfect fluid is

$$\dot{\rho} + 3H(\rho + P) = 0, \tag{2.7}$$

which is not independent from the Einstein equation as can be derived from a combination of Eq. (2.4) and Eq. (2.5). In most cases, it is useful to describe this perfect fluid with an equation of state $P = w\rho$ and a sound speed $c_s^2 = \delta P/\delta\rho$. In the simplest case of constant w, from the conservation equation Eq. (2.7) we have the evolution of the density

$$\rho(t) \propto a^{-3(1+w)}. \tag{2.8}$$

From the acceleration equation, we see that the expansion can be accelerating if $w < -1/3$.

2.1.2 The multi-fluid Universe

We see that our Universe is not composed by a single fluid, but several components are present: radiation, matter and vacuum. To make the basic Friedmann-Robertson-Walker (FRW) model more realistic, we need to take into account these components, defining separate quantities for them: we can assume that the total density is $\rho(t) = \sum_i \rho_i(t)$, summing over the components, including curvature.

The total density parameter is now decomposed as a sum of its parts: $\Omega_m(t) \equiv \rho_m(t)/\rho_{\text{crit}}(t)$ for matter, $\Omega_r(t) \equiv \rho_r(t)/\rho_{\text{crit}}(t)$ for radiation, $\Omega_\Lambda(t) \equiv \rho_v/\rho_{\text{crit}}(t)$ for the vacuum energy, so $\Omega(t) = \Omega_m(t) + \Omega_r(t) + \Omega_\Lambda(t)$. We know from observations that the matter content is composed by usual (baryonic) matter plus an additional part of dark matter: $\Omega_m(t) = \Omega_b(t) + \Omega_{dm}(t)$. This extra component is generally modeled as cold dark matter (CDM), but part of it can be in form of massive neutrinos, also called hot dark matter (HDM) so that we have $\Omega_{dm}(t) = \Omega_c(t) + \Omega_{\nu m}(t)$. As for the radiation part, it has contributions from photons and relativistic neutrinos, so that $\Omega_r(t) = \Omega_\gamma(t) + \Omega_\nu(t)$. We usually express the present value of these parameters when we drop the argument t. We can also define the physical parameters $\omega_i \equiv \Omega_i h^2$.

Let us go briefly through them, following Dodelson [2003].

Photons

Photons can interact with with electrons via Compton scattering. Therefore, as long as there were free electrons in the Universe, the photons were in thermal equilibrium with them, forming a primordial plasma; they eventually decoupled after the formation of neutral hydrogen atoms, called recombination. Since then, the Universe has become transparent, and photons propagate freely without interacting with matter. For this reason, in any direction in the sky, it is now possible to observe cosmological photons directly streaming from the last scattering surface, where the last Compton scattering happened, at a redshift $z_\star \simeq 1100$. The free streaming radiation is called *cosmic microwave background* (CMB), and is very well approximated by a black body at a temperature $T = (2.726 \pm 0.002)$ K today [Fixsen et al., 1998].

We can obtain the energy density of the photons from the measurement of T by a simple thermodynamical argument. An integration over the photons' Bose-Einstein distribution function shows that the photons' energy density depends on the temperature:

$$\rho_\gamma = \frac{\pi^2}{15} T^4 \propto a^{-4}, \tag{2.9}$$

here the proportionality depends on the effect of the expansion onto the wavelength of the photons ($\propto a^{-1}$) and thus on their energy. We know very well T from the observations of the CMB, and so we see that the current contribution of this species to the total energy balance is small:

$$\Omega_\gamma h^2 \simeq 2.47 \cdot 10^{-5}. \tag{2.10}$$

We can then study the evolution of this component: for small a, photons were more important. In particular, in the period when this was the dominant component, we have

$$\rho_\gamma(t) \propto a^{-4}, \tag{2.11}$$

and for the expansion we get from the Friedmann equation

$$a(t) \propto \sqrt{t}. \tag{2.12}$$

The equation of state in this case can be obtained from the conservation equation

$$w_\gamma = 1/3. \tag{2.13}$$

We can introduce a variable which we will need in the following, the *optical depth* $\mathfrak{K}$, defined as

$$\mathfrak{K} = \int_\tau^{\tau_0} d\tau' n_e x_e \sigma_T a, \tag{2.14}$$

where n_e is the electron density, x_e the ionisation fraction and σ_T is the Thomson scattering cross-section. This quantity is maximum before recombination. A derived quantity is the visibility function g

$$g(\tau) \equiv \dot{\mathfrak{K}} e^{-\mathfrak{K}}. \tag{2.15}$$

The peak of this function defines the recombination time, after which it will steadily decrease unless reionisation happens.

Neutrinos

Neutrinos constitute the rest of the radiative contribution to the energy density. We can assume that this component too was once in equilibrium with the primordial plasma, to decouple from it earlier than the photons and, in particular, earlier than the electron-positron annihilation, which caused a reheating of the plasma. For this reason, from a calculation of the entropy of this process, it is possible to find that for the neutrino temperature it holds

$$\frac{T_\nu}{T_\gamma} = \sqrt[3]{\frac{4}{11}}. \tag{2.16}$$

For neutrinos we can use the Fermi-Dirac statistics;

$$\rho_\nu = 6 \int \frac{d^3 p}{(2\pi^3)} \frac{1}{e^{E/T_\nu} + 1} \sqrt{p^2 + m_\nu^2}. \tag{2.17}$$

If we assume that neutrinos are massless, the integration over the distribution function yields

$$\Omega_\nu h^2 = 1.68 \cdot 10^{-5}, \tag{2.18}$$

while for massive neutrinos with mass m_ν we have

$$\Omega_\nu h^2 = \frac{m_\nu}{94\text{eV}}. \tag{2.19}$$

Baryons

Measurements of the baryonic density are possible from the study of primordial big bang nucleosynthesis (BBN). The abundance of the heavy elements after this process depends on the abundance of protons and neutrons: this is the baryonic density at the time of nucleosynthesis, and depends on the physical volume, thus scales as

$$\rho_b \propto a^{-3}. \tag{2.20}$$

From the measurement of the abundances of these light elements today, we can estimate the baryonic density $\Omega_b h^2$. In particular, it is possible to measure the abundance of deuterium in high-redshift objects, so that the abundance is not too different from the primordial one. From observations by Kirkman et al. [2003] we know that

$$\Omega_b h^2 = 0.0214 \pm 0.0020. \tag{2.21}$$

This result agrees with observations from the amount of gas in galaxies and in the intergalactic medium, and with the CMB.

Dark matter

When measuring matter density with methods which do not use interaction with light, such as the rotational velocities of galaxies, we always find a completely different result for the total matter density; this can be explained if we assume the existence of a new component, called dark matter, which amounts to the majority of the total matter density. For example, the result obtained from the CMB data from WMAP 5 yr is [Dunkley et al., 2008]

$$\Omega_{dm} = 0.214 \pm 0.027. \tag{2.22}$$

The currently favoured model for this component is cold dark matter (CDM), which is supposed to be composed by collisionless, heavy particles ($m \sim 1$GeV). A possible alternative is the hot dark matter (HDM) model, where this role is played by massive neutrinos.

Since density is again fixed by the physical volume, we have in this case as well as for baryons

$$\rho_{dm}(t) \propto a^{-3}. \tag{2.23}$$

This means that, after radiation, the Universe will be in a matter dominated era. In this case

$$a(t) \propto t^{2/3}, \tag{2.24}$$

and the equation of state is given by the conservation equation

$$w_{dm} = 0. \tag{2.25}$$

Curvature

We can consider curvature as any other energy component by defining an energy density

$$\rho_k(t) = -\frac{3K}{\kappa a^2}. \tag{2.26}$$

If this is treated as a perfect fluid, it has an equation of state

$$w_k = -1/3. \tag{2.27}$$

It follows that, if $K \neq 0$, the matter era will be followed by a curvature era, with expansion law

$$a(t) \propto t. \tag{2.28}$$

There is currently no observational evidence for curvature; the current limits on it from WMAP 5yr are $-0.2851 < \Omega_k < 0.0099$ at 95 % c. l. [Dunkley et al., 2008].

Vacuum

A last component that can be added is the energy of the vacuum, with a constant density $\rho_v(t)$ and equation of state $w_v = -1$. It follows that, if this component is present, the era of curvature will be followed by an era of vacuum, with an exponentially accelerating expansion law (see Section 2.2).

By combining all the known and conjectured components, the Friedmann equation can therefore be written as

$$\left(\frac{H}{H_0}\right)^2 = \frac{\Omega_r}{a^4} + \frac{\Omega_m}{a^3} + \frac{\Omega_k}{a^2} + \Omega_v, \tag{2.29}$$

from which the expansion history of the Universe can be integrated given the present day parameters Ω_i. From this equation we can study the dynamics of the Universe in different scenarios.

Depending on the value of the parameters, the behaviour of the Universe can be different: in the flat case, all components lead to a decelerated expansion with the exception of positive vacuum energy, which leads to acceleration. In the future, the Universe may expand forever or recollapse to a big crunch, depending on the balance between the attractive contribution of matter or the repulsive effect of vacuum energy. Conversely, by observing the evolution of the expansion history we can determine the energy content and the value of the parameters. A particularly effective technique to do so is to observe distant supernovae, as we will see in the next section.

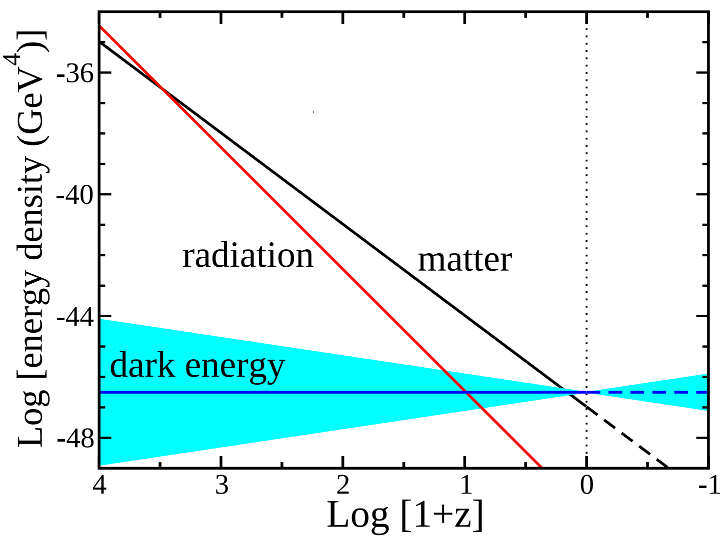

Figure 2.1: Evolution of the energy density for radiation, matter and vacuum (dark) energy. For the latter, the bands correspond to $w = -1 \pm 0.2$. Reprinted from Frieman et al. [2008b].

We can see the qualitative behaviour of the scaling of the energy densities for all the components in Fig. 2.1, which also shows the times of equality.

2.1.3 Distances and horizons

Let us fix some notation. A useful method to measure distances in cosmology is the redshift of the sources z, which is produced by the Doppler shift of the spectral lines due to cosmic expansion. It is related to the scale factor by the $1 + z = a^{-1}$.

The limited speed of light means that there exists a particle horizon, which is the distance light can travel in the lifetime of the Universe t_0. Particles further away can never have been in causal connection. In particular, in a time dt light travels a distance dx/a ($c = 1$). The total distance that light could have travelled since the big bang corresponds to the *particle horizon*, and at any moment is equal to the conformal time

$$\tau = \int_0^t \frac{dt'}{a(t')} = \int_0^a \frac{da'}{a'^2 H(a')} = \int_z^\infty \frac{dz'}{H(z')}. \tag{2.30}$$

By changing the order of integration, we can also define the *comoving distance* χ light could have travelled as between a source at a scale factor a and the observer today as

$$\chi = \int_t^{t_0} \frac{dt'}{a(t')} = \int_a^1 \frac{da'}{a'^2 H(a')} = \int_0^z \frac{dz'}{H(z')} \tag{2.31}$$

The *Hubble radius* $H^{-1}(t)$ represents the time and space scale of the Universe expansion, and therefore discriminates between phenomena which can be in causal contact at the time t. Its value coincides with the particle horizon for a radiation dominated Universe.

The *sound horizon* is the distance that sound, as opposed to light, could travel since the big bang. It is therefore $r_s(\tau) = \int_0^\tau c_s(\tau')d\tau'$ for a sound speed c_s.

The *angular distance* is defined as the distance to an object of dimension l subtending an angle ϑ: $d_A = l/\vartheta$; it is related to the comoving distance by the

$$d_A = \frac{a}{H_0\sqrt{|\Omega_k|}} \cdot \mathrm{sins}\left(\sqrt{\Omega_k} H_0 \chi\right), \tag{2.32}$$

where the function $\mathrm{sins}(x)$ is defined as $\sin(x)$, x or $\sinh(x)$ depending on Ω_k being negative, zero or positive respectively.

Finally, the *luminosity distance* d_L represents the distance to an object with known luminosity L and flux $F = \frac{L}{4\pi d_L^2(a)}$, and is related to the others by the

$$d_L = \frac{1}{aH_0\sqrt{|\Omega_k|}} \cdot \mathrm{sins}\left(\sqrt{\Omega_k} H_0 \chi\right). \tag{2.33}$$

2.2 Dark energy

Observational evidence suggests that a new energy component is present in the Universe, which is called *dark energy* and whose contribution is starting to dominate in recent times. We follow the reviews by Carroll [2001], Copeland [2007], Frieman et al. [2008b].

2.2.1 Observational evidence

A model with no vacuum component or dark energy runs into several observational problems.

CMB

The first point is the constraint on flatness we see in the cosmic microwave background (CMB). As it will be discussed in more detail later, the CMB radiation is not perfectly isotropic but has small angular fluctuations; the angular power spectrum of these presents detailed, observable features that depend on the cosmological parameters.

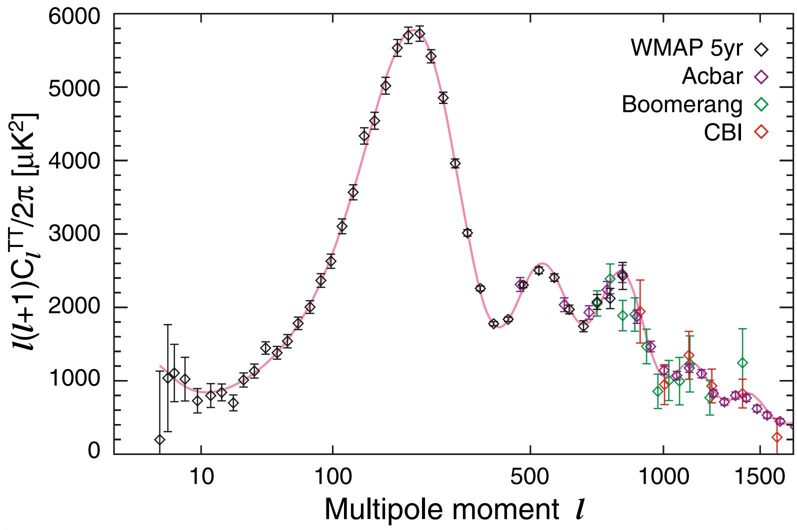

Figure 2.2: Current status of the measurements of the CMB temperature anisotropies spectrum, including data from WMAP5, ACBAR, BOOMERANG and CBI. The red line is the standard ΛCDM theory. Reprinted from Nolta et al. [2008].

In particular, the total energy density of the Universe is measured by the position of the first peak l_1: this is because this scale corresponds to the angular dimension of the Universe at the epoch of last scattering. The dependence approximately $l_1 \sim 220\sqrt{\Omega}$ and, from the accurate measurements available today and summarised in Fig. 2.2, we can conclude that $\Omega \simeq 1$. However, this is in clear contrast with the sum of the observed components of the Universe: the only solution is to introduce heuristically a new component X with energy density $\Omega_X \simeq 0.7$, i.e. dark energy.

Supernovae

A second point comes from the observation of distant supernovae (SNe) of type Ia, which are thought to be explosions of white dwarf stars in binary systems capturing matter from the companion star. When the stellar mass reaches the Chandrasekhar limit ($\simeq 1.4 M_\odot$), the pressure can not balance gravitational infall. The resulting collapse produces a violent explosion. We know that these sources are standardisable candles [Phillips, 1993]: after correcting their luminosity curve, their absolute magnitude is constant, $M = -19.3$, which means that from the observed magnitude m we can reconstruct their total flux and therefore the luminosity distance d_L in function of redshift, which depends on the expansion history. This is commonly expressed by defining the distance modulus μ:

$$\mu \equiv m - M = 5\,\mathrm{Log}\, d_L + 25. \tag{2.34}$$

The observations have been showing from 1998 [Perlmutter et al., 1999, Riess et al., 1998] that distant SNe appear fainter that they should given a purely matter dominated expansion, so that we need to introduce a late acceleration in the model in order to fit these data. This is achieved with the introduction of a positive vacuum energy component (dark energy). We show in Fig 2.3 the updated Hubble diagram of SNe from several projects, as compiled by Kowalski et al. [2008].

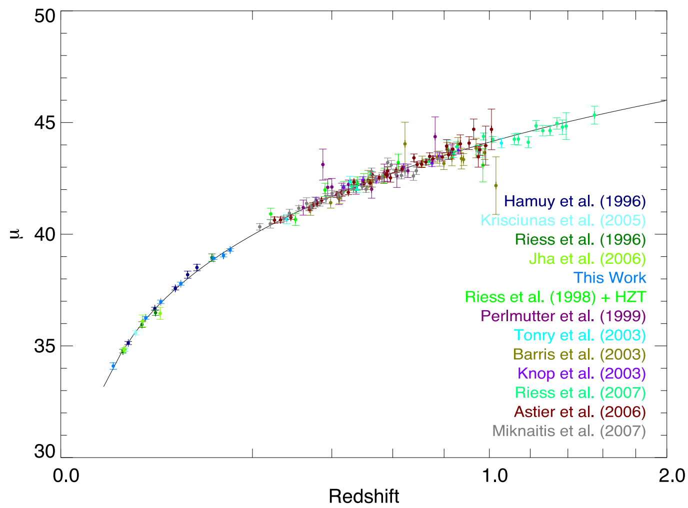

Figure 2.3: Current status of the measurements of the Hubble diagram of type Ia supernovae. Reprinted from Kowalski et al. [2008]. The plot shows the distance modulus $\mu \equiv |m - M|$ in function of z. The line is the best fit model ($\Omega_m = 0.29$, $\Omega_\Lambda = 0.71$).

Ages

Another reason in favour of dark energy is the age of the Universe t_0, which for an Einstein-de Sitter (matter only) model is $t_0 = \frac{2}{3H_0} \simeq 9$ Gyr. This is in contradiction with the age of the oldest observed objects, such as globular clusters, which instead gives

12 Gyr $< t_0 <$ 15 Gyr [Krauss and Chaboyer, 2003]. Once again, the introduction of dark energy solves the puzzle, increasing the age of the Universe and thus bringing the expected value in line with the observational facts.

Other probes

Further evidence for dark energy comes from the observation of the large scale structure in the Universe. The baryon acoustic oscillations (BAO), besides leaving the big oscillatory pattern in the CMB, also produce much smaller oscillations in the matter power spectrum, corresponding to a single bump in the matter angular correlation function at a scale of $\simeq$ 100 Mpc, as shown in Fig. 2.4. A measurement of this feature in a catalogue of sources (e.g. luminous red galaxies) is an accurate estimation of the angular distance to the scale of the sources, whose value again indicates the presence of dark energy [Eisenstein et al., 2005, Percival et al., 2007b].

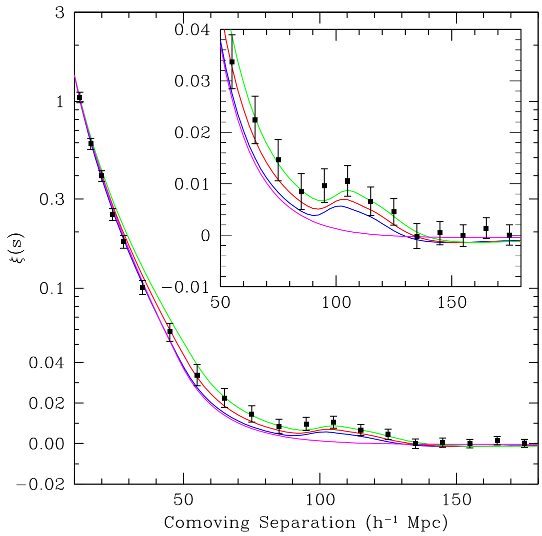

Figure 2.4: Detection of the baryon oscillations in the clustering of luminous red galaxies from SDSS by Eisenstein et al. [2005]. The plot shows the 2-point galaxy correlation function in redshift space; the inset is an expanded view. Curves are ΛCDM predictions for $\Omega_m h^2 = 0.12$ (green), 0.13 (red), and 0.14 (blue). Magenta curve is a ΛCDM model without BAO.

Weak gravitational lensing [Schneider, 2005] is a powerful technique to map the distribution of dark matter in the Universe by observing the distortion of background galaxies by the foreground dark matter distribution. This has been detected since 2000 [Bacon et al., 2000, Kaiser et al., 2000, van Waerbeke et al., 2000, Wittman et al., 2000], and its observation puts constraints on the matter energy density $\Omega_m \simeq 0.25$, again pointing at a dark energy dominated Universe. It is currently conjectured that this technique has the potential to become one of the most powerful methods to constrain dark energy in the near future [Huterer, 2002], with the deployment of a new generation of almost full-sky lensing surveys such as Pan-STARRS.

Further evidence of dark energy comes from the measurement of the integrated Sachs-Wolfe effect, which we will describe in detail in the following.

2.2.2 Phenomenological interpretation

If we try to construct a model based on the observations, the requirement from it is that it should explain the observed acceleration of the Universe and the low value of the matter energy density without deviating significantly from the observed flatness. If we consider a fluid model with a constant equation of state w_{de}, which can also be extended to include a redshift dependence $w_{de}(z)$, this means that the acceleration Eq. (2.5) becomes

$$\frac{\ddot{a}}{a} = -\frac{\kappa}{6}\sum_i \rho_i(1+3w_i), \tag{2.35}$$

and therefore an accelerating model requires $w_{de} < -\frac{1}{3\Omega_{de}}$, which for a flat model with $\Omega_m \simeq 0.3$ means

$$w_{de} < -1/2; \tag{2.36}$$

this condition has to be satisfied independently from the theoretical model.

It is common practice to include this dark energy fluid in the model and compare the resulting predictions with the observations. We can see in Fig. 2.5 the current constraints on the parameters from many of the probes described above. We can see from these plots that a flat model with $\Omega_\Lambda \simeq 0.7$, $\Omega_m \simeq 0.3$ and $w \simeq -1$, which is at the moment purely based on phenomenology, satisfies all observational tests, and is therefore called the concordance model of cosmology. From this, it follows that the matter-radiation equality happened at $z^r_{\rm eq} \simeq 3000$, while the matter-vacuum is happening at much more recent times $z^v_{\rm eq} \simeq 0.5$.

If we perform a more generic analysis allowing free values for both curvature and dark energy equation of state, then the uncertainties become moderately bigger, but the result is still consistent with the concordance model. It is interesting to notice that small departures from $w = -1$ are not equivalent on either side, since a particular scenario appears if $w < -1$. In this case, the solution of the Friedmann equation is

$$a(t) = (t_r - r)^{\frac{2}{3(1+w)}}, \tag{2.37}$$

where t_r is a constant. The Hubble rate grows as

$$H = -\frac{2}{3(1+w)(t_r - t)}, \tag{2.38}$$

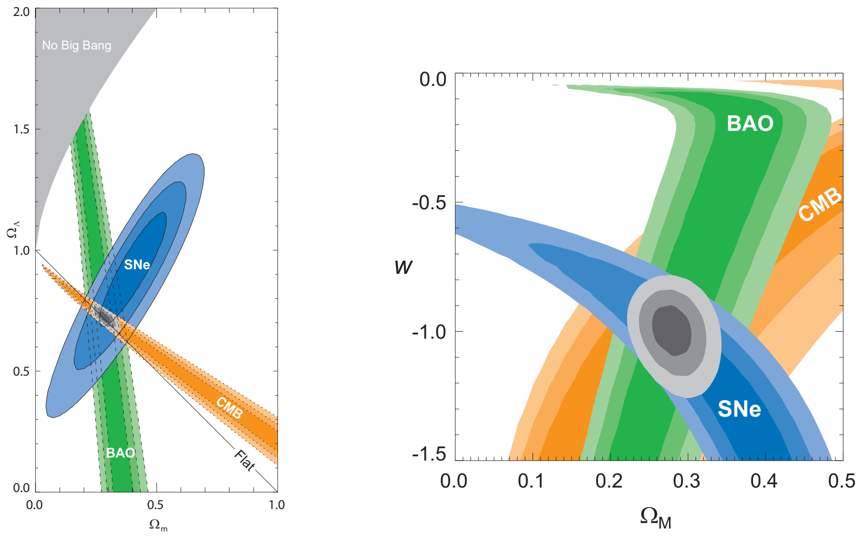

Figure 2.5: Current constraints on the fundamental cosmological parameters from the intersection of several observations. Reprinted from Kowalski et al. [2008]. The left panel shows the constraints for curved models with $w = -1$ (cosmological constant), while on the right are considered flat models with different values of w.

which diverges for $t \to t_r$. This is called a Big Rip singularity and is a peculiarity of these models that may represent a non-physical problem, possibly solved in quantum gravity scenarios.

In many theoretical frames, the dark energy equation of state is a quantity which can evolve in time. To account for such a possibility, it is common practice to parametrise such an evolution with two parameters w_0, w_a in the form

$$w(a) = w_0(1-a)w_a. \tag{2.39}$$

Current constraints on the evolution of w are still weak, as we can see from Fig. 2.6.

Another quantity that can be studied is the sound speed of dark energy, c_s, which in the perfect fluid model is purely adiabatic

$$c_a^2 \equiv \frac{\dot{P}}{\dot{\rho}} = w - \frac{\dot{w}}{3H(1+w)}. \tag{2.40}$$

In this case, the sound speed is completely fixed by w; however, this definition can be extended to more general models where non-adiabatic processes are possible, by substituting the derivatives with small increments:

$$c_s^2 \equiv \frac{\delta P}{\delta \rho}. \tag{2.41}$$

A measurement of this quantity would be interesting to estimate the clustering of the dark energy fluid. However, current data are not accurate enough to yield significant

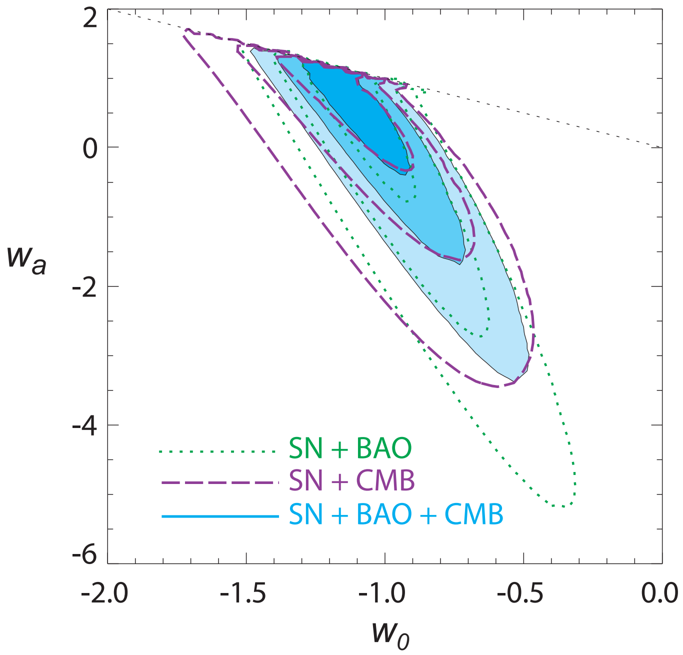

Figure 2.6: Current constraints on the evolution of w at 1, 2, and 3 σ, from Kowalski et al. [2008].

constraints on this parameter [Bean and Dore, 2004, Hannestad, 2005], especially since around the favoured value of $w = -1$ the dependence on c_s^2 vanishes.

2.3 Models of dark energy

2.3.1 Cosmological constant

The simplest model which can explain the current observations is called ΛCDM, and it is obtained from a matter model by adding a cosmological constant Λ. This can be done because we can always add a constant in the action for gravity, as

$$S = \frac{1}{2\kappa} \int d^4x \sqrt{-g}(R - 2\Lambda). \tag{2.42}$$

The variation of this action gives then a new Einstein equation

$$G_{\mu\nu} + \Lambda g_{\mu\nu} = -\kappa T_{\mu\nu}, \tag{2.43}$$

from which a new Friedmann equation follows

$$H^2 = \frac{\kappa}{3}\rho - \frac{K}{a^2} + \frac{\Lambda}{3}. \tag{2.44}$$

This reduces to the standard form Eq. (2.4) as described before if we include an effective density and pressure for Λ:

$$\rho_\Lambda = \frac{\Lambda}{\kappa} = \text{constant}. \tag{2.45}$$

In this model, after matter domination, the Universe will enter a dark energy era during which the scale factor will undergo exponential expansion:

$$a(t) \propto e^{Ht}, \tag{2.46}$$

with $H = \sqrt{\Lambda/3}$.

This constant had been first introduced by Einstein in order to achieve a static Universe, which can be found with a positive curvature and is anyway unstable. Afterwards, Λ had become redundant with the discovery of the Hubble expansion, only to become once again popular in the 1990s to explain the observed acceleration.

Another consequence of Λ is the Newtonian limit of the 00 component of Eq. (2.44): the Poisson equation for the potential becomes $\nabla^2\Phi = \frac{\kappa}{2}\rho - \Lambda$. This means that, to reproduce the Newtonian limit, the scale at which Λ becomes dynamically important has to be much larger than the scales at which Newtonian gravity works well, i.e. solar system scales.

Vacuum energy

By looking at particle physics, we can think of an interpretation of the cosmological constant and dark energy, since this can be identified with the vacuum energy. If we consider a scalar field ψ with potential energy $V(\psi)$, the action is

$$S = \int d^4x \sqrt{-g} \left[\frac{1}{2} g^{\mu\nu} \partial_\mu \psi \partial_\nu \psi - V(\psi) \right], \tag{2.47}$$

and the energy-momentum tensor is

$$T_{\mu\nu} = \frac{1}{2} \partial_\mu \psi \partial_\nu \psi + \frac{1}{2} \left(g^{\rho\sigma} \partial_\rho \psi \partial_\sigma \psi \right) g_{\mu\nu} - V(\psi) g_{\mu\nu}. \tag{2.48}$$

The state of minimum energy for the field will be the one with no kinetic contribution, which is given by

$$T^0_{\mu\nu} = -V(\psi_0) g_{\mu\nu} \equiv \rho_v g_{\mu\nu}, \tag{2.49}$$

where ψ_0 is the value of the field for which V is minimum. We have then introduced the vacuum energy density ρ_v, which is in general non zero. We can then think of the vacuum as a perfect fluid, with equation of state -1, and identify $\rho_v \equiv \rho_\Lambda$.

There are many theoretical contributions to the vacuum energy: besides the potential V and a bare constant Λ_0, there are several other additions. It is known that in quantum mechanics the study of a harmonic oscillator presents an issue: the state of minimum energy has $E = \frac{1}{2}\hbar\omega$, which can be artificially set to zero because we do not consider gravity. This problem deepens in quantum field theory, as the vacuum energy we obtain is infinite. The theory can then be fixed thanks to the introduction of the UV cutoff, i.e. considering that the theory will not be valid for energies greater than some $k_{\max}$; in this way the vacuum energy becomes $\rho_v \sim \hbar k_{\max}^4$, which is a constant and can be again eliminated if we do not consider gravity; however this needs to be considered in cosmology.

A good way to understand vacuum energy is to think of it as the possibility of creating and destructing particle-antiparticle pairs, as in the vacuum closed-loop Feynmann diagrams. This phenomenon has an observable consequence, the Casimir effect [Casimir, 1948], which has been experimentally observed [Lamoreaux, 1997].

Problems of dark energy

Unfortunately, this theory is problematic, as we can see when we try to estimate the vacuum energy quantitatively: the contributions to the vacuum energy from the standard model of particle physics come from the electro-weak symmetry breaking and quantum-chromodynamics. To these terms, we have to add other contributions due to grand unification theories that we suppose were valid in primordial times, and the cutoff due to the Planck scale. If we compare these terms with the cosmological observations, we have that

$$\frac{\rho_v^{\text{theory}}}{\rho_v^{\text{observed}}} \sim 10^{120}. \tag{2.50}$$

This discrepancy of 120 orders of magnitude, or of 30 orders of magnitude if we consider the equivalent masses, is possibly the worst prediction of today's physics, and is known as the cosmological constant problem [Weinberg, 1989]: even if it is possible in principle that different contributions cancel out by summing up with opposite signs, this does not appear realistic. It would be even more absurd to imagine that these contributions do not perfectly cancel out, but originate the small cosmological constant we observe. This is why this is called the *fine tuning problem*.

There are several attempts to explain this apparent paradox, although the problem is still open. A first possible path is given by supersymmetry theories (SUSY), which are based on the idea that every fermionic particle in the standard model has an equal-mass SUSY bosonic partner and vice versa. In this way, the contributions to the vacuum energy from bosons and fermions cancel out, thus leading to a cancellation of it [Zumino, 1975]. The problem is that, in reality, the supersymmetry break can not happen at an energy lower than $\sim 10^3$ GeV, since we have not yet detected any supersymmetric particle. Therefore we can only solve the paradox half way: $M_{\text{SUSY}}/M_v^{\text{cosmo}} \sim 10^{15}$. The new large hadronic collider (LHC) facility at CERN will soon start a new search for supersymmetric particles, and it may shed new light on this problem.

Another possibility is given by string theory. However the various types of string theories are defined in space-times with extra dimensions, and it has not yet been possible to create a theory leading to a compactification of the extra dimensions, the breaking of supersymmetry and the production of a small but non-zero vacuum energy. An even different possible path to the solution of this puzzle is given by loop quantum cosmology.

A second type of problem which remains open is related to the *why now* question: it appears that we are living in the cosmologically short epoch in which matter and vacuum energy densities are of the same order of magnitude. The epoch of matter-vacuum equality is $z^v_{\rm eq} \simeq 0.5$.

There exists a possible solution to this apparent coincidence which is based on anthropic arguments [Weinberg, 1987]: in particular, we may suppose that a necessary condition for the existence of observers is the formation of structure which can not happen during a vacuum dominated phase. Since the first galaxies had already formed at $z \simeq 4$, the matter-vacuum equality must happen later. From this condition, however, we can only obtain a weak limit, $\Omega_v/\Omega_m < 125$. The anthropic viewpoint can be combined with a multiverse string theory if we imagine that the cosmological constant is a random variable which assumes different values in different realisations of the Universe. In this case, the anthropic principle would bias us to observe a small value of Λ [Bousso and Polchinski, 2000, Susskind, 2003].

2.3.2 Scalar fields and other models

Since the identification of dark energy with the vacuum presents the aforementioned difficulties, a range of possible alternatives is currently being explored. It is important however to bear in mind that, from the current observations, there is no evidence for an evolving dark energy component, and everything remains perfectly consistent with the simplest model of the cosmological constant.

The confrontation with these problems, and especially the *why now* question, has led theorists to speculate that vacuum energy may be not a constant, but a dynamical quantity, which can happen to be small today because the Universe is old. A dynamical vacuum energy is usually called *quintessence*. Perhaps the most natural and popular way to realise a dynamical model is to introduce one ore more scalar fields which are added to the total energy density of the Universe. This class of models was introduced by Wetterich [1988], Ratra and Peebles [1988]. For a review, see Linder [2008].

In this scenario the fields are minimally coupled to gravity and, if a suitable potential is chosen, it can drive the observed acceleration. Let us assume a single scalar field $\varphi(x^\mu)$ for simplicity, with Lagrangian density $\mathcal{L}_\varphi = \partial^\mu \partial_\mu \varphi - V(\varphi)$, where $V(\varphi)$ is the field potential and the kinetic contribution is assumed to be canonical. The stress-energy tensor for such a field can be identified with the result for a perfect fluid with density and pressure given by

$$\begin{aligned} \rho_\varphi &= \frac{\dot{\varphi}^2}{2} + V(\varphi) + \frac{1}{2}(\nabla\varphi)^2 \\ P_\varphi &= \frac{\dot{\varphi}^2}{2} - V(\varphi) - \frac{1}{6}(\nabla\varphi)^2. \end{aligned} \tag{2.51}$$

The gradient terms can be neglected because, to explain acceleration, we need a very light field, whose Compton wavelength will be greater than the Hubble scale, and will therefore be spatially smooth on sub-horizon scales.

From the conservation equation Eq. (2.7), we obtain the equation of motion of the field:

$$\ddot{\varphi} + 3H\dot{\varphi} + V'(\varphi) = 0. \tag{2.52}$$

This is the Klein-Gordon equation, and it describe a particle moving through a potential $V(\varphi)$ with a friction $-3H\dot{\varphi}$: the field will roll towards a smaller $V(\varphi)$, until it reaches a minimum of the potential. This could be the value of the observed cosmological constant, but unfortunately we do not have any reason why its value should be small.

We can obtain the equation of state parameter w for the field from Eq. (2.51):

$$w = \frac{-1 + \dot{\varphi}^2/2V}{1 + \dot{\varphi}^2/2V}, \tag{2.53}$$

from which we can see that $-1 <= w <= 1$, and the phantom disaster does not happen. If the time evolution is slow, then $w \simeq -1$, and the field behaves like a slowly varying vacuum energy.

The original proposal for the potential $V(\varphi)$ was

$$V(\varphi) = M^{4+\alpha}\varphi^{-\alpha}, \tag{2.54}$$

which has been studied in detail by Zlatev et al. [1999]; however there is no particular reason to favour one form of the potential with respect to others. A different classification of quintessence theories has recently been proposed by Caldwell and Linder [2005], and consists in the two classes of *thawing* and *freezing* models, depending on whether the field picks up speed or slows down as the time progresses.

From the equivalence of the field and the fluid treatments, we could think of inverting the problem and constrain the potential and kinetic laws from the observed fluid quantities ρ and w, as proposed by Sahni and Starobinsky [2006]. However, many issues affect this possibility, such as the need to use not only the fluid parameters but also their much less constrained derivatives, and the fact that if the field is as we think extremely flat, our limited spatial range of observations will only be able to constrain it weakly.

Other more complicated scalar-field models have been proposed, including fields with the opposite sign of the kinetic term [Caldwell, 2002] which can be useful to obtain equivalent fluids with $w < -1$, although they are generally unstable [Carroll et al., 2003]. K-essence theories, on the other hand, feature an even more complex kinetic term which depends on the field [Armendariz-Picon et al., 2001].

In general, dynamical models of dark energy can give some sort of explanation, but at the present can not deliver a complete solution to the puzzle. In fact, while the coincidence problem may be solved by some classes of models, the smallness of the cosmological constant or, in this context, the smallness of the minimum of the potential, remains obscure. Also, to explain acceleration on the observed scales, the field potentials must be very flat, which translates into an extremely light mass for the fields ($m_\varphi \simeq 10^{-42}$ GeV), which makes it difficult to connect them with realistic particle physics theories.

2.3.3 Modified gravity theories

The evolution history of the Universe is given by the Einstein equation. We have seen that, to explain the observed late time acceleration, we need to introduce some additional component to the stress-energy tensor with certain properties which will induce the desired behaviour at late times. An interesting alternative is to modify the geometrical part instead, i.e. the left hand side of the Einstein equation. Such modifications can arise for example due to corrections depending on higher order curvature terms in the Einstein-Hilbert action while remaining in the normal 4D framework, and this is the case of the $f(R)$ theories. A more drastic approach is to assume that the 4D Universe we observe is in reality embedded in a higher dimensionality bulk, whose extra dimensions are unobservable thank to some mechanism. These latter models are called braneworld.

Let us go through some basic points of these approaches, focusing on the metric $f(R)$ theories and the DGP braneworld model. We follow the reviews by Sotiriou and Faraoni [2008], Lobo [2008], Nojiri and Odintsov [2008], Copeland [2007].

$f(R)$ theories

It is known that a quadratic term in the Ricci scalar R will lead to an inflationary solution in the early Universe [Starobinsky, 1980], while terms containing its inverse powers may produce late time acceleration [Capozziello et al., 2003], although these models often break solar system constraints [Chiba, 2003].

In more detail, the generic action for a gravity theory is given by

$$S = \int d^4x \sqrt{-g}[f(R) + \mathcal{L}_m], \tag{2.55}$$

where $f(R)$ is a generic function of the Ricci scalar R and $\mathcal{L}_m$ is the matter Lagrangian density. The variation of this with respect to the metric yields the field equation for the Einstein tensor

$$FR_{\mu\nu} - \frac{1}{2} f g_{\mu\nu} - \nabla_\mu \nabla_\nu F + g_{\mu\nu} \Box F = -\kappa T^m_{\mu\nu}, \tag{2.56}$$

where $F \equiv \partial f / \partial R$ and $T^m_{\mu\nu}$ is the matter stress-energy tensor. This equation can be rewritten by moving all the modifications from standard GR to the r.h.s., as

$$G_{\mu\nu} \equiv R_{\mu\nu} - \frac{1}{2} R g_{\mu\nu} = -\kappa T^{\text{eff}}_{\mu\nu}, \tag{2.57}$$

introducing an effective stress-energy tensor $T^{\text{eff}}_{\mu\nu} = T^c_{\mu\nu} + T^m_{\mu\nu}/F$. The curvature part of this tensor $T^c_{\mu\nu}$ contains now all the effects of the modification of gravity.

If we consider a FRW metric, we can now derive the new generalised Friedmann equations, which are identical to the GR form Eqs. (2.4, 2.5) with $\rho_{\rm eff} = \rho_{\rm m} + \rho_c$ and $P_{\rm eff} = P_{\rm m} + P_c$. The density and pressure of the curvature fluid can be found to be [Capozziello et al., 2003, Sotiriou, 2007]

$$\begin{aligned} \rho_c &= \frac{1}{\kappa F}\left\{\frac{1}{2}[f - Rf] - 3\frac{\dot{a}}{a}\dot{R}F'\right\}, \\ P_c &= \frac{1}{\kappa F}\left\{2\frac{\dot{a}}{a}\dot{R}F' + \ddot{R}F' + \dot{R}^2F'' - \frac{1}{2}[f - RF]\right\}. \end{aligned} \tag{2.58}$$

In absence of matter $P_{\rm m} = \rho_{\rm m} = 0$ and we can define an effective equation of state $w_{\rm eff} \equiv P_{\rm eff}/\rho_{\rm eff} = P_c/\rho_c$. If we for example choose $f(R) \propto R^n$, we will have the following expansion law:

$$a \propto t^{\alpha}, \qquad \alpha = \frac{-2n^2 + 3n - 1}{n - 2}, \tag{2.59}$$

valid for $n \neq 1$, which corresponds to the effective equation of state

$$w_{\rm eff} = -\frac{6n^2 - 7n - 1}{6n^2 - 9n + 3}, \tag{2.60}$$

where as usual acceleration can be achieved if $w_{\rm eff} < -1/3$. This model becomes de Sitter ($w_{\rm eff} = -1$) for $n \to \infty$.

If instead we parametrise the action with some $n > 0$ [Carroll et al., 2004]

$$f(R) = R - \mu^{2(n+1)}R^{-n}, \tag{2.61}$$

it is possible to show that the evolution of the scale factor is given by $\alpha = (2n+1)(n+1)/(n+2)$, and the effective equation of state becomes

$$w_{\rm eff} = -1 + \frac{2(n+2)}{3(2n+1)(n+1)}. \tag{2.62}$$

We see that for $n = 1$ we get $w_{\rm eff} = -2/3$, while for $n \to \infty$ the spacetime becomes de Sitter.

Many of these models can reproduce the observed acceleration of the Universe. However, $f(R)$ gravity is affected by several problems. As shown by Chiba [2003], it is possible to derive the $f(R)$ equations of motions from a scalar-tensor theory by introducing a transformation $\{R, f\} \to \{\varphi, V\}$, which has Lagrangian density $\mathcal{L}_{BD} = \varphi R - V(\varphi)$, i.e. a Brans-Dicke parameter $\omega_{BD} = 0$, which contradicts current constraints from solar system observations [Bertotti et al., 2003]. Some more complex $f(R)$ models have been proposed that may be able to solve this problem [Nojiri and Odintsov, 2003]. Another serious issue has been discovered by Amendola et al. [2007b]: in most of the $f(R)$ models the scale factor in the matter dominated era does not evolve like $a \propto t^{2/3}$, but as $a \propto t^{1/2}$, in contradiction with the observations. It may be possible to find models which escapes these constraints and issues, but at the price of greater complication.

Braneworlds and the DGP model

As we have seen, it is difficult to produce correct infrared modifications of GR with simple modifications of the action, since the resulting theories are often unstable[2], and generally do not have any physical motivation. For this reason, a different approach is possible, by extending the theory to account for extra dimensions, which corresponds to the addition of infinite degrees of freedom from the 4D point of view.

The idea of braneworld [Maartens, 2004, Koyama, 2008] has been developed in the context of string theory. In particular, M-theory is a temptative unification theory of all the existing superstring theories [Becker et al., 2007] which attempts to unify all known physics in an 11 dimensional context. To recover the observed 4D in our Universe, we need to confine the remaining 7. This can be done with a compactification technique à la Kaluza-Klein, i.e. assuming that some dimensions are only observable at a very small scale. An alternative is to use branes, which are extended objects found in the theory, and have a higher dimension than strings. An important class of branes are D-branes, upon which open strings can end. Since matter and radiation are in this context described by open strings while gravity is represented by closed ones, this means that the former will stay localised on the brane, while the latter will move freely in the bulk. All extra dimensions are inaccessible to us, who are living on a brane. For this reason, the behaviour of the standard model of particle physics is left unchanged, while gravity can act in very different ways. Gravitational and cosmological tests on these models are therefore important insights into the machinery of string theory and at the same time can test whether any of these models can solve cosmological questions, and especially the dark energy problem.

The first braneworld model to be proposed was the Arkani-Hamed-Dimopoulos-Dvali (ADD) [Arkani-Hamed et al., 1998], which would address the hierarchy problem by lowering the Planck scale due to the effect of extra dimensions, based on the idea that the gravitational constant in $4+d$ dimensions of scale L is $G = G_{4+d}/L^d$. The two Randall-Sundrum models [Randall and Sundrum, 1999b,a] add into the model the self gravity on the brane and present modification of the gravitational behaviour at high energy. However, to attempt an explanation of the dark energy problem, we need a modification at low energy, which is instead attempted by the Dvali-Gabadadze-Porrati (DGP) model, introduced by Dvali et al. [2000] and extended to cosmology by Deffayet [2001]. See Lue [2006] for a review.

In the DGP case, we have our 4D Universe embedded in a 5D Minkowsky space-time. Gravity is bound to the brane at small scales, thus recovering GR, but it leaks off into the bulk at large scales. This transition happens around a crossover scale

$$r_c = \frac{\kappa_5}{2\kappa}. \tag{2.63}$$

[2] In dynamical systems a model is unstable if models in its vicinity in the phase space evolve away from it [Amendola et al., 2007a].

The 5D action for this model is given by

$$S = \frac{1}{2\kappa_5}\int d^5x\sqrt{-g^{(5)}}R^{(5)} + \frac{1}{2\kappa}\int d^4x\sqrt{-g}R - \int d^4x\sqrt{-g}\mathcal{L}_m, \tag{2.64}$$

where the 5 denotes 5D quantities.

The energy conservation equation remains unchanged but, from the variation of the action, and after the application of the junction conditions at the brane [Israel, 1966], the projected Friedmann equation is different from the GR case and contains two branches:

$$H^2 + \frac{K}{a^2} \mp \frac{1}{r_c}\sqrt{H^2 + \frac{K}{a^2}} = \frac{\kappa}{3}\rho + \frac{\Lambda}{3}. \tag{2.65}$$

Here we account for curvature K and we include a possible tension of the brane Λ which has the same phenomenology of a cosmological constant. We can see that there are two possible solutions: the minus and plus signs correspond respectively to a self accelerating branch (SA), where the Universe accelerates in recent times even with $\Lambda = 0$, and a normal branch (NB), which behaves in a more traditional way, and needs some brane tension to account for acceleration.

We can see that this theory starts departing from GR at a scale fixed by r_c: it reduces to the standard GR for $r_c \to \infty$, but if we tune this parameter to a value $r_c \simeq H_0$, we will instead observe a transition at the current time, as confirmed by the observations [Deffayet et al., 2002b].

The leakage of gravity into the bulk at late times screens the cosmological constant and the phenomenology can be described by an effective dark energy density ρ_{eff} with an equation of state w_{eff}. If we ignore curvature for simplicity, we obtain that at the current time

$$w_{\mathrm{eff}}(0) = -\frac{1}{1+\Omega_m} \quad \text{(SA)} \tag{2.66}$$

$$w_{\mathrm{eff}}(0) = -1 - \frac{(\Omega_m + \Omega_\Lambda - 1)\Omega_m}{(1-\Omega_m)(\Omega_m + \Omega_\Lambda + 1)} \quad \text{(NB)}. \tag{2.67}$$

These equations show that the NB presents a phantom-like behaviour ($w_{\mathrm{eff}}(0) \leq -1$) [Lue and Starkman, 2004].

The SA model has the same number of parameters as the standard LCDM, with Λ replaced by r_c, while the NB requires one extra parameter. It is interesting to compare the theoretical predictions for these models with the current observations to see whether a departure from GR is preferred.

A first class of tests which can be imposed to these models is based on the simple expansion history of the Universe. We can express the Friedmann equation (2.65) in term of the density parameters, and we have for the two branches

$$E^2(a) \equiv \frac{H^2(a)}{H_0^2} = \frac{\Omega_k}{a^2} + \left[\sqrt{\frac{\Omega_m}{a^3} + \Omega_\Lambda + \Omega_{r_c}} \pm \sqrt{\Omega_{r_c}} \right]^2 , \tag{2.68}$$

where we have defined $\Omega_{r_c} \equiv \frac{1}{4H_0^2 r_c^2}$. If we evaluate this expression at present time, we can express one parameter in terms of the others:

$$\pm 2\sqrt{\Omega_{r_c}}\sqrt{1-\Omega_k} + \Omega_m + \Omega_k + \Omega_\Lambda = 1. \tag{2.69}$$

This expression is the equivalent of $\Omega_m + \Omega_\Lambda + \Omega_k = 1$ in GR, and we remind that in the SA case we take $\Omega_\Lambda = 0$. These parameters have been tested against observations of supernovae, baryon oscillations and the CMB [Fairbairn and Goobar, 2006, Rydbeck et al., 2007, Maartens and Majerotto, 2006, Song et al., 2007, Barger et al., 2007, Lazkoz et al., 2006]. The current constraints on these parameters are disfavouring a flat DGP universe. In particular, a flat SA model is excluded at several sigmas, while the best fit model for a flat NB theory is in correspondence with the standard GR case. However, current data are still allowing a part of the parameter space in the curved case.

A second possibility is to study the perturbation theory for these models, which we will briefly describe in Appendix B, to derive the laws of the growth of structure; this can help to break the degeneracy which exists between DGP theories and an equivalent dark energy model with the same effective equation of state [Lue et al., 2004, Fang et al., 2008, Nesseris and Perivolaropoulos, 2008]. The linear growth of structure in this theory is different from GR, and it is enhanced in the NB and hindered in the SA branch. This test can be done using different data, as weak lensing [Munshi et al., 2008] and direct tests of the growth rate such as the redshift space distortions [Guzzo et al., 2008]. Another possibility is to observe the cross-correlation of the large scale structure with the CMB, to measure the integrated Sachs-Wolfe effect. We will show how it is possible to use this effect to improve the constraints in Chapter 7.

2.3.4 Old gravity

While a great effort is being made to find a solution to the dark energy problem with the introduction of interesting new physics, in the form of quintessence fields of new gravitational theories, it is still possible for current observations to be explained by well known gravitational effects. This can happen if at large scales we drop the homogeneity condition on which the FRW metric is based: by doing so, non-linear gravitational effects arise which can be similar to the effects of a homogeneous accelerating Universe [Kolb et al., 2006]. Several attempts exist to build models which could satisfy all pieces of observational evidence, generally based on the idea that if we happen to be in an underdense region, gravity will appear locally weaker as matter is attracted to denser regions elsewhere. This concept is sometimes called *Hubble bubble*, and can be realised by models such as the Lemaître-Tolman-Bondi (LTB) Enqvist [2008], although the Copernican principle would be violated and the consistency with observations is still to be proven.

2.4 Perturbed Universe

The homogeneous and isotropic Universe is successful in describing the overall behaviour of the expansion and its relation with the energy content. However, if we look at our Universe closer, we see that isotropy and homogeneity are broken on small scales, and therefore we would like to form a more complex model to describe more of the details we observe, such as the structure of the matter distribution and the anisotropies in the CMB. This can be achieved by a first order perturbative theory built over the zero-order homogeneous theory of the previous section.

The goal of this section is to obtain the evolution laws for the perturbations in the form of a system of differential equations, which will be coupled since the evolution of each component is strongly coupled with the others. This theory was first introduced by Lifshitz [1946]; we follow the classic papers by Kodama and Sasaki [1984], Mukhanov et al. [1992], Ma and Bertschinger [1995], the review by Bertschinger [1993] and the book by Weinberg [2008].

2.4.1 Perturbative variables

Metric perturbations

We introduce metric perturbations on the homogeneous FRW metric $\bar{g}_{\mu\nu}$ in the form

$$g_{\mu\nu} = \bar{g}_{\mu\nu} + h_{\mu\nu}, \tag{2.70}$$

and we want to analyse the form of $h_{\mu\nu}$. We use the RW metric from Eq. (2.2), with a 3D metric γ_{ij} which is equal to δ_{ij} in the flat case. Then, the most general form to introduce perturbations is

$$ds^2 = -(1+E)\,dt^2 + a\,V_i\,dt\,dx^i + a^2\left[(1+A)\,\gamma_{ij} + T_{ij}\right]dx^i\,dx^j, \tag{2.71}$$

with $\gamma^{ij}T_{ij} = 0$. The perturbations are described by two scalar fields $E(x^\mu)$, $A(x^\mu)$, one vector field $\mathbf{V}(x^\mu)$ and a symmetric traceless tensor $\mathsf{T}(x^\mu)$. The metric tensor $g_{\mu\nu}$ has ten independent components and we have ten independent components in the perturbative fields; of these, four are not physically independent, and can be arbitrarily fixed by gauge conditions. This is because we are free to transform the coordinates without changing the physics, given by ds^2. Therefore we are left with $10 - 4 = 6$ physical degrees of freedom.

The decomposition theorem states that we can decompose a vector into longitudinal and transverse parts:

$$\mathbf{V} = \mathbf{V}_{\parallel} + \mathbf{V}_{\perp}, \tag{2.72}$$

where this means that for the two parts it holds $\nabla \wedge \mathbf{V}_{\parallel} = \nabla \cdot \mathbf{V}_{\perp} = 0$. From the first of these conditions, it follows that $\mathbf{V}_{\parallel}$ can be expressed as the gradient of a scalar field: it exists a scalar field F such that $V_{\parallel i} = \partial_i F$, while the transverse one is a truly vectorial component, which we can rename as $V_{\perp i} = G_i$. For a tensor this can be extended to:

$$\mathsf{T} = \mathsf{T}_{\parallel} + \mathsf{T}_{\perp} + \mathsf{T}_{\mathsf{T}}, \tag{2.73}$$

where the three parts are called longitudinal, solenoidal and transverse. There exists a scalar field B such that $T_{\parallel ij} = \partial_i \partial_j B$, and a vector field $\mathbf{C}$ such that $T_{\perp ij} = \partial_i C_j + \partial_j C_i$. The transverse is the truly tensorial part of this perturbation, so that we redefine it as $T_{\mathsf{T}ij} = D_{ij}$

The most general perturbation to the FRW metric is therefore composed by four scalar parts (E, A, B, F), two vector parts $(\mathbf{C}, \mathbf{G})$, and one tensor traceless part D. The perturbed part of the metric can be written as

$$\begin{aligned} h_{00} &= -E\,, \\ h_{i0} &= a\left(\partial_i F + G_i\right)\,, \\ h_{ij} &= a^2\left(A\gamma_{ij} + \partial_i\partial_j B + \partial_j C_i + \partial_i C_j + D_{ij}\right)\,, \end{aligned} \tag{2.74}$$

where the perturbations satisfy the conditions $\partial_i C_i = \partial_i G_i = \partial_i \partial_j D_{ij} = D_{ii} = 0$ [Weinberg, 2008]. We now want to eliminate the unphysical degrees of freedom by choosing a gauge.

The first [Lifshitz, 1946] possible choice is the *synchronous gauge*. Its purpose is to impose that perturbations are localised onto the spatial part of the metric, leaving the other parts unperturbed. This is achieved with the gauge conditions

$$E = 0\,, \qquad\qquad V_i = 0, \tag{2.75}$$

which eliminate two scalars (E, F) and one vector (G_i). The perturbed metric is then

$$h_{00} = 0\,, \quad h_{i0} = 0\,, \quad h_{ij} = a^2\left(A\gamma_{ij} + \partial_i\partial_j B + \partial_j C_i + \partial_i C_j + D_{ij}\right)\,. \tag{2.76}$$

The full metric in this case is often written as

$$ds^2 = -dt^2 + a^2(\gamma_{ij} + h_{ij})dx^i dx^j, \tag{2.77}$$

where $h_{ij} \equiv T_{ij} + A\gamma_{ij}$. This choice of gauge is particularly useful for computational purposes, but it can introduce pathologies in the theory through remaining unphysical degrees of freedom [Bardeen, 1980].

A second possibility is given by the *Poissonian gauge*. This is fixed by the conditions

$$\nabla \cdot \mathbf{V} = 0 \qquad\qquad \nabla \cdot \mathsf{T} = 0, \tag{2.78}$$

similarly to the definition of the Coulomb gauge in electromagnetism. We are now left with two scalars (E, A), a transverse vector ($\mathbf{G}$) and the traceless transverse tensor (D). This case as well contains some residual gauge invariances, which are related to the freedom in the choice of the origins in the scales of distance and time.

We can eliminate this residual gauge freedom by restricting ourselves to a particular case: the *Newtonian longitudinal* (or *conformal*) *gauge*, specified by the condition $V_i = T_{ij} = 0$ [Mukhanov et al., 1992]. This condition can be imposed if we are interested in the scalar perturbations only. For this reason, these are not technically gauge condition, since they may eliminate some physical phenomena. This is nevertheless a good choice of gauge, because the correction are of higher order in the perturbations, and we will use this choice in the following. It is customary to redefine the scalar perturbations as $E \equiv 2\Phi$, $A \equiv 2\Psi$, so that the metric becomes in this case

$$ds^2 = -(1+2\Phi)dt^2 + a^2(1+2\Psi)\gamma_{ij}dx^i dx^j. \tag{2.79}$$

In a stationary case and in the classic limit, Ψ corresponds to the Newtonian gravitational potential.

Finally, it is also possible to construct a fully gauge invariant theory. This can be done by using the gauge invariant variables by Bardeen [1980], which are simply related with the Newtonian gauge variables by $\Phi_A = \Psi$ and $\Phi_H = -\Phi$. For further discussion on possible choices of gauge, see Kodama and Sasaki [1984].

Stress-energy perturbations

In a similar way we can introduce perturbative variables for the energetic content of the Universe. We can define fields which describe each species, like the temperature for photons and neutrinos, and the density, pressure and velocity for matter. For example, a small perturbation on a density field $\rho = \rho(t, \mathbf{x})$ can be described by $\delta\rho$ added on top of the homogeneous background, so that we can decompose the field as

$$\rho(t, \mathbf{x}) = \rho(t)[1 + \delta(t, \mathbf{x})], \tag{2.80}$$

where the density perturbation is defined as $\delta(t, \mathbf{x}) \equiv \delta\rho/\rho$. We can define such variables to study the evolution of inhomogeneities for each component: we introduce $\Theta \equiv \delta T/T$ for photons' temperature, $\mathcal{N} \equiv \delta T_\nu / T_\nu$ for neutrinos, and $\delta_i \equiv \delta\rho_i/\rho_i$ for the overdensity of any component i.

We can use these variables to obtain a perturbed expression for the stress-energy tensor $T_{\mu\nu}$ analogous to Eq. (2.74). We know that for a fluid with anisotropic stress π^μ_ν

$$T^\mu_\nu = (P+\rho)u^\mu u_\nu + p\delta^\mu_\nu + \pi^\mu_\nu, \tag{2.81}$$

and we can perturb this expression as we did with the metric: $T^\mu_\nu = \bar{T}^\mu_\nu + \delta T^\mu_\nu$. The velocity perturbations can be decomposed in a scalar part δu plus a vector part δu^V, while the anisotropic stress contains a scalar π^S, a vector π^V, and a tensor π^T parts. We can thus obtain, following Weinberg [2008]:

$$\begin{aligned}
\delta T^0_0 &= -\delta\rho\,, \\
\delta T^i_0 &= a^{-2}(P+\rho)(a\partial_i F + aG_i - \partial_i\delta u - \delta u^V_i)\,, \\
\delta T^0_i &= (P+\rho)(\partial_i\delta u + \delta u^V_i)\,, \qquad (2.82)\\
\delta T^i_j &= \delta_{ij}\delta P + \partial_i\partial_j\pi^S + \partial_i\pi^V_j + \partial_j\pi^V_i + \pi^T_{ij}, \\
\delta T^\mu_\mu &= 3\delta P - \delta\rho + \nabla^2\pi^S. \qquad (2.83)
\end{aligned}$$

Power spectra and angular expansions

The perturbative variables are random fields which exist in the physical space (if 3D) or the celestial sphere (if projected). Any random field is defined by its distribution functions at $n = 1, ..., N$ given points, which are the probability distributions of the array $(\delta(\mathbf{x}_1), \delta(\mathbf{x}_2), ...\delta(\mathbf{x}_N))$ for each $\mathbf{x}_1$, ..., $\mathbf{x}_N$. If we assume that the fields are homogeneous and isotropic, then the 2-point function will depend only on the distance between the points. We call a random field δ *ergodic* if the ensemble average is equivalent to spatial average; we generally assume this holds in cosmology since we do not have the possibility to perform ensemble averages having only one Universe. If the fluctuations have a Gaussian distribution, then a homogeneous and isotropic random field that lives on an infinite space such as $\mathbb{R}^n$ is ergodic. This is not the case for compact manifolds such as S^n: in this case the ergodicity holds only at scales smaller than the scale of the manifold, and is the reason for which cosmic variance arises. The 2-point function is defined as

$$\xi(x) \equiv \langle\delta(\mathbf{x}_1)\delta(\mathbf{x}_2)\rangle, \tag{2.84}$$

which completely describes a Gaussian random field. We pass to Fourier space, and define

$$\delta(\mathbf{k}) = \int e^{-i\mathbf{k}\cdot\mathbf{x}}\delta(\mathbf{x})d^3x. \tag{2.85}$$

With this transform we can define the power spectrum of the perturbations $P(k)$ as

$$\langle\delta^*(\mathbf{k})\delta(\mathbf{k}')\rangle = (2\pi)^3\delta_{\text{Dirac}}(\mathbf{k}-\mathbf{k}')P(k). \tag{2.86}$$

The auto-correlation function and the power spectrum of a random field are a pair of Fourier transforms. This means that we can obtain the power spectrum as

$$P(k) = 4\pi \int \frac{\sin kr}{kr} \xi(r) r^2 dr. \tag{2.87}$$

For observational purposes, a spherical coordinate system is sometimes preferable. To obtain the power spectra in this case, we need to use a basis on the sphere, which is formed by the spherical harmonics

$$Y_{lm}(\vartheta, \varphi) = \sqrt{\frac{2l+1}{4\pi} \frac{(l-m)!}{(l+m)!}} P_l^m(\cos\vartheta) e^{i\varphi}, \tag{2.88}$$

where P_l^m are Legendre's polynomials, and the indices are bound by $l, m \in \mathbb{Z} : l \geq 0, |m| \leq l$. We can thus expand a generic function $\Delta(\vartheta, \varphi)$ on this base, as

$$\Delta(\vartheta, \varphi) = \sum_{l=0}^{\infty} \sum_{m=-l}^{l} a_{lm} Y_{lm}(\vartheta, \varphi), \tag{2.89}$$

where the coefficients can be obtained from the condition of orthonormality of this base:

$$a_{lm} = \int Y_{lm}^*(\vartheta, \varphi) \Delta(\vartheta, \varphi) d\Omega. \tag{2.90}$$

This can also be extended to an expansion of a 3D quantity $\Delta'(r, \vartheta, \varphi)$ on a 3D basis by including the expansion of the Fourier modes in spherical Bessel functions

$$a'_{lm}(r) = i^l \int \frac{d^3k}{2\pi^2} \int Y_{lm}^*(\vartheta, \varphi) \Delta'(r, \vartheta, \varphi) j_l(kr) d\Omega. \tag{2.91}$$

From a more physical point of view, we know that the harmonics with the same l form a multipole. We can now project any random field, (e.g. the density field) on the celestial sphere, and define an angular auto-correlation function as

$$c(\vartheta) = \langle \Delta(\hat{\mathbf{n}}) \Delta(\hat{\mathbf{n}}') \rangle \tag{2.92}$$

which corresponds to Eq. (2.84) in the Cartesian case. The analogue of Eq. (2.86) is instead

$$\langle a_{lm}^* a_{l'm'} \rangle = \delta_{ll'} \delta_{mm'} C_l, \tag{2.93}$$

which introduces the angular power spectrum C_l. As in the Cartesian case, we have a correspondence between the angular correlation function and the angular power spectrum, which are related by a Legendre transform:

$$c(\vartheta) = \frac{1}{4\pi} \sum_{l=0}^{\infty} (2l+1) C_l P_l(\cos\vartheta), \tag{2.94}$$

where $\hat{\mathbf{n}} \cdot \hat{\mathbf{n}}' = \cos\vartheta \equiv \mu$. The analogue of (2.87) is

$$C_l = \frac{1}{(-i)^l} \int_{-1}^{1} \frac{d\mu}{2} P_l(\mu)\Delta(\mu). \tag{2.95}$$

2.4.2 Perturbation equations

Generic gauge

By combining the metric perturbations from Eq. (2.74) with the perturbed stress-energy tensor Eq. (2.82), one can obtain the perturbed Einstein equations in a generic gauge. These equations can be naturally divided in scalar, vector and tensor parts following the shown classification. We remind that here the dot represents proper time derivative $\dot{} \equiv \frac{\partial}{\partial t}$, while the prime represents conformal time derivative $' \equiv \frac{\partial}{\partial \tau}$.

The scalar modes represent compression. They are the most complicated and are described by the following equations [Weinberg, 2008]:

$$\begin{aligned} &\frac{1}{2}a\dot{a}\dot{E} + (2\dot{a}^2 + a\ddot{a})E + \frac{1}{2}\nabla^2 A - \frac{1}{2}a^2\ddot{A} - 3a\dot{a}\dot{A} \\ &-\frac{1}{2}a\dot{a}\nabla^2\dot{B} + \dot{a}\nabla^2 F = -\frac{\kappa}{2}a^2\left[\delta\rho - \delta P - \nabla^2\pi^S\right], \end{aligned} \tag{2.96}$$

$$\partial_j\partial_k\left[E + A - a^2\ddot{B} - 3a\dot{a}\dot{B} + 2a\dot{F} + 4\dot{a}F + 2\kappa a^2\pi^S\right] = 0, \tag{2.97}$$

$$-\dot{a}\partial_j E + a\partial_j\dot{A} = \kappa a(P+\rho)\partial_j\delta u, \tag{2.98}$$

$$\begin{aligned} &-\frac{1}{2a^2}\nabla^2 E - \frac{3\dot{a}}{2a}\dot{E} - \frac{1}{a}\nabla^2\dot{F} - \frac{\dot{a}}{a^2}\nabla^2 F + \frac{3}{2}\ddot{A} + \frac{3\dot{a}}{a}\dot{A} - \frac{3\ddot{a}}{a}E \\ &+\frac{1}{2}\nabla^2\ddot{B} + \frac{\dot{a}}{a}\nabla^2 B = -\kappa\left[\delta\rho + 3\delta P + \nabla^2\pi^S\right]. \end{aligned} \tag{2.99}$$

The vector modes describe vorticity, and produce equations which describe quickly decaying modes, damped as a^{-2} for a perfect fluid, and are therefore of little interest in cosmology. The tensor modes, on the other hand, are determined by one field equation

$$\nabla^2 D_{ij} - a^2\ddot{D}_{ij} - 3a\dot{a}\dot{D}_{ij} = -2\kappa a^2\pi^T_{ij}. \tag{2.100}$$

This equation describes the wave equation of gravitational radiation, which is sourceless if the anisotropic stress vanishes.

Two additional equations can be derived from the conservation of energy $T^{\mu}_{\nu;\mu} = 0$. This condition is equivalent to the Eq. (2.7) at the background level, and in perturbation theory it yields [Weinberg, 2008]:

$$
\begin{aligned}
\partial_j \left[\delta P + \nabla^2 \pi^S + \partial_0 [(P+\rho)\delta u] + \frac{3\dot{a}}{a}(P+\rho)\delta u + \frac{1}{2}(P+\rho)E \right] = 0 \\
\dot{\delta\rho} + \frac{3\dot{a}}{a}(\delta P + \delta\rho) + \nabla^2 \left[-\frac{1}{\dot{a}}(P+\rho)F + \frac{1}{a^2}(P+\rho)\delta u + \frac{\dot{a}}{a}\pi^S \right] \\
+\frac{1}{2}(P+\rho)\partial_0 \left[3A + \nabla^2 B \right] = 0.
\end{aligned}
\tag{2.101}
$$

Newtonian gauge

By fixing this gauge, we have $B = F = 0$, and we can redefine the scalar perturbations as $E = 2\Phi$ and $A = 2\Psi$. It is useful at this point to pass to Fourier space. Thus, the spatial derivatives transform according to the rule $\partial_i \to -ik/a$. It is also common, when dealing with the scalar perturbations only, to make the following change of variables:

$$
\delta \equiv \frac{\delta\rho}{\rho}, \qquad \vartheta \equiv -\frac{k^2}{a}\delta u, \qquad \sigma \equiv \frac{2}{3}\frac{k^2}{(p+\rho)}\pi^S. \tag{2.102}
$$

We can now write the Einstein equations in this gauge from Eq. (2.79) [Ma and Bertschinger, 1995]:

$$
\frac{2k^2\Phi}{a^2} + 6H\left(\dot{\Phi} - H\Psi\right) = \kappa\rho\delta \tag{2.103}
$$

$$
2\left(\dot{\Phi} - H\Psi\right) = -\kappa\frac{a}{k^2}(\rho + P)\,\vartheta \tag{2.104}
$$

$$
\ddot{\Phi} + H\left(2\dot{\Phi} - \dot{\Psi}\right) - \left(3H^2 + 2\dot{H}\right)\Psi + \frac{k^2}{3a^2}(\Phi + \Psi) = -\frac{\kappa}{2}\delta P \tag{2.105}
$$

$$
\Phi + \Psi = -\kappa a^2 \frac{3}{2}\frac{(P+\rho)}{k^2}\sigma. \tag{2.106}
$$

These equations are valid for a single fluid; when considering the multi-fluid mix of the Universe, the stress-energy tensor perturbative quantities of Eq. (2.82) can be defined for each component; the total perturbations will be the sum over all components $\delta T^\mu_\nu = \sum_i \delta T^\mu_{\nu(i)}$. For example, for the density perturbation we have that $\delta\rho = \sum_i \delta\rho_i = \rho_{dm}\delta_{dm} + \rho_b\delta_b + 4\rho_\gamma\Theta_0 + 4\rho_\nu\mathcal{N}_0$.

The energy conservation equations can be obtained from the Eq. (2.101) by applying the simplifications of the Newtonian gauge. If we collect all the terms at the same order in the perturbations, we obtain for a fluid with equation of state w and sound speed c_s:

$$
\begin{aligned}
\dot{\delta} &= -(1+w)\left(\frac{\vartheta}{a} + 3\dot{\Phi}\right) - 3H(c_s^2 - w)\delta \\
\dot{\vartheta} &= -H(1-3w)\vartheta - \frac{\dot{w}}{1+w}\vartheta + \frac{c_s^2}{1+w}\frac{k^2}{a}\delta - \frac{k^2}{a}\sigma + \frac{k^2}{a}\Psi.
\end{aligned}
\tag{2.107}
$$

We can better understand the meaning of the previous equations by noting that in the Newtonian limit for a matter fluid with potential Φ, density ρ and velocity $\mathbf{v}$, Eqs. (2.107) and Eq. (2.103) correspond to the classical fluid evolution described by the continuity, Euler and Poisson equations respectively:

$$\dot{\delta} = -\frac{1}{a}\nabla\cdot(1+\delta)\mathbf{v} \tag{2.108}$$

$$\dot{\mathbf{v}} = -\frac{1}{a}(\mathbf{v}\cdot\nabla)\mathbf{v} - \frac{\dot{a}}{a}\mathbf{v} - \frac{1}{a}\nabla\Phi \tag{2.109}$$

$$\nabla^2\Phi = \frac{\kappa}{2}\rho a^2\delta. \tag{2.110}$$

2.4.3 Evolution of the perturbations

We will now describe the evolution equations for radiation and matter, following Dodelson [2003], Ma and Bertschinger [1995].

Boltzmann equations

The equilibrium between the different species in the Universe is quantified by the Boltzmann equation

$$\frac{df}{dt} = C(f), \tag{2.111}$$

which relates the variation of the abundance of a given species, given by the total derivative of its distribution function, to the rate of the collisions with other species and the metric, given by C.

We can perturb the distribution function for each component to the first order. For example, reminding that $\Theta \equiv \delta T/T$, the distribution function for photons in the phase space is given by

$$f(\mathbf{x}, p, \hat{\mathbf{p}}, t) = \left[\exp\left\{\frac{p}{T(t)[1+\Theta(\mathbf{x}, \hat{\mathbf{p}}, t)]}\right\} - 1\right]^{-1}, \tag{2.112}$$

which can be decomposed into

$$f \simeq f_0 - \frac{\partial f_0}{\partial p} p\Theta, \tag{2.113}$$

where f_0 is the zero order part, i.e. the Bose-Einstein distribution function.

For any component we can also decompose the distribution function in zeroth and first order by introducing a new variable Ξ and writing

$$f(\mathbf{x}, \mathbf{p}, t) \equiv f_0(q)[1 + \Xi(\mathbf{x}, q, \hat{\mathbf{q}}, t)], \tag{2.114}$$

where we have defined $q_i \equiv a p_i$, the comoving moments.

We can express the total derivative of the distribution function as a sum of partial derivatives in function of the variables $\mathbf{x}, q, \hat{\mathbf{q}}, t$

$$\frac{df}{dt} = \frac{\partial f}{\partial t} + \frac{\partial f}{\partial x^i}\frac{\partial x^i}{\partial t} + \frac{\partial f}{\partial q}\frac{\partial q}{\partial t} + \frac{\partial f}{\partial \hat{q}^i}\frac{\partial \hat{q}^i}{\partial t}. \tag{2.115}$$

We pass to Fourier space and then, by considering only the part at first order in the perturbations, we obtain after some rather long calculations the generic form for perturbed Boltzmann equation

$$\frac{\partial \Xi}{\partial t} + i\frac{q}{\epsilon}k\mu\Xi - \frac{\partial \ln f_0}{\partial \ln q}\left[\Psi' + i\frac{q}{\epsilon}k\mu\Psi\right] = \frac{1}{f_0}\left(\frac{df}{dt}\right)_C, \tag{2.116}$$

where the right hand side represents the collisional term.

Let us now apply this expression to each species.

Massless neutrinos

These particles do not interact, so we can set to zero the collisional terms. We can define the angular perturbation function for this species as the integral over q of the first order perturbations $f_0\Xi$ normalised with respect to the zero order:

$$F_\nu(\mathbf{x}, \hat{\mathbf{n}}, t) \equiv \frac{1}{4}\frac{\int q^2 dq q f_0(q)\Xi(\mathbf{x}, q, \hat{\mathbf{q}}, t)}{\int q^2 dq q f_0(q)}. \tag{2.117}$$

We can then expand this function in a Legendre series to obtain

$$F_\nu(\mathbf{x}, \hat{\mathbf{n}}, t) = \sum_{l=0}^{\infty}(-i)^l(2l+1)F_{\nu l}(\mathbf{k}, t)P_l(\mu). \tag{2.118}$$

By writing the stress-energy tensor perturbed components in the phase space, it can be proven [Ma and Bertschinger, 1995] that the already introduced perturbative variables $\delta, \vartheta, \sigma$ can be identified with the first coefficients of the angular perturbation function:

$$\delta_\nu = F_{\nu 0}\,; \qquad \vartheta_\nu = \frac{3}{4}kF_{\nu 1}\,; \qquad \sigma_\nu = \frac{1}{2}F_{\nu 2}\,. \tag{2.119}$$

We also find that the angular perturbation function is proportional to the temperature perturbation: $F_\nu = 4\mathcal{N}$. We can then apply the same procedure of momentum integration and normalisation to Eq. (2.116) to find the Boltzmann equation for massless neutrinos:

$$\mathcal{N}' + ik\mu\mathcal{N} = -\Phi' - ik\mu\Psi. \tag{2.120}$$

The Legendre expansion of this equation yields the Boltzmann hierarchy:

$$\delta_\nu' = -\frac{4}{3}\vartheta_\nu - 4\Phi' \tag{2.121}$$

$$\vartheta_\nu' = k^2\left(\frac{1}{4}\delta_\nu - \sigma_\nu\right) + k^2\Psi \tag{2.122}$$

$$\mathcal{N}'_l = \frac{k}{2l+1}[l\mathcal{N}_{l-1} - (l+1)\mathcal{N}_{l+1}], \quad l \geq 2. \tag{2.123}$$

This is an infinite system of coupled differential equations for all perturbative modes, where the equation for the multipole l is coupled only to the multipoles $l \pm 1$.

Photons

In this case the particles interact with electrons, and therefore we have to calculate the collisional term in the Boltzmann equation. We also have to account for the polarisation of photons, which is described by Θ_P. By using the definition Eq. (2.95), we can expand in Legendre series the temperature and polarisation perturbations Θ, Θ_P:

$$\Theta_{l(P)} \equiv \frac{1}{2(-i)^l} \int_{-1}^{1} d\mu P_l(\mu) \Theta_{(P)}(\mu); \tag{2.124}$$

we then have:

$$\left(\frac{d\Theta}{dt}\right)_C = -\mathfrak{K}' \left[\Theta_0 - \Theta + \hat{\mathbf{n}} \cdot \mathbf{v}_e - \frac{1}{2}(\Theta_2 + \Theta_{P0} + \Theta_{P2}) P_2\right], \tag{2.125}$$

$$\left(\frac{d\Theta_P}{dt}\right)_C = -\mathfrak{K}' \left[-\Theta_P - \frac{1}{2}(\Theta_2 + \Theta_{P0} + \Theta_{P2})(1 - P_2)\right], \tag{2.126}$$

where $P_2(\mu) = (2\mu^2 - 1)/2$ and we remind that $\mathfrak{K}' = -an_e\sigma_T$.

The angular perturbation function for photons' temperature and polarisation, $F_{\gamma(P)}$ can be defined in the same way as for the massless neutrinos Eq. (2.117). After expanding $F_{\gamma(P)}$ in its Legendre coefficients $F_{\gamma l(P)}$, these can be identified with the perturbative variables $\delta, \vartheta, \sigma$ in the same way as we did in Eq. (2.119). It also holds $F_{\gamma(P)} = 4\Theta_{(P)}$.

By substituting in Eq. (2.116), we have the Boltzmann equations for photons' temperature and polarisation:

$$\Theta' + ik\mu\Theta = -\Phi' - ik\mu\Psi - \mathfrak{K}' \left[\Theta_0 - \Theta + ik\mu\vartheta_b - \frac{1}{2}P_2(\mu)\Pi\right] \tag{2.127}$$

$$\Theta_P' + ik\mu\Theta_P = -\mathfrak{K}' \left[-\Theta_P + \frac{1}{2}P_2(\mu)\Pi\right], \tag{2.128}$$

where the term $\Pi = \Theta_2 + \Theta_{P2} + \Theta_{P0}$ represents the coupling between the two.

The left hand side of the Boltzmann equations is now still identical to the case of neutrinos, so that we can pass to Fourier space and find the following differential equations for the temperature perturbations:

$$\delta_\gamma' = -\frac{4}{3}\vartheta_\gamma - 4\Phi' \tag{2.129}$$

$$\vartheta_\gamma' = k^2\left(\frac{1}{4}\delta_\gamma - \sigma_\gamma\right) + k^2\Psi - \mathfrak{K}'(\vartheta_b - \vartheta_\gamma) \tag{2.130}$$

$$\Theta_2' = 8\sigma_\gamma' = \frac{32}{15}\vartheta_\gamma - \frac{3}{5}k\Theta_3 + \frac{36}{5}\mathfrak{K}'\sigma_\gamma - \frac{1}{10}\mathfrak{K}'(\Theta_{P0} + \Theta_{P2}) \tag{2.131}$$

$$\Theta_l' = \frac{k}{2l+1}[l\Theta_{l-1} - (l+1)\Theta_{l+1}] + \mathfrak{K}'\Theta_l, \qquad l \geq 3 \tag{2.132}$$

while for polarisation it holds

$$\begin{aligned}\Theta'_{Pl} &= \frac{k}{2l+1}[l\Theta_{P(l-1)} - (l+1)\Theta_{P(l+1)}] \\ &- \mathfrak{K}'\left[\Theta_l + \frac{1}{2}\Pi\left(\delta_{l0} + \frac{\delta_{l2}}{5}\right)\right],\end{aligned} \tag{2.133}$$

where δ_{ln} is a Kronecker delta.

Dark matter

If we assume the cold dark matter model, this can interact only through gravity, and so can be considered as a perfect fluid with $P = 0$. By writing the conservation equations Eqs. (2.107) in Fourier space, and remembering that $\delta_c \equiv \delta\rho_c/\rho_c$, we have

$$\delta'_c + \vartheta_c = -3\Phi' \tag{2.134}$$

$$\vartheta'_c + aH\vartheta_c = k^2\Psi. \tag{2.135}$$

Baryons

In this case we need to consider interactions with photons, which introduce a collision term

$$C \propto R^{-1}\sigma_T n_e(\vartheta_\gamma - \vartheta_b), \tag{2.136}$$

where R is the ratio between baryon and photons densities: $R \equiv \frac{3\rho_b}{4\rho_\gamma}$. The conservation equations in this case yield

$$\delta'_b + \vartheta_b = -3\Phi' \tag{2.137}$$

$$\vartheta'_b + aH\vartheta_b = k^2\Psi + c_s^2k^2\delta_b - R^{-1}\mathfrak{K}'(\vartheta_\gamma - \vartheta_b). \tag{2.138}$$

Dark energy

The introduction of perturbations in the dark energy component is related to its sound speed, and it behaves differently depending on the particular model we choose [Bean and Dore, 2004, DeDeo et al., 2003, Weller and Lewis, 2003, Gordon and Wands, 2005, Dent et al., 2008]. We can introduce the entropy perturbation Γ, which is related to the difference between the adiabatic and real sound speeds

$$w\Gamma = (c_s^2 - c_a^2)\delta. \tag{2.139}$$

If $\Gamma \neq 0$, then the sound speed is necessary to determine the perturbations in addition to the equation of state. Since the non-adiabatic sound speed depends on the reference frame, we can introduce an invariant sound speed $\hat{c}_s$ [Kodama and Sasaki, 1984] as

$$\hat{\delta} = \delta + 3H(1+w)\frac{\vartheta}{k}. \tag{2.140}$$

With this expression, we can write the conservation equation for the dark energy density from Eq. (2.107)

$$\delta' = -(1+w)\left\{\frac{\vartheta}{k^2}[k^2 + 9H^2(\hat{c}_s^2 - c_a^2)] + 3\Phi'\right\} - 3H(\hat{c}_s^2 - w)\delta. \tag{2.141}$$

We can see that in the case of cosmological constant ($w = -1$) the dark energy perturbations cancel.

Since the perturbation equations are a coupled system, the modifications introduced by different values for the dark energy sound speed will also affect the perturbations in the other components, including the matter density. This will affect the potential evolution at late times, and as we will see the ISW effect, which can thus be used to constrain the dark energy sound speed parameter [Dent et al., 2008].

2.4.4 Line of sight integration method

We now have differential equations for the multipole moment of all perturbative variables. When trying to solve this system, the first problem is to choose a truncation of it at high l; after finding an acceptable solution to this problem, for example setting an $l_{\max} = 1500$, we still have to solve numerically a system of several thousands coupled differential equations.

A much quicker approach to the problem is the line of sight integration method by Seljak and Zaldarriaga [1996], which is used by modern codes such as CMBfast[3] and CAMB[4] and which we describe here. Instead of expanding the anisotropies in multipole moments and solve their full hierarchy, one can formally integrate the Boltzmann equations along the past light-cone, obtaining

$$\begin{aligned}\Theta &= \int_0^{\tau_0} d\tau e^{ik\mu(\tau-\tau_0)} e^{-\mathfrak{K}} \left\{ g\left[\Theta_0 - \mu\frac{\vartheta_b}{k} + \frac{1}{2}P_2(\mu)\Pi\right] - \Phi' - ik\mu\Psi \right\} \\ \Theta_P &= -\frac{1}{2}\int_0^{\tau_0} d\tau e^{ik\mu(\tau-\tau_0)} g[1 - P_2(\mu)]\Pi. \end{aligned} \tag{2.142}$$

It is possible to simplify these expressions integrating by parts and thus eliminating the μ dependency. The simplified result for the temperature (polarisation) anisotropies is

$$\Theta_{(P)} = \int_0^{\tau_0} d\tau e^{ik\mu(\tau-\tau_0)} S_{(P)}(k,\tau), \tag{2.143}$$

[3]This program was written by Seljak and Zaldarriaga [1996] based on a previous Boltzmann code by Ma and Bertschinger [1995]. The code is available at `www.cmbfast.org`.

[4]This program is based on CMBfast and was written by A. Lewis and A. Challinor. It is available at `camb.info`.

where the source term is given in the two cases by

$$\begin{aligned} S(k,\tau) &= g\left(\Theta_0 + \Psi + \frac{\vartheta_b'}{k^2} - \frac{\Pi}{4} - \frac{3\Pi''}{4k^2}\right) + \\ &+ e^{-\mathfrak{K}}\left(\Phi' - \Psi'\right) + g'\left(\frac{\vartheta_b}{k^2} - \frac{3\Pi'}{4k^2}\right) - \frac{3g''\Pi}{4k^2} \qquad (2.144) \\ S_P(k,\tau) &= -\frac{3}{4k^2}\left[g(k^2\Pi + \Pi'') + 2g'\Pi' + g''\Pi\right]. \qquad (2.145) \end{aligned}$$

The first two terms in the temperature source are the intrinsic temperature anisotropy and the effect of the gravitational potential, while the third and the $g'\vartheta_b/k$ form the velocity term: these are the contributions of the primary anisotropies in the CMB, as we will see in the next chapter. The term containing the derivatives of the potentials describes the integrated Sachs-Wolfe effect, and will be discussed in detail in the following. Finally there are terms including the effects of polarisation, which represent a small correction.

If we ignore polarisation, the temperature source Eq. (2.144) corresponds in the Newtonian limit to the simple form

$$S'(k,\tau) = g\left(\Phi + \frac{\delta}{3}\right) + (gv)' + e^{-\mathfrak{K}}\Phi' \qquad (2.146)$$

To calculate the angular power spectrum, we can now expand in Legendre series

$$C_l = (4\pi)^2 \int dk P(k) k^2 |\Theta_l(k,\tau_0)|^2, \qquad (2.147)$$

where the present time multipole moments are given by

$$\Theta_{(P)l}(k,\tau_0) = \int_0^{\tau_0} d\tau S_{(P)}(k,\tau) j_l[k(\tau-\tau_0)], \qquad (2.148)$$

where j_l are the spherical Bessel functions. The great advantage of this approach is in its capacity of separating the physical part of the problem, given by the calculation of the source terms, from the geometrical part, which is limited to the calculation of the Bessel functions.

Chapter 3

The cosmic microwave background

In this chapter we will describe in more detail the cosmic microwave background (CMB) and its sources, with the purpose of clarifying the physical meaning of the anisotropies and explain their causes. Temperature fluctuations are usually classified as primary and secondary, plus tertiary foregrounds, depending on the time they have been generated. We follow Tegmark [1995], Dodelson [2003], Hu [1995], Valiviita [2005].

3.1 Recombination and primary anisotropies

Most of the features of the CMB have been determined in the first place at the surface of last scattering, at a distance $r_\star$. At that time the Universe was a largely homogeneous plasma, but small fluctuations were present, which we think were sourced by primordial quantum fluctuations and then amplified by inflation. These fluctuations were present in the fundamental fields of the plasma, such as the density, the velocity of the particles, and the gravitational potential. When recombination happened, the information contained in these inhomogeneities at the place of last scattering transferred onto the CMB photons.

If the local gravitational field or the overdensity were positive, or if the peculiar velocity was pointing towards us, we have an increase in the photon's energy, or a decrease in the opposite situation. This is described by the equation

$$\Theta(\hat{\mathbf{n}}) = \Phi(r_\star) + \frac{1}{3}\delta(r_\star) - \hat{\mathbf{n}} \cdot \mathbf{v}(r_\star). \tag{3.1}$$

which is only a qualitative approximation, but gives us an important idea of the physics. We can analyse more in detail the origin of the primary anisotropies, and think of them as generated in two distinct phases: before and after recombination.

3.1.1 Large scales

If we assume that on large scales the potentials Φ and Ψ are constant in time after the last scattering, the only non-zero source term for the CMB anisotropies gives

$$\Theta = [\Theta_0 + \Psi](\tau_\star, \mathbf{x}_\star), \tag{3.2}$$

where the star indicates quantities at the last scattering. This combination is called the *ordinary Sachs-Wolfe effect* [Sachs and Wolfe, 1967], and it is responsible for most of the angular power of the CMB at large scales. Adiabatic initial conditions mean that $\Theta_0 = -\frac{2}{3}\Psi$, thus yielding

$$\Theta_{\mathrm{SW}} = \frac{1}{3}\Psi_\star. \tag{3.3}$$

This effect dominates the CMB at large scales ($l \lesssim 20$). The physical meaning of this phenomenon is that a difference in the gravitational potential between the source and the observer will introduce an energy shift to the CMB photons.

3.1.2 Small scales

We know that in the early Universe until recombination photons and baryons were in equilibrium, forming a homogeneous plasma. For this reason, we can work in the *tight coupling approximation*, which consists in considering the scattering rate much greater than the expansion rate or, in other words, we assume that the optical depth before recombination was $\mathfrak{K} \gg 1$. It can be proved that in this limit $\Theta_l \sim \Theta_{l-1}/\mathfrak{K}$, and therefore we can neglect all higher order anisotropies for the temperature perturbations: we assume that $\Theta_l = 0$ for $l > 1$. The photons behave like a fluid fully described by the variables ρ and ϑ.

In this approximation the Boltzmann hierarchy for photons reduces to

$$\Theta_0' = -k\Theta_1 - \Phi' \tag{3.4}$$
$$\Theta_1' = \frac{k\Theta_0}{3} + \frac{k\Psi}{3} + \mathfrak{K}'\left[\Theta_1 + \frac{\vartheta_b}{3k}\right]. \tag{3.5}$$

We can also write the Boltzmann equation for the baryons in this approximation, assuming $\vartheta_b \simeq 3k\Theta_1$ in the r.h.s,

$$\vartheta_b \simeq 3k\Theta_1 + \frac{R}{\mathfrak{K}'}\left[3k\Theta_1' + aHk\Theta_1 - k^2\Psi\right]. \tag{3.6}$$

We can now substitute this expression in the photons' equation Eq. (3.5), to obtain

$$\Theta_1' + aH\frac{R}{R+1}\Theta_1 - \frac{k}{3(1+R)}\Theta_0 = \frac{k\Psi}{3}. \tag{3.7}$$

The two coupled differential equations Eqs. (3.4,3.7) form a system to be solved for the two moments Θ_0, Θ_1. The solutions may be found by transforming the two first order equations into one at second order. This new equation is

$$\left[\frac{d^2}{d\tau^2} + \frac{R'}{1+R}\frac{d}{d\tau} + k^2 c_s^2\right](\Theta_0 + \Phi) = \frac{k^2}{3}\left(\frac{1}{1+R}\Phi - \Psi\right), \tag{3.8}$$

where the sound speed in this fluid is $c_s \equiv \sqrt{\frac{1}{3(R+1)}}$. We can see that this equation reduces to a forced harmonic oscillator in the special case $\Phi' = c_s^{2\prime} = R' = 0$ and $\Phi = -\Psi$. These conditions are met before recombination, and the Eq. (3.8) in this case becomes

$$\Theta_0'' + c_s^2 k^2 \Theta_0 = \text{constant}, \tag{3.9}$$

which as anticipated represents a harmonic oscillator with frequency $\omega = kc_s^2$. This is the origin of the so-called *Doppler peaks*, which are the major feature of the CMB power spectrum at small scales.

General solutions of Eq. (3.8) can be found using the WKB approximation, as found by Hu and Sugiyama [1996]. With the adiabatic initial conditions, the solutions are for the monopole and dipole

$$\begin{aligned}\Theta_0(\tau) + \Phi(\tau) &= [\Theta_0(0) + \Phi(0)]\cos(kr_s) \\ &+ \frac{k}{\sqrt{3}}\int_0^\tau d\tau'[\Phi(\tau') - \Psi(\tau')]\sin[k(r_s(\tau) - r_s(\tau'))]\end{aligned} \tag{3.10}$$

$$\begin{aligned}\Theta_1(\tau) &= \frac{1}{\sqrt{3}}[\Theta_0(0) + \Phi(0)]\sin(kr_s) \\ &- \frac{k}{3}\int_0^\tau d\tau'[\Phi(\tau') - \Psi(\tau')]\cos[k(r_s(\tau) - r_s(\tau'))].\end{aligned} \tag{3.11}$$

This result is a good approximation of the exact solution of the full Boltzmann hierarchy at small scales, and it is important because it reduces a set of several thousands equations to a compact form which we can qualitatively understand. We see that the first acoustic peak is located at a scale $k_1 = \pi/r_s(\tau_\star)$, while the following will be at $k_n = n\pi/r_s(\tau_\star)$. This means that in the angular space the position of the n-th peak is $l_n = n\pi d_\star^A/r_s(\tau_\star)$. We can also see that the monopole and the dipole are in opposite phase: for this reason the spectrum is not zero anywhere, and when passing to the angular power it has the consequence that the odd peaks become higher than the even ones

The acoustic oscillations are caused by the competition between the gravitational infall and the photons' pressure. So the first peak is produced by a k mode which has had time to oscillate one half of a period before the last scattering. The second peak is caused by a mode which has oscillated for a full period, and so on. For this reason, odd peaks represent the maxima of compression, while even peaks are maxima of rarefaction. The baryons then increase the effective mass of the plasma, and cause it to fall deeper into the potential wells, until finally pressure wins and rarefaction starts.

3.1.3 Recombination and damping

Once photons begin to decouple from matter, this treatment based on a homogeneous plasma breaks down. In particular, when the mean free path of the photons is greater than the wavelength of a perturbative mode, this mode will be damped until the decoupling is complete. This effect is also known as diffusion or Silk damping [Silk, 1968]. An analytic estimation of this effect can be done by extending the tight coupling approximation to the next order by accounting for the quadrupole moment of the perturbations Θ_2. It can be shown [Dodelson, 2003] that the monopole and dipole parts of the perturbations are damped at scale $k > k_D$, so that

$$\Theta_0, \Theta_1 \sim \exp\left(-\frac{k^2}{k_D^2}\right). \tag{3.12}$$

The damping scale can be translated on the harmonic space by the $\ell_D = k_D D_\star^A$, and is given by

$$\ell_D \simeq 1400 \tag{3.13}$$

for the standard ΛCDM model [Hu et al., 2001].

Additional damping is introduced at small scales because the last scattering surface is not infinitesimally thin, but has some finite thickness $\delta\tau_\star$. Therefore, oscillations on scales smaller than $\delta\tau_\star$ will not be observable. In particular, recombination starts at $z_{rec} = 1300$ and is complete at $z_\star = 1100$. In a matter dominated model, the distance between the two is $\delta\tau \simeq 0.0024\tau_0$, which corresponds to a multipole $\ell = 2\pi d_A^\star/\delta\tau_\star = 2600$.

In addition to these effects, the power spectrum of the perturbations is also altered by the projection on the sphere which happens when we pass to the multipole space. This happens because the power on a given multipole ℓ is sourced by fluctuations in a range of scales with finite width δk. Finally curvature, if present, will shift the power spectrum to higher or lower multipoles.

3.2 The integrated Sachs-Wolfe effect

Secondary anisotropies can be produced on the CMB after recombination. We will now describe how different types of reionisation and gravity can alter the power spectrum at more recent times, beginning with the integrated Sachs-Wolfe effect. When streaming through space from the last scattering surface, the CMB photons undergo the effect of the local gravitational field. This can be integrated along the line of sight γ, and is expressed by the Sachs-Wolfe equation

$$\Theta_{\mathrm{ISW}}(\hat{\mathbf{n}}) = -2\int_\gamma \Phi'\left[\tau, \hat{\mathbf{n}}(\tau_0 - \tau)\right] d\tau, \tag{3.14}$$

We can see that such an effect can happen only if the gravitational potential decays. If this happens due to its linear evolution, this is usually referred to as the integrated Sachs-Wolfe effect [Sachs and Wolfe, 1967], and if the potential decay is a result of non-linear evolution, as in clusters, it is referred to as the Rees-Sciama effect [Rees and Sciama, 1968].

The physical picture is very straightforward; as a CMB photon falls into a gravitational potential well, it gains energy; as the photon climbs out of a potential well, it loses energy. These effects exactly cancel if the potential is time independent, but can result in a net kick if the potential evolves as the photon passes through it. In the linear perturbation theory, the gravitational potential follows the Poisson equation

$$\nabla^2\Phi = \frac{\kappa}{2}a^2\rho\delta, \tag{3.15}$$

which in the matter dominated era becomes

$$\nabla^2\Phi = \frac{3}{2}H_0^2\Omega_m\frac{\delta_m}{a}, \tag{3.16}$$

where δ_m is the perturbation to the matter density ρ_m. In Fourier space this becomes

$$\Phi = \frac{3}{2k^2}H_0^2\Omega_m\frac{\delta_m}{a}, \tag{3.17}$$

and since in the matter dominated case $\delta_m \propto a$, we obtain that Φ is a constant, and therefore there is no production of ISW anisotropies in this case.

This changes if other components, such as radiation, dark energy or curvature become important at other times: in this case, $\Phi' \neq 0$ and additional CMB anisotropies will be produced. This will typically happen before or after the matter domination.

It is interesting to remark that in most modified gravity scenarios the gravitational potentials have different time evolution even during the matter era, thus making this effect a potential discriminant between different theories, as shown by Lue et al. [2004].

3.2.1 Early ISW effect

A first possibility to create some ISW signal is to have a non-negligible radiation component in the energy balance. We know that, for a standard ΛCDM model, this happens for some time after recombination, and thus the gravitational potentials are decaying for some time after the creation of the CMB. In this case, some *early ISW* effect is created. We know that at those early times the horizon size was much smaller than today, which means that the additional anisotropies will be produced on higher multipoles, at scales comparable with the first acoustic peak ($\ell \simeq 200$).

Different values of the cosmological parameters will naturally affect this effect. Maybe its most interesting application is to study the number of neutrino species, and in general the contribution of relativistic particles $\Omega_r = \Omega_\gamma + N_\nu\Omega_\nu$. Here we can include in the number of neutrinos other possible particles too, such as e.g. Majorana neutrinos, so that we can write $N_\nu = 3 + \Delta N$. The effect of neutrinos on the cross-correlation has been described by Bowen et al. [2002], Ichikawa and Takahashi [2008], Lesgourgues et al. [2008], where the effect on the growth factor at late times is also considered.

An early ISW effect may be also produced by a tracking time depending dark energy model, whose equation of state follows the dominant energy component, and would therefore behave as radiation at early times [Pogosian et al., 2005]. For this reason, a measurement of this phenomenon may be useful to constrain this class of models [Schaefer, 2008a]. However, the relative signal is embedded in the primary CMB anisotropies, which are much larger and make a direct measurement challenging. Furthermore, since this signal originated at an early time, the cross-correlation techniques which are helpful in the case of the late effect are not available.

3.2.2 Late ISW

A second possibility to produce ISW anisotropies occurs at late times. In fact, if the Universe undergoes a transition from matter domination to a curvature or dark energy phase, the cancellation of the scale factor from the Poisson equation does not happen any more [Kofman and Starobinsky, 1985]. Under these circumstances, a *late ISW* effect is produced. In the standard ΛCDM case, the matter-dark energy equality happens very recently, and so the new anisotropies are formed at recent times, when the horizon size is comparable with its current value. Therefore the affected scales are generally the largest, at multipoles $l < 100$.

This phenomenon is very interesting because, as we have described, it can be produced only if the Universe deviates from matter domination. Furthermore, since from the observations of the CMB we are generally able to exclude curvature, a measurement of the late ISW is directly related to dark energy and its properties. From a quantitative point of view, the amplitude of the ISW power spectrum is at most $\sim 10\%$ of the total CMB, as we can see from Fig. 3.1, and therefore it is difficult to measure directly. A further problem is that this maximum is located at the largest scales, which are the ones mostly affected by cosmic variance.

By measuring this effect, we can estimate some fundamental quantities of dark energy and curvature, such as the energy densities Ω_{de}, Ω_k, the dark energy equation of state w_{de} and sound speed c_s^2. Another very interesting feature is that we may be able to estimate the evolution in time of these parameters if we can measure the ISW effect at different redshifts [Hu and Scranton, 2004]. Much of the following will be dedicated to the techniques of detection for the late ISW.

3.2.3 Rees-Sciama effect

At smaller angular scales, the photons from the CMB may undergo some energy shift when they cross a high density region, like a galaxy cluster. In this case linear theory breaks down, and again $\Phi' \neq 0$ even in a matter dominate era. This effect represents the nonlinear part of the ISW, and is known as Rees-Sciama [Rees and Sciama, 1968]. Since it is sourced by small non-linear regions, its power spectrum typically peaks at small scales. Theoretical calculations of the spectrum for this effect have been derived in perturbation theory [Martinez-Gonzalez et al., 1994, Tuluie et al., 1996, Seljak, 1995, Cooray, 2002] and from $N-$body simulations [Puchades et al., 2006]. We show in Fig. 3.1 the prediction by Cooray [2002]: we can see that this effect is maximum at $\ell \simeq 100$ and is always much smaller than the primary CMB. A possible approach to the measurement of this phenomenon has been proposed by Schaefer [2008b], which is based on the measurement of the 3-point functions between the CMB and the large scale structure.

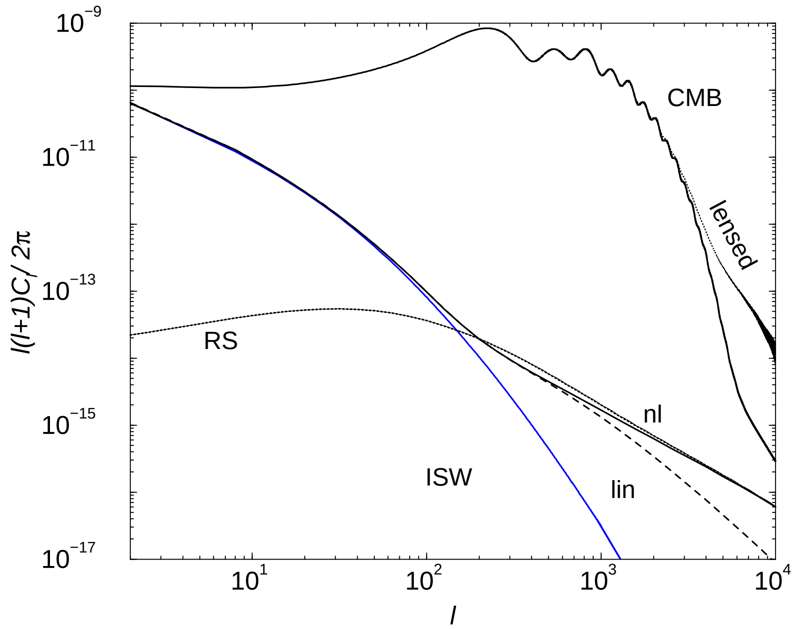

Figure 3.1: Comparison of the linear and non-linear (Rees-Sciama) parts of the ISW power spectrum with the primary CMB anisotropies. The curve 'nl' is the full non-linear contribution, which includes a suppression at $100 < \ell < 1000$ due to a cross term between momentum and density fields. The 'lin' curve is obtained from second order perturbation theory. From Cooray [2002].

3.3 Other secondary anisotropies

If the coupling between photons and baryons is restored at some time after recombination, then new anisotropies will be created in the CMB for exactly the same reasons the primary anisotropies did, as described by Eq. (3.1). As we shall now describe, this can happen either locally or globally.

3.3.1 The Sunyaev-Zel'dovich effect

A first example of local reionisation is a high density region, like a galaxy cluster. In this case, the free electrons may be dense enough to reactivate the inverse Compton scattering. If this happens, the energy level of the scattered CMB photons will change, due to the high temperature of these free electrons. The consequence of this *thermal Sunyaev-Zel'dovich* (tSZ) [Sunyaev and Zeldovich, 1970] effect is therefore to modify the CMB black body spectrum, introducing in particular a frequency dependence: the power in the Wien region will be increased, and conversely decreased in the Rayleigh-Jeans part of the spectrum. A similar effect, called *kinetic Sunyaev-Zel'dovich* (kSZ), arises because of the peculiar velocities of the electrons [Sunyaev and Zeldovich, 1980].

The tSZ temperature anisotropies are related to the matter density and temperature along the line of sight γ, which are linearly related the electron pressure p_e. The frequency spectrum of the anisotropies has the form

$$\Theta_{SZ}(\nu) = -A(x) \int_\gamma \delta p_e[(t_0 - t)\hat{\mathbf{n}}, t] dt, \tag{3.18}$$

where $A(x) \equiv \frac{\sigma_T}{m_e}[4 - \coth\left(\frac{x}{2}\right)]$ and $x \equiv h\nu/(kT)$. We can see that this is strictly related to astrophysical quantities, such as the properties of the gas in the cluster and the electron temperature. The spectrum typically features an excess luminosity at high frequencies and a decrease at low frequencies. This is useful, because we can take advantage of this unique frequency dependence to isolate this from other effects, as the ISW.

The kSZ, instead, does not have any frequency dependence, since it is only produced as a Doppler effect by the velocity of the gas with respect to the CMB. This means that it is more difficult to extract.

We know that both flavours of the SZ effect are very dependent on the astrophysics of the clusters, and also on the amplitude of the matter power spectrum. Because their sources are localised inside the clusters, at very small scales, their addition to the CMB angular power spectrum is relevant only at very high ℓ, such as $\ell > 3000$, as shown in Fig. 3.3. The theoretical spectra for these effects have been calculated for various models by several authors, e.g. by Rephaeli [1995], Rephaeli and Sadeh [2008]. On the observational side, the SZ effect has been detected by imaging of more than 50 clusters [Carlstrom et al., 2002], and the quality of the detections will dramatically improve in the near future with the deployment of new high-resolution instruments, such as the South Pole telescope.

3.3.2 Global reionisation

If the whole Universe becomes ionised again at a time after recombination, the CMB photons will start scattering off the free electrons again, and their anisotropies will be modified. Qualitatively, we can think that a reionisation surface will smooth the CMB signal, averaging in each point the radiation coming from its past light cone. Then, the CMB will be smeared at scales smaller than the horizon scale at reionisation. More in detail, if the CMB photons at a temperature $T(1+\Theta)$ enter a reionised region with optical depth $\mathfrak{K}$, a fraction $e^{-\mathfrak{K}}$ will pass through, and in addition another fraction $1-e^{-\mathfrak{K}}$ will be re-emitted from the region. This means that the final observed temperature is

$$T(1+\Theta)e^{-\mathfrak{K}} + T(1-e^{-\mathfrak{K}}) = T(1+\Theta e^{-\mathfrak{K}}). \tag{3.19}$$

The first consequence of this is that the observed anisotropy will be damped by a factor $e^{-\mathfrak{K}}$, while the damping of the power spectrum will be $e^{-2\mathfrak{K}}$, on sub-horizon scales. A second consequence is that new anisotropies will be produced following the same mechanism of the primary part, now sourced by the local conditions at the time of rescatter, such as density and velocity. The velocity term in particular produces a small secondary Doppler effect on the CMB at intermediate scales, which is potentially measurable, as we will see in more detail in Chapter 6. We can see the power spectra of these effects in Fig. 3.2. A last effect of reionisation at linear order is the introduction of additional polarisation on large scales.

Current CMB data from WMAP constrain the optical depth to $\mathfrak{K}_r = 0.092 \pm 0.030$ [Spergel et al., 2007]; if reionisation happened instantly, this would correspond to a redshift $z_r^{\mathrm{CMB}} = 11$. On the other hand, measurements of the Gunn-Peterson troughs[1] in the Lyman-α part of the spectra for distant quasars from the SDSS [Fan et al., 2002, White et al., 2003] suggest that the Universe is completely ionised out to a redshift $z_r^{\mathrm{QSO}} = 6.10 \pm 0.15$ [Gnedin and Fan, 2006]. The scattering up to this redshift accounts for nearly half of the total observed optical depth. It is currently thought that the Universe was reionised by the UV radiation emitted by the ignition of the first objects, such as distant quasars, but the details of how the process happened between z_r^{CMB} and z_r^{QSO} are still matter of debate.

3.3.3 Gravitational lensing

An additional effect of the gravitational potentials is to lens the CMB photons. While the ISW effect can be though of as a momentum kick to the photons in a direction parallel to its motion, the gravitational field can also kick them in a transverse direction through lensing. The biggest effect of observing the CMB through an irregular gravitational field is a small smoothing of the anisotropies, which transfers some of the power from the acoustic peaks to the troughs [Bartelmann and Schneider, 2001, Seljak, 1996, Lewis and Challinor, 2006].

We can understand how lensing modifies the CMB more quantitatively following Bartelmann and Schneider [2001]. If a light ray which starts at an angle $\vec{\vartheta}$ passes through

[1] The Gunn-Peterson trough is a feature appearing in the spectrum of a quasar due to presence of neutral hydrogen in the intergalactic medium. The absorption causes a suppression of the spectrum at wavelenghts less than the Lyman-α line [Gunn and Peterson, 1965]. This feature has been observed for quasars at redshift $z > 6$, indicating that hydrogen was ionised after that time.

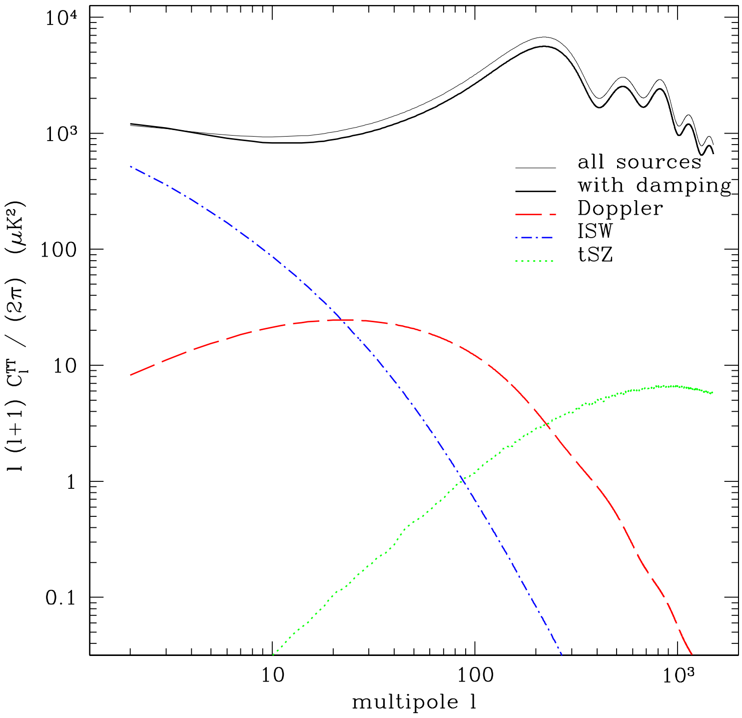

Figure 3.2: Total temperature anisotropies power spectrum for the best fit *WMAP* third year ΛCDM model, with (thick solid line) and without (thin solid line) reionisation. The Doppler anisotropies produced after reionisation (dashed line) are significantly smaller than the ISW anisotropies (dot-dashed line) on very large scales, but can be comparable on degree scales. At even smaller scales, the thermal SZ effect becomes relevant (the dotted theoretical curve is obtained by Schafer et al. [2006] using the N-body simulation method by Springel and Hernquist [2002]), although it can be distinguished from the other effects taking advantage of its frequency dependence. We assume a step model for reionisation.

density inhomogeneities, it will intercept the surface of last scattering at another angle $\vec{\beta}$ given by

$$\vec{\beta} = \vec{\vartheta} - \vec{\alpha}(\vec{\vartheta}), \tag{3.20}$$

where $\vec{\alpha}(\vec{\vartheta})$ is the deflection angle. Because of this, the CMB temperature we observe in a direction $\vec{\vartheta}$ is actually coming from the direction $\vec{\beta}$, and the 2-point temperature correlation function between two points separated by φ is corrected to

$$\xi'_T(\varphi) = \langle \Theta[\vec{\vartheta} - \vec{\alpha}(\vec{\vartheta})]\Theta[\vec{\vartheta} + \vec{\varphi} - \vec{\alpha}(\vec{\vartheta} + \vec{\varphi})]\rangle. \tag{3.21}$$

By expanding this in 2D Fourier modes in the flat sky approximation, one finds the temperature power spectrum $P_T(l)$

$$\xi'_T(\varphi) = \int \frac{ldl}{2\pi} P_T(l) \exp\left[-\frac{1}{2}l^2\sigma^2(\varphi)\right] J_0(l\varphi), \tag{3.22}$$

where J_0 is the zeroth order Bessel function, and $\sigma(\varphi)$ is the dispersion of the deflection angles. We can see from this equation that the primary CMB spectrum is convolved with a Gaussian function in l, with dispersion σ^{-1}. This means that the effect of lensing is to smooth out the primary CMB fluctuations on scales smaller than σ. If we assume for simplicity that $\sigma(\varphi) = \epsilon\varphi$, with $\epsilon \ll 1$, then we find how the unlensed power spectrum P is transformed by the lensing to P':

$$P'_T(l') = \int \frac{dl}{\epsilon l \sqrt{2\pi}} P_T(l) \exp\left[-\frac{(l-l')^2}{2\epsilon^2 l^2}\right]. \tag{3.23}$$

This equation shows again how modes on angular scales φ are mixed with modes at scales $\varphi \pm \sigma$. This effect can be large at small scales, but is negligible at large scales; we can see how the CMB power spectrum is affected in Fig. 3.3

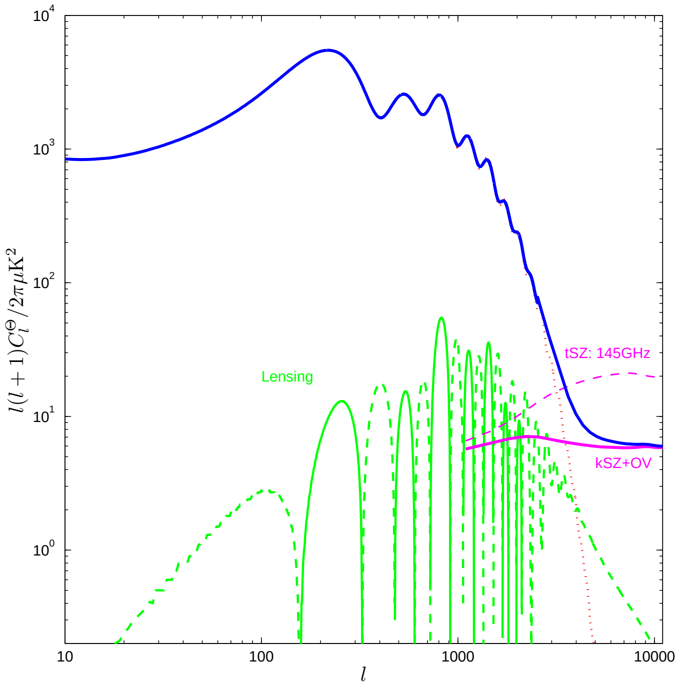

Figure 3.3: Comparison of some secondary sources of CMB anisotropy with the primary power spectrum (blue, solid). We can see the lensing contribution in green (thin solid) and the thermal and kinetic SZ (pink). The red (dotted) line represents the primary term without lensing. From Lewis and Challinor [2006].

3.4 Foregrounds

On top of the aforementioned secondary anisotropies which can be formed on the CMB, other phenomena can produce microwave radiation which can contaminate the CMB signal as a foreground. The knowledge of these effects is needed to extract the cosmological signal from the experimental observations.

A first class of contaminations is formed by extragalactic point sources, which must be removed. This can be done if we have a catalogue of such sources, but unfortunately our knowledge of them is not exhaustive in the microwave region. Another option is to impose a cut on the flux, eliminating pixels over a given threshold.

The Galaxy itself contains many microwave sources, which again have to be taken into account. Most of the emission comes from the galactic plane, which has generally to be discarded; most of the contaminating signal come from dust, free-free and synchrotron radiation. Finally, the solar system and the atmosphere contribute to the contamination too.

The frequency region which is least affected by noise, and therefore is used by all CMB measurements, is typically 30 GHz $< \nu <$ 500 GHz.

3.5 Measuring the ISW

We have seen that the measurement of the ISW effect is made difficult by the embedding of the small ISW signal in the much larger (10 times) primary CMB anisotropies. Furthermore, the total ISW signal is due to all the density fluctuations, both positive and negative, along the line of sight. On small scales, the individual temperature differences are small and they tend to cancel out. The most significant ISW effect results from the coherent large scale potentials, but unfortunately these scales are precisely where cosmic variance is most troublesome.

3.5.1 The cross-correlation technique

This problem can be overcome by cross-correlating the observed CMB map with some tracer of the matter density [Crittenden and Turok, 1996]. The primary CMB anisotropies have been generated at the surface of last scattering, and therefore are completely uncorrelated from the large scale structure present in recent times; on the other hand, the ISW temperature correlates with the density of galaxies, which should trace the potential wells and hills which bring about the anisotropies. We can then extract the late ISW signal by measuring the cross-correlation of some tracer of the large scale structure with the CMB.

If we assume a linear bias $b(z)$ between the visible density and the underlying total matter distribution, $\delta_g(\hat{\mathbf{n}}, z) = b(z)\delta_m(\hat{\mathbf{n}}, z)$, then the observed galaxy density contrast in a given direction $\hat{\mathbf{n}}_1$ will be

$$\delta_g(\hat{\mathbf{n}}_1) = \int b_g(z) \frac{dN}{dz}(z) \delta_m(\hat{\mathbf{n}}_1, z) dz, \tag{3.24}$$

where dN/dz is the selection function of the survey, and δ_m the matter density perturbations. Since the density δ_m is related to the potential Φ by the Poisson equation, the observed galaxy density will be correlated with the ISW temperature fluctuation in the nearby direction $\hat{\mathbf{n}}_2$, which is

$$\Theta(\hat{\mathbf{n}}_2) = -2 \int g(z) \frac{d\Phi}{dz}(\hat{\mathbf{n}}_2, z) dz, \tag{3.25}$$

where $g(z)$ is the visibility function of the photons, which accounts for the effect of photons re-scattering following reionisation.

The galaxy bias, $b_g(z)$, can evolve in time or as a function of scale; however, we will generally assume that it is time and scale independent for simplicity. For our purposes, a time dependent bias is equivalent to changing the selection function of the survey. Scale dependence of the bias is more problematic, but on the very large scales ($>$ 10 Mpc) we are considering, the scale dependence is expected to be weak [2] [Blanton et al., 1998, Percival et al., 2007a]. In the future, it will be possible to use dark matter maps reconstructed from weak lensing surveys to do this correlation in the place of galaxies to avoid the bias issue altogether.

Given a map of the CMB and a survey of galaxies, the angular auto-correlation and cross-correlation functions are defined as

$$C^{gg}(\vartheta) \equiv \langle \delta_g(\hat{\mathbf{n}}_1) \delta_g(\hat{\mathbf{n}}_2) \rangle \tag{3.26}$$

$$C^{Tg}(\vartheta) \equiv \left\langle \frac{\Delta T}{T}(\hat{\mathbf{n}}_1) \delta_g(\hat{\mathbf{n}}_2) \right\rangle, \tag{3.27}$$

with the average carried over all the pairs at the same angular distance $\vartheta = |\hat{\mathbf{n}}_1 - \hat{\mathbf{n}}_2|$.

It is possible to express these quantities in the harmonic space with the use of the Legendre polynomials P_l:

$$C^{Tg}(\vartheta) = \sum_{l=2}^{\infty} \frac{2l+1}{4\pi} C_l^{Tg} P_l[\cos(\vartheta)], \tag{3.28}$$

and the auto- and cross-correlation power spectra are given by

$$C_l^{Tg} = 4\pi \int \frac{dk}{k} \Delta^2(k) I_l^{ISW}(k) I_l^g(k) \tag{3.29}$$

$$C_l^{gg} = 4\pi \int \frac{dk}{k} \Delta^2(k) I_l^g(k) I_l^g(k), \tag{3.30}$$

where $\Delta(k)$ is the scale invariant matter power spectrum $\Delta^2(k) \equiv 4\pi k^3 P(k)/(2\pi)^3$ and the two integrands are respectively

$$I_l^{ISW}(k) = -2 \int e^{-\tau(z)} \frac{d\Phi_k}{dz} j_l[k\chi(z)] dz \tag{3.31}$$

$$I_l^g(k) = \int b_g(z) \frac{dN}{dz}(z) \delta_m(k,z) j_l[k\chi(z)] dz, \tag{3.32}$$

[2] This is not the case if the perturbations are substantially non-Gaussian, as shown by Dalal et al. [2008]; in this case the bias becomes scale-dependent on large scales, and thus a measurement of it can constrain non-Gaussianity [Slosar et al., 2008, Afshordi and Tolley, 2008].

where $\Phi_k, \delta_m(k,z)$ are the Fourier components of the gravitational potential and matter perturbations, $j_l(x)$ are the spherical Bessel functions and χ is the comoving distance. We can see that the ISW source can be obtained from Eq. (2.144) by considering only the terms containing the derivatives of the potentials.

3.5.2 Theoretical signal-to-noise

Unfortunately the ability to detect the cross-correlation is limited because the signal falls off on small scales. Not only is cosmic variance an important factor, but there is also the problem of accidental correlations between the galaxy surveys and the CMB anisotropies produced at last scattering. Many independent measurements are needed to reduce the impact of such accidental correlations. The signal to noise ratio of the CCF with a particular survey is given by

$$\left(\frac{S}{N}\right)^2 = \sum_l (2l+1) \frac{[C_l^{Tg}]^2}{C_l^{gg} C_l^{TT} + [C_l^{Tg}]^2}. \tag{3.33}$$

This is because the expected variance of a cross-correlation measurement between two fields X and Y can be written as $\mathrm{Var}(XY) = [(C_l^{XY})^2 + C_l^{XX} C_l^{YY}]/(2l+1) f_{\rm sky}$ [Cooray and Melchiorri, 2006], and we assume full sky coverage for simplicity. For the ISW, we are usually in the weak correlation regime, so that $C_l^{Tg}/\sqrt{C_l^{gg} C_l^{TT}} \ll 1$.

The signal to noise can be separated to obtain the contribution as a function of redshift; for a standard ΛCDM cosmology, most of the signal is expected at $z < 3$, with the peak around a redshift of $z \simeq 0.5$ [Afshordi, 2004]. While the signal is highest at low redshifts, more independent volumes are available for higher z. The signal to noise scales roughly as the square root of the fraction of the sky observed.

The most optimistic case is when the distribution of galaxies follows precisely the evolution of the ISW effect. In this case, $C_l^{Tg} = C_l^{gg} = C_l^{ISW}$ where C_l^{ISW} is the spectrum of the ISW temperature anisotropies alone, which is assumed to be much smaller than the total CMB anisotropy, $C_l^{ISW} \ll C_l^{TT}$. Thus, the signal to noise reduces to [Crittenden and Turok, 1996]

$$\left(\frac{S}{N}\right)^2 \simeq \sum_l (2l+1) \frac{C_l^{ISW}}{C_l^{TT}}. \tag{3.34}$$

This gives an optimistic total $S/N \simeq 7 - 10$ for a standard ΛCDM cosmology. The ISW constraints which might arise from realistic future surveys can be found in Pogosian et al. [2005].

3.5.3 Current measurements of the ISW effect

As we have summarised in Chapter 1, many groups have detected the late ISW effect in the past five years with the cross-correlation technique, using WMAP data for the CMB and several galaxy catalogues. The signal has been found using a range of different surveys, at different redshifts and in different regions of the electromagnetic spectrum.

In more detail, the first measurement has been performed by Boughn and Crittenden [2004a] using the NVSS radio galaxies at a median redshift of $\bar{z} = 0.9$, which have been studied again by Nolta et al. [2004]. Other groups used the X-ray background from HEAO, [Boughn and Crittenden, 2004a], less deep ($\bar{z} = 0.1$) infrared data from 2MASS [Afshordi et al., 2004, Rassat et al., 2007], and finally visible surveys such as SDSS and APM ($\bar{z} \simeq 0.5$) [Fosalba et al., 2003, Scranton et al., 2003, Fosalba and Gaztanaga, 2004, Padmanabhan et al., 2005, Cabre et al., 2006]. All the results are generally compatible with the expectations from the ΛCDM model. We will describe in Chapter 4 how we measured this signal using a catalogue of high redshift quasars from the SDSS, and we will see in Chapter 5 how we re-analysed all data to obtain a consistent measurement. A similar complete re-analysis has also been performed recently be Ho et al. [2008] using a different approach.

We have seen above that the cross-correlation function and the cross-power spectrum are a pair of Legendre transforms, and therefore are mathematically equivalent. This means that it is possible to measure the correlation in either the real or harmonic space. However, the actual data contain cuts and masks, and thus the equivalence between the two treatments is partially broken. In the real approach it is easier to deal with the data and the masks, while the harmonic space has the nice feature of producing less covariant results, and has been used by Afshordi et al. [2004], Padmanabhan et al. [2005], Ho et al. [2008]. We will use the real space in the next chapters. Other authors have also introduced more sophisticated techniques to perform the correlation. For example, Vielva et al. [2004], McEwen et al. [2007a] used a wavelet technique, which consists in imposing a particular transformation to the data, with the purpose of isolating the scales at which we expect to find the signal. A particular kind of wavelets, called *needlets*, have been used by Pietrobon et al. [2006]. This particular choice of wavelet is claimed to be more useful to measure the cross-correlation because it is easier to understand its localisation on both the real and the harmonic spaces. A last technique has been recently introduced by Granett et al. [2008], and is based on detecting the correlation in a localised way: these authors consider the luminous red galaxies from the SDSS, and study regions in the sky surrounding superclusters and supervoids of scale ~ 100 Mpc, and then stack the CMB signal in the surrounding area. The result shows that the CMB appears in average hotter around the clusters and colder around the voids, at a significance of 4σ. This is an interesting result because it represents the first localisation of the ISW signal, but it has the drawback of being dependent on the particular choice of supercluster and on the radius adopted.

Chapter 4

A high redshift detection of the ISW

The work in this chapter has been published as Giannantonio et al. [2006].

4.1 Introduction

In this chapter we describe the measurement of the ISW obtained by cross-correlating a catalogue of quasars from the Sloan digital sky survey with the CMB data from WMAP.

We use the NBC-KDE (non-Bayesian classifier – kernel density estimator) quasar catalog [Richards et al., 2004, Myers et al., 2006] from the SDSS. Objects in the NBC-KDE catalog are distributed around a median redshift $\bar{z} \sim 1.5$, making this the highest redshift sample ever used to probe the ISW effect. We find a positive signal, suggesting that the dark energy behaves in a way compatible to the cosmological constant up to a redshift of 1.5. In the following we briefly describe the quasar catalog used (Section 4.2), and calculate its auto-correlation (Section 4.3). Next we perform the cross-correlation with the CMB map (Section 4.4). Finally we describe the resulting constraints in Section 4.5, followed by the conclusions.

4.2 The quasar catalog

The quasar data was derived from SDSS DR4 [Adelman-McCarthy et al., 2006, Fukugita et al., 1996, Gunn et al., 1998, 2006, Hogg et al., 2001, Ivezic et al., 2004, Lupton et al., 1999, Pier et al., 2003, Smith et al., 2002, Stoughton et al., 2002, York et al., 2000], using a nonparametric Bayes classifier method based on kernel density estimation (NBC-KDE) described in Richards et al. [2004]. Briefly, this algorithm classifies quasars based on prior multi-color data on known quasars and stars, and is $> 95\%$ complete, with $\sim 5\%$ stellar contamination, to $i = 21$ [Richards et al., 2004, Myers et al., 2006]. The catalog contains $N_q = 344,431$ objects with photometric redshift between 0.1 and 2.7 (see Fig. 4.1), covering two distinct regions of the northern hemisphere of the Galaxy plus three narrow stripes in the southern, covering a total area of 6,670 square degrees.

The stellar contamination is a potentially important systematic. Even if it does not contribute to the cross correlation (assuming the Galaxy has been cleaned from the CMB maps), it will still contribute to the quasar autocorrelation function. The stellar spatial overdensities adds power on fairly large angular scales, which is difficult to explain with quasars alone. Even a stellar contamination as small as 5% can produce significant angular overdensities in the $5-10°$ range, where little contribution is expected from the quasars. For this reason, whenever modeling the expected behavior of our sample, we will assume that it is actually composed by a fraction k of stars and $1-k$ of quasars. In section 4.3 we will show the contamination is $k = 0.05 \pm 0.01$.

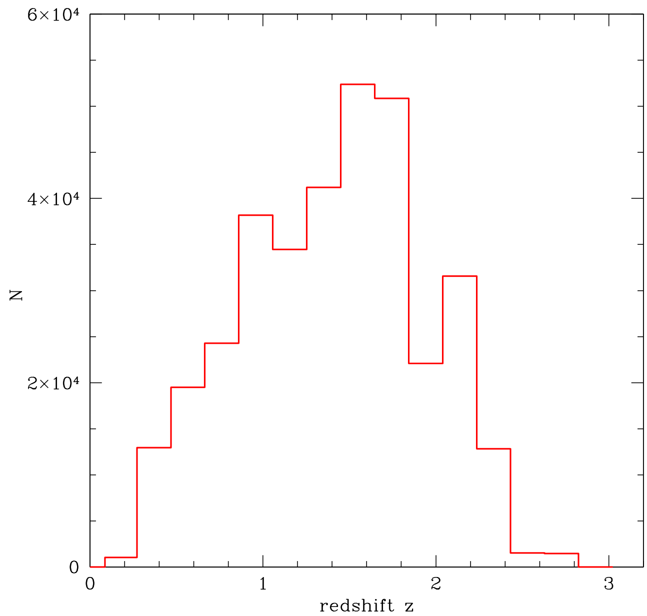

Figure 4.1: Redshift distribution of the quasars. A spline fit of this is used for the theoretical calculations.

4.2.1 Pixellation mask

We are principally interested in the large scale correlations; to calculate these, we pixelize the quasar maps using the same *HEALPix* scheme [Gorski et al., 2005] used to pixelize the *WMAP* maps. We perform most correlations with a resolution parameter $N_{\rm side} = 64$, corresponding to $N_{\rm pix} = 49{,}152$ pixels of $0.92°$ resolution. Due to the partial sky coverage of the survey, only 16% of these pixels actually contain sources.

Clearly the *HEALPix* pixelization will not exactly align with the SDSS regions where the quasars are observed. Some edge pixels will thus be only partially filled and it is important to take these effects into account: in the coarse pixelization described above, up to 20% of the pixels will be partially filled. To account for such effects, we use a high-resolution ($N_{\rm side}^{\rm high} = 512$) pixelization to determine the mask of the actual sky coverage of

DR4, which will determine the fraction of each edge pixel that is matching the observed area. We base the mask on a random sample of galaxies in the DR4 database to ensure roughly uniform sampling in all directions. (A much larger stellar sample would be needed because of the high concentration of sources close to the Galactic plane.) By using a sufficiently large number of random galaxies ($5 \cdot 10^6$) we can be sure to have good sampling when pixelized in the higher resolution. In the high-resolution map there are $N_{\rm pix}^{\rm high} = 3 \cdot 10^6$ total pixels, of which only $5 \cdot 10^5$ cover the area of the survey, which means an average of 10 objects per pixel. In this way we estimate the coverage fraction of each low-resolution pixel, f_i, as

$$f_i = \frac{N_{\rm mask}^{\rm high}(i)}{64}, \tag{4.1}$$

where $N_{\rm mask}^{\rm high}(i)$ is the number of high-resolution pixels within the mask for each coarse pixel i, and for these resolutions, there are 64 high resolution pixels in each coarse pixel.

We correct the maps by dividing the observed number of quasars in a coarse pixel by the fraction of the sky within the pixel that was observed, yielding n_i/f_i. For our correlation estimator, we down-weight such edge pixels by the fraction of sky they measure; this effectively accounts for the additional variance. A more conservative approach is to simply drop these edge pixels, ignoring all quasars in them (although at this resolution they contain roughly 20% of the catalog): we repeated our cross-correlation analysis using this schema and we found compatible results.

We use the higher resolution to calculate the average number of quasars per coarse pixel, $\bar{n}$: this quantity is the total number of quasars divided by the total area of pixels covered by the survey in the higher resolution, rescaled to the pixel surface area in the lower resolution:

$$\bar{n} = \frac{N_q}{N_{\rm mask}^{\rm high}} \times 64, \tag{4.2}$$

where $N_{\rm mask}^{\rm high} = \sum_i N_{\rm mask}^{\rm high}(i)$ is the total number of higher resolution pixels within the mask.

4.2.2 Foregrounds

There are a number of possible systematics in the catalog which could introduce errors resulting in a lack of completeness, bad redshift measurement or further stellar contamination; these could introduce artificial structures in the maps and contaminate the measurements. We checked a number of these, including extinction by dust in our Galaxy, sky brightness, bright star obscuration and poor seeing in two different bands (r and g).

The SDSS imaging data is obtained using drift-scanning, which produces long thin strips of data across the sky. Two adjacent strips are combined to make a stripe, which are then chopped into individual fields of dimension 10×10 arcmins [York et al., 2000]. Clearly, this observing strategy could introduce small correlations along a strip (or stripe), which could extend to very large angles (over 100 degrees) in the imaging data, e.g. systematic differences in the zero-point calibration of the photometry in each strip. Such photometric calibration uncertainties were recently explored by Padmanabhan et al. [2007] and shown to be less than 2%, consistent over the whole SDSS area. This is below other statistical (shot noise) and systematic (extinction, seeing) errors and therefore is not considered further here. We also note that the SDSS scanning strategy is not aligned with any cosmological or galactic signal and would therefore only introduce extra noise into our ISW detection rather than mimicing the signal.

While the extinction is a quantity measurable for each observed object, sky brightness, seeing and number of point sources are global quantities of each 10×10 arcmins field of view. However, given an object we can find the foreground quantities associated to it through the ID number of its field of view and, because the fields are smaller ($\sim 1/25$) than our pixels, we can consider the distribution of all these quantities in each pixel in the same way.

From our random sample of SDSS galaxies, we find the value of each of these foreground quantities associated with each object (the extinction) or each field of view (sky brightness, seeing and number of point sources), and we build their distribution in each pixel. Then we take the median and we find the distributions of the medians of all pixels. Finally, we produce the masks for each foreground excluding the worst 20% pixels, i.e. the pixels whose median value for a given foreground is in the upper 20% tail of the distribution of the medians of that foreground. These masks are shown in Fig. 4.2 for the r band.

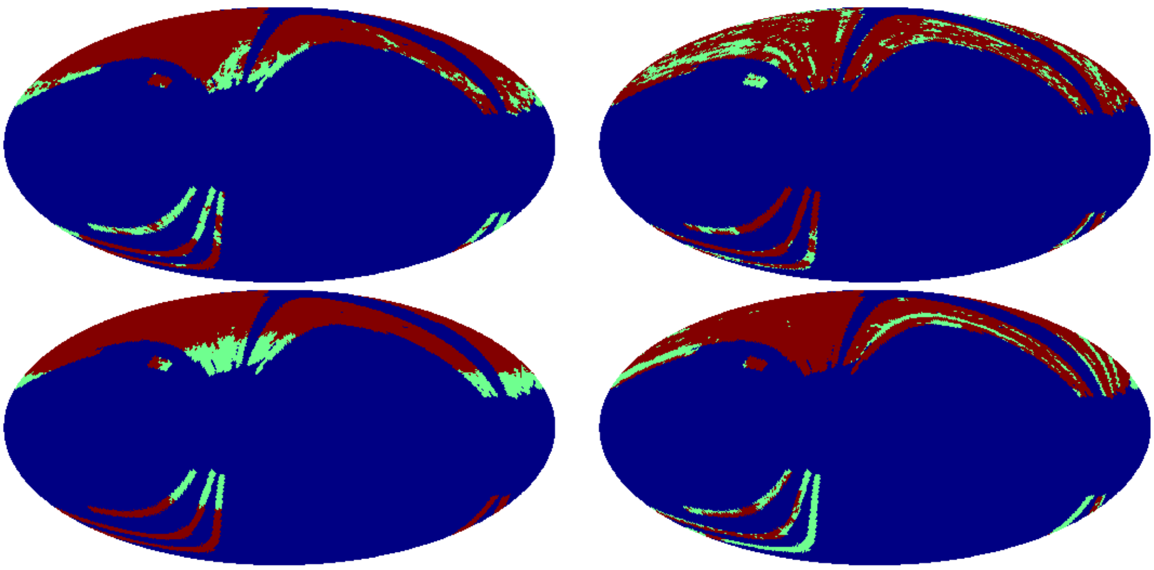

Figure 4.2: Foregrounds masks for extinction (top left), seeing (top right), point sources (bottom left) and sky brightness (bottom right) in the r band. The 20% of pixels with the worst contamination are shown in light green. The most relevant of these effects is the extinction of the sources.

4.3 The auto-correlation

To check the consistency of our method and to probe how biased our quasar sample relative to the underlying dark matter, it is useful to measure first the auto-correlation function (ACF) of the quasar catalog. To do this, we use the estimator $\hat{c}^{tt}$, where the index tt refers to the total catalog (including possible contaminations):

$$\hat{c}^{tt}(\vartheta) = \frac{1}{N_\vartheta} \sum_{i,j} f_i f_j \left(\frac{n_i}{f_i} - \bar{n} \right) \left(\frac{n_j}{f_j} - \bar{n} \right), \tag{4.3}$$

where the sum runs over all the pixels with a given angular separation. As defined above, f_i is the i-th pixel coverage fraction, n_i is the number of sources in the i-th pixel, $\bar{n}$ is the expectation value for the number of objects in the pixel. For each angular bin centered around ϑ,

$$N_\vartheta = \sum_{i,j} f_i f_j \tag{4.4}$$

is the number of pixels pairs separated by an angle within the bin, weighted with the coverage fractions.

Here we present results using $N_b = 5$ bins of ϑ, in the range $0.5^\circ < \vartheta < 10^\circ$. We tried various angular binning schemes and the results seem fairly independent assuming a sufficient number of bins are used. Fig. 4.3 shows the ACF with and without the r band based foreground masks of Fig. 4.2, and the results are very similar using g band based masks. We find that the dominant effect is the extinction; the result obtained with this mask is close to the one given by the application of all masks together. This removal of the areas with the highest 20% of the extinction values is equivalent to cutting pixels with a reddening in the g band $A_g > 0.18$, which is effectively what was done by Myers et al. [2006]; for these reasons, we will use the reddening mask and not the others, in order not to excessively reduce the sample. We have also checked that a stricter cut in reddening (30%) does not change the result. For the other masks the 20% threshold is likely much more aggressive than required, but the independence of the cross-correlation function (henceforth CCF) on these cuts shows that they are not significant contaminants.

This detection is consistent with the previous measurements [Myers et al., 2006, Croom et al., 2004, Porciani et al., 2004]; these previous results used smaller data sets and were focused on smaller angular scales. In Fig. 4.4 we directly compare, using a similar binning, our detection to that of Myers et al. [2006] which analyzed 80,000 objects from SDSS DR1 photometric catalog.

We can model the total theoretical ACF $c^{tt}(\vartheta)$ as composed by the quasar and the star ACFs, $c^{qq}(\vartheta)$ and $c^{ss}(\vartheta)$, in the form

$$c^{tt}(\vartheta) = (1-k)^2 c^{qq}(\vartheta) + k^2 c^{ss}(\vartheta), \tag{4.5}$$

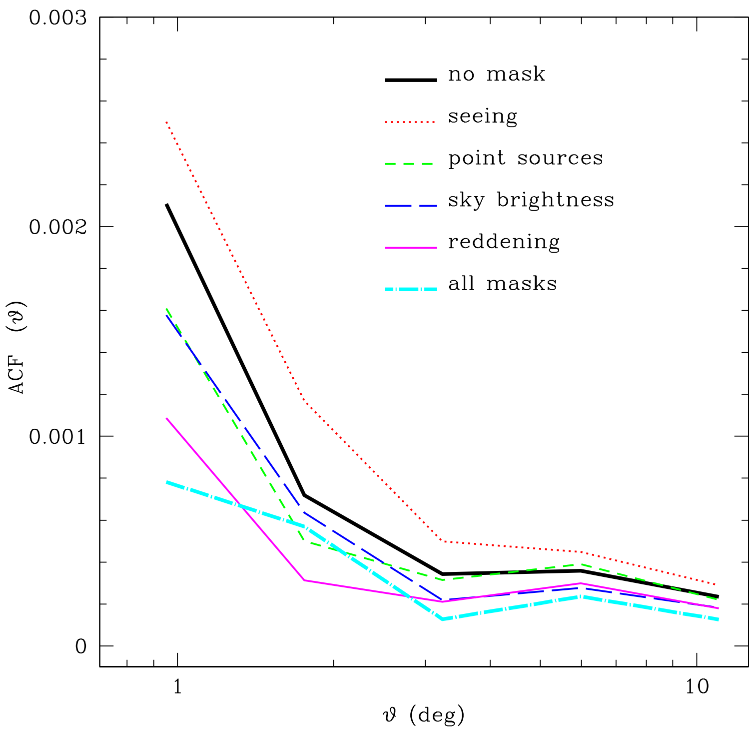

Figure 4.3: Auto-correlation function of the quasars measured for all the sample, for a single foreground mask and for all masks joint. A similar result is obtained for g band masks.

where k is the fraction of stellar contamination and we assume there is not any cross-term, due to the independence of stars and quasars (see Myers et al. [2006].) We obtain the stellar $c^{ss}(\vartheta)$ from the average of 1000 subsamples of kN_q stars (the number of stars we expect to have in the catalog) from a random sample of $2 \cdot 10^6$ stars from the SDSS survey DR4 catalog; the quasar $c^{qq}(\vartheta) = b^2 c^{mm}(\vartheta)$ is calculated from the matter power spectrum for the best fit *WMAP* third year model (*WMAP* 3), produced with `cmbfast` [Seljak and Zaldarriaga, 1996] with a given source redshift distribution and assuming a linear bias factor, b relating the quasar clustering to the matter distribution. We have also to take in account the window function $w(\vartheta)$ associated with our pixelization, that is given by the *HEALPIX* team: the theoretical ACF $c^{qq}(\vartheta)$ is convolved with the window function $w(\vartheta)$. The best values for the parameters are $k = 0.05 \pm 0.01$ and $b = 2.3 \pm 0.2$. The stellar contamination is thus in agreement with the expected value and both the stellar contamination and bias are consistent with those measured by Myers et al. [2006].

We have calculated the errors on the total ACF shown in Fig. 4.4 by producing 1000 random quasar maps, with the same statistics as the total catalog and an added Poisson noise.

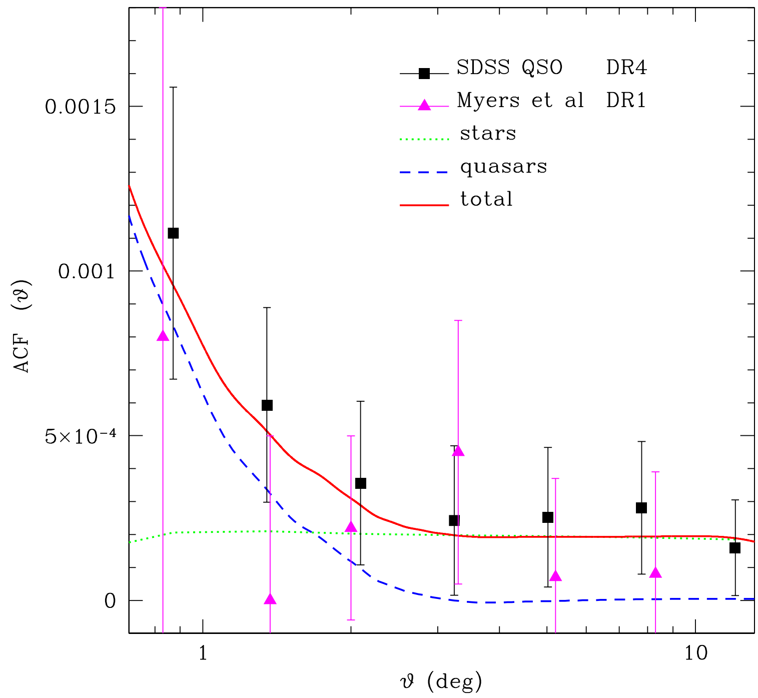

Figure 4.4: The auto-correlation function of the quasar catalog with the reddening mask. The square (black) points are the observations $\hat{c}^{tt}$, the dashed line is the expectation c^{tt}, and the solid and pointed lines are its component (theoretical quasars and stellar contamination). We plot also the last points (red triangles) of the ACF measured by Myers et al. [2006] for comparison.

4.4 The cross-correlation

For the cross-correlation analysis, we use the *WMAP internal linear combination* (ILC) map derived from the third year *WMAP* data [Hinshaw et al., 2007], pixelized in the same way and with the same resolution as the quasar map. Even though this ILC map was already built to minimize the Galactic and other foreground contaminations, we have applied to it the most severe mask given by *WMAP* , the *kp0* mask, which corresponds to a cut of 32% of the sky. We checked that the results do not change significantly if we use the different frequency band maps V and W, corresponding respectively to 61 and 94 GHz, all with the same masking; the results change slightly using the Q band map, which is the most affected by Galactic synchrotron contamination (see section 4.4). We have also checked that the result remains consistent using the *WMAP* 1st year ILC map, and also does not depend on whether we use the smoothed or the raw single band maps.

To measure the cross-correlation function (CCF) between the quasar map and the *WMAP* ILC map, we used the estimator

$$\hat{c}^{Tt}(\vartheta) = \frac{1}{N_\vartheta} \sum_{i,j} f_i \left(T_j - \bar{T}\right) \left(\frac{n_i}{f_i} - \bar{n}\right), \tag{4.6}$$

where T_j is the CMB temperature in the j-th pixel and $\bar{T}$ is the expectation value for the CMB temperature respectively. We again down-weight the partially filled pixels and N_ϑ is defined as above, but with a single weighting factor. We calculated this function in $N_b = 13$ bins of ϑ, in the range $0^\circ < \vartheta < 12^\circ$, with and without using the foreground masks of Fig. 4.2, obtaining the results shown in Fig. 4.5. We obtain very similar results using the r and g band masks. The reddening mask is the one that yields the lowest CCF; to be conservative and consistent with the ACF measure, we choose to apply this same mask. As expected, however, the reddening dependence is weaker for the cross-correlation measurement than for the quasar ACF.

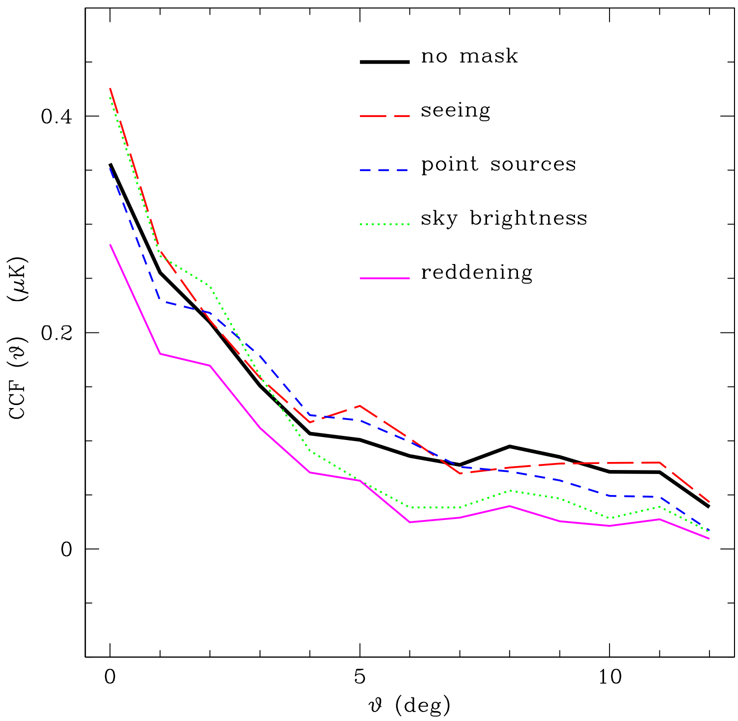

Figure 4.5: Cross-correlation function of the quasars and the CMB measured for various foreground masks. Similar results are obtained for g band masks.

Fig. 4.6 displays the CCF between the WMAP3 ILC map and our NBC-KDE quasar sample. In reality, this is a measure of the cross-correlation between the CMB and a mixed sample of quasars and stars: although one does not expect a correlation between the cosmic radiation and local stars, we measured a small but non zero result. This indicates that the *WMAP* 3 ILC map, even after the most severe *kp0* masking, still has a small residual Galactic contamination. The stellar correlation has to be subtracted from the total detection yielding

$$\hat{c}^{Tq}(\vartheta) = \frac{\hat{c}^{Tt}(\vartheta) - k\hat{c}^{Ts}(\vartheta)}{1-k}. \tag{4.7}$$

We compare this to the theoretical expected function $c^{Tq}(\vartheta)$ calculated again from the ΛCDM model with the *WMAP* 3 best fit parameters, using a program based on `cmbfast` [Seljak and Zaldarriaga, 1996]. Our code, which was first described in Corasaniti et al. [2005], produces for a given model the CMB-matter and matter-matter power spectra in addition to the standard output.

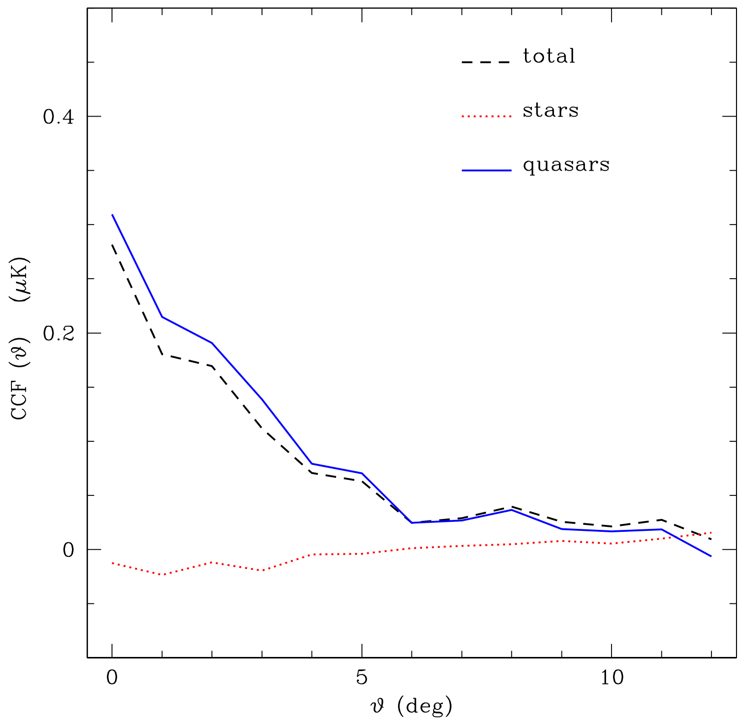

Figure 4.6: The cross-correlation with the quasar catalog shows a small stellar contamination in the *WMAP* 3 ILC map with the *kp0* mask. The dashed line is the measured total CCF $\hat{c}^{Tt}$, while the point-dashed line is the measured stellar CCF, $\hat{c}^{Ts}$. The solid line is the difference between the two, which is our estimator for the true quasar CCF, $\hat{c}^{Tq}$.

To estimate the errors on the CCF and the covariance matrix, we use three different Monte Carlo methods. The first method is to produce a high number (2000) of random CMB maps with the *WMAP* best fit parameters and cross-correlate them with the true quasar map, after the application of the same *kp0* mask. Alternatively, we can do the reverse: use the true temperature map and make random maps of the quasars using the *WMAP* parameters and our observed bias, to which we add the Poisson error on the counts in the pixels. Both of these approaches produce similar answers, showing the covariances seem to be independent of any peculiarities of either of the two observed maps.

These approaches give the covariances assuming the absence of correlations; while this should work well assuming any true correlations are weak, it is important to understand the extent to which the presence of correlations will bias the covariance calculation. Indeed, if there are strong correlations, then these approaches should overestimate the errors. To account for correlations, we want to generate random temperature and quasar maps with the same ACF and CCF of the measured maps, including also the Poisson uncertainty in the quasar counts.

Based on the standard ΛCDM model, we can generate the expected angular power spectra for the anisotropies $C_l^{TT}, C_l^{Tq}, C_l^{qq}$ for the temperature only, the cross-correlation and the quasar autocorrelation. Here, the cross spectrum is assumed to arise solely from the ISW effect. From these power spectra, we can generate three random maps and use them to calculate the errors in the cross-correlation [Boughn et al., 1998]. We begin by making random temperature maps, T_i^r, based on C_l^{TT}. (We neglect any noise which is thought to be small on the scales of interest.) We then decompose the quasar power spectrum into two parts:

$$C_l^{qq} \equiv C_l^{qq\parallel} + C_l^{qq\perp}, \tag{4.8}$$

where the parallel and orthogonal signs indicate completely correlated and uncorrelated with respect to the temperature map, and

$$\begin{aligned} C_l^{qq\parallel} &\equiv \frac{(C_l^{Tq})^2}{C_l^{TT}} \\ C_l^{qq\perp} &\equiv C_l^{qq} - \frac{(C_l^{Tq})^2}{C_l^{TT}}. \end{aligned} \tag{4.9}$$

Using $C_l^{qq\parallel}$ and the same phases as for the temperature map, we create a correlated quasar density map, $\delta_i^{r\parallel}$; we add to this an uncorrelated quasar density map,$\delta_i^{r\perp}$ created using $C_l^{qq\perp}$, with independent random phases. The total quasar density is $\delta_i^r = \delta_i^{r\parallel} + \delta_i^{r\perp}$, and we can now build a random total quasar map n_i^r, as

$$n_i^r = (1 + \delta_i)\bar{n}. \tag{4.10}$$

Finally, we can add random Poisson noise to this, which we derive from the quasar number in each pixel.

Generating 2000 Monte Carlo simulations n_i^r and correlating them with the random temperature map T_i^r we can now find the covariance matrix due to sample variance, R_{ij}^{samp}. The results are consistent with what we obtain with the errors in the temperature only.

The errors in the estimate made from Eq. (4.7) should also include measurement errors; assuming the mask is known, these can arise from uncertainties in k, the fraction of stellar contamination, or from the assumed stellar cross correlation c^{Ts}. The full covariance is thus approximately:

$$R_{ij}^{Tq} \simeq R_{ij}^{\mathrm{samp}} + k^2 R_{ij}^{Ts} + \gamma_{ij}\sigma_k^2, \tag{4.11}$$

where

$$\gamma_{ij} = (\hat{c}_i^{Tt} - \hat{c}_i^{Ts})(\hat{c}_j^{Tt} - \hat{c}_j^{Ts}) \tag{4.12}$$

and we have assumed the stellar contamination $k \ll 1$ and σ_k is its error. We account for the uncertainty of the star CCF R_{ij}^{Ts} calculating cross-correlations between random samples of kN_q stars and the CMB map. The best fit and diagonal errors are shown in Fig. 4.7.

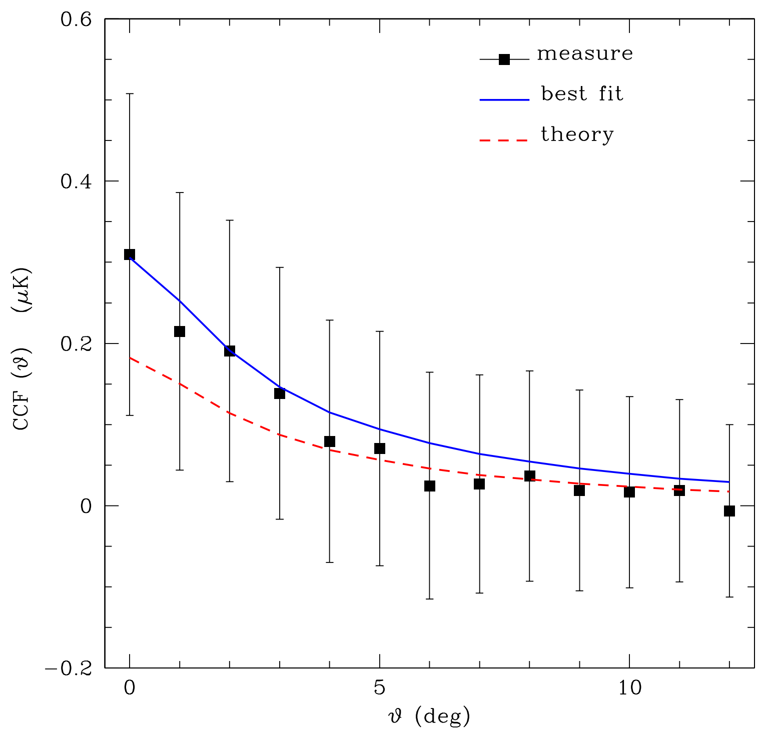

Figure 4.7: The measure of the cross-correlation. The points are the observed correlation between WMAP and the quasars, the solid line is the best fit ΛCDM theoretical model and the dashed line is the prediction for the *WMAP* 3 best fit model with $b = 2.3$. The points are highly correlated: the typical level of correlation between two neighbouring bins is $\sim 95\%$.

Three of the points in Fig. 4.7 are more than 1σ greater than zero, but the points are all highly correlated: the total significance of the ISW detection is found to be conservatively 2.1σ. Making less conservative choices in the analysis can lead to slightly higher significance, but it does not exceed 2.5σ. This significance is based on a theoretical model for the expected ISW signal; using a modified version of the `cmbfast` code, we calculated the predicted cross-correlation function for the *WMAP* 3 best fit ΛCDM model, for a matter map with the redshift selection function shown in Fig. 4.1. We include the pixel window function and bin the expected correlation into the $N_b = 13$ c_i in the same way as we calculated the experimental CCF.

We can compare the theoretical CCF c_i (the index Tq is understood) with the observed values $\hat{c}_i$ and assume a Gaussian likelihood model as

$$\mathcal{L} = (2\pi)^{-N/2}[\det R_{ij}]^{-1/2} \exp[-\sum_{ij} R_{ij}^{-1}(\hat{c}_i - c_i)(\hat{c}_j - c_j)/2], \tag{4.13}$$

where R_{ij} is the CMB-quasar cross-correlation function covariance matrix defined in Eq. (4.11). It would also be possible to perform a likelihood analysis using a non-Gaussian statistic, although this would require a particular model for non-Gaussianity which is currently not available nor observationally motivated. The Gaussian assumption is known to be a good approximation for the CMB field, at least at large scales; some small non-Gaussian contribution is thought to exsist in the density field, but we can safely assume that the resulting effect on the cross-correlation will be small. As suggested by Cabre et al. [2007], this can be tested by comparing the error bars obtained by using the real density map or a simulated Gaussian map.

Another important point is the model dependence of our measured covariance matrix R_{ij}. We have generated it using the WMAP best fit model, and so one should in principle recalculate it iteratively with the parameters of the new best fit model. However, since our best model is not very different from the best WMAP one, we can safely assume that this effect would not lead to a significance change in the results.

For a given distribution of sources, the shape of the theoretical curves remains unchanged to a good approximation; however, the amplitude of the cross correlation strongly depends on the cosmological model, so that we can write [Boughn et al., 1998]

$$c^{Tq}(\vartheta) = A(\Omega_m, w) g^{Tq}(\vartheta), \tag{4.14}$$

where $g^{Tq}(\vartheta)$ is normalized to 1 at $0°$. We found the best value for A maximizing the likelihood, i.e.

$$A = \frac{\sum_{i,j=1}^{N} R_{ij}^{-1} g_i \hat{c}_j}{\sum_{i,j=1}^{N} R_{ij}^{-1} g_i g_j}, \tag{4.15}$$

and the variance

$$\sigma_A^2 = \left[\sum_{i,j=1}^{N} R_{ij}^{-1} g_i g_j \right]^{-1}. \tag{4.16}$$

The best fit for the CCF is $A = (0.30 \pm 0.14)\mu$K.

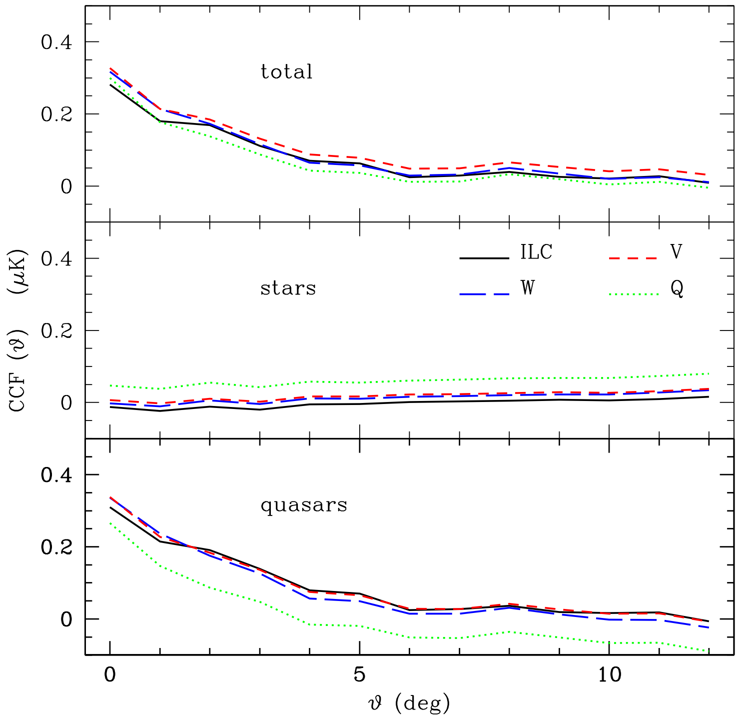

Figure 4.8: Frequency dependence of the cross-correlation, for the ILC map (black, solid), W (blue, long dashed), V (red, short dashed) and Q (green, dotted) bands. The first panel shows the measured CCF with the reddening corrected KDE catalog; in the second panel we plot the observed CCF with our random star samples (see text); the last panel shows the subtraction of the stellar contamination.

In order to study the frequency dependence of our result, we measure the cross-correlation using the single band CMB maps (W, V and Q); in the first panel of Fig. 4.8 we show the measured CCF for the single band maps, and we can see that the measure is almost frequency independent. We see in the second panel that the correlation with the random star sample is different for the different maps, being low as expected for the ILC map, increasing for the W and V bands, in which the Galactic contamination is more relevant, and being even bigger for the Q band, which is significantly affected by synchrotron radiation. The effect of the subtraction is shown in the last panel: the resulting CCF is still frequency independent and very consistent for the ILC and the V and W bands, while the galactic contamination starts to be important in the Q band, actually hindering the measure of the cross-correlation for this band.

4.5 Cosmological constraints

To compare with these observations, we calculate the expected ISW cross-correlations based on linear theory using a modified version of the `cmbfast` code [Corasaniti et al., 2005]. We calculate the quasar auto-correlations in the same way and assume a non-evolving linear bias factor. For the purposes of calculating the expected cross correlation, we use the actual measured redshift selection function of the sample $\varphi = dN/dz$ normalized to unity. Were the quasar bias to evolve with redshift (e.g., as detected by Porciani et al. [2004], Croom et al. [2004], Myers et al. [2006]), this would effectively shift the redshift weighting. We use the measurements of the quasar auto-correlation function to determine this bias to be $b = 2.3 \pm 0.2$, consistent with previous measurements made at smaller scales [Porciani et al., 2004, Croom et al., 2004, Myers et al., 2006].

Assuming the cross-correlation that we see is due to the ISW effect, we can put some constraints on the nature of dark energy. First, consider the pure CDM model without any dark energy, ($\Omega_m = 1, \Omega_\Lambda = 0$); by relaxing some assumptions, such as using a strongly broken power law for the primordial power spectrum, such models might be consistent with the *WMAP* data [Blanchard et al., 2003]. However, these models would predict no ISW correlations, so would be disfavored at the 2σ level with this data alone, and even more strongly when other ISW observations are included.

Next, consider a flat dark energy dominated model (wCDM) with constant equation of state w. We first explore the likelihood function of the parameters Ω_m, w with the constraint that the values of $\omega_b \equiv \Omega_b h^2, \omega_m \equiv \Omega_m h^2$ and the other parameters are fixed to the *WMAP* 3 best fit values ($\omega_b = 0.0223, \omega_m = 0.128$) [Spergel et al., 2007]. Here and below, the Hubble parameter is $100h\mathrm{kms}^{-1}\mathrm{Mpc}^{-1}$. We obtain the result shown in Fig. 4.9.

We can see that the data are in favor of the ΛCDM model, but due to the weak detection only models far away from this are actually ruled out. Most notably, models with a very small matter fraction predict too large a correlation and are inconsistent with the measurement. Fixing $w = -1$ yields the 1σ interval for the matter fraction $0.075 \le \Omega_m \le 0.475$.

While we have used *WMAP* constraints on the matter and baryon densities above, most models will actually be inconsistent with the positions of the CMB Doppler peaks. It is interesting to consider the family of models which are consistent with the full temperature power spectrum measurements: for this, we need the angular scale of the Doppler features to be fixed to the observations. The sound horizon scale is effectively fixed when we fix ω_m and ω_b, so we must add the additional constraint that the models have the same comoving distance to the last scattering surface, D_*^A, given by

$$D_*^A = \frac{1}{H_0} \int_{1/(1+z_*)}^{1} \frac{1}{\sqrt{\Omega_\Lambda a^{4-3(1+w)} + \Omega_m a}} da, \tag{4.17}$$

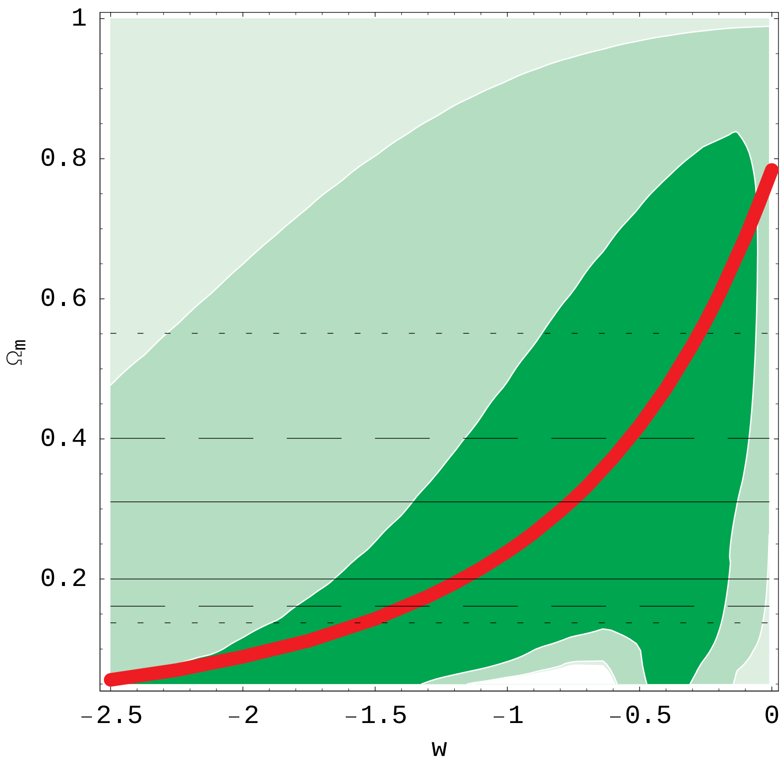

Figure 4.9: Likelihood contours within 1, 2 and 3 σ on $w - \Omega_m$ inferred from this ISW detection alone. On the thick red line lies the family of the models whose TT spectrum matches the *WMAP* measured one, having the right comoving distance to the LSS, according to Eq. (4.17). The thin black lines are the constraints on the Hubble parameter h [Freedman et al., 2001] at 1, 2 and 3 σ (solid, dashed and dotted) assuming $\omega_m = 0.128$.

where z_* is the redshift of the last scattering surface, weakly dependent on ω_m. D_*^A is kept constant if the variations in w are compensated by changes in the Hubble parameter h and the matter density Ω_m: in Fig. 4.9 we show the family of the models fulfilling this condition, and we see that most of them are compatible with our ISW detection.

This range of models is consistent both with the CMB autocorrelation and cross-correlation measurements: for instance, we show in Fig. 4.10 the temperature power spectra of two of these models; it is slightly different from the *WMAP* 3 best fit only at very large scales.

Note however that many of these models are inconsistent with direct measurements of the Hubble constant. For $w = -0.5$, the Hubble constant would have to be as low as $h = 0.55$, while for $w = -2.0$ the Hubble constant would be unreasonably high, $h = 1.20$. Current limits on the Hubble constant, e.g. $h = 72 \pm 8$ [Freedman et al., 2001], would constrain our measured w in the range $-1.18 \leq w \leq -0.76$. Models with w in the range are practically indistinguishable from the best fit cosmological constant model plotted in Fig. 4.11.

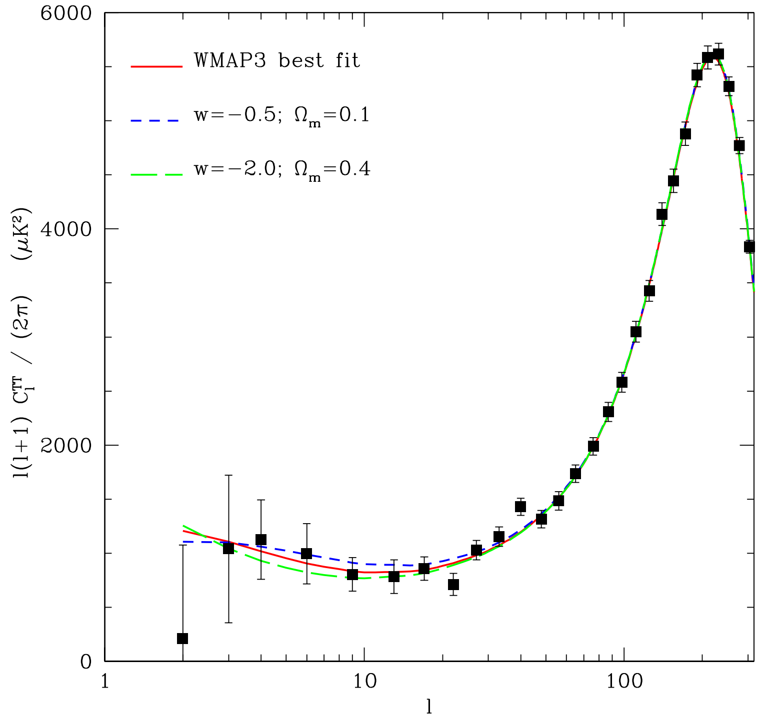

Figure 4.10: Temperature power spectrum of models with the same angular diameter distance to the last scattering surface as the *WMAP* 3 best fit compared with the binned *WMAP* 3 data (points). Changes in w are compensated by changes in Ω_m, but h undergoes considerable variations.

We have also investigated different classes of models which might be more likely to produce a significantly different ISW signal at the quasar redshift. There are two ways models might be strongly ruled out given our relatively weak detection: either they predict a correlation of the opposite sign, or they predict a much higher amplitude of correlation. Producing a negative correlation requires that the gravitational potential grow in time rather than decay, which is difficult to arrange in typical dark energy scenarios because the accelerated expansion tends to slow down the growth of structure; one possibility is a closed model without dark energy, as suggested by Nolta et al. [2004].

Producing a much larger signal at high redshifts is also difficult, given the other constraints on dark energy. For the models discussed above where dark energy scales as a power law, its fractional density tends to be small at a redshift of $z \sim 1.5$. In a cosmological constant model, $\Omega_{DE}(z = 1.5) = 0.16$; while this density can be higher for $w > -1$, the transition to dark energy domination becomes less sudden, leading to a smaller effect. If however there were a sharp drop in the dark energy density, it would be possible to be for the dark energy to be large at high redshifts while still remaining compatible with constraints from lower redshifts. In such a model, our measurement can limit the dark energy density at $z = 1.5$; models with $\Omega_{DE}(z = 1.5) < 0.5$ would produce a much higher cross correlation than is observed, and can be ruled out at the 3σ level.

An alternative explanation of the dark energy problem is to modify the laws of gravity on large scales; such theories may have consequences for structure formation which are significantly different to dark energy models, even if the background expansion appears the same. The ISW correlations are an important way of probing these differences, particularly at high redshift [Lue et al., 2004]. There are many ways of implementing such changes, but much recent work has focused on the extra-dimensional model of Dvali, Gabadadze and Porrati (DGP) [Dvali et al., 2000, Koyama and Maartens, 2006]; under some assumptions, Song et al. [2007] have recently shown the ISW signal to be comparable to dark energy at low redshift, but significantly higher above $z = 1$ in an open DGP model. At a redshift of $z = 1.5$, this enhancement increases the expected cross correlation by a factor of two; while still consistent with our present observations, larger quasar samples could be used to constrain such models in the future.

4.5.1 Comparison of ISW detections

We can now compare our detection with previous ones. Following previous convention [Gaztanaga et al., 2006, Corasaniti et al., 2005], we plot the observed CCF at 6° in function of the mean redshift of the survey in Fig. 4.11. This angular scale is chosen to avoid possible contamination from other effects that are dominant on smaller scales, such as lensing and SZ; however, it should be remembered that this representation is a one dimensional slice of the correlation function data. This approach can suppress the high redshift measurements, where a given angle corresponds to a larger physical scale. In the figure, we also add a conservative 30% error on the estimation of the mean redshift of the surveys.

We also plot the theoretical expected values for the CCF at these redshifts for the models of Fig. 4.10. As above, we assume consistency with the CMB power spectrum, i.e. we fix the comoving distance to the last scattering surface defined in Eq. (4.17), while other parameters are fixed to the best fit *WMAP* 3 values. We see that the behavior is largely that expected from a cosmological constant model, with the amplitude dropping off at high redshifts. While many of the measurements are actually higher than expected, the differences are largely within the expected errors. This provides further support that the observed cross-correlations are due to the ISW effect.

4.6 Conclusions

Here we have presented evidence of a weak correlation between the CMB and the distribution of high redshift quasars detected in the SDSS. Its amplitude, angular dependence and independence of the CMB frequency are all consistent with the interpretation as due

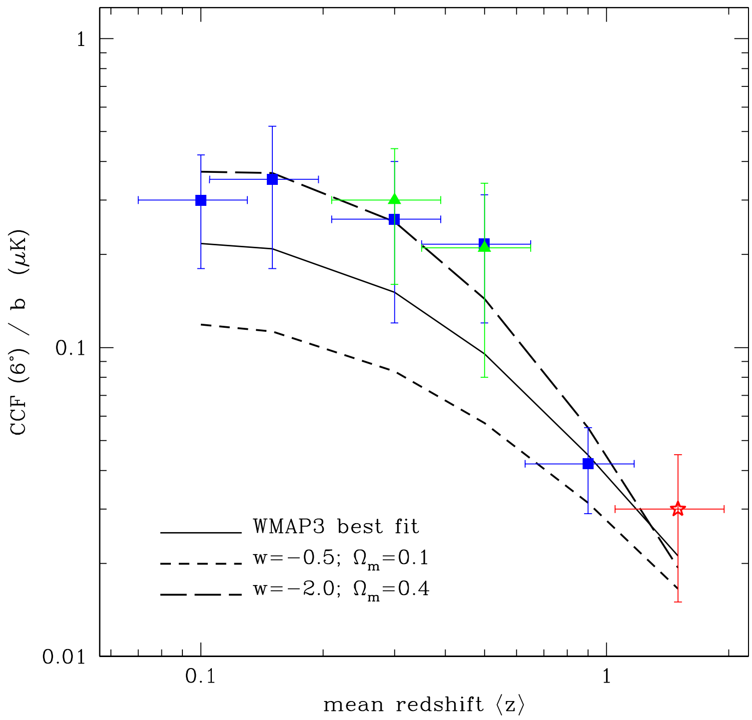

Figure 4.11: Summary of the detections of the ISW effect through cross-correlation with different catalogs, compared with *WMAP* 3 best fit model. The blue (squared) points are in the order the correlations with 2MASS, APM, SDSS, SDSS high-z, NVSS+HEAO, as collected by Gaztanaga et al. [2006]; the green (triangular) points are the measure by Cabre et al. [2006], while the red (star) point is our KDE-QSO measure. The lines are the theoretical expectations for *WMAP* 3 best fit model (solid), and two models with $w = -2$ (long dashed) and $w = -0.5$ (short dashed) respectively (see text for details of the models).

to the integrated Sachs-Wolfe effect, with a significance in the range $2 - 2.5\sigma$, robust to changes in the mask and assumptions about stellar contamination.

Without dark energy, no such correlation is expected. With a mean quasar redshift of $z = 1.5$, this represents the earliest evidence yet for dark energy and gives us a means to further probe its evolution. Our measurements directly limit the density of dark energy at high redshifts, independent of its lower redshift behavior. They can also potentially provide interesting limits on alternative models with modified gravity.

These measurements will be improved when the photometrically classified quasar data set is extended to the entire SDSS area. With a data set 40% larger, the photometric redshifts could be used to split the sample into two broad redshift bins, above and below $z = 1.5$, potentially allowing the evolution of the ISW effect to be seen within one self-consistent sample.

To obtain even stronger cosmological constraints, all the various ISW measurements will be combined in the next chapter, including possible covariances which arise from the overlap of the different surveys in sky coverage and redshift.

Chapter 5

Combined analysis of the ISW

The work in this chapter has been published as Giannantonio et al. [2008b].

5.1 Introduction

As described in Chapter 3, many groups have detected the CMB-density correlation using the accurate WMAP CMB data and various density probes distributed at a range of redshifts and in different regions of the electromagnetic spectrum. These measurements span a range of redshift going from $z = 0.1$ to $z = 1.5$, where the ISW effect has been measured at significance levels typically around $2 - 3\sigma$, and appear generally compatible with the expectation from the ΛCDM model.

Although indicative of the presence of dark energy, none of these measures alone has significant power to constrain models due to their low significance. Thus, it is important to combine the various observations; but some care must be taken in doing so. The surveys are often overlapping both in sky coverage and in redshift range, meaning there are likely covariances between them that may be important when considering a large scale effect like the ISW. In addition, these measurements have been made with a variety of techniques, using angular correlations, Fourier modes, or a range of wavelet techniques [Vielva et al., 2004, McEwen et al., 2007b, Pietrobon et al., 2006, McEwen et al., 2007a]. The error bars themselves have also been estimated using different techniques, using both jack-knife approaches and Monte Carlo simulations of the CMB sky.

A combined analysis has been attempted in the past adding several measures in order to extend the constraining power in redshift and learn more about the behaviour of dark energy and other cosmological parameters [Gaztanaga et al., 2006, Corasaniti et al., 2005, Cooray et al., 2005, Giannantonio and Melchiorri, 2006]. However, this analysis largely ignored the differences in the observations and accounted for the covariances between experiments in a fairly arbitrary way. Here we perform a combined analysis by reanalysing all the observations in a consistent way, measuring directly the covariances between the different observations using a number of different methods and looking at the cross-correlations between all the various data sets. In this way we hope to give a definitive result for the ISW evidence for dark energy and the resulting cosmological constraints.

This chapter is structured as follows: we begin in Section 5.2 by giving a brief theoretical description of the ISW effect, how the cross-correlation is measured, and the important issue of estimating the covariance between observations. In Section 5.3 we describe the catalogues used for the cross-correlation, and in Section 5.4 we show the measurements of the various cross-correlation functions between the different catalogues and their cross-correlation with the CMB. We discuss the significance of the measurements in Section 5.5 and show the resulting cosmological constraints in Section 5.6, before some concluding remarks in Section 5.7.

5.2 Method

5.2.1 Correlation estimators

Our aim is to estimate the correlation between several galaxy surveys and the CMB: as described above, this measure can be performed in the real space using the CCF or in the harmonic space with the cross-correlation power spectrum. The two methods are theoretically equivalent for a full sky analysis and both have been used to detect the ISW cross-correlations. However, when one moves away from the ideal full-sky scenario, it is more straightforward to account for the sky mask using the real space correlations, and therefore we will follow this approach here. This part follows closely the treatement described in Chapter 4 for a single catalogue.

The matter density and CMB temperature as well as their projections onto the celestial sphere are in principle continuous fields; however, we only have access to the sampling of these fields experimentally obtained by measuring the CMB temperature in some fixed directions and counting the number of galaxies in a given patch of sky. In practise, we pixelise these maps using the HEALPix pixelisation scheme [Gorski et al., 2005], using a relatively coarse resolution: $N_{\mathrm{side}} = 64$, corresponding to $N_{\mathrm{pix}} = 49{,}152$ pixels with dimensions $0.92^\circ \times 0.92^\circ$. This resolution is sufficient for a large scale correlations like the ISW and makes it tractable to perform large numbers of Monte Carlo simulations. A finer resolution ($N_{\mathrm{side}} = 128$) was explored, but the results did not change significantly.

In making the maps, we assign the average temperature or the total number of galaxies to each pixel. The maps are masked according to the particular requirements for each catalogue and the most relevant foregrounds as discussed below. It is inevitable that some pixels are only partially covered in the original survey, either because only part of the area was observed, or because some of this area was masked out. In such cases, predominately occurring on the edge of the survey, the number of galaxies in a pixel is estimated as $n'_i = n_i / f_i$ where f_i is the fraction of the pixel observed. The mask was obtained through sampling all objects in each catalogue in a higher resolution ($N_{\rm high} = 512$) as described in Giannantonio et al. [2006].

From these maps, both the auto- and cross-correlations were estimated, down-weighting those pixels with partial coverage proportionally to f_i. For the auto-correlation functions (ACFs), we used the estimator,

$$\hat{C}(\vartheta) = \frac{1}{N_\vartheta} \sum_{i,j} f_i \left(\frac{n_i}{f_i} - \bar{n} \right) f_j \left(\frac{n_j}{f_j} - \bar{n} \right), \tag{5.1}$$

where $\bar{n}$ is the average number of galaxies in a pixel for the survey of interest, and $N_\vartheta = \sum_{ij} f_i f_j$ is the weighted number of pairs of pixels with separation ϑ. For the temperature maps, we simply replace n_i and $\bar{n}$ with the pixel temperature and average temperature of the CMB maps.

More generally, we are interested in the cross-correlation function between the survey p and the survey q; this is estimated similarly, accounting for the fact that the pixel weighting and mean number per pixel will depend on the survey,

$$\hat{C}^{pq}(\vartheta) = \frac{1}{N_\vartheta^{pq}} \sum_{i,j} f_i^p \left(\frac{n_i^p}{f_i^p} - \bar{n}^p \right) f_j^q \left(\frac{n_j^q}{f_j^q} - \bar{n}^q \right). \tag{5.2}$$

The number of pairs of pixels at a given separation, $N_\vartheta^{pq} = \sum_{ij} f_i^p f_j^q$, will depend on both of the surveys under consideration. This again extends to the density-CMB CCFs in the obvious way.

We use $N_b = 13$ angular bins in the range $0^\circ < \vartheta < 12^\circ$. We use a linear binning, and have explored the dependence of our results on the choice of binning, changing both the number and trying a logarithmic binning; neither had significant impact on the results.

5.2.2 Covariance estimators

An important aspect of this calculation is the estimation of the covariance of the cross-correlation measurements. As described most recently by Cabre et al. [2007], there are a number of different ways to calculate the errors on this measurement, each with their own advantages and drawbacks. Here, we calculate our errors in three ways: a Monte Carlo method (MC1), where the covariance matrix is estimated by measuring the CCF between random CMB maps while keeping fixed the observed density map; a second Monte Carlo method (MC2), similar to MC1 but including also random density maps which are correlated at the expected level with the random temperature maps; and jack-knife errors (JK) which are estimated by looking at the variance of the CCF when patches of the sky are removed.

The first approach is to generate random Monte Carlo maps of the CMB assuming the *WMAP* best fit cosmology, and estimating the covariance matrix cross-correlating these maps with the true density maps (MC1).

The *WMAP* third year fiducial model we use throughout this paper has baryon density $\Omega_b = 0.04185$, matter density $\Omega_m = 0.2402$, Hubble constant $H_0 = 73.0$, scalar spectral index $n_s = 0.958$, optical depth $\tau = 0.092$ and amplitude of density fluctuations $A = 0.80$ at $k = 0.002$ Mpc^{-1}.

The MC1 is the most widely used estimator in the literature, though here we extend the usual calculation to account for covariances between the CCFs of the CMB with different surveys. This method is reasonably fast to implement and accounts for the cosmic variance and the accidental correlations with the CMB which are the primary source of error. However, it is asymmetrical, in that it does not account for the variance in the density maps or its Poisson noise; the MC1 method also assumes there are no cross-correlations, though the expected (and observed) weakness of the cross-correlation indicate that this should not introduce a large bias. Finally, like all Monte Carlo approaches, it is model dependent and could fail if the data model is poorly understood (e.g. foregrounds or non-Gaussianity of the maps).

However, some of these problems can be avoided if we also generate random density maps for each catalogue based on the *WMAP* cosmology and the redshift distribution, with the addition of Poisson noise to the maps (MC2). In this case, we have the ability to account for the expected correlations between the maps as described in Appendix A. This method is more time demanding, in that it requires more random maps for each correlation measurement; it also retains the unwanted model dependence, and unlike the previous method has no explicit dependence on any of the observed maps.

To estimate the covariance between the different angular bins of a single CCF following the MC1 and MC2 methods for each catalogue k we use the following estimator of the full covariance matrix:

$$\mathcal{C}_{ij} = \frac{1}{M} \sum_{k=1}^{M} \left[\hat{C}_k^{Tg}(\vartheta_i) - \bar{C}^{Tg}(\vartheta_i) \right] \left[\hat{C}_k^{Tg}(\vartheta_j) - \bar{C}^{Tg}(\vartheta_j) \right], \tag{5.3}$$

where $\bar{C}^{Tg}(\vartheta_i)$ are the mean correlation functions in the i-th angular bin over M realisations; the diagonal part of these matrices gives the variance of the CCF in each bin, $\mathcal{C}_{ii}^k = \sigma_i^2$, while the off-diagonal part represents the covariance between the points.

The last method to estimate the covariance (jack-knife) consists in estimating the variance by generating mock density maps from the true ones, simply discarding a small patch of them. In practise, we can divide the original density map in M patches which have roughly equal area, and discard in turn a different patch to calculate the CCF. The estimator for the covariance matrix is in this case,

$$\begin{aligned} \mathcal{C}_{ij} = \frac{M-1}{M} \sum_{k=1}^{M} & \left[\hat{C}_k^{Tg}(\vartheta_i) - \bar{C}^{Tg}(\vartheta_i) \right] \\ \times & \left[\hat{C}_k^{Tg}(\vartheta_j) - \bar{C}^{Tg}(\vartheta_j) \right], \end{aligned} \tag{5.4}$$

The advantage of this method is its model independence, but it has the big drawback of giving different answers depending on the size and number of the discarded areas. It also implicitly assumes independence of the various patches, which is not always the case.

Our ultimate goal is to measure the total covariance matrix between all the catalogues. To do so, we need to estimate the total covariance matrix $\mathcal{C}_{ij}^{pq}$, as the matrix that has in the diagonal blocks the single catalogue $\mathcal{C}_{ij}^{pp}$, and in the off-diagonal parts is

$$\mathcal{C}_{ij}^{pq} = \frac{1}{M} \sum_{k=1}^{M} \left[\hat{C}_k^{Tp}(\vartheta_i) - \bar{C}^{Tp}(\vartheta_i) \right] \left[\hat{C}_k^{Tq}(\vartheta_j) - \bar{C}^{Tq}(\vartheta_j) \right] . \tag{5.5}$$

For simplicity, we redefine the indexes i, j in a way that they run from 1 to $N_{\mathrm{tot}} = N_{\mathrm{bin}} \times N_{\mathrm{cat}}$, i.e. redefining the data, theory and mock arrays as the concatenation of all catalogues' CCFs with the CMB. In this way, the covariance matrix is simply the square matrix $\mathcal{C}_{ij}$, identical to the Eq. (5.5) but now with dimension N_{tot}. A similar expression can be easily obtained for the JK case.

5.3 The catalogues

To best detect the ISW effect through the cross-correlation technique, we ideally require surveys covering large fractions of the sky, so that accidental correlations will cancel out. The surveys also need to be sufficiently deep, in order to probe the gravitational potentials where the ISW effect is being created. Ideally, we would like to span the redshift range $0 < z < 3$, separated into subsamples of different depths so as to measure the redshift dependence of the effect and get some handle on the evolution of the dark energy. However, only rather coarse redshift information is required, so redshift errors of $\Delta z \sim 0.1$ obtainable through photometric methods should be sufficient for these purposes. This is beyond the present state of the observations, but the differences in the redshift distributions of the various samples does provide some limited information on the dark energy evolution.

At present, the best surveys available for this purpose (and where ISW detections have previously been found) include the following: the optical Sloan Digital Sky Survey (SDSS), the infrared 2 Micron All-Sky Survey (2MASS), the X-ray catalogue from the High Energy Astrophysical Observatory (HEAO) and radio galaxy catalogue from the NRAO VLA Sky Survey (NVSS). The high quality of the SDSS data allows us to extract some further subsamples from it, consisting of Luminous Red Galaxies (LRG) and quasars (QSO) in addition to the main galaxy sample [Peiris and Spergel, 2000]. These are the samples we use in our analysis below, and include most of the significant reports of the ISW detection. Because the data has not been publicly released and since it is not significantly deeper than 2MASS, we omit the APM galaxy survey, which has also been reported to have evidence for ISW cross-correlations [Fosalba and Gaztanaga, 2004].

We show in Fig. 5.1 the redshift distributions dN/dz of the catalogues we use, normalised to unity; we can see that they span a redshift range $0 < z < 2.5$, similar to the theoretical requirement, although the overlap between different samples is significant. This means that the covariance between the measures could be large: one of the goals of this paper is to quantify it.

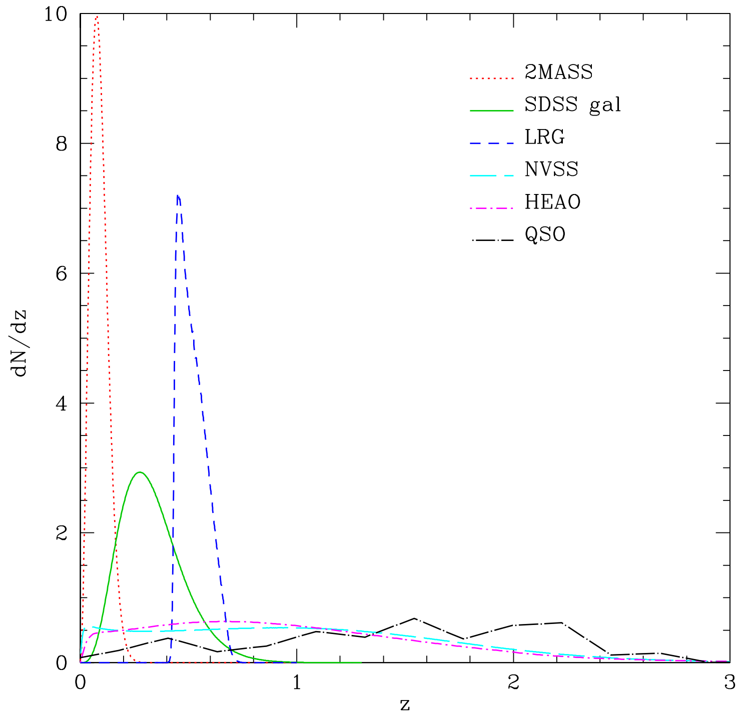

Figure 5.1: The redshift distributions of all catalogues dN/dz normalised to unity. The significant overlap between redshift distributions (especially for the X-ray and radio surveys) results in a covariance matrix with significant non-diagonal elements.

In the rest of this section, we will present the characteristics of all the samples we use, in order of increasing redshift.

5.3.1 2MASS

The 2 Micron All Sky Survey (2MASS) is an infrared catalogue; its extended source catalogue (XSC) [Jarrett et al., 2000] contains $\sim 800,000$ galaxies with median redshift $z \sim 0.1$ and, unlike the point source catalogue (PSC) is almost free of stellar contamination. Some evidence for ISW cross-correlations has been seen in 2MASS previously [Afshordi et al., 2004, Rassat et al., 2007], and we largely follow the galaxy selection of those previous analyses here.

Accordingly, we select galaxies according to their K_s-band isophotal magnitude K_{20} (k_m_i_20_c, - 20 mag / arcsec^2). These magnitudes are corrected for Galactic extinction using the infrared reddening maps by Schlegel et al. [1998], as $K'_{20} = K_{20} - A_K$, where the extinction is $A_K = 0.367(B - V)$. The requirement of completeness of the catalogue is satisfied by imposing a cut in magnitude $K'_{20} < 14.0$, while we can exclude low redshift sources with the condition $K'_{20} > 12.0$. We only include objects with a uniform detection threshold (use_src $= 1$), and remove known artifacts (cc_flag $\neq$ a and cc_flag $\neq$ z); we also exclude a small fraction of objects where the magnitude or its error were not recorded.

In addition to the pixelisation geometry mask, we follow earlier analyses [Afshordi et al., 2004, Rassat et al., 2007] excluding areas of the sky with high reddening, discarding pixels with $A_k > 0.05$; this leaves 69% of the sky and 718,000 galaxies after excluding artifacts. It is reported by Afshordi et al. [2004], Rassat et al. [2007] that the redshift distribution of these galaxies is well approximated by the function:

$$\frac{dN}{dz} = \frac{1}{\Gamma\left(\frac{m+1}{\beta}\right)} \beta \frac{z^m}{z_0^{m+1}} \exp\left[-\left(\frac{z}{z_0}\right)^{\beta}\right] \tag{5.6}$$

where the parameters are $z_0 = 0.072$, $\beta = 1.752$ and $m = 1.901$. This distribution is shown together with the others in Fig. 5.1.

To check the consistency of the dataset and its bias we calculate its auto-correlation function (ACF). The measure is in good agreement with the predictions for the best fit *WMAP* model with a galactic bias $b_g = 1.4$ as found by Rassat et al. [2007], as we can see in Fig. 5.2.

5.3.2 SDSS galaxies

The SDSS Sixth Data Release (DR6) [Adelman-McCarthy et al., 2008, York et al., 2000] is the largest wide optical galaxy survey available at the present for the northern hemisphere. From this catalogue we select a magnitude limited subsample $18 < r^\star < 21$; this catalogue contains 30 million galaxies. Here $r^\star$ is the extinction corrected r SDSS übercalibrated model magnitude, i.e. using the SDSS variables $r^\star =$ ubercal.modelMag_r $-$ extinction_r: this corresponds to the procedure of Cabre et al. [2006], with the difference of using the sixth data release and the übercalibrated model magnitude instead of the Petrosian magnitude, which is less reliable for faint objects. We apply the pixelisation geometry mask and, in addition, we discard the pixels most affected by reddening, with $A_r > 0.18$. We also discard the southern stripes, since they are most affected by foregrounds and edge effects.

We select only objects with photometric redshifts between $0.1 < z < 0.9$ and with an error on the redshift $\sigma_z < 0.5z$, leaving 23.5 million galaxies in the catalogue. We could use these photometric redshifts as the basis of the theoretical calculations; however, since the distribution of the photometric redshifts can be affected by singularities in the redshift determination procedure, we use instead a fit to their distribution with the smooth function of Eq. (5.6). The best fit parameters are in this case $z_0 = 0.113$, $\beta = 1.197$ and $m = 3.457$, corresponding to a median redshift $z_{\rm med} = 0.32$. (The results are actually independent of whether the fit or the actual redshift distribution is used). The fit is shown together with the others in Fig. 5.1.

The ACF is in agreement with the prediction for the *WMAP* best fit cosmology and a bias $b_g = 1$, as we can see in Fig. 5.2.

5.3.3 SDSS LRG

Luminous Red Galaxies (LRGs) from the SDSS have been used often to find evidence for the ISW effect, as they have a deeper redshift distribution than the ordinary galaxies, with a mean redshift of $z \sim 0.5$ [Fosalba et al., 2003, Scranton et al., 2003, Padmanabhan et al., 2005]. In this analysis we use the MegaZ LRG sample [Collister et al., 2007, Blake et al., 2006] which contains 1.5 million objects from the SDSS DR6 selected with a neural network [1]. To ensure completeness we require that $i < 20$. To reduce stellar contamination we implement cuts on δ_{sg}, which is a variable of the MegaZ neural network estimator, defined such that $\delta_{sg} = 1$ if the object is a galaxy, and $\delta_{sg} = 0$ if it is a star [Collister et al., 2007]. Following the conservative suggestion by Collister et al. [2007], we choose a cut $\delta_{sg} > 0.2$, which is reported to reduce stellar contamination below 2% while keeping 99.9 % of the galaxies. Stricter cuts have been tried with no significant changes to the CCF.

The mask we apply to this catalogue is a combination of the pixel geometry mask and two foreground masks, to account for seeing (cutting pixels with median seeing in the red band greater than 1.4 arcsec) and reddening (cutting pixels with median extinction in the red band $A_r > 0.18$). The redshift distribution function in this case is found directly from the photometric redshifts that are given in the catalogue, and is shown in Fig. 5.1.

We show the auto-correlation function in Fig. 5.2, where we can see that this is in agreement with the theoretical prediction from the best fit *WMAP* cosmology and a bias $b_g = 1.8$, which is compatible with the estimate $b_g = 1.7 \pm 0.2$ shown by Blake et al. [2006], although some excess power at large scales is present, which might be explained as being produced by a residual stellar contamination.

5.3.4 NVSS

The NRAO VLA Sky Survey (NVSS) is a flux limited radio survey at a frequency of 1.4 GHz, with a minimum flux of ~ 2.5 mJy. It is complete for declinations $\delta > -40°$, covering roughly 80% of the sky and contains $1.8 \cdot 10^6$ sources. The mask to this catalogue is a combination of the most aggressive *WMAP* mask (*kp0*) plus a cut around point sources

[1] While the DR4 MegaZ data is public, the DR6 data used here was provided thanks to F. Abdalla, C. Blake and O. Lahav, personal communication.

as described in Boughn and Crittenden [2002], which also describes corrections made for a systematic in the mean density as a function of declination. The cross-correlations between NVSS and *WMAP* have been observed by a number of groups, both in the correlation function [Boughn and Crittenden, 2004a, Nolta et al., 2004] and using an array of wavelet techniques [Vielva et al., 2004, McEwen et al., 2007b, Pietrobon et al., 2006, McEwen et al., 2007a].

The redshift distribution is uncertain; we base ours on models by Dunlop and Peacock [1990] which seem to be still widely accepted, and are largely consistent with observations of cross-correlations with other surveys (though see below for further discussion). We calculate the auto-correlation function and present it in Fig. 5.2; there is good agreement with the theory from the *WMAP* best fit model and a galactic bias $b_g = 1.5$, compatible with the result $b_g = 1.5 \pm 0.2$ by Boughn and Crittenden [2002], although we see some excess power at small scales.

5.3.5 HEAO

The High Energy Astrophysical Observatory (HEAO1-A2) data set is a full sky flux map of hard X-rays counts in the $2 - 10$ keV energy range [Boldt, 1987]. We use the map and the mask determined by Boughn et al. [1998, 2002]: the map is masked for the galactic plane, a round area around the galactic centre and patch areas around bright point sources. The redshift distribution is also uncertain and provided by modelling the X-ray background, as described in Boughn et al. [1998], Boughn and Crittenden [2004b].

The modelling of the theoretical ACF for this catalogue is more complex than those considered above, in that we are looking at flux rather than number counts and the experimental beam is large compared to the pixel size. (The point spread function of the beam is well modelled by a Gaussian with a full width, half maximum size of $\vartheta_{\mathrm{FWHM}} = 3.04^\circ$ [Boughn et al., 2002]). In addition, the number of photons is small, so there is an additional contribution from the photon shot noise. Thus, the observed correlation is the sum of three terms: the intrinsic correlations, the Poisson correlations due to finite numbers of sources and shot noise due to the finite number of photons. The variance of the X-ray map is dominated by photon shot noise (41%) and Poisson correlations (45%) while intrinsic correlations are relatively small (14%). However, the shot noise contributes only to the 0° ACF while the Poisson correlations fall off more quickly with angle than intrinsic correlations and become sub-dominant for $\theta > 4^\circ$. Consequently, the combination of shot noise and Poisson correlations are not the primary component of the total noise in the ISW signal. We can see in Fig. 5.2 that the total modelled ACF fits the observations on large angles, assuming the *WMAP* best fit model and a galactic bias $b_g = 1.06$, as found by Boughn and Crittenden [2004a].

5.3.6 SDSS QSO

The quasar survey we use comes from the SDSS DR6 through the NBC-KDE catalogue by Richards et al. [2004], Richards et al., that contains over a million quasars. This new DR6 edition of the catalogue does not include as many parameter cuts as did the previous DR4 version. To obtain the cleanest possible dataset, and for consistency with our previous measure of the cross-correlation [Giannantonio et al., 2006], we only used quasar candidates selected via the UVX-only criteria used in the previous version of this photometric quasar catalogue. In addition, we consider only objects with a *good* (positive) quality flag. Following our previous results [Giannantonio et al., 2006] we impose a cut in reddening, discarding areas with $A_g > 0.18$. After these cuts, we are left with $N \simeq 500,000$ quasars.

This catalogue comes with estimated photometric redshifts, upon which we base the redshift distribution shown in Fig. 5.1. There is evidence of some excess power in the ACF on large angular separations that indicate faint stars are still present in the catalogue after these cuts, as seen before in Giannantonio et al. [2006]. The amount of stellar contamination is $\sim 3\%$, as found by Richards et al., from comparison with the ACF of a random sample of stars taken from the SDSS, and does not contribute to the correlation with the CMB, as expected. We can see in Fig. 5.2 the ACF for this sample; this is in good agreement with theoretical expectations and determines the bias of $b_g = 2.3$, as previously found in Myers et al. [2006], Giannantonio et al. [2006].

5.4 Results

In this section we present the measurements of the all the correlation functions between the data sets we consider and their covariance.

5.4.1 Density-density cross-correlations

We begin by examining the cross-correlations between the different density maps. These measurements are shown in Fig. 5.2, with the auto-correlation measurements along the diagonal. This is the first measurement of the cross-correlations between most of these data sets. The error bars are estimated by Monte Carlo realisations of all the data sets (MC2, as described above).

The measurements largely agree with their theoretical predictions, which are based on the *WMAP* best fit model using the visibility functions in Fig. 5.1 and a linear bias for each. The agreement is to be expected for the auto-correlations, which were the basis for the estimates of the linear bias. However, the cross-correlation measurements provide a useful consistency check for our model, and in particular for the visibility functions, since the cross-correlations are most sensitive to the degree that the measurements overlap in redshift.

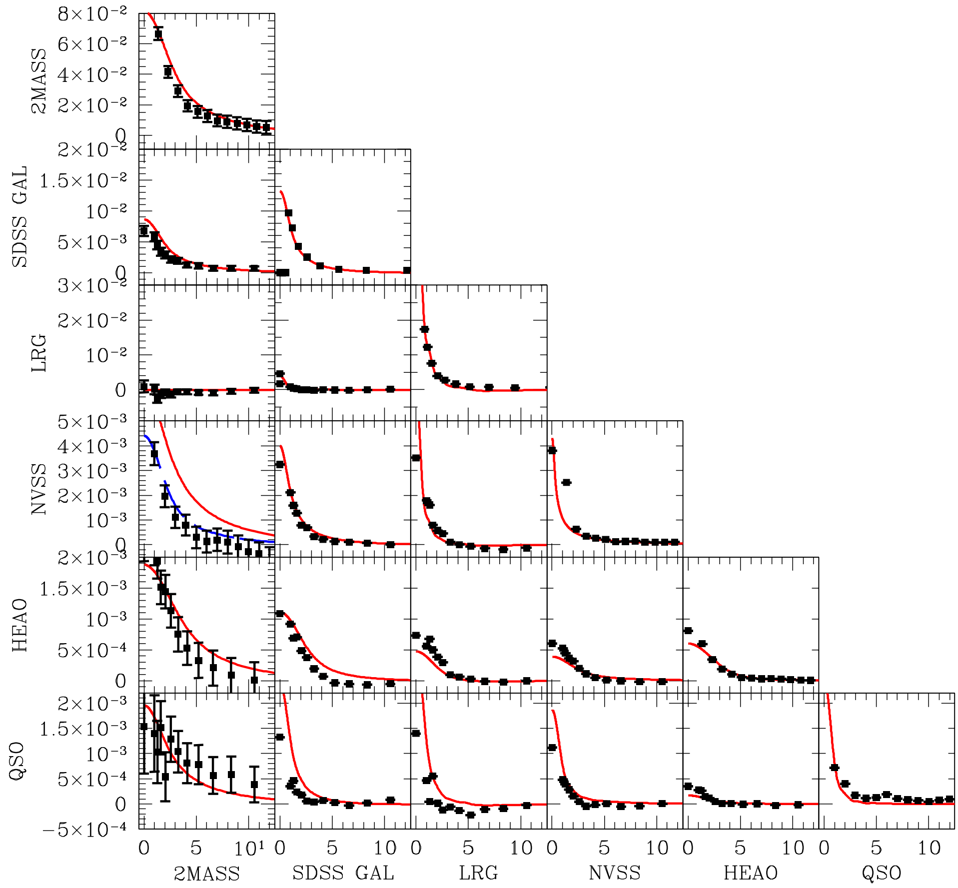

Figure 5.2: Measures of the two-point correlation functions between all the combinations of catalogues, where the units in the x-axis are degrees. The auto-correlations are on the diagonal, and the solid (red) lines show the theory from *WMAP* best fit cosmology and the galactic bias from the literature. The largest discrepancy with theory, in the NVSS-2MASS CCF, can be addressed by a small change in the assumed NVSS redshift distribution (blue dashed line).

The largest discrepancy between the measurements and theory is in the NVSS-2MASS cross-correlation, where the theory is roughly twice as large as expected. This is perhaps not unexpected, since the NVSS visibility function is known to be uncertain, and the overlap with 2MASS is in a narrow region of redshift. It does indicate that less of the NVSS correlations are arising from the 2MASS redshift range than expected in the model. This could be because either the low redshift tail of the NVSS visibility function is overestimated relative to the high redshift region, or because the bias of the radio galaxies increases as we move to higher redshift. This can be addressed by a small change in the visibility function, as demonstrated by the blue dashed line in the panel (in this case we arbitrarily imposed a low redshift exponential damping in the visibility function, leaving the rest unchanged). Such a change does not significantly affect the expected CMB cross-correlations considered here.

5.4.2 Temperature-density cross-correlations

We next turn our attention to the cross-correlation functions between each density map and the CMB maps from *WMAP* 3. We use the *internal linear combination* (ILC) maps from *WMAP* , which are the cleanest data, although we have checked that the results do not depend on the frequency (see below), and we also apply the *kp0* mask to them, cutting the galactic plane region. As we can see in Fig. 5.3, the measures are again largely in agreement with the theoretical predictions for the *WMAP* best fit model.

We have also checked the results obtained with the new *WMAP* 5 data, and we have not found any difference in the correlations. This is expected, since *WMAP* maps are already cosmic variance limited at large scales.

We now discuss the results obtained following the three methods of error estimation discussed in §5.2 above.

Temperature-only Monte Carlo errors

We generate 5000 Monte Carlo simulations of the CMB anisotropy map with the *WMAP* best fit parameters. We estimate the covariance matrix for each catalogue using Eq. (5.3), and the total covariance matrix follows from its generalisation.

These are the errors shown in the top panel of Fig. 5.3; as we can see, the errors are quite large, especially for the low redshift catalogues, and the significance is further decreased by the high correlation between the points. We have checked that these errors converge; the convergence is already good after $\sim$ 700 Monte Carlos for each single catalogue, and after $\sim$ 3000 Monte Carlos for the full covariance matrix. The covariance between the points is shown in Fig. 5.5.

Full Monte Carlo errors

In this case, in addition to 5000 new mock CMB maps, we also generate 5000 mock density maps for each catalogue, correlated as expected theoretically, based on the *WMAP* best cosmology and their redshift distributions. This process is described in detail in Appendix A. In addition, the Poisson noise is added due to the expected number of objects per pixel.

The result calculated in this way is shown in the bottom panel of Fig. 5.3, and the relative full covariance matrix in the bottom panel of Fig. 5.5. We can see that the errors estimated in this way are generally consistent with their MC1 counterparts.

The largest difference between the approaches is in the covariance between the cross-correlations measured with different data sets (Fig. 5.5). Using the observed density maps yields both positive and negative covariance, while the covariance is only positive

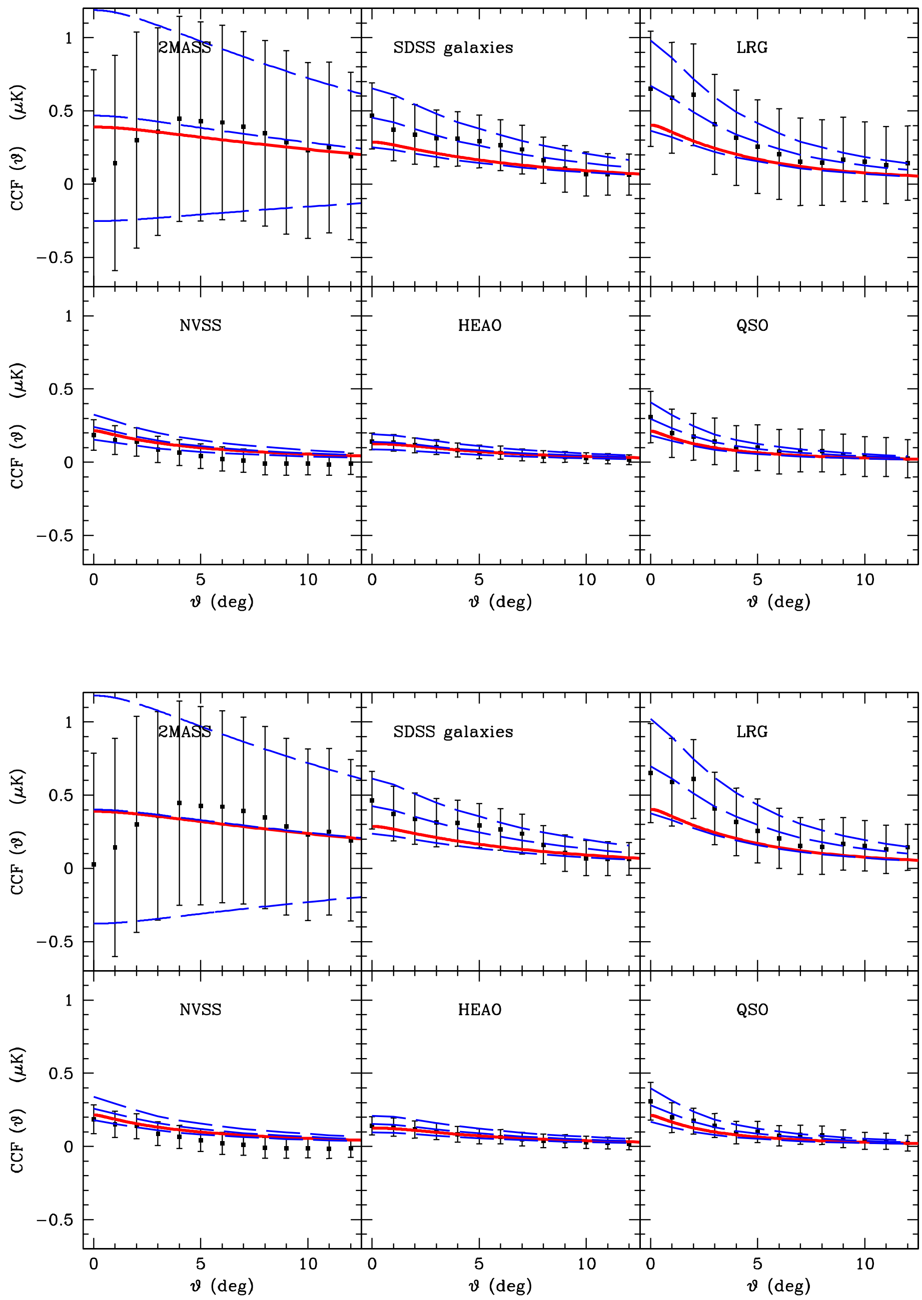

Figure 5.3: Monte Carlo error estimation. Measurements of the cross-correlation functions between all the catalogues and the *WMAP* CMB maps (black points), compared with the theory from *WMAP* best fit cosmology and the galactic bias from the literature (red solid lines). The best fit amplitudes and their $1-\sigma$ deviations are shown in blue (dashed). In the top panel, the errors are calculated with 5000 temperature-only Monte Carlos and, in the bottom panel, Monte Carlos for temperature and density including expected correlations. We see that the errors are comparable for individual observations. Because of known contamination from the Sunyaev-Zeldovich effect in the 2MASS data [Afshordi et al., 2004], the four smallest angle bins were excluded from the fits.

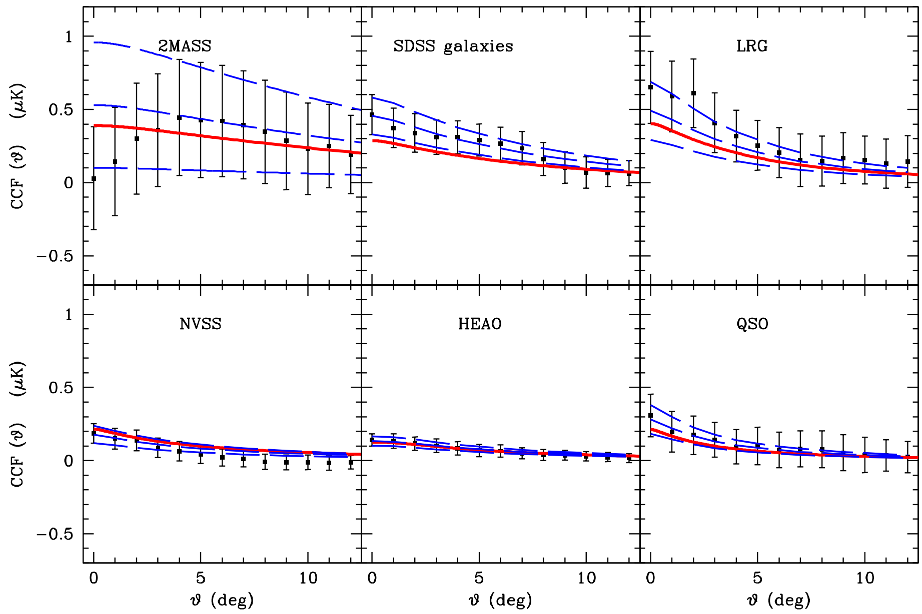

Figure 5.4: Jack-knife error estimation. The lines are the same as in Fig. 5.3. The errors are somewhat smaller than seen from the Monte Carlo estimates, possibly due to correlations between the jack-knife subsamples.

when all the maps are simulated. In the first approach, the strongest correlations are between the SDSS subsamples and 2MASS. In the second approach, which is purely theoretical, the largest covariances are between 2MASS, NVSS and HEAO. The NVSS-HEAO covariance is expected to be large, since they are both essentially all sky maps and have similar redshift coverage. The large covariance between 2MASS-HEAO and 2MASS-NVSS is more surprising given the differences in the redshift distributions, but seem to be driven by the low redshift tail of the NVSS and HEAO distributions. As noted above, the cross-correlations are smaller than expected theoretically for 2MASS-NVSS (and to a lesser extent for 2MASS-NVSS). This indicates that the overlap of 2MASS with NVSS and HEAO is less than assumed, and that we have likely overestimated the covariance somewhat. However, the low significance of the 2MASS CCF means this has a small impact on the final result.

The differences between the two methods appear large for the off-diagonal elements. The reasons for these differences are unclear, but they suggest that the observed density maps are somewhat atypical of those simulated. However, it is not surprising that any particular realisations would appear atypical in some way. Despite these differences, these covariance matrices give comparable final significance, as is discussed below.

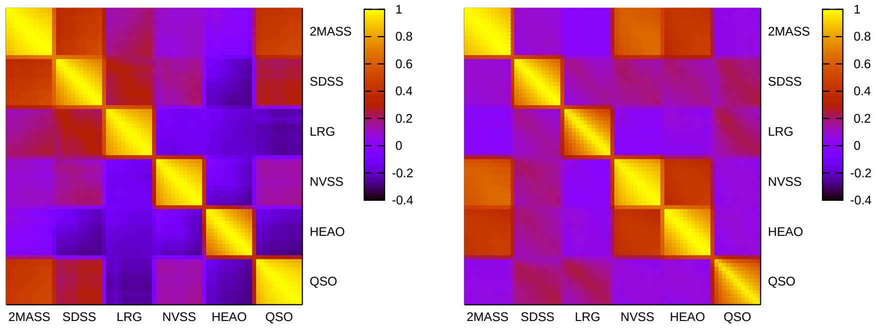

Figure 5.5: The total covariance matrix obtained with 5000 Monte Carlos, normalised. The left panel shows the temperature-only Monte Carlos, while the right panel is the result of the full Monte Carlos. While the diagonal (single experiment) covariances are similar, those between experiments (off-diagonal) are somewhat different.

Jack-knife errors

For completeness, we also present the errors estimated from a jack-knife method. However, there is more ambiguity in implementing this method, leading to uncertainty in the resulting estimates in the errors.

One issue is what patch size to use. Ideally for the jack-knife approach one would like the cross-correlation observations to be uncorrelated between patches. In reality, some correlation is inevitable. We also need enough patches to estimate the full covariance matrix without it becoming singular, which drives the size of the patches down. Thus, some kind of compromise is required.

Since we are interested in the CCF on scales of a few degrees, we choose a patch size of order 10 square degrees. Because the surveys have different geometry and masks, the number of sectors M will be different in each one. The number of patches we can have in this way is generally low (~ 100), so we cannot estimate the total covariance matrix which, having a dimension $N_{\mathrm{tot}} = 78$, requires at least a few hundred independent random measures to be correctly estimated.

Cross-correlation measurements also introduce other issues, since the CMB and density maps are often covering different regions of the sky.

In the end, we tried to be conservative and ensure the most independence between the subsamples by only including data which were in the CMB and the density maps, and masking out both maps in the jack-knife estimates. The results we obtained are shown in Table 5.1, where we compare the results obtained with jack-knife of the density map only and of both density and temperature maps using identical masks.

The jack-knife ambiguities are even more problematic when calculating the full covariance between observations using different density maps, since the density maps often will not overlap on the sky. For this reason, and because such a large number of jack-knifes are required to estimate the total covariance matrix, we do not attempt to estimate it here.

The error bars we estimate using the jack-knife method are of the same order of magnitude as those seen in the Monte Carlo approaches, but are somewhat smaller leading to higher significance in the detection. This could be due to the lack of independence of the jack-knife patches, or because some aspect of the data is missing from the Monte Carlo approach. We will use the Monte Carlo estimates below, focusing primarily on the results from MC2.

It is worth noting that this result is not in complete agreement with what found by Cabre et al. [2007], where a better match was reported between the JK and MC methods. In that paper, it was noted that the conditions of equal area and shape of the JK patches were paramount to achieve consistent results, and while this is possible in a simulation, it is only approachable to a certain accuracy when dealing with real data which are masked in an irregular way. As an example of the variability of the JK result, we show in Fig. 5.6 the changes of the best fit amplitude and its error for ten different procedures of calculating the JK errors.

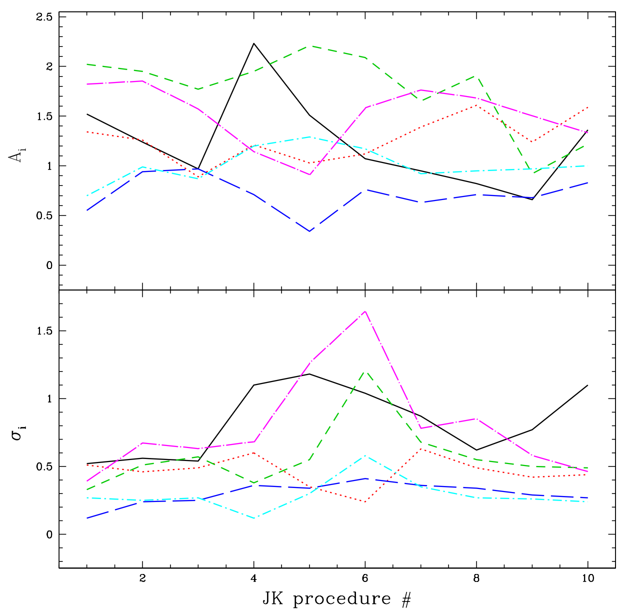

Figure 5.6: Different results obtained for the best fit amplitudes A_i (top) and relative errors σ_i for each catalogue using ten different JK procedures. The catalogues are: 2MASS (black, solid), SDSS gal (red, dotted); LRG (green, short dash); NVSS (blue, long dash); HEAO (cyan, short dash-dot); QSO (magenta, long dash-dot). The JK methods are in order: three different numbers of azimuthal slices, whose angle are chosen to preserve roughly equal areas; three different choices of disk subtractions; four different choices of rectangular sector subtractions.

5.4.3 Foregrounds & systematics

Since the ISW effect is gravitational in origin, it is frequency independent as are the resulting CMB-density cross-correlations. However, a frequency dependence may in principle be introduced by foregrounds and local contamination, such as the SZ effect. In Fig. 5.7 we compare the CCF obtained with the different frequency bands from *WMAP* (ILC, W, V and Q bands), and we see that the result is substantially independent of frequency, with the exception of the 2MASS catalogue. However, the 2MASS CCF detection is of low significance and our final answers are not greatly sensitive to its inclusion.

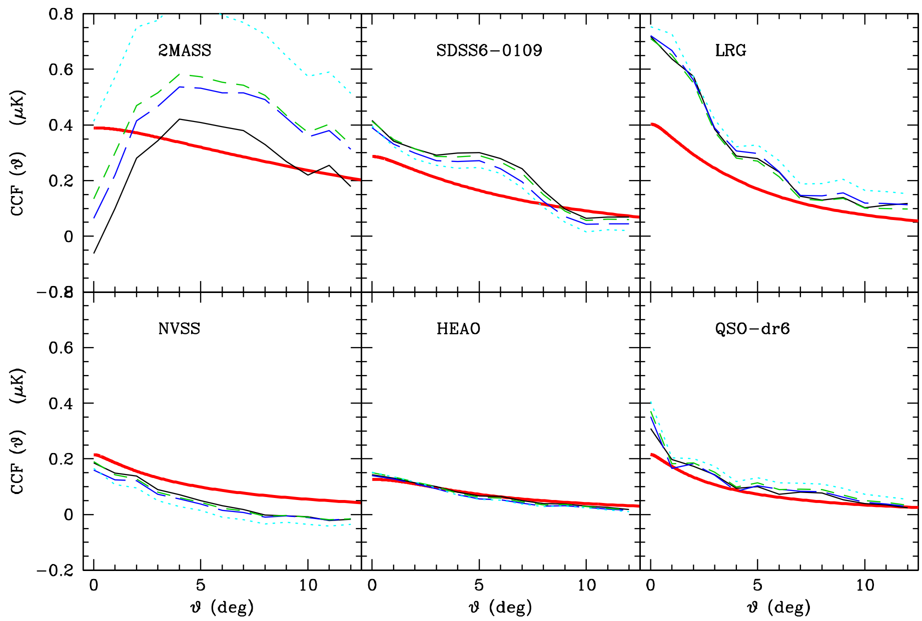

Figure 5.7: Comparison of the CCF functions obtained with the different *WMAP* frequency bands. The black (solid) is using the internal linear combination map; the blue (long-dashed) uses the W band, the green (short-dashed) uses the V-band and the cyan (dotted) uses the Q-band. The thick red curves show the ΛCDM prediction.

Foreground contamination of the ISW signal is generally produced at low redshifts. A good way to make sure that such effects are not dominating the measurement is to check for the sensitivity to the masking of these foregrounds (e.g. Giannantonio and Melchiorri [2006]). For samples derived from the SDSS (galaxies, LRGs and QSO), we test for foreground effects by cutting the 20% of pixels with the highest reddening (extinction), seeing, sky brightness, and number of unresolved point sources. The most relevant masks are the reddening and seeing masks which do not substantially change the results. For the other samples (2MASS, HEAO and NVSS), we do not explore the masking, but we refer to the foreground analyses presented in earlier papers [Afshordi et al., 2004, Rassat et al., 2007, Boughn and Crittenden, 2002, Boughn et al., 2002].

5.4.4 Comparison with previous measures

We briefly compare our CCF measurements to others in the literature.

2MASS

From Fig. 5.3 it is clear that the CCF for the 2MASS survey is consistent with zero. Previous analyses of these data found some evidence for a positive correlation [Afshordi et al., 2004, Rassat et al., 2007]; however, these were performed in Fourier space and included modelling of the SZ effect, which manifests itself with anti-correlations at small angular scales. Indeed, it appears in Fig. 3 that the observed CCF turns over at small angles. If the smallest four angular bins are removed, the fit to the CCF is consistent with the ΛCDM theory; however, it is only significant at the $\sim 1\sigma$ level. In any case, 2MASS appears to have the least significant evidence for cross-correlations.

SDSS galaxies

The main galaxy sample from the SDSS has a measured CCF which is also in good agreement with the theory. In this case, we note that we do not find agreement with the previous result of Cabre et al. [2006], who reported a measured CCF of almost double the amplitude that we detect.

After discussions with the authors [Cabre et al., 2006], we jointly found this discrepancy resulted from an additional cleaning cut, where they discarded all galaxies with a large error on their Petrosian r magnitude, imposing the condition `petroMagErr_r` < 0.2. Imposing this same condition, we found that we could reproduce their result. Further, masking those areas with high proportion of Petrosian error also gave similar results.

However, the motivation for such a cut is unclear. It is known that the Petrosian magnitudes are not accurate for faint objects, for which the best estimator is the `model` magnitude [Ade, 2007]. While having objects with a well measured magnitude is desirable, we see no reason why cutting galaxies on the basis of a poor estimate of their magnitudes should double the correlation with the CMB. This could happen if it were produced by some foreground mechanism, such as seeing or reddening, but we checked that none of the possible foreground maskings raised the CCF in any way comparable to the aforementioned cut.

Therefore, lacking a valid reason to include this cut, and preferring to be conservative, we do not make the Petrosian error cut and our CCF is thus lower than seen by Cabre et al. [2006]. While it is worrying that a choice of masking has such a dramatic effect on the amplitude of the observed cross-correlation, it should be noted that the cross-correlation was largely independent of other masking choices.

SDSS MegaZ LRGs

The result for the LRG is the highest in comparison with the ΛCDM theory. It agrees with the result of Cabre et al. [2006]. A direct comparison with Scranton et al. [2003] and Padmanabhan et al. [2005] is more difficult because these analyses use multiple photometric redshift bins. Concentrating on Scranton et al. [2003] (since it also does its analysis in physical space, rather than Fourier space), we find approximately the same detection significance as their single redshift bin measurements for similar data sets. An updated version of this paper (available on the astro-ph archive, but also unpublished) calculates a global χ^2 value using all four of their LRG samples, and detects a CCF with significance somewhat higher than we measure in this work. This is likely due in part to a somewhat larger redshift baseline for their measurement as well as the fact that they calculated their covariance matrix using a method similar to our MC1 case. As one can see from Fig. 5.5, samples which cover very similar areas and have significant redshift overlap (as is the case with their LRG photometric redshift samples) can result in stronger anti-correlation between samples than one observes in covariance matrices generated with the MC2 method. This, in turn, would lead to a moderate over-estimation of the detection significance.

Other measurements

Not surprisingly, since we use the same maps generated from HEAO and NVSS, our results are in agreement with previous measures by Boughn and Crittenden [2004a], Nolta et al. [2004], and the amplitudes are consistent with the theoretical predictions. As discussed above, the new Monte Carlo approach give consistent answers for individual experiments as the temperature-only Monte Carlo approach used in earlier analyses.

We found that the measured CCF for the quasars is consistent with the earlier measurement and the expectation from theory, and it is independent from the cleaning level of the catalogue.

In conclusion, all the measured CCF agree with the previous results and with the ISW theory for a ΛCDM model, although they are in some cases marginally higher than theory predicts.

5.5 Significance of the result

Having established the measures of the CCFs and the total covariance matrix, we discuss the significance of this result and its consequences.

5.5.1 Single catalogue significance

Assuming that the detected cross-correlations are due to the integrated Sachs-Wolfe effect, we can assign a significance value to the measure if the errors on the cross-correlation are taken to be Gaussian. For each catalogue, we can compare the measured CMB-density cross-correlation $\hat{C}(\vartheta_i)$ with the theoretical expectation obtained from the *WMAP* best fit cosmological parameters with our modified version of the `cmbfast` code [Seljak and Zaldarriaga, 1996].

We perform the likelihood analysis first described in Boughn et al. [1998]. The shape of the CCF for each catalogue is assumed to follow the ΛCDM predictions. The theory template is

$$\bar{C}(\vartheta_i) = Ag(\vartheta_i), \tag{5.7}$$

where $g(\vartheta_i)$ is theoretical prediction of the *WMAP* best fit model and A is the fit amplitude, which will depend on the visibility function of the catalogue in question. Maximising the likelihood

$$\begin{aligned} \mathcal{L} &= (2\pi)^{-N/2}[\det \mathcal{C}_{ij}]^{-1/2} \\ &\times \exp\left[-\sum_{ij}(\mathcal{C}_{ij})^{-1}(\hat{C}_i - \bar{C}_i)(\hat{C}_j - \bar{C}_j)/2\right], \end{aligned} \tag{5.8}$$

we can find the best value for each A,

$$A = \frac{\sum_{i,j=1}^{N} \mathcal{C}_{ij}^{-1} g_i \hat{C}_j}{\sum_{i,j=1}^{N} \mathcal{C}_{ij}^{-1} g_i g_j}, \tag{5.9}$$

and the variance

$$\sigma_A^2 = \left[\sum_{i,j=1}^{N} \mathcal{C}_{ij}^{-1} g_i g_j\right]^{-1}. \tag{5.10}$$

We can also simply obtain the signal to noise ratio as $S/N = A/\sigma_A$.

The results obtained in this way with errors calculated with the three methods are summarised in Table 5.1, and the resulting amplitudes and their errors can be seen in Fig. 5.3 and Fig. 5.4. Here we have allowed a separate amplitude A for each catalogue. Note that while the observed CCF is the same for the different methods, differences in the covariance matrices can result in different best fit amplitudes.

It is possible to check that the Monte Carlo estimation has converged after N realisations by estimating the uncertainty on the errors. In detail, we use a jack-knife approach consisting in observing the effect of removing $M = 10$ different subsets of the $N = 5000$ realisations of the MC2 method. The estimator of the uncertainty on S/N is

$$\sigma_{S/N}^2 = \frac{M-1}{M} \sum_{i=1}^{M} \left[(S/N)_i - \overline{S/N}\right]^2, \tag{5.11}$$

where $(S/N)_i$ are the signal to noise ratios obtained with each subset of $N - M$ Monte Carlos, and $\overline{S/N}$ is their average. We find in this way that the uncertainty on the S/N is less than 5%, indicating the level to which our Monte Carlos have converged.

	5000 T-only MCs		5000 full MCs		JK - δ only		JK - δ and T	
data	A	S/N	A	S/N	A	S/N	A	S/N
2MASS	1.22 ± 1.87	0.7σ	1.00 ± 1.96	0.5σ	0.66 ± 0.77	0.9σ	1.36 ± 1.10	1.2σ
SDSS	1.58 ± 0.70	2.2σ	1.48 ± 0.66	2.2σ	1.24 ± 0.42	3.0σ	1.59 ± 0.44	3.6σ
LRG	1.67 ± 0.76	2.2σ	1.73 ± 0.80	2.2σ	0.92 ± 0.50	1.8σ	1.22 ± 0.49	2.5σ
NVSS	1.12 ± 0.40	2.8σ	1.20 ± 0.37	3.3σ	0.68 ± 0.29	2.4σ	0.83 ± 0.27	3.1σ
HEAO	1.10 ± 0.41	2.7σ	1.22 ± 0.45	2.7σ	0.97 ± 0.26	3.7σ	1.00 ± 0.24	4.2σ
QSO	1.40 ± 0.53	2.6σ	1.33 ± 0.54	2.5σ	1.50 ± 0.58	2.6σ	1.33 ± 0.46	2.9σ
TOTAL	$\mathbf{1.02 \pm 0.23}$	**4.4σ**	$\mathbf{1.24 \pm 0.27}$	**4.5σ**	—	—	—	—

Table 5.1: The amplitudes and their significance for different methods of calculating the covariance. The left columns show the two Monte Carlo methods, while the right two show the jack-knife method with equal area (10 deg^2), in one case masking only patches of the density map, and in the other masking both density and temperature maps. We do not calculate the full covariance matrix or the total significance for the jack-knife cases. For 2MASS, we have cut the first four angular bins because of their SZ contamination; the total significance is obtained discarding these bins.

5.5.2 Joint significance

We can easily generalise this to combine the different catalogues and obtain a single significance. Redefining the indexes i, j in a way that they now run from 1 to $N_{\text{tot}} = N_{\text{bin}} \times N_{\text{cat}}$, running over each of the bins of the of the observed (and theoretical) cross-correlation functions for each of the density catalogues. Using the full covariance matrix, we can follow again the same procedure, and find a single best fit amplitude.

The results obtained in this way are shown at the bottom of Table 5.1. The significance of the two different Monte Carlo methods, MC1 and MC2, are 4.4σ and 4.5σ respectively. We also find that the uncertainty on the S/N for the joint amplitude is again less than 5%.

The two MC methods produce similar detection significances, but this could be a lucky coincidence, since the covariance matrices relating different surveys are much different. Both methods suggest some pairs of observations should be strongly correlated, but which pairs are strongly correlated depends on the method. If the covariance between surveys were ignored, the total significance would be about 5.8σ. Perhaps it is not surprising then that adding similar levels of covariance between experiments with comparable individual detection levels would have a similar effect on the total significance.

As in the case of fits to individual correlation functions, strong covariances can have results which are counter-intuitive. For example, the fit for the total amplitude using the MC1 approach is smaller than any single survey would suggest. Also, adding the small angle 2MASS CCF, believed to be suppressed by SZ, actually increases the fits by about 0.2σ despite the points themselves being lower than the theory. These effects suggest that the degree of covariance between the different measurements might be overestimated, which would not be surprising given the much different systematics in each experiment. Even adding a small degree (5%) of diagonal noise is enough to increase the total MC1 amplitude to $A = 1.14 \pm 0.26$, with a corresponding $S/N = 4.4$, so that it is more consistent with the amplitudes of the individual experiments. The MC2 result is not affected by such a change, because the total amplitude is already consistent with the individual survey measurements.

Note that the theoretical model associated with a particular best fit amplitude is not unique. While increasing the dark energy density will generally increase the ISW effect, the effect will generally be redshift dependent and could impact different catalogues differently. However, the ΛCDM model without any tweaking ($A = 1$) improves the likelihood at $\sim 4.5\sigma$ compared to the absence of cross-correlations. Below we compare to specific alternative cosmologies without any scaling amplitude.

5.5.3 χ^2 Tests

Another way to assess the significance of the measure with respect to a theory is simply to look at the χ^2, defined as

$$\chi^2 = \sum_{ij} C_{ij}^{-1}(\hat{C}_i - \bar{C}_i)(\hat{C}_j - \bar{C}_j), \tag{5.12}$$

where the inverse covariance matrix and the data can be referred either to a single catalogue or to the total measure. Whereas the likelihood method discussed above looks at how well a model can reduce χ^2, it is also worth simply looking at the magnitude of χ^2 for the null hypothesis test, where we calculate the χ_0^2 assuming the theoretical cross-correlation is zero.

catalogue	f	χ_0^2	χ^2_{bestfit}	$\chi^2_{\Lambda\text{CDM}}$
2MASS	9	5.4	5.2	5.2
SDSS	13	17	11	12
LRG	13	9.6	4.9	5.7
NVSS	13	17	6.0	6.3
HEAO	13	18	10	10
QSO	13	9.7	3.7	4.0
TOTAL	74	67	47	48

Table 5.2: A comparison of the absolute χ^2 for the various experiments.

In Table 5.2, we the show the χ^2 for the null hypothesis, as well as for the ΛCDM and best-fit models. We use the MC2 errors, dropping the first four bins of 2MASS which appear to be affected by SZ. While there is much variation, in most cases there is not clear evidence against the null hypothesis, in that its χ_0^2 is not significantly greater than the number of data points. However, the χ^2 values are significantly reduced if one assumes one of the models, like ΛCDM , which predict a non-zero cross-correlation.

The reasons for the particularly low χ^2 for the LRG case is unclear, and we investigate this more below. It might be an indication that the error estimates are in some sense too large, or that the covariance between angular bins is different than expected from the simple Monte Carlo simulations, perhaps as a result of foregrounds. However, it should be emphasised that the χ^2 for the null hypothesis is fairly conservative, and unlike the Bayesian likelihood approach, it fails to account for the fact that we have strong theoretical expectations for the signal we are looking for.

5.5.4 Eigenmode decomposition

To better understand the covariance of our data, and especially to understand the χ^2, it is useful to study the eigenmode decomposition of the covariance matrix. As a worst-case example, we will use here the measurement and covariance matrix for the LRG sample calculated with the MC2 method (dimension $n = 13$).

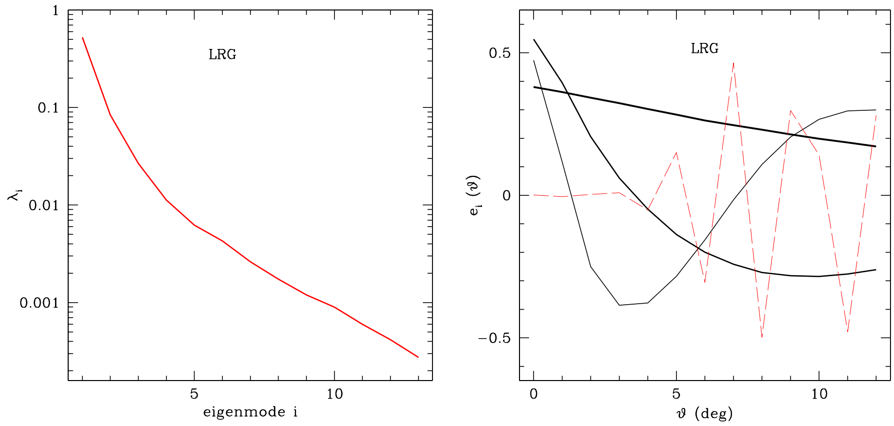

Figure 5.8: Eigenvalues of the MC2 covariance matrices of the cross-correlation between the LRG sample and the CMB (left panel), and first three eigenvectors (right panel). The red dashed line shows the highest frequency mode.

We can factorise the covariance matrix into the form

$$C_{ij} = \sum_{k,l=1}^{n} U^T_{ik} \Lambda_{kl} U_{lj}, \tag{5.13}$$

where $\Lambda_{ij} = \lambda_i \delta_{ij}$ is a diagonal matrix whose elements are the eigenvalues of C_{ij}; the rows of U_{ij} are the 13 eigenvectors $\hat{\mathbf{e}}_i$ of the covariance matrix. We plot the variances, $\lambda_i = \sigma_i^2$, in the left panel of Fig. 5.8, and some of the eigenvectors are shown in the right panel. There, we can see that the modes associated with the biggest variance are the low frequency ones, while the low variance modes oscillate significantly. This reflects the fact that the greatest differences between the Monte Carlo realisations is in the low frequency behaviour of the cross-correlation functions.

Both the measured and theoretical CCFs can be decomposed into this eigenvector basis. In particular, any cross-correlation vector can be written as $\mathbf{v} = \sum_i A_i \hat{\mathbf{e}}_i$, where $A_i \equiv \mathbf{v} \cdot \hat{\mathbf{e}}_i$. We show in Fig. 5.9 the decomposition of the data and theory divided by the square root of the variance, σ_i. For a typical CCF from the Monte Carlos, these amplitudes should be Gaussian distributed with unit variance. We can see how the smooth shape of the theoretical real space CCF is reflected in this eigenmode decomposition: the theoretical amplitude is very well approximated by the first two modes only. However, this is not the case for the measured CCF, for which higher frequency modes are also significant.

We next look at the contributions to the χ^2 from the different eigenmodes. We show in Fig. 5.10 the evolution of the cumulative χ_i^2, i.e. the cumulative contribution to the χ^2 from each eigenmode. Here we compare the raw χ^2 from the observed cross-correlation function to that for the residuals when the theoretical models (ΛCDM and the best fit amplitude) are subtracted off. As expected, the theoretical models only impact the lowest two eigenmodes. The low χ^2, however, is largely the result of the higher frequency modes, which seem to have slightly lower amplitudes than is seen in the Monte Carlos.

If we consider only those two modes which are expected theoretically, the χ^2 for the null hypothesis is actually fairly high: $\chi_2^2 = 4.8$. This would exclude the null hypothesis at more than the 90% level.

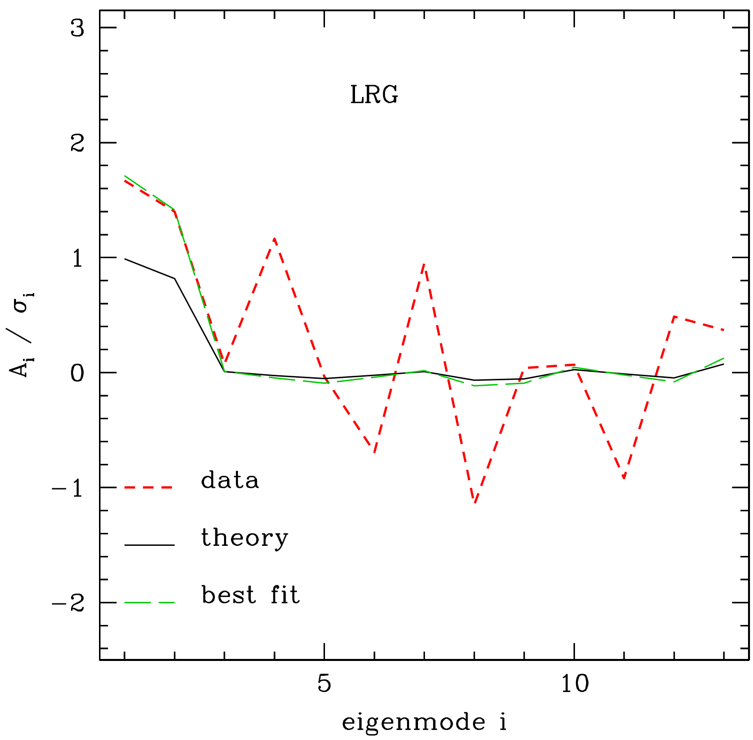

Figure 5.9: Eigenmode decomposition of the amplitude of the measured (red dashed), theoretical (black solid) and best fit (green long dashed) CCF.

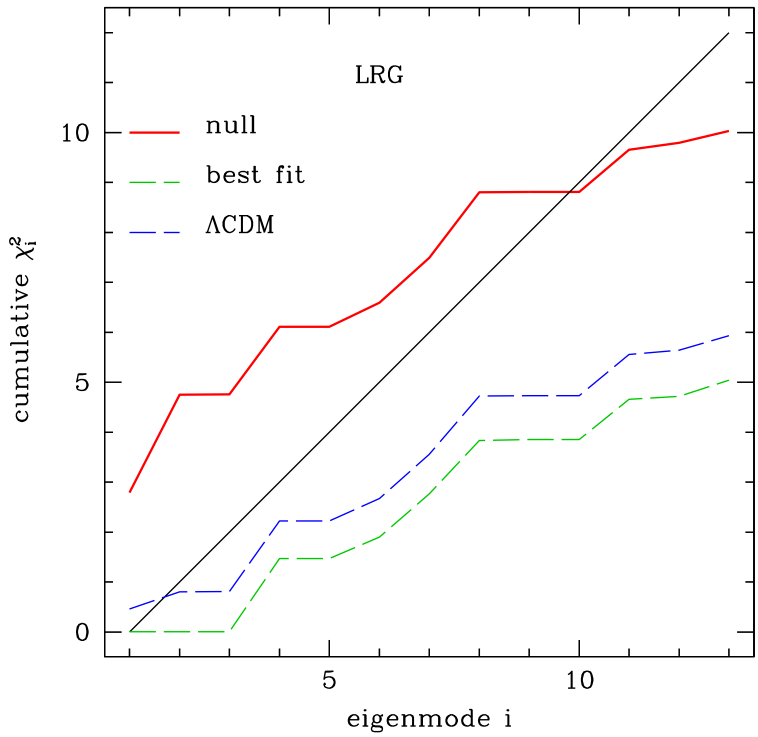

Figure 5.10: Cumulative χ_i^2 obtained summing the contribution up to the i-th eigenmode, for the three models: null hypothesis (red solid), best fit and ΛCDM .

5.6 Cosmological constraints

Assuming the observed cross-correlations are produced by the ISW effect, we can compare them with the theory predictions to obtain cosmological constraints. As described above, the ISW temperature anisotropies are produced as a result of time variation in the gravitational potential, and it is the evolution of the potential which our measurements constrain most directly. The cosmological parameters which impact the linear evolution of the potential are the dark energy density and its evolution, and the curvature of the Universe.

The actual cross-correlation measurements will also depend on the nature of the large-scale structure probe, its spectrum and its bias. For example, if we normalise to the large scale CMB, changing the shape of the power spectrum (e.g., by changing the Hubble constant or the dark matter density) will change the variance of the dark matter distribution on smaller scales, quantified by σ_8. Since the ACFs of the surveys are fixed by observations, changing σ_8 effectively means a different bias will be inferred for each survey.

The cross-correlations will rise and fall with the amount of structure in the probe. Thus, instead one could focus on the dimensionless cross-correlation, effectively

$$r = \frac{C_\ell^{Tg}}{\sqrt{C_\ell^{TT} C_\ell^{gg}}} = \frac{C_\ell^{T\delta}}{\sqrt{C_\ell^{TT} C_\ell^{\delta\delta}}}, \tag{5.14}$$

which removes the dependence on bias (assuming it is linear) and probes more directly the ISW effect itself. The ISW effect arises on fairly large scales, e.g. $k \sim 0.01h\mathrm{Mpc}^{-1}$, depending on the redshift distribution of the survey. Equivalently, for each model, we calculate the bias of each survey based on the observed ACF, and use this to find the predicted CCF for the model.

This makes our measurements largely independent of parameters other than Ω_{DE}, w, c_s and Ω_k. In practise, we choose to keep the dark matter physical density fixed $\omega_m \equiv \Omega_m h^2 = 0.128$ to the *WMAP* best fit value, but the constraints are largely independent of this assumption.

5.6.1 Models without dark energy

While many independent probes seem to indicate the existence of dark energy, it is worth exploring models which might account for the observations without dark energy; recently, an attempt has been made that does this, but which requires a significantly lower Hubble constant, modifications to the primordial power spectrum and other non-standard features [Blanchard et al., 2003]. Such models would be dark matter dominated today, and have no late-time ISW effect. Our observations of the ISW cross-correlations rule out such models at the $\sim 4.5\sigma$ level, based on the difference in the χ^2 between the null hypothesis and the ΛCDM model in Table 5.2. Such models also struggle to fit the recent observations of the angular scale of baryon oscillations [Blanchard et al., 2006].

5.6.2 Flat ΛCDM models

Next, we study the likelihood of a family of flat models with varying Ω_m, $\Omega_\Lambda = 1 - \Omega_m$. As we can see in Fig. 5.11, the ΛCDM model is an excellent fit to our data: the 1σ interval for the parameter is $\Omega_m = 0.26^{+0.09}_{-0.07}$ using the MC1 covariance estimate. A higher ISW signal and slightly lower estimate for Ω_m results from the MC2 errors ($\Omega_m = 0.20^{+0.09}_{-0.07}$); this is due to the higher best fit amplitude in this case. The error bars can be seen to be very asymmetric, as the ISW effect increases dramatically when the matter density becomes small. Models with $\Omega_m < 0.1$ would predict a much greater cross-correlation than is observed.

5.6.3 Flat wCDM models

We next study the likelihood of a family of flat dark energy models, where we allow the dark energy density to evolve with equation of state w. The results are shown in Fig. 5.12,

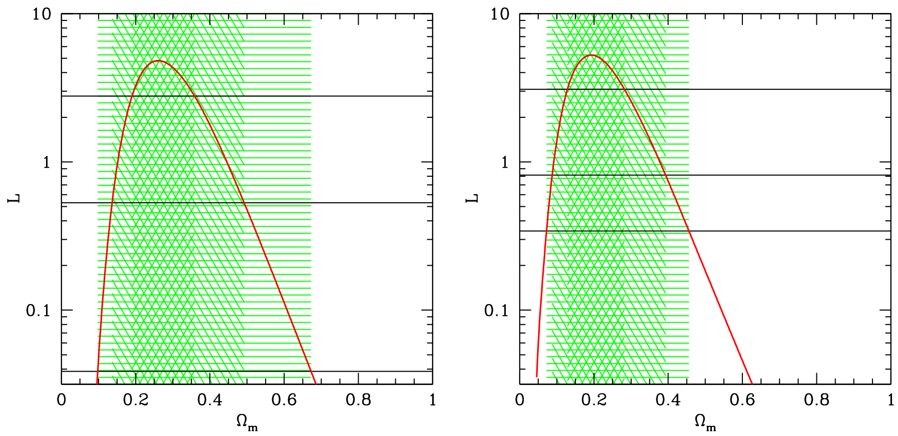

Figure 5.11: Likelihood for flat models with varying Ω_m from the MC1 and MC2 errors. The shaded areas represent 1, 2 and 3 σ intervals for Ω_m. ΛCDM is a good fit to the data.

from which we can see that ΛCDM ($w = -1$) is very consistent with the measures. We can understand this if we observe that the measured excess in the ISW signal is largely redshift independent, while models along the same degeneracy line with a lower (higher) w would predict an excess at low (high) redshifts respectively.

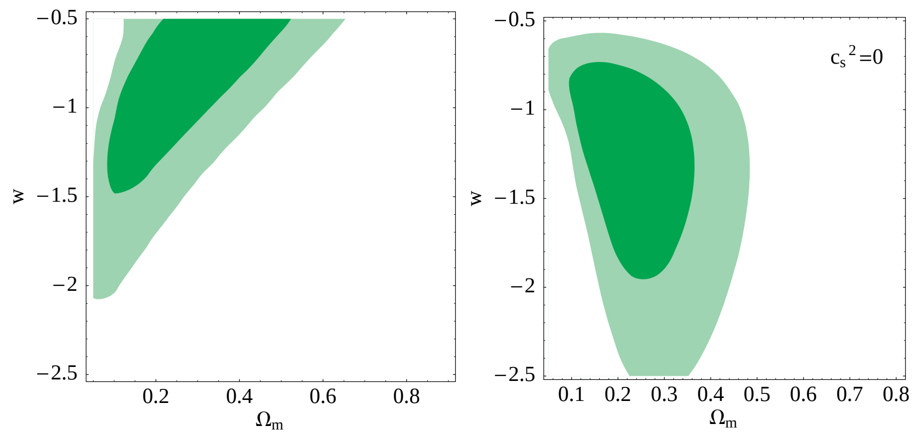

Figure 5.12: Likelihood for flat models with varying Ω_m and w from the MC2 errors. The shaded areas represent 1 and 2 σ intervals. The left panel assumes relativistic sound speed, such as would occur in a quintessence model, while the right panel assumes the opposite extreme of zero sound speed.

Initially we assume the dark energy sound speed is $c_s^2 = 1$, as is typical in scalar field models like quintessence. We also show the same range of models, but with a different dark energy sound speed $c_s^2 = 0$ in Fig. 5.12. We can see that in this case the degeneracy line changes direction due to the clustering of dark energy. ΛCDM is still a good fit to the data, as the cosmological constant likelihoods are not affected by the sound speed, and there is no clustering in that case.

The constraint on the sound speed itself is very weak. There are too many dark energy parameters (density, equation of state, sound speed) to expect any strong constraint. We reduce the numbers by assuming the CMB shift parameter is fixed to the observed value, coupling the equation of state to the dark energy density. The results can be seen in Fig. 5.13. Even with this additional constraint, the sound speed is weakly constrained because the data are consistent with a ΛCDM model, where there is no dependence on the sound speed possible.

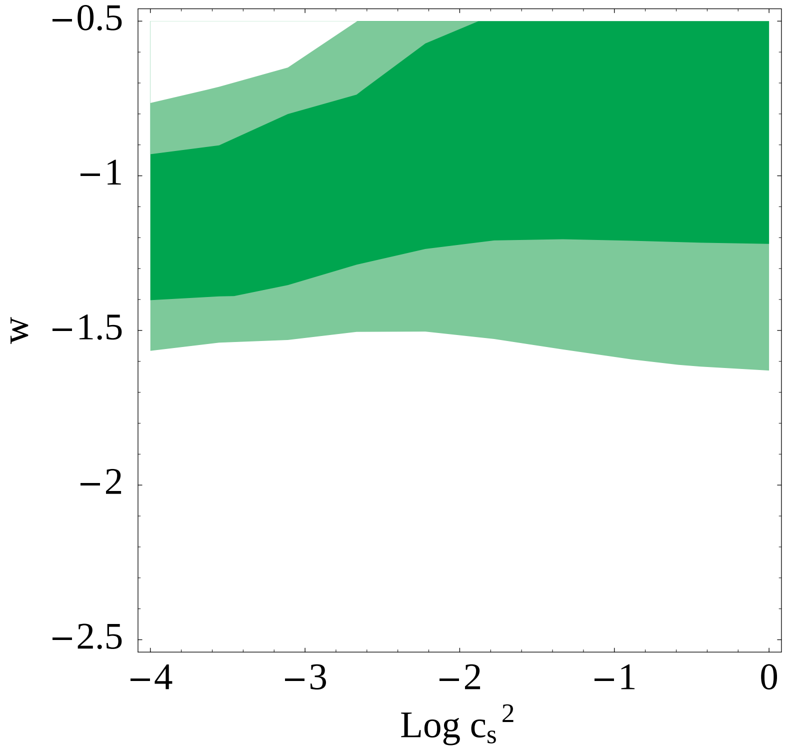

Figure 5.13: Likelihood for flat models with dynamical dark energy as a function of the sound speed, where we fix the matter density based on the equation of state, assuming the CMB shift constraint. 1 and 2 σ intervals are shown. No constraint is possible for the cosmological constant limit ($w = -1$).

5.6.4 Curved ΛCDM models

Since curvature can also cause the gravitational potential to evolve, we explore the constraints if we relax the flatness condition. However, for simplicity we assume the dark energy is a cosmological constant. We study the likelihood of Ω_m, with a corresponding curvature $\Omega_k = 1 - \Omega_\Lambda - \Omega_m$. We explore the full $\Omega_m - \Omega_\Lambda$ space; we see the relative likelihoods in Fig. 5.14, which is obtained with MC2 errors.

From this figure, we see that ΛCDM is still a good fit to the data. An interesting feature of this figure is the degeneracy line between Ω_m and Ω_Λ: this is related to the relative efficiency of the curvature and dark energy as sources of ISW. Closed models (above the flat line) give negative ISW, and can cancel the effect of increasing the cosmological constant, while the opposite happens for open models (below the flat line).

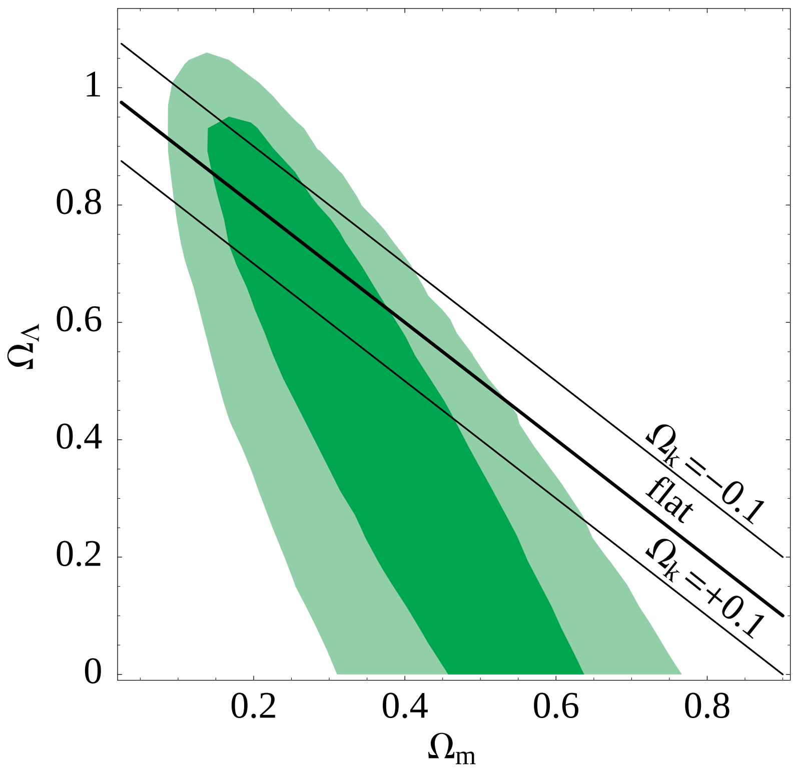

Figure 5.14: Likelihood for curved models with varying Ω_m and Ω_Λ from the MC2 errors. The shaded areas represent 1 and 2 σ intervals. ΛCDM is a good fit to the data.

5.6.5 Comparison with other constraints

Finally, we wish to compare the ISW constraints to those arising from other cosmological observations, including the CMB power spectrum, baryon oscillations and type Ia supernovae. For the latter, we use measurements of the luminosity distance from the Supernova Legacy Survey [Astier et al., 2006].

For the CMB observations, most of the dark energy information (at least that independent of the ISW effect) is distilled in the CMB *shift* parameter, defined as

$$R \equiv \sqrt{\Omega_m} H_0 \cdot (1 + z_\star)\, d_A(z_\star), \tag{5.15}$$

where $d_A(z)$ is the angular diameter distance and $z_\star$ is the redshift of the last scattering surface ($z_\star = 1090$); this expression in the flat case reduces to

$$R = \sqrt{\Omega_m} H_0 \int_0^{z_\star} \frac{dz'}{H(z')}. \tag{5.16}$$

R has been measured to be $R = 1.70 \pm 0.03$ [Wang and Mukherjee, 2006]. We can see from Fig. 5.15 that this constraint has a degeneracy direction parallel to the ISW degeneracy in the flat case, but is less so in the general curved case.

Finally, for the baryon oscillation (BAO) measurements [Percival et al., 2007b] we use the constraint on the volume distance measure defined as

$$d_V(z) \equiv [(1+z)^2 d_A^2(z) z\, c/H(z)]^{1/3}, \tag{5.17}$$

The constraint on this parameter by Percival et al. [2007b] is $d_V(0.35)/d_V(0.2) = 1.812 \pm 0.060$.

The SN data is orthogonal to the ISW constraints, and jointly they are consistent with the ΛCDM model; there is little evidence for additional curvature or evolving dark energy. The CMB shift constraint is similarly consistent with the cosmological constant concordance model, though the constraints are not as orthogonal to the ISW constraints. The ΛCDM model preferred by the SN and ISW measurements is consistent with the CMB shift combined with the measurements of the Hubble constant from the HST Key Project [Freedman et al., 2001].

The exception to this concordance picture comes when the BAO data is considered. The BAO contours are similar to those from the SN, but shifted. In the flat dark energy case, the combination with the ISW prefers a larger dark energy density which has increased with time (phantom). When all observations are combined, the BAO data are swamped by the SN data, and the result is fully consistent with the concordance model as found by Percival et al. [2007b].

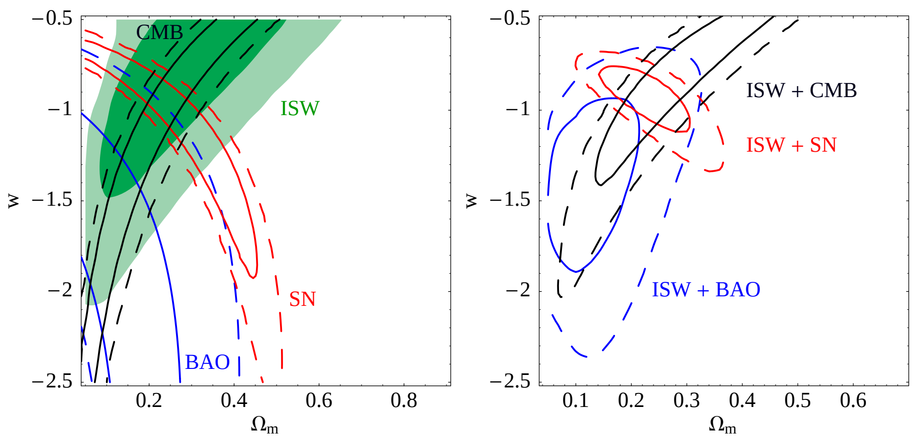

Figure 5.15: Comparison with constraints from other observations, including CMB shift (black), SNe (red) and BAO (blue) (left panel), and combined likelihoods using the ISW + each one of these other constraints (right panel, same colour coding). 1 and 2 σ contours are shown (solid and dashed lines respectively). The MC2 errors are used.

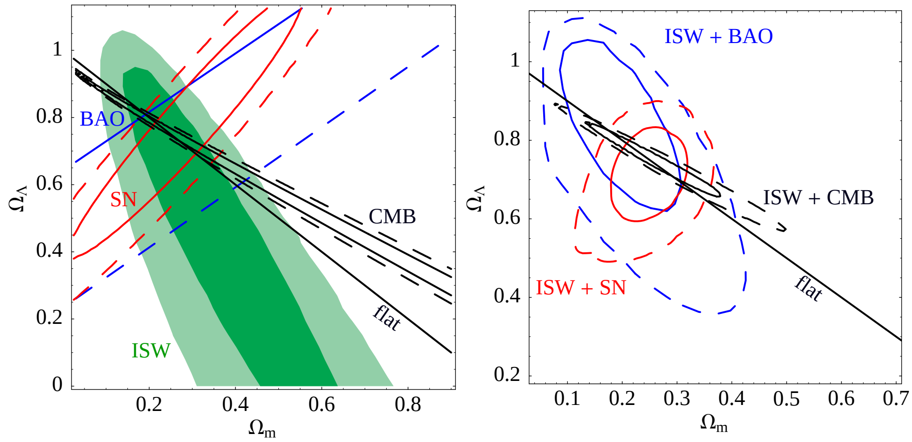

Figure 5.16: Same as Fig. 5.15 for the curved case.

5.7 Conclusions

In this chapter we have presented the measurement of the cross-correlation between the CMB and a large range of probes of the density in a consistent way, and have calculated their covariance taking into account their overlapping sky coverage and redshift distributions. While individual measurements vary somewhat depending on how the data are cleaned and how the covariance is calculated, the overall significance of the detection of cross-correlations is at the $\sim 4.5\sigma$ level.

These observations provide important independent evidence for the existence and nature of the dark energy. The observed cross-correlations are consistent with the expected signal arising from the integrated Sachs-Wolfe effect in the concordance model with a cosmological constant. The observed signal is slightly higher than expected, higher than the expectation from WMAP best fit model by about 1σ, thus favouring models with a lower Ω_m. However, we do not see any significant trend for the excess as a function of redshift, and so there is no indication of an evolving dark energy density. By combining these results with other cosmological data, we find a generally consistent picture of the behaviour of the Universe, which is converging towards the ΛCDM model although the uncertainties remain considerable. The only partial exception to this picture is the BAO result which, even when combined with our ISW measurement, is in slight tension with the ΛCDM model (at $\sim 1\sigma$).

Chapter 6

The effect of reionisation on the CMB-density correlations

The work in this chapter has been published as Giannantonio and Crittenden [2007].

6.1 Introduction

Two of the most important local sources of temperature anisotropies contributing to the cross-correlations are the integrated Sachs-Wolfe (ISW) effect [Sachs and Wolfe, 1967] and the Sunyaev-Zeldovidich (SZ) effect [Sunyaev and Zeldovich, 1970]. Both of these effects provide means of following the growth rate of structure at late times, and through it can tell us about the recent accelerated expansion of the Universe. As we have described in the previous chapters, evidence for both of these effects has been seen in cross-correlation studies between the CMB anisotropies seen by the WMAP satellite [Bennett et al., 2003, Hinshaw et al., 2007] and various surveys of large scale structure. Large angular correlations consistent with the ISW effect have been observed in cross-correlations with radio, infrared, x-ray and optical data. The SZ effect is usually observed in targeted cluster observations, but evidence for it has also been seen in cross-correlations studies, for example between WMAP and the 2MASS infrared survey [Afshordi et al., 2004].

While the ISW and SZ effects appear to be the dominant sources of cross-correlations (once more mundane foregrounds have been excluded, e.g. [Giannantonio et al., 2006]), there are other local sources of correlations which are potentially important to understand in order to accurately interpret the observations. On large scales, it has recently been shown that gravitational magnification can project local inhomogeneities onto higher redshift surveys, causing the matter density at those redshifts to appear more correlated with the ISW anisotropies than would be expected otherwise [LoVerde et al., 2007]. On smaller scales, non-linear effects like the kinetic SZ, Rees-Sciama and the Ostriker-Vishniac effect [Ostriker and Vishniac, 1986] could tell us much about the evolution of structure, and particularly help probe its velocity on these scales [Iliev et al., 2006, McQuinn et al., 2005, Schaefer and Bartelmann, 2006, Stebbins, 2006].

In this chapter we examine another possible source of cross-correlations. Like the kinetic SZ and Ostriker-Vishniac effects, it results from Doppler scattering off of moving electrons, leading to CMB anisotropies with the same frequency dependence as the primordial anisotropies. However, unlike those effects, it is linear and so it can appear on large angular scales; thus, it could potentially affect the interpretation of the ISW effect. The impact of this effect on the CMB temperature power spectrum is well understood, where it is known to be subdominant [Dodelson and Jubas, 1995, Sugiyama et al., 1993, Hu et al., 1994, Cooray and Hu, 2000], as we have described in Chapter 3. Alvarez et al. [2006] showed that reionisation can produce a significant correlation between the 21cm HI radiation and the CMB; here we focus on its impact on CMB-galaxy cross-correlation measurements, where the effect can be comparable to the ISW at high redshifts, and if unaccounted for, would bias the estimation of parameters.

In Section 6.2, we discuss reionisation and outline the late time linear contributions to the CMB auto- and cross-correlation spectra; in Section 6.3 we present the results coming from a version of CMBFAST [Seljak and Zaldarriaga, 1996], an extension of modifications made in Corasaniti et al. [2005]. We discuss the prospects for observing the effect in Section 6.4, before drawing conclusions in Section 6.5.

6.2 The effects of reionisation

6.2.1 Reionisation history

As we have described in Chapter 3, cosmic reionisation is currently thought to be caused by the UV radiation emitted by the first luminous objects, and is experimentally constrained by the optical depth to electron scattering of CMB photons, given by *WMAP* as $\mathfrak{K}_r = 0.092 \pm 0.030$ [Spergel et al., 2007]. It is also constrained by measurements of the Gunn-Peterson troughs in the Lyman-α part of the spectra of distant quasars from the SDSS [Fan et al., 2002, White et al., 2003]. These suggest that the inter-galactic medium (IGM) was fully ionised out to a redshift $z_r' = 6.10 \pm 0.15$ [Gnedin and Fan, 2006]. As noted by Shull and Venkatesan [2007], the scattering up to this redshift accounts for nearly half of the total observed optical depth.

Precisely how reionisation happened prior to this is a topic of some debate; the minimal assumption is that the universe became completely ionised very quickly at a single redshift (around a redshift of $z_r = 11$ to be consistent with the optical depth constraint.) However, the process could have been more complex. In the following, we focus on two other models: a "double step" model with ionisation fraction brought first to 1/2 at $z_1 = 15$ and then to 1 at $z_2 = 6$, and a parametrisation of the double reionisation model by Cen [2003], which again has two distinct phases at $z_1 = 15$ and $z_2 = 6$, but with an evolving ionisation fraction between them. Figure 6.1 shows the visibility function $g(z)$

as a function of redshift in these different reionisation scenarios. Here, the visibility function gives the probability that a photon last scattered at a given redshift, and is related to the optical depth by $g(r) \equiv n_e \sigma_T a e^{-\mathfrak{K}(z)}$.

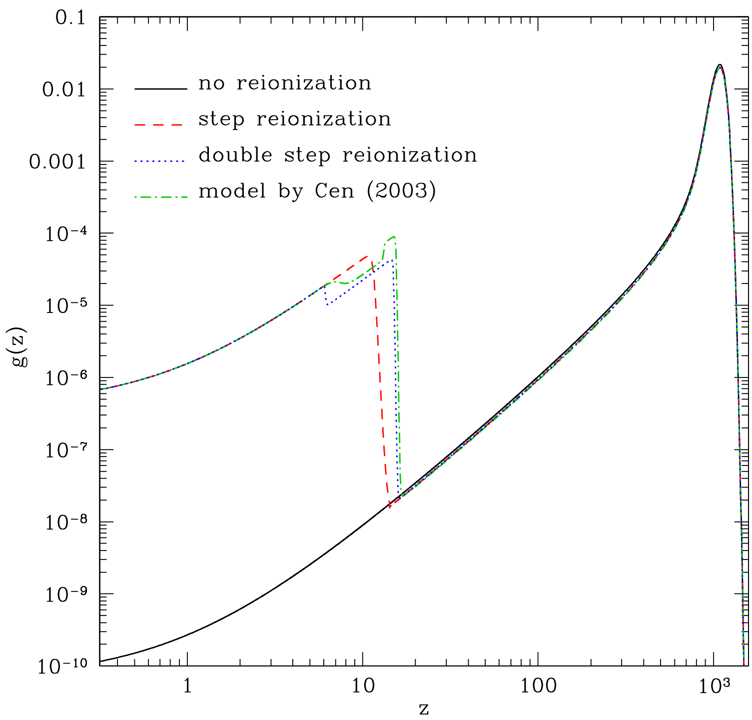

Figure 6.1: Visibility function $g(z)$ for the best fit *WMAP* third year ΛCDM model, with and without reionisation. Double reionisation models are also shown, for a double step case and for the Cen [2003] scenario.

6.2.2 CMB anisotropies from reionisation

When reionisation is introduced, a second peak appears in the visibility function, corresponding to the restored coupling between photons and matter at late times. Because the CMB photons can now again scatter off free electrons, their properties will thus be altered by the temperature, potential, and velocity of the scatterer, exactly in the same way it happened at the last scattering surface at $z = 1100$; these however are suppressed by the small fraction of photons that are rescattered at this time. At linear order, there are three main effects of reionisation [Sugiyama et al., 1993, Hu and Dodelson, 2002]:

- Damping of anisotropies on small scales,
- Secondary anisotropy production after reionisation,
- Additional polarisation on large scales.

In addition, other nonlinear effects such as the Ostriker-Vishniac effect and patchy reionisation will be relevant at smaller angular scales ($\ell > 1000$). The small scale damping is by far the dominant effect, affecting the temperature power spectrum at small scales ($\ell \gg 10$) by a factor $\sim e^{-\mathfrak{K}}$. The polarisation production is also well studied and is responsible for breaking the degeneracy between the optical depth and the spectral index of the primordial perturbations in the WMAP data [Page et al., 2007].

Here we focus on the impact of the anisotropies generated after the photons rescatter, which are largely dominated by the motion of the scattering electrons. Along any given line of sight, one expects electron velocities to be moving towards us at some redshifts and moving away from us at other redshifts, leading to a cancellation of the Doppler effects. However, the scattering probability is not uniform, causing the Doppler effect to be dominated by the redshifts soon after reionisation. For this reason, there is a net anisotropy produced in the CMB temperature, which is correlated with the additional polarisation produced at this time. The greater the gradient of the scattering probability, the less the cancellation and the larger the anisotropies.

Figure 3.2 shows the total anisotropy power spectrum without and with reionisation and the single late time contributions in the reionisation case. The damping on small scales is the biggest contribution, and we can see the small role played by ISW and velocities, while the combined effect of density and gravitational potential perturbations is negligible, as found by Hu et al. [1994] and Dodelson and Jubas [1995]. In a scenario without reionisation, gravitational effects like the ISW would be the only source of anisotropies at late times. The Doppler contribution, while always subdominant, is actually larger than the ISW contribution on sufficiently small scales. At even smaller scales, the thermal SZ effect is important, although it can be distinguished from the other effects taking advantage of its frequency dependence.

More interesting is to consider how the Doppler contribution might be correlated with the density. Consider matter falling into a large over-density at some redshift z_0; the matter on the far side ($z > z_0$) will be travelling towards us, while the matter on the near side ($z < z_0$) will be travelling away from us. Scattering from both sides will contribute to temperature anisotropies, but because the scattering is more likely at higher redshifts, the electrons moving towards us will be more likely to scatter. Thus the over-density will be associated with a temperature hot-spot, and in the same way under-densities will be associated with CMB cold-spots.

In the following, we will show that the effect of this secondary rescattering, though always negligible for the temperature power spectrum, is present and can be important in the temperature-matter correlations at high redshift, and in particular is comparable to the magnification bias effect; therefore this effect must be taken into account to produce precise cross-correlation predictions.

6.2.3 Power spectra

We next describe how to calculate the power spectra for these secondary Doppler temperature anisotropies and their cross-correlations with the density. These will be proportional to the fraction of photons that are scattered and to the velocity of the scattering electrons $\mathbf{v}$ relative to the observers line of sight $\hat{\mathbf{n}}$:

$$\Delta^T(\hat{\mathbf{n}}) = -\int_{\tau_i}^{\tau_0} d\tau\, g(\tau)\, \mathbf{v}(\mathbf{x}, \tau) \cdot \hat{\mathbf{n}}, \tag{6.1}$$

where $\mathbf{x} = (\tau_0 - \tau)\hat{\mathbf{n}}$, τ_0 is the present conformal time and τ_i is taken to be the time just prior to the beginning of reionisation. While the physical effect will be gauge invariant, this expression is implicitly in the Newtonian gauge. By the epoch of reionisation, the electrons will have fallen into the dark matter wells and will be effectively at rest with respect to the dark matter particles; in the synchronous gauge, where the numerics are usually performed, their peculiar velocities will be very small.

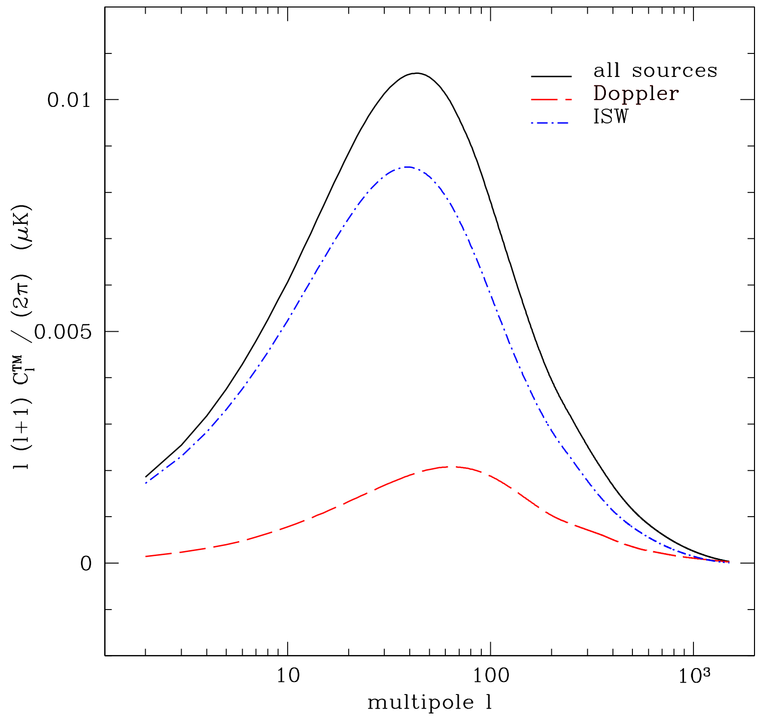

Figure 6.2: Total temperature-density correlation power spectrum for the best fit *WMAP* third year ΛCDM model and a matter visibility function centred in $\bar{z} = 3$, with reionisation. The galaxy bias is set to 1.

We usually work in the harmonic space using a Fourier expansion for quantities like the velocity

$$\mathbf{v}(\mathbf{x}, \tau) = \sum_{\mathbf{k}} \hat{\mathbf{k}}\, v(\mathbf{k}, \tau)\, e^{i\mathbf{k}\cdot\mathbf{x}}, \tag{6.2}$$

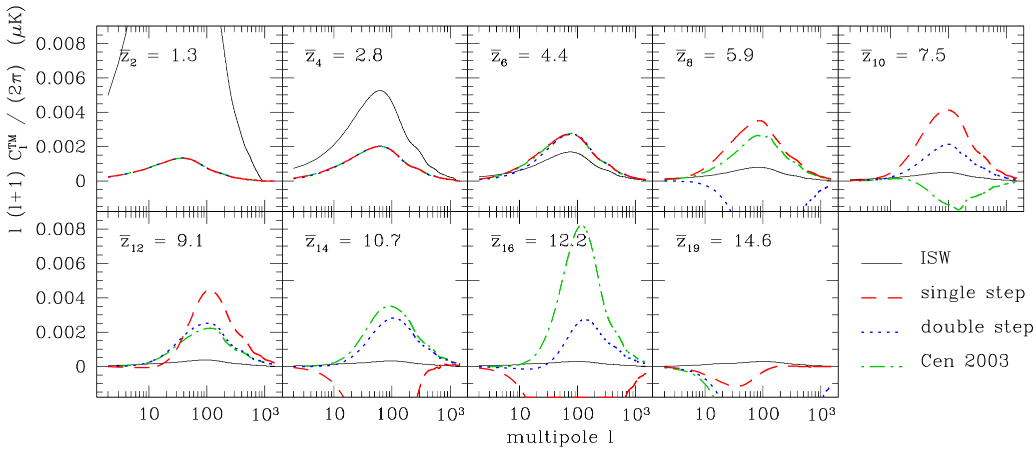

Figure 6.3: Temperature-density correlation power spectrum for the best fit *WMAP* third year ΛCDM model in function of z, with the set of galaxy selection functions defined in Eq. (6.18) (redshift tomography). We see the different evolution of the three different reionisation histories described in Figure 6.1: to every change in the sign of the visibility function derivative corresponds a change in the sign of the cross-correlation. The galaxy bias is always set to 1.

(where we have assumed the velocity is irrotational.) Following Ma and Bertschinger [1995], we can relate the Newtonian gauge velocities to those in the synchronous gauge by,

$$\mathbf{v} = \mathbf{v}_s - i\mathbf{k}\alpha, \tag{6.3}$$

where $\alpha \equiv \frac{\dot{h}+6\dot{\eta}}{2k^2}$, h and η parameterise the metric degrees of freedom in synchronous gauge and dots refer to derivatives with respect to the conformal time. Since we know the synchronous gauge velocities will be small ($v_s \simeq 0$), the Doppler term will be dominated by the term proportional to α. We can relate this to the dark matter density fluctuation using its conservation equation:

$$\dot{\delta} = -\frac{\dot{h}}{2} = -k^2\alpha + 3\dot{\eta} \simeq -k^2\alpha. \tag{6.4}$$

The Einstein equations give $\dot{\eta} \propto v_s$; so, assuming we can neglect the synchronous velocities, we find:

$$\mathbf{v} \simeq \frac{i\mathbf{k}}{k^2}\dot{\delta}. \tag{6.5}$$

Going back to the anisotropies, and defining as usual $\mu \equiv \hat{\mathbf{k}} \cdot \hat{\mathbf{n}}$, we have

$$\Delta^T(\hat{\mathbf{n}}) = -\int_{\tau_i}^{\tau_0} d\tau \sum_{\mathbf{k}} e^{ik\mu(\tau_0-\tau)} i\mu g(\tau) \frac{\dot{\delta}(\mathbf{k},\tau)}{k}, \tag{6.6}$$

which can be integrated by parts; dropping the surface terms where the visibility function is small, we find

$$\Delta^T(\hat{\mathbf{n}}) = -\int_{\tau_i}^{\tau_0} d\tau \sum_{\mathbf{k}} e^{ik\mu(\tau_0-\tau)} \frac{1}{k^2}\frac{d}{d\tau}\left[g(\tau)\dot{\delta}(\mathbf{k},\tau)\right]. \tag{6.7}$$

If we assume linear theory for the growth of density perturbation so that $\delta(\mathbf{k},\tau) = D(\tau)\delta(\mathbf{k},0)$, we can then expand the exponential in terms of spherical harmonics to show

$$\begin{aligned}\Delta^T(\hat{\mathbf{n}}) &= -\int_{\tau_i}^{\tau_0} d\tau \sum_{\mathbf{k}} \delta(\mathbf{k},0)\frac{4\pi}{k^2}\sum_{l,m} i^l j_l(k(\tau_0-\tau))Y_{lm}(\hat{\mathbf{n}})Y^*_{lm}(\hat{\mathbf{k}}) \\ &\quad \times\frac{d}{d\tau}\left[g(\tau)\dot{D}(\tau)\right].\end{aligned} \tag{6.8}$$

From this expression, we find the harmonic coefficients for the Doppler anisotropies to be

$$a^T_{lm} = \sum_{\mathbf{k}} \delta(\mathbf{k},0)\, 4\pi i^l\, Y^*_{lm}(\hat{\mathbf{k}})\, \Delta^l_T(k), \tag{6.9}$$

where

$$\Delta^T_l(k) = -\frac{1}{k^2}\int_{\tau_i}^{\tau_0} d\tau\, j_l(k(\tau_0-\tau))\,\frac{d}{d\tau}\left[g(\tau)\dot{D}(\tau)\right]. \tag{6.10}$$

The expectation of the square of these coefficients gives the Doppler power spectrum

$$C^{TT}_l = \frac{2}{\pi}\int dk k^2 P(k)|\Delta^T_l|^2, \tag{6.11}$$

where $P(k)$ is the matter power spectrum today.

Following similar arguments, we can find similar equations for the anisotropies in the matter density (see e.g. Boughn et al. [1998]). Specifically, we find

$$a^g_{lm} = \sum_{\mathbf{k}} \delta(\mathbf{k},0)\, 4\pi i^l\, Y^*_{lm}(\hat{\mathbf{k}})\, \Delta^l_g(k), \tag{6.12}$$

but instead

$$\Delta^g_l(k) = \int_{\tau_i}^{\tau_0} d\tau b_g(\tau)\, D(\tau)\, W(\tau)\, j_l(k(\tau_0-\tau_i)), \tag{6.13}$$

where $b_g(\tau)$ is the possibly evolving galactic bias and $W(\tau)$ the matter selection function normalised to unity. We can then use these to derive the matter auto-correlation and the matter-temperature power spectra

$$\begin{aligned}C^{gg}_l &= \frac{2}{\pi}\int P(k)k^2|\Delta^g_l(k)|^2 dk \\ C^{Tg}_l &= \frac{2}{\pi}\int P(k)k^2\Delta^T_l(k)\Delta^g_l(k)dk.\end{aligned} \tag{6.14}$$

For the following discussion, we implement these in a numerical Boltzmann code, a modified version of CMBFAST.

At sufficiently small angular scales, it is possible to simplify the calculations using the small angle approximation. Here, we can integrate the complete evolution Eq. (6.11) in an approximate analytical form using the Limber formula:

$$\begin{aligned} C_l^{TT} &\simeq \frac{2}{\pi}\int \frac{dr}{r^2} P\left(\frac{l+1/2}{r}\right)\left\{\frac{d}{dr}\left[-\frac{g(r)\dot{D}(r)}{(l+1/2)^2}\right]\right\}^2 \\ C_l^{Tg} &\simeq \frac{2}{\pi}\int \frac{dr}{r^2} P\left(\frac{l+1/2}{r}\right) b_g W(r) D(r) \frac{d}{dr}\left[-\frac{g(r)\dot{D}(r)}{(l+1/2)^2}\right], \end{aligned} \tag{6.15}$$

where $r \equiv \tau_0 - \tau$ is the conformal distance. However, on large scales this approximation will not be valid, and therefore throughout we compute all our results using the full-sky Boltzmann code.

We can see from Eq. (6.15) how this effect depends on the cosmological parameters: the derivative of the visibility function g will bring a dependency on the reionisation history, as we will see in more detail in section 5.4; on the other hand, the derivative of the growth factor depends on the matter parameters Ω_m, σ_8, and also on the dark energy equation of state. However, in typical models the visibility function will change more dramatically than the growth function, and will dominate the effect.

Here we have focused on the cross-correlation with the matter density; the cross-correlation with the 21 cm line depends on instead on the neutral hydrogen density which can be more complicated [Alvarez et al., 2006]. If reionisation were uniform, peaks in the matter density would be associated with a higher neutral hydrogen density; however, ionisation is expected to be produced by the early structures formed in the highest peaks, causing the peaks in the matter density to have less neutral hydrogen. Depending on the competition between these effects, the CMB-21 cm cross-correlation can have the opposite sign from what is derived above [Alvarez et al., 2006]. However for the discussion below, we will always assume the tracers are positively correlated with the total matter density.

6.2.4 Double scattering

As noted by Cooray and Hu [2000], double scattering processes can produce higher order corrections to the Doppler signal. These corrections have a power spectrum which, for scales smaller than the width of the visibility function, can be approximated by

$$\Delta_l^{T,ds} \simeq \frac{1}{k^2}\int_{\tau_i}^{\tau_0} d\tau j_l[k(\tau_0-\tau)] g(\tau) \dot{\mathfrak{K}}(\tau) \dot{D}(\tau). \tag{6.16}$$

Their effect is small, always $< 5\%$ at the peak, and we will therefore neglect it, this being anyway a conservative choice.

6.3 Results

6.3.1 Low redshift signal

The expected cross-correlations will depend on many factors, but the biggest are the depth of the survey and the assumed history of reionisation. To begin, we look at the amplitude of the effect at low redshifts. Figure 6.2 shows the expected cross-correlation with a broad selection function at mean redshift $\bar{z} = 3$. This assumes a selection function of the form,

$$W_t(z) = \frac{3}{2}\frac{z^2}{z_0^3} e^{-\left(\frac{z}{z_0}\right)^{3/2}} \tag{6.17}$$

where $\bar{z} = 1.41 z_0$, which is a good approximation to the distribution of objects in a flux limited survey, without any imposed cut in redshift. For comparison, we show the ISW cross-correlation for the same survey depth. For this depth, the effects are actually comparable, though this is in part because the ISW effect peaks around $z \simeq 1$ and is already dying off at these redshifts.

6.3.2 Reionisation history dependence

The low redshift signal is largely independent of assumptions of the reionisation history, since we believe the Universe to be totally ionised at that time. However, the signal will increase as we probe higher and higher redshifts and will provide us with a way to probe the visibility function evolution. To study the time evolution of this effect, we use narrower selection functions corresponding to the imposition of redshift cuts on a survey; to be specific, we use a redshift slicing proposed by Hu and Scranton [2004] for an LSST type survey. There they assumed the total selection function could be divided into many narrower bins at different redshifts. The i-th selection function was assumed to be

$$W_i(z) \propto W_t(z) \times \left\{ \mathrm{erfc}\left[\frac{(i-1)\Delta - z}{\sigma(z)\sqrt{2}}\right] - \mathrm{erfc}\left[\frac{i\Delta - z}{\sigma(z)\sqrt{2}}\right] \right\}, \tag{6.18}$$

where $\Delta = 0.8$, $\sigma(z) = 0.02(1+z)$ and every slice is normalised to unity. To study the evolution out to the time of reionisation, we will consider $i = 1, ..., 19$, corresponding to mean redshifts $\bar{z}_i$ from 0.5 to 15.

We can see how the effect evolves with redshift in Figure 6.3. The ISW effect is dominant at low redshifts (where dark energy is dynamically important) and becomes negligible at high redshifts. The Doppler contribution largely depends on the time derivative of the visibility function. At late times, once the Universe is fully reionised, the visibility function decreases smoothly as the universe expands and the density of scatterers decreases; the resulting cross-correlations evolve relatively slowly. However, the picture can change dramatically once we reach redshifts where the ionisation fraction changes, which can drastically alter the visibility function. This is particularly the case if we had a survey sensitive to the beginning of the ionisation history, which for the *WMAP* 3 best fit model is at $z \simeq 11$. There, the sign of the correlation becomes negative and the amplitude can be large if ionisation occurs quickly.

This dependency on the visibility function makes it a sensitive probe of the reionisation history. In Figure 6.3, we compare the signal for different histories: the single step reionisation, a simple double step reionisation, and a more complicated reionisation based on Cen [2003]. At low redshifts, all models are fully ionised and have equivalent cross-correlations. When the histories diverge ($z > 4$), the cross-correlation can be reduced or change signs twice if we are able to see two epochs of the visibility function increasing.

The most prominent feature is actually the negative cross-correlation which occurs at the primary epoch of reionisation. Assuming a single step process, the amplitude of this effect depends on two factors: the total optical depth and how long it takes to ionise the universe. The total optical depth determines the redshift of reionisation as well as height of the peak of the visibility function. However, since the time derivative of the visibility function comes into the integral, the duration of reionisation is also important.

The full impact of these factors is most easily seen in the temperature spectrum, which sums the anisotropies from all redshifts. Increasing the optical depth raises the signal and shifts the spectrum to slightly smaller scales. On the other hand, shortening the duration of reionisation allows the resolution of velocities on smaller scales, and so adds small scale power to the anisotropies.

6.3.3 Comparison with magnification

It is interesting to compare the late Doppler effect with the gravitational magnification effect described by LoVerde et al. [2007]; while no additional temperature fluctuations are created by the magnification, this effect can make the low redshift density distribution appear to be in a higher redshift sample, thereby causing it to be more correlated with the ISW anisotropies than one might expect. The amplitude of these will depend on how the number density of objects depends on the flux cutoff. Since no new anisotropies are created, the effect introduces covariances between the low and high redshift cross-correlations.

LoVerde et al. [2007] showed that ignoring the magnification effect can bias the value of the dark energy equation of state which would be inferred from the cross-correlation measurements. We show in Figure 6.4 that the additional cross-correlations from the Doppler effect are of a similar magnitude to the gravitational magnification effect, so one would expect a similar kind of bias in the equation of state if they were ignored. But unlike the magnification effect, the Doppler correlations represent true new correlations at these redshifts, so the covariance between the higher and lower redshift measurements will be much smaller. We studied the bias that would be obtained by ignoring the Doppler correlation (but including magnification) with a Fisher matrix analysis, as done by LoVerde et al. [2007]. The inferred values for w obtained with marginalising over the other parameters Ω_m, Ω_b, n_s, h and σ_8 with priors errors of 5% are shown in Figure 6.5. The overall inferred w differs from the "true" one that we put into the calculation by almost 2σ.

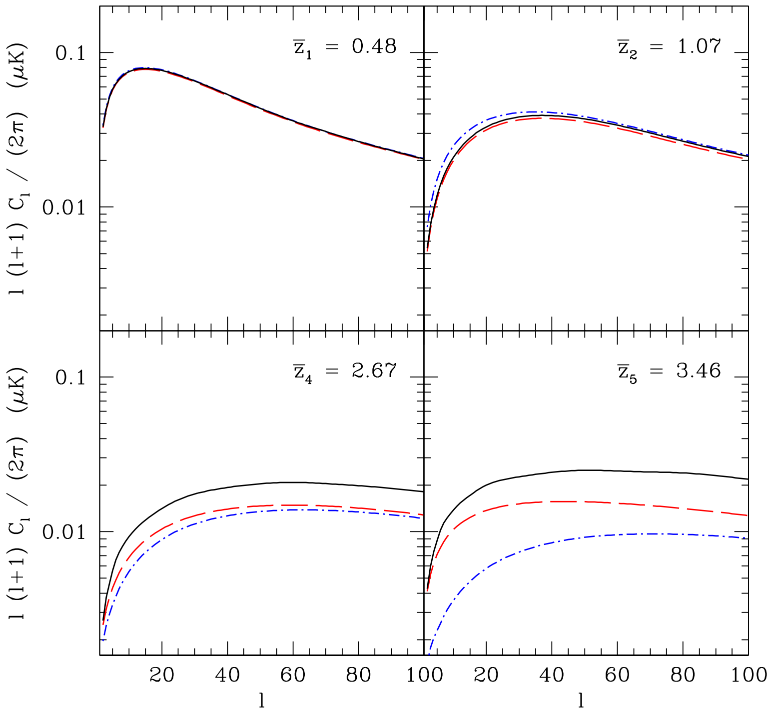

Figure 6.4: Comparison of the magnification and Doppler cross-correlations. We show the ISW effect alone (blue, dot-dashed), the effect of adding corrections from cosmic magnification (red, dashed) and all three effects together (black, solid). Here we have reproduced the calculations of LoVerde et al. [2007] using the same cosmology and assumptions about the galaxy samples (mock catalogue I) and dN/dF.

6.4 Observability

The ISW effect itself is difficult to detect from cross-correlation measurements, principally because of the presence of large primordial CMB anisotropies originating at a redshift of $z \sim 1000$. These fundamentally limit the significance which the the cross-correlations can be observed to a signal to noise level of $7-10$. It is worth exploring if the late Doppler anisotropies are similarly limited.

We first consider the most optimistic picture possible, in which we had a full sky map out to a given redshift and were able to reconstruct a map of the predicted late Doppler

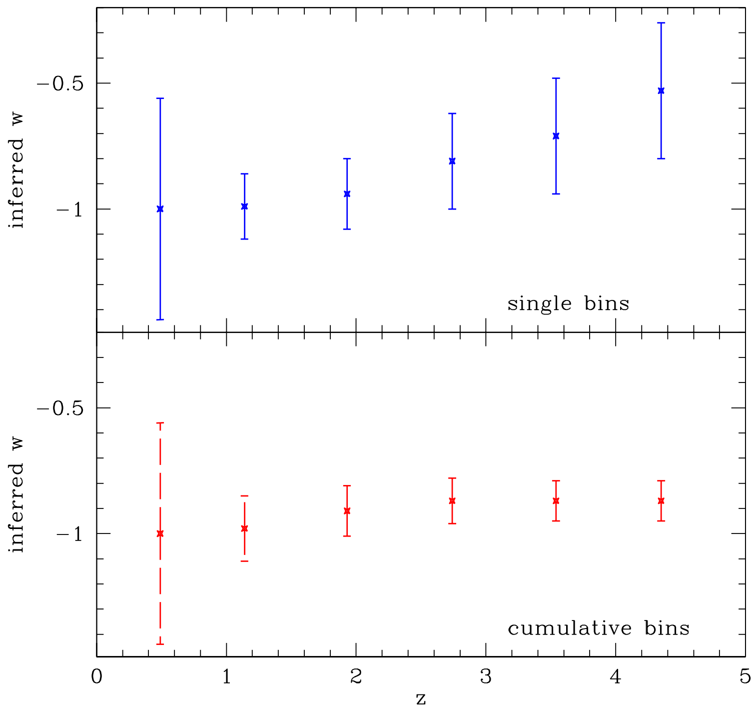

Figure 6.5: The inferred value of the dark energy equation of state parameter w obtained ignoring the effect of reionisation, for the samples of LoVerde et al. [2007]. The input model had $w = -1$. The top panel shows the result for the single redshift bins, while in the bottom panel we present the effect of adding up to the i-th bin.

anisotropies. In this case the expected signal to noise is given by Crittenden and Turok [1996]

$$\left(\frac{S}{N}\right)^2 \simeq \sum_l (2l+1)\frac{C_l^{\mathrm{T-Dop}}}{C_l^{\mathrm{T-tot}}}. \tag{6.19}$$

By looking at the auto-correlations in Figure 3.2, we see that for large ℓ, the Doppler anisotropies exceed the ISW anisotropies. Thus we might hope that since the signal to noise weights the large multipoles more, the total signal to noise might be higher than the ISW case. This is indeed the case, as demonstrated by Figure 6.6. When we include the whole signal, which includes the cross-correlations from the epoch of reionisation, the signal to noise can be much larger than for the ISW. For a typical model ($\mathfrak{K} = 0.092$) we find a total optimal signal to noise of order $S/N \sim 20$. This can rise to as high as 30 with a higher optical depth and shorter duration of reionisation, or drop as low as 10 if we take these parameters to the other extreme. However, the figure also shows that the much of the small angle anisotropies arise at very high redshift, and it would take a very deep survey before the significance could exceed more than a few.

The above calculations are for the most optimistic case. A more realistic estimate can be found using the calculated cross-correlations functions for the galaxy selection

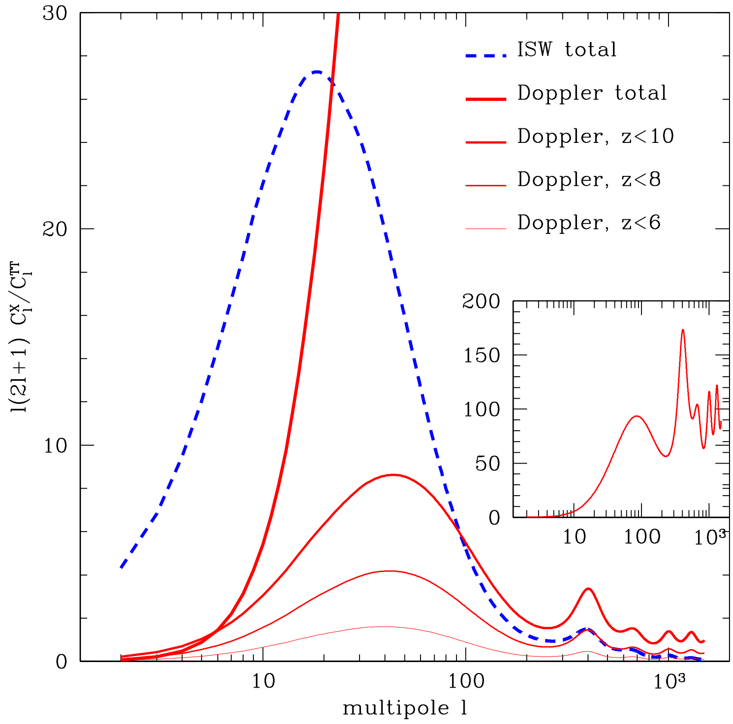

Figure 6.6: The total signal to noise for ISW and rescattering Doppler effect, for the single step reionisation history. The different lines represents different redshift cuts, respectively from top to bottom: no cut and cuts at redshift 10, 8, 6. The insert shows the total signal to noise (without redshift cuts) for the velocity effect. At high ℓ, cross-correlations from non-linear effects will become important.

functions described above. In this case, the signal to noise is given by

$$\left[\frac{S}{N}(z_i)\right]^2 = \sum_l (2l+1)\frac{[C_l^{Tm}(z_i)]^2}{C_l^{mm}(z_i,z_j)C_l^{TT}+[C_l^{Tm}]^2}. \tag{6.20}$$

We show this signal to noise ratio for the Doppler contribution compared to the naive ISW effect in Figure 6.7, for the *WMAP* best fit model of quasi instantaneous reionisation and the series of redshift tomography proceeding from the matter visibility functions defined in Eq. (6.18). We can see how a small but non negligible S/N is produced at high redshift, while a much larger signal is generated at the deeper reionisation epoch.

A small but potentially measurable signal to noise is present at redshifts $z < 7$, where we know that we can find galaxies and other collapsed density tracers; the signal can be enhanced if the ionisation is still evolving at these low redshifts. A much larger signal is expected at higher redshifts, but there the best density probe is probably the 21-cm radiation as suggested by Alvarez et al. [2006].

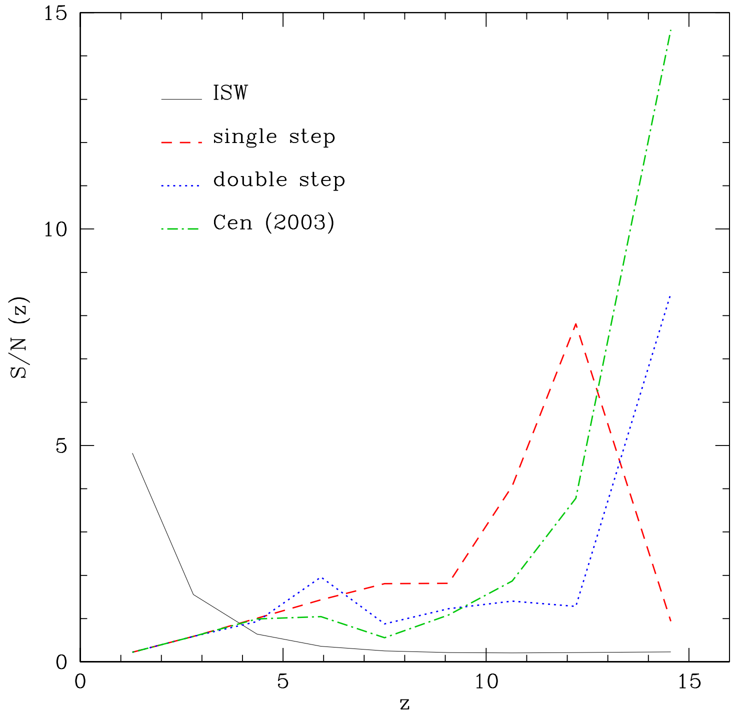

Figure 6.7: Evolution of the signal to noise as a function of redshift for the Doppler effect in different reionisation scenarios compared with the ISW.

6.5 Conclusions

In this chapter we have focused on the linear contributions to cross-correlations arising from the rescattering of CMB photons. These arise from scales of order $k \sim 0.01h\,\mathrm{Mpc}^{-1}$ and are seen on degree scales. However, it should be emphasised that these are by no means the only such sources of cross-correlations; non-linear effects such as patchy reionisation, the Ostriker-Vishniac effect and high redshift SZ sources all could potentially contribute to cross-correlations from the reionisation epoch (see the recent paper by Slosar et al. [2007]). These cross-correlations will typically be at much smaller angular scales. While the linear effect is sensitive to the bulk properties of reionisation, such non-linear cross-correlations could potentially provide useful information on the detailed physics of the reionisation process itself.

At low redshifts, these cross-correlations are small but could still be important in the interpretation of the integrated Sachs-Wolfe signal. For example, we have shown that they are comparable to the effect of gravitational magnification. A high redshift ISW signal has also been shown to be a potential means of discriminating dark energy models from those in which the laws of gravity are modified [Song et al., 2007]; to test such models correctly, including the cross-correlations from rescattering would be essential.

Detecting these cross-correlations in their own right will clearly be a challenge since it requires deep probes of the matter density. One possibility is to use galaxy or quasars found with an optical survey such as the DES (for quasars) [Abbott et al., 2005], LSST [Tyson, 2006], and possibly the panoramic survey of the SNAP, which is still in the proposal stage, which could probe the Universe to a redshift of $z = 3$. Alternatively, radio instruments such as LOFAR [Rottgering et al., 2006] or the SKA [Blake et al., 2004, Torres-Rodriguez and Cress, 2007] could potentially go as deep or deeper by finding 21 cm HI emission from early galaxies; or, if the near-infrared background is dominated by the first generation of structure formation [Santos et al., 2002, Salvaterra and Ferrara, 2003], it might be useful as a proxy for the density at high redshifts. Finally, as discussed by Alvarez et al. [2006], the 21-cm emission from the neutral gas at reionisation could be observed directly by an experiment like SKA, providing a probe of the density precisely where the ionisation is changing most dramatically.

Chapter 7

Constraints on modified gravity theories

The work in this chapter has been published as Giannantonio et al. [2008a].

7.1 Introduction

In the framework of conventional general relativity, the expansion of the Universe at late times is dominated by a *dark energy* with negative pressure and equation of state $w \equiv P/\rho < -1/3$. Several current observations suggest $w < -1$, which is often called *phantom* dark energy, although the fiducial ΛCDM model with $w = -1$ is still preferred if we combine all the data sets [Percival et al., 2007b]. From a theoretical point of view, it is extremely difficult to realise dark energy models with $w < -1$: the easiest way to obtain such a model is to consider a ghost scalar field with the wrong sign for the kinetic term, although this leads to the instability of the vacuum [Caldwell, 2002]. There are a few successful models that lead to $w < -1$ without having theoretical pathologies [Onemli and Woodard, 2002, 2004, Csaki et al., 2006, Libanov et al., 2007]; among them, we focus on a braneworld model proposed by Sahni and Shtanov [2003] and further developed by Lue and Starkman [2004].

We study a model based on the Dvali-Gabadadze-Porrati (DGP) model of the 5D brane-world which we have introduced in Chapter 2 [Dvali et al., 2000]. The 4D gravity on the brane is recovered by the induced 4D Einstein-Hilbert action on the brane. In this model there are two branches of the solutions [Deffayet, 2001]: in the first branch, known as *self-accelerating* (SA, or sDGP), the late time acceleration can be realised without introducing any dark energy, while in the other, known as the *normal* branch (NB, or nDGP), a cosmological constant is needed to explain the late time accelerated expansion of the Universe; nevertheless, the extra-dimensional effects modify gravity on large scales and the model deviates from the standard ΛCDM . In particular, at the background level, the Universe behaves as if there were a phantom-like dark energy $w < -1$.

Besides the fact that this model mimics a phantom behaviour, it is known to be free of ghosts and thus represents a healthy modified gravity theory. This is in contrast with the self-accelerating branch of the DGP model (hereafter sDGP) where there exists a ghost at the linearised level (for a review see Koyama [2007]). Another advantage of the model is that there is a mechanism to recover general relativity on small scales. Thus with this model we can modify gravity on large scales significantly without spoiling the success of general relativity on the solar system scales, providing the basis for the test of the large distance modification of general relativity.

In this chapter, we study the phenomenological consequences of the normal branch DGP model (hereafter nDGP). We first present in Section 7.2 the geometrical tests on nDGP, looking for a parameter space which can be tested from structure formation, which is summarised in Section 7.3. Then we present the ISW-galaxy correlations as a powerful tool to distinguish between ΛCDM and nDGP models in Section 7.4. Section 7.5 is devoted to the conclusion.

7.2 Geometrical tests

The cosmic expansion of the nDGP model depends on the usual 4D FRW metric plus the gravitational effect of the 5D bulk on the brane. The cosmic acceleration is then introduced by the brane tension, which works as a cosmological constant on the brane. The gravity at large scales is modified by the 5D gravity effects on the brane, which are parameterised by a transition scale from 4D gravity to 5D gravity. The crossover distance r_c is defined as the ratio between 4D and 5D Planck mass scales

$$r_c = \frac{M_4^2}{2M_5^3}, \tag{7.1}$$

where M_4 and M_5 are the Planck scales in the 4D and 5D spacetime respectively. The late time expansion history is determined by two free parameters, the cosmological constant (or brane tension) Λ and the crossover distance r_c.

As we have seen in Chapter 1, the Friedmann equation for an nDGP model with curvature $K = -\Omega_k H_0^2$ is given by

$$H^2 - \frac{\Omega_k H_0^2}{a^2} + \frac{1}{r_c}\sqrt{H^2 - \frac{\Omega_k H_0^2}{a^2}} = \frac{8\pi G}{3}\rho_m + \frac{\Lambda}{3}. \tag{7.2}$$

The free parameter r_c can range in theory from 0 to the infinity; however, it has been shown that the deviations from general relativity on solar system scales are also controlled by r_c, and the current constraints require that $r_c > H_0^{-1}$. We can see that if r_c approaches infinity, then Eq. (7.2) converges to GR, while if r_c approaches H_0^{-1}, then the 5D gravitational effect on the expansion history becomes maximal.

The modification of gravity at late time screens the cosmological constant and makes the effective equation of state less than -1. We define the effective energy density of dark energy $\rho_{\rm eff}$ as [Lazkoz et al., 2006]

$$
\begin{aligned}
H^2 - \frac{\Omega_k H_0^2}{a^2} &= \frac{8\pi G}{3}\rho_m + \frac{8\pi G}{3}\rho_{\rm eff} \\
\rho_{\rm eff} &= \frac{1}{8\pi G}\left(\Lambda - \frac{3}{r_c}\sqrt{H^2 - \frac{\Omega_k H_0^2}{a^2}}\right) .
\end{aligned}
\tag{7.3}
$$

It is clearly seen that the 5D effects make the effective dark energy density $\rho_{\rm eff}$ smaller. From the continuity equation of $\rho_{\rm eff}$

$$
\dot{\rho}_{\rm eff} + 3H(1 + w_{\rm eff})\rho_{\rm eff} = 0 \,,
\tag{7.4}
$$

we can derive $w_{\rm eff}$ as

$$
\begin{aligned}
w_{\rm eff} &= -1 - \frac{\sqrt{\Omega_{r_c}}\Omega_m a^{-3}}{\Omega_\Lambda - 2\sqrt{\Omega_{r_c}}(E^2 - \Omega_k/a^2)^{1/2}} \\
&\quad \times \frac{1}{(E^2 - \Omega_k/a^2)^{1/2} + \sqrt{\Omega_{r_c}}} .
\end{aligned}
\tag{7.5}
$$

At the current time, the effective equation of state becomes

$$
w_{\rm eff}(a=1) = -1 - \frac{(\Omega_m + \Omega_\Lambda - 1)\Omega_m}{(1-\Omega_m)(\Omega_m + \Omega_\Lambda + 1)} ,
\tag{7.6}
$$

where we neglected the curvature for simplicity. Provided that $\Omega_m < 1$, we have the phantom behaviour $w_{\rm eff} < -1$.

We revisit the geometrical test on the nDGP [Lazkoz et al., 2006, Lazkoz and Majerotto, 2007]. The geometrical test on the nDGP with a flat curvature prior is not in favour of the cases for the significant screening effect, which rules out observable modified gravity effects in the nDGP. However we find that measurable screening effects are allowed with the inclusion of curvature. We exploit the leverage arm in the geometrical tests at both ends of low and high redshifts. At low redshifts, we use the Gold SN data set [Riess et al., 2004]. At high redshifts, we fix the distance to the last scattering surface at $z_{\rm lss} = 1088^{+1}_{-2}$ by fitting the harmonic space scale of the acoustic peak $l^A = 302^{+0.9}_{-1.4}$ and matter density $\Omega_m h^2 = 0.1268^{+0.0072}_{-0.0095}$ [Spergel et al., 2003]. In addition to that, we constrain the expansion constant H_0 with the Hubble constant measurement, $H_0 = 72^{+8}_{-8}$ [Freedman et al., 2001].

With a fixed CMB prior on $\Omega_m h^2$, best fit values for w and H_0 are correlated with each other. The theoretical models predicting $w < -1$ have a smaller best fit value for H_0 compared with ΛCDM ($w = -1$). Since the measured comoving distance to $z_{\rm lss}$ is consistent with a best fit value for H_0 in flat ΛCDM , the comoving distance to $z_{\rm lss}$ in phantom-like braneworld models becomes longer than the measured distance. This

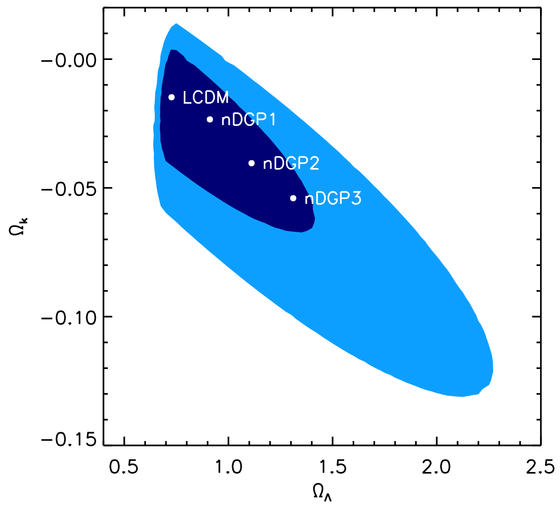

Figure 7.1: Geometrical test on the nDGP by using SN+CMB+H_0 observations. There is correlation observed in the projected Ω_k and Ω_Λ plane after marginalisation of all other cosmological parameters.

worse fit for the large distance measured by CMB in the models with $w < -1$ can be cured by introducing a positive curvature which makes the distance shorter without significantly affecting the fit for the shorter distance measured by SNe. Consequently, a larger Ω_Λ, which realises larger screening effects and $w < -1$, is allowed with a positive curvature ($\Omega_k < 0$) as is shown in Fig. 7.1. Hence if the curvature is added, there appears a degeneracy in the geometrical tests and the models with large modified gravity effects are allowed. This degeneracy can be broken by the structure formation test.

7.3 Structure formation tests

There are three regimes of gravity in the nDGP model on different scales. On super-horizon scales, gravity is significantly influenced by 5D effects. In this regime, we cannot ignore the time evolution of metric perturbations and the dynamical solutions should be obtained by solving the 5D equations of motion. The dynamical solutions have been obtained in the following two methods in the literature: a first derivation is obtained by the scaling ansatz in the sDGP [Sawicki et al., 2007] and in the nDGP [Song, 2007], and the other is found from the full 5D numerical simulations [Cardoso et al., 2007]. It has been shown that both approaches give identical results, and the solutions for the perturbations are shown to be insensitive to the initial conditions for the 5D metric perturbations.

On sub-horizon scales, we can ignore the time dependence of the metric perturbations and the quasi-static approximations can be used [Lue and Starkman, 2003, Koyama and Maartens, 2006]. Even on scales smaller than r_c, gravity is not described by general relativity due to an extra scalar degree of freedom introduced by the modification of gravity. In this regime, gravity can be described by a Brans-Dicke theory and the growth of structure becomes scale independent.

We use the Newtonian gauge

$$ds^2 = -(1+2\Psi)\, dt^2 + a(t)^2(1+2\Phi)\, \delta_{ij} dx^i dx^j, \tag{7.7}$$

to describe the metric perturbations. Fig. 7.2 shows the behaviour of metric perturbations $\Phi_- \equiv (\Phi - \Psi)/2$ which determines the integrated Sachs-Wolfe (ISW) effect both for the dynamical solutions and scaling solutions, for the models of Table 7.1. In the literature, the spatial curvature was not introduced in the calculations, and thus we derive the quasi-static solutions with curvature in Appendix B.

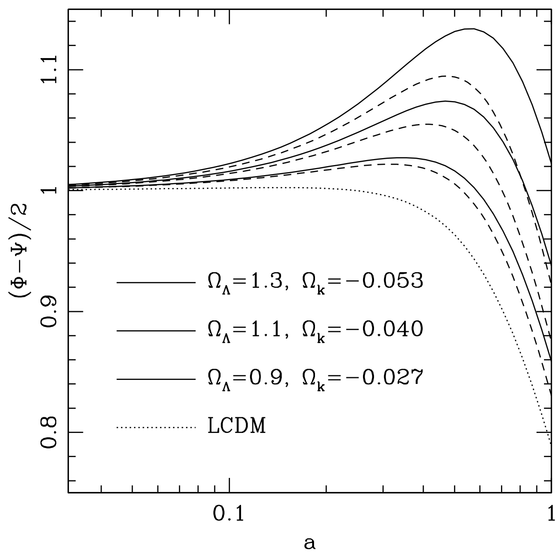

Figure 7.2: We plot the solutions of structure formation of three nDGP models in the $1-\sigma$ contour of Fig. 7.1, compared with the ΛCDM (dotted line). Solid curves represent the quasi-static solutions of nDGP models with different Ω_Λ, and the dashed curve attached to each solid curve represents the dynamic solution of each nDGP model at $k = 10^{-3}$ Mpc^{-1}.

Finally, once the non-linearity of density perturbations becomes important, the theory approaches general relativity [Lue and Starkman, 2003, Koyama and Silva, 2007]. This transition to general relativity is crucial to satisfy the tight constraints from the solar system experiments [Deffayet et al., 2002a, Dvali et al., 2003], and will play a crucial role for weak lensing measures. On the other hand, for the ISW effect, we can safely ignore the non-linear physics.

The dynamical solutions are relevant to the scales of the large scales CMB anisotropies. We have checked that the difference in the large scales CMB anisotropies from ΛCDM are small given the constraints from the geometrical tests because, due to the large cosmic

	ΛCDM	nDGP 1	nDGP 2	nDGP 3
Ω_m	0.30	0.32	0.34	0.37
Ω_b	0.052	0.056	0.060	0.064
Ω_k	-0.014	-0.027	-0.040	-0.053
Ω_Λ	0.72	0.90	1.1	1.3
H_0	66	63	61	59

Table 7.1: Details of the cosmological models used. The other parameters are for all models: scalar spectral index $n_s = 0.95$, optical depth $\tau = 0.10$, and amplitude of the primordial scalar perturbations $A = 2.04 \cdot 10^{-9}$ at a pivot scale $k = 0.05$ Mpc^{-1}.

variance, we do not expect that the CMB anisotropies on these scales can give strong constraints on the models. The quasi-static solutions are relevant to the scales of ISW-galaxy cross-correlations. In the next section, we will study how they can be used to break the degeneracy that arises from the geometrical tests.

7.4 ISW-galaxy correlations

The gravitational potential well Φ_- is shallower in the nDGP model than in the ΛCDM model due to the modification of gravity. This is the opposite from what happens in the self-accelerating models [Song et al., 2007] where the gravitational potential well is deeper than in ΛCDM . The nDGP model predicts an earlier variation of the gravitational potential than the ΛCDM model. By cross-correlating galaxies at different redshifts with the CMB, one can in principle trace the redshift history of the decay of the potential. Furthermore, the cross-correlation arises from the well understood quasi-static (QS) regime of nDGP (solid curves in Fig. 7.2).

The cross-power spectrum of the CMB and a set of galaxies g_i is given by Eq. (3.29) Pogosian [2005], Corasaniti et al. [2005]. First, we investigate the current status of the observations using the data set obtained in Giannantonio et al. [2008b] and described in Chapter 5. We reproduce in Fig. 7.3 the measured CCF for the six galaxy catalogues from Giannantonio et al. [2008b], in order of increasing redshift: 2MASS (excluding the small scale contaminated data), the main galaxy sample from the SDSS, the SDSS Luminous Red Galaxies, NVSS, HEAO and the SDSS quasars, with the relative error bars which should be remembered are highly correlated. Looking at the theoretical curves in Fig. 7.3, we can see that the nDGP models have a very different prediction from the ΛCDM for the CCF at high redshift. This is in agreement with their peculiar potential evolution: the rise in the potential Φ_- at high redshift produces an expected negative CCF, while the following steeper decay leads to a positive CCF which becomes eventually higher than the ΛCDM one.

However, it is clear that these predictions represent a poor fit to the high redshift data. Remembering that all three nDGP models in Fig. 7.3 are inside the 1σ region from the geometry test of Section 7.2, we can qualitatively see that the ISW test will produce

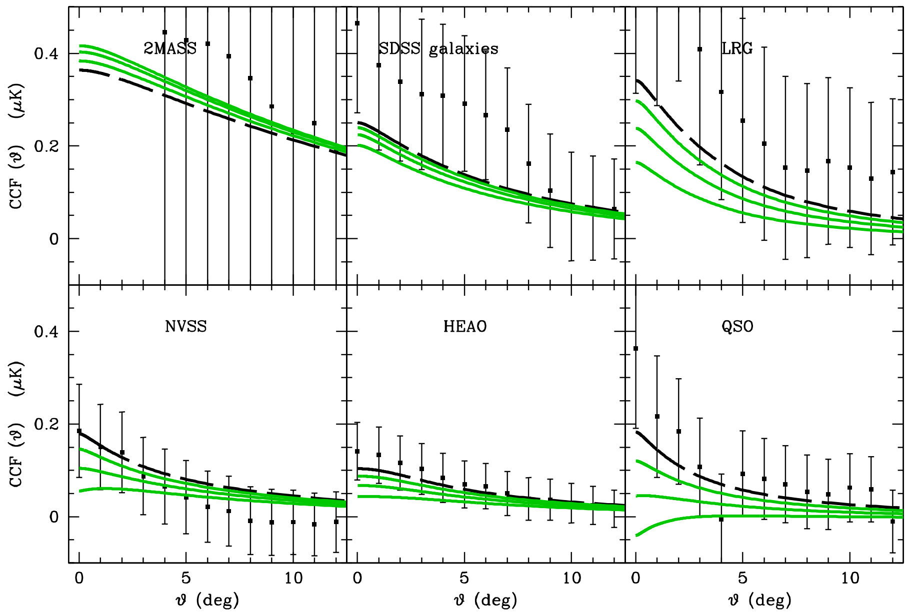

Figure 7.3: Measurement of the cross-correlation functions between six different galaxy data sets and the CMB, reproduced from Giannantonio et al. [2008b]. The curves show the theoretical predictions for the ISW-galaxy correlations at each redshift for the ΛCDM model (black, dashed) and the three nDGP models of Fig. 7.2 (green, solid), which describe the $1-\sigma$ region of the geometry test from Fig. 7.1. The cosmological parameters for the models are reported in Table 7.1; in particular, we fix the amplitude of scalar peturbations A from WMAP.

stricter constraints by noticing e.g. that the quasar CCF alone has a significance level of 2σ, which means that at least two of the nDGP models will be excluded at above this level.

Then, we study the best possible constraints which can be obtained by this technique with future surveys. For definiteness, we assume that the galaxy sets come from a net galaxy distributions of

$$n_g(z) \propto z^2 e^{-(z/1.5)^2}\,, \tag{7.8}$$

where the normalisation is given by the LSST expectation of 35 galaxies per arcmin^2. For the subsets of galaxies, we assume that this total distribution is separated by photometric redshifts which have a Gaussian error distribution with rms $\sigma(z) = 0.03(1+z)$. The redshift distributions are then given by Hu and Scranton [2004]

$$n_i(z) = \frac{A_i}{2} n_g(z) \left[\mathrm{erfc}\left(\frac{z_{i-1} - z}{\sqrt{2}\sigma(z)} \right) - \mathrm{erfc}\left(\frac{z_i - z}{\sqrt{2}\sigma(z)} \right) \right]\,,$$

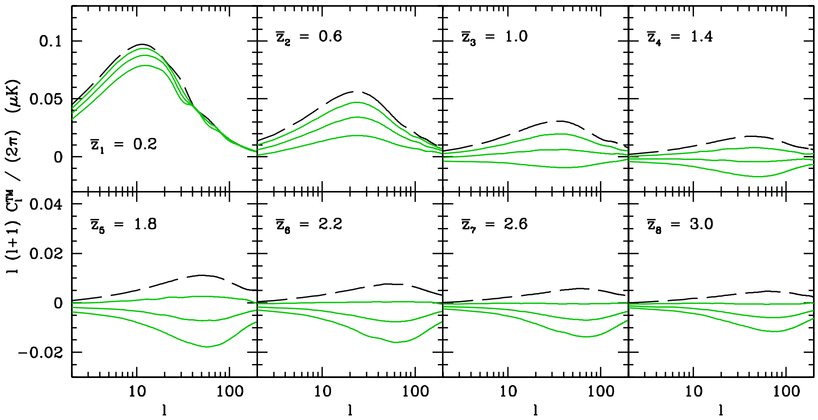

Figure 7.4: The theoretical predictions for the ISW-galaxy cross power spectra at each redshift for the ΛCDM model (black, dashed) and the three nDGP models of Fig. 7.2 (green, solid), which describe the $1-\sigma$ region of the geometry test from Fig. 7.1.

where erfc is the complementary error function and A_i is determined by the normalisation constraint.

We show in Fig. 7.4 the predicted cross power spectra obtained using this redshift tomography for the models of Table 7.1. The theoretical possibility to distinguish between them is given by the signal to noise ratio

$$\left(\frac{S}{N}\right)^2 = \sum_l f_{\rm sky}(2l+1)\frac{[C_l^{Ig}]^2}{C_l^{gg}C_l^{TT}+[C_l^{Ig}]^2}, \tag{7.9}$$

where C_l^{TT} is the temperature power spectrum. This is summarised in Table 7.2.

$\bar{z}$	ΛCDM	nDGP 1	nDGP 2	nDGP 3
0.2	2.8	2.9	2.6	2.2
0.6	4.0	3.5	2.5	1.3
1.0	3.4	2.2	0.68	1.1
1.4	2.5	1.2	0.69	2.6
1.8	1.9	0.52	1.3	3.2
2.2	1.5	0.16	1.6	3.3
2.6	2.4	0.18	1.6	3.1
3.0	0.96	0.22	1.5	2.9

Table 7.2: Theoretical signal to noise ratio for the models of Table 7.1 with $f_{\rm sky}=1$.

Although the geometrical test is not able to easily break the degeneracy between curvature and the screening effect, the alternative consequence for the structure formation by the screening effect is measurable from the ISW-galaxy cross-correlations. The screening of the cosmological constant in nDGP2 and nDGP3 becomes effective before the decay of the growth factor which occurs when the matter component becomes subdominant. This early screening enhances the growth factor which makes the potential Φ_- grow. This generates anti-correlations in the ISW-galaxy cross-correlations at high redshifts, which leaves observable signatures as is shown in Fig. 7.4. From Table 7.2, it is expected that this effect on the structure formation can be observed at around 50% noise level for nDGP2 and 25% noise level for nDGP3. This is an illustration how we can break the degeneracy between curvature and the screening effect in the geometrical tests by using the structure formation tests.

7.5 Conclusion

In this chapter we presented the observational constraints on the normal branch DGP model in which a phantom-like behaviour occurs only with cold dark matter and a cosmological constant. The geometrical tests using the gold SN data set, CMB and the HST key project are not enough to rule out models in which gravity is significantly modified on cosmological scales. We then showed that the structure formation tests performed using the integrated Sachs-Wolfe (ISW) effect can break the degeneracy in the parameter space.

The current measurements of the ISW effect obtained in Giannantonio et al. [2008b] and described in Chapter 5 are indeed as competitive as the geometrical tests. This is due to the fact that, in the nDGP model, the cross-correlation with galaxies becomes negative at high redshift due to the peculiar behaviour of the metric perturbations caused by the modification of gravity. This demonstrates that the structure formation tests are very promising tools to distinguish between general relativity and modified gravity models. We also showed that it is possible to track the evolution of the potentials by cross-correlating the ISW with galaxies at each redshift in future observations. It is very likely that in the future the ISW effect will provide one of the strongest constraints on the model.

Chapter 8

Conclusion

In this thesis we have tried to obtain information about the nature of dark energy and other properties of the Universe from a combination of large scale structure data and the late time anisotropies of the CMB.

After the introduction of Chapter 1, and the short review of the standard model of cosmology of Chapter 2, we have presented in Chapter 3 the CMB and its primary and secondary sources of anisotropies. Amongst the latter, we have seen that the integrated Sachs-Wolfe effect is a peculiar feature which can arise only in special circumstances, for example if dark energy is present; we have thus shown that the measurement of this effect is a method to constrain cosmology in general and dark energy in particular. We have described the cross-correlation technique to measure the ISW, its current state-of-the-art measurement, its limitations, and some of the possible applications.

We have described in Chapter 4 the measurement of the integrated Sachs-Wolfe effect obtained by cross-correlating the CMB with a high redshift catalogue of quasars from the Sloan Digital Sky Survey. The result of this study is the detection of a positive correlation between the two datasets, in agreement with the prediction of the ΛCDM model. A large number of possible contaminating foreground effects have been studied and excluded. The significance of this detection is at about 2σ. This allows us to rule out some particular models, such as theories with a quickly evolving dark energy equation of state, but is not in general high enough to obtain precision constraints on the cosmological parameters.

To raise the significance level and obtain more information about the Universe, we have performed the same measurement with other datasets and combined the results: this has been described in Chapter 5. We have used a set of six catalogues, including most of the data which had been used in the literature to detect the ISW signal, and obtained similar results. The observed cross-correlation between the CMB and the LSS is similar to the expectations from a ΛCDM cosmology, although is generally higher (a 1-σ excess is present). We have estimated the errors in three different ways, following the jack-knife approach and two different Monte Carlo techniques. After the estimation of the full covariance matrix between the catalogues, we have found that the resulting level of significance is about 4.5σ.

This dataset, which is publically available, can be used to constrain cosmology with a higher accuracy than any previous ISW measurement, and corresponds to more than half of the maximum theoretical significance for an ideal measurement of the ISW effect given the standard ΛCDM model. By using only these data, the obtained constraint on the matter density is $\Omega_m = 0.20^{+0.12}_{-0.11}$ at 95 % confidence level. We have also explored the constraints on flat wCDM models and curved ΛCDM models, obtaining new independent likelihood contours which can be intersected with the results of other experiments, such as the CMB spectra, supernovae, and baryon acoustic oscillations. In particular, we found that in the curved case the degeneracy between the dark energy and curvature energy densities makes the likelihood contours elongate in a direction which is different from the other experiments, thus increasing the constraining power of a joint analysis.

However, the ISW effect is not the only possible source of correlation between the CMB and the LSS. Other sources include the Sunayev-Zel'dovich effect, the cosmic magnification by interposed matter, and reionisation. In fact, if the Universe becomes ionised again at low redshift, the CMB photons will scatter off free electrons in the same way as they did before recombination, thus producing new additional secondary anisotropies. These new fluctuations are correlated with the matter density as they are formed at a late time, when the matter structures have already collapsed. This correlation will produce a signal at the redshift of reionisation, which will depend on the particular reionisation history. Chapter 6 has been dedicated to the possibility of measuring the history of cosmic reionisation by cross-correlating the CMB with some density tracer at high redshift. In particular, we found that an observable signal may exist at redshifts $3 < z < 10$ for several common reionisation models. At the lower end of this range, this could possibly be detected in the future by using some deep quasar catalogues, and it will represent a correction to the ISW signal; at higher redshifts, a measurement will be possible thanks to the upcoming 21-cm datasets such as LOFAR, and will be of great interest to constrain the history of reionisation.

An interesting approach to the dark energy problem is to consider the possibility that the observed discrepancy between theory and observations is not due to a new mysterious component of the Universe, but to an infrared correction of general relativity (GR). We can apply the ISW measurement to this context thanks to its potential ability to distinguish between different gravity theories. In particular, if the Universe undergoes a departure from GR, there will be in general an evolution of the gravitational potentials even in a matter dominated phase; this means that a particular ISW effect may be produced at different redshifts. Braneworld models are an interesting class of modified gravity theories which are based on the idea that our observable Universe lies on a 4D brane embedded in a higher dimensional bulk. The DGP model belongs to this class, and is characterised by a 5D Minkowski bulk, where only the gravitational force can leak. This model features two branches of solutions for the equations of motion. In the first branch, the late time acceleration happens spontaneously, and it is therefore called self-accelerating (SA); in the second, we still need an extra parameter such as a brane tension to act as a cosmological constant, and we call this the normal branch (NB). Currently, observations are in tension with the predictions of both of these branches in the flat case, but most of these constraints have been performed using the background expansion history only. In the curved case, much of the parameter space remains unconstrained.

The ISW effect, by probing the late time evolution of the potentials, is a very sensitive tool to extend these tests beyond the background level. In Chapter 7 we showed how our ISW dataset can discriminate between GR and the normal branch DGP model, including curvature. In this analysis we found that the gravitational potentials have a peculiar feature in this model, as they first increase and then decay at late times, as opposed to the simple decay of ΛCDM . For this reason, the expected ISW signal would be negative at high redshifts. Since we always observe a positive correlation, we can rule out much of the parameter space for the NB DGP with this test, including much of the region which was still allowed by background tests.

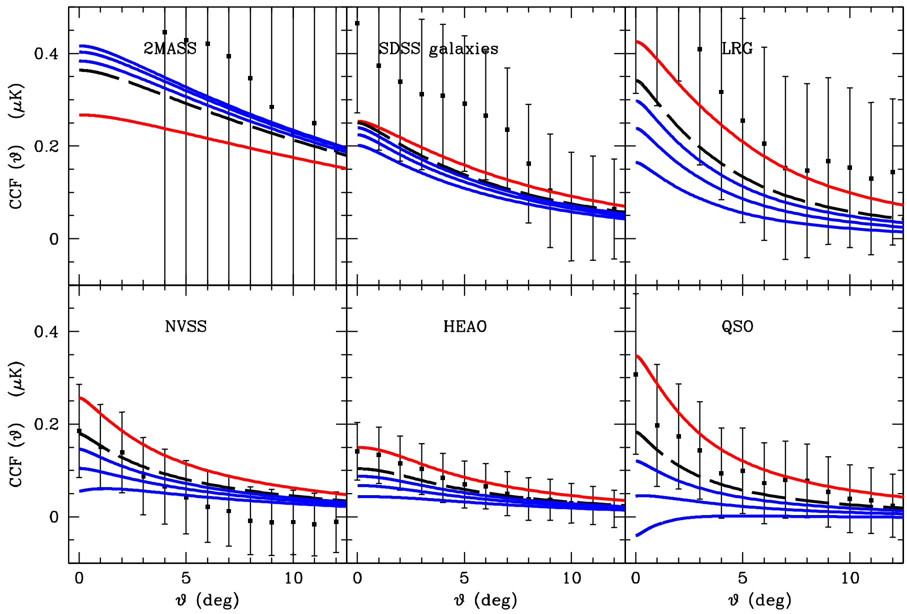

Figure 8.1: Cross-correlation functions for three NB DGP models (in blue), for the ΛCDM (in black) and for the corresponding SA model (red), superimposed to our ISW dataset for the six catalogues.

Many applications of the main ISW dataset we have obtained remain to be explored. A first extension of the DGP work we have discussed is to account for both branches of this theory and to perform a full likelihood analysis with a Monte Carlo Markov Chain (MCMC) method. The different time evolution of the potentials means that, while the NB predicts a negative ISW at high redshift, the SA branch features an always positive signal, generally higher than the GR, as we can see from Fig. 8.1. Since the data are generally higher than the GR predictions, we expect that the SA DGP model will be somewhat favoured, and it will be interesting to quantify this with a full MCMC analysis.

Another context in which it is possible to apply the ISW data is the study of the initial conditions of the perturbations. Primordial perturbations can be a mixture of two modes: adiabatic and isocurvature. The physical meaning of these modes is a perturbation of the spatial curvature of the Universe in the first case, and a perturbation of the density of the different particles in the second case, with an unperturbed curvature. These two different conditions for the primordial perturbations propagate into very different behaviours for the CMB anisotropies. In most cases of the literature, adiabatic initial conditions are assumed as they agree well with the observations, while pure isocurvature initial conditions are excluded [Bean et al., 2006]. However, the picture changes if we consider the two modes to become mixed, allowing for a small fraction of isocurvature perturbations to contribute to the total. In this case a small amount of isocurvature is still allowed by the data, and a non-zero contribution of these modes appears actually to be favoured by WMAP 3rd year data [Keskitalo et al., 2007], although present observations are still consistent with pure adiabatic conditions [Kawasaki and Sekiguchi, 2007]. In the CMB anisotropy power spectrum, isocurvature initial conditions present the characteristic sign of an enhanced power at large scales, corresponding to an increased ISW effect. For this reason we are performing a full MCMC analysis of these models, including all standard cosmological parameters plus the four additional parameters of a mixed isocurvature-adiabatic model, to see whether the ISW data may improve the current upper bounds on isocurvature, or on the contrary, favour it.

A further application of the ISW data occurs in the field of non-Gaussianity. We know that different models of inflation predict different degrees of departure from a pure Gaussian distribution of primordial perturbations: therefore, a measure of non-Gaussianity would help to distinguish between the many inflationary scenarios now available. The amount of local non-Gaussianity (NG) is usually quantified by a single parameter $f_{\rm NL}$, which is zero in a purely Gaussian model, while current constraints from the CMB are $-9 < f_{\rm NL} < 111$ at 2σ from WMAP 5-year results [Komatsu et al., 2008]. It has been recently shown by Dalal et al. [2008] with both analytic estimates and numerical simulations that a non-zero value for $f_{\rm NL}$ would have an effect on the process of structure formation and in particular on the clustering of dark matter halos. The observable consequence of this is a new relationship between the dark and visible matter distributions, which leads to a strongly scale-dependent bias; in particular, the bias of a distribution of sources is found to be deviating from the purely Gaussian case by an amount $\Delta b \propto f_{\rm NL} k^{-2}$. This strong scale dependence leads to no modifications at medium and small scales, but to an explosion of the predicted signal at large scales for both the galaxy power spectrum and the galaxy-temperature cross-correlation. The fact that we actually do not observe such a divergence means that we can obtain quite strong constraints on the amount of non-Gaussianity: it was anticipated by Dalal et al. [2008] that we should be able to constrain $f_{\rm NL}$ with this technique to a degree of accuracy similar to that of the CMB. In the last few months, this measurement has been performed by two separate groups [Slosar et al., 2008, Afshordi and Tolley, 2008] using the ISW analysis by Ho et al. [2008], obtaining contrasting results. In more detail, the first group does not find any constraints by using the cross-correlation alone (although a strong constraint is obtained from the matter power spectra), while the second group claims a result $f_{\rm NL} = 236 \pm 127$ at 2σ. The reason of this difference lies in the different methods for the analysis: the first group marginalises over the Gaussian biases for each dataset assuming a redshift dependence of them, while the second group keeps these parameters constant. While this latter approach appears clearly simplistic and prone to an underestimation of the errors, we have found that the first method strongly depends on the particular form chosen for the redshift dependence $b(z)$. For this reason, we have decided to perform a new analysis, trying to take into account the dependence on $b(z)$ and choosing a better motivated form for this function, to obtain constraints for non-Gaussianity from our ISW dataset.

We are also interested in extending the range of datasets to combine with the ISW measurements, to see how much we can improve the constraints on cosmology. As an example, we have combined the ISW likelihood contours with the results from the Hubble diagram of the supernovae from the SDSS [Frieman et al., 2008a]. We obtain in this case for the dark energy equation of state a value of $w = -0.85^{+0.20}_{-0.35}(\text{stat}) \pm 0.15(\text{sys})$ [Lampeitl et al., 2008].

To conclude this list of possible applications of the ISW dataset, it is worth mentioning that many more parametrisations can be explored. If we assume that dark energy is based on a field theory model, we can think of constraining a parametrisation different from w, such as the one chosen by Crittenden et al. [2007], which is based on the analogy between slow roll inflation and dark energy. On the other hand, if we prefer to think that the acceleration phenomenology is based on a modification of the laws of gravity, we may use the ISW dataset to constrain some parameter which describes the departure from general relativity. Amongst the many possible choices, we would like to highlight the proposed parameter ϖ by Daniel et al. [2008], which quantifies the discrepancy between the two gravitational potentials Φ and Ψ, a feature of many modified gravity theories. It has been shown that the ISW data can constrain this parameter.

To conclude, the work presented in this thesis can be described as an attempt to better understand some of the fundamental properties of the Universe from the synthesis of observations of the large scale structure and the secondary anisotropies created in the CMB at low redshift. We have obtained an independent set of measurements which confirm the presence of dark energy at the 4.5σ level and out to a redshift of ~ 1.5, and can both constrain the value of the cosmological parameters as well as help to distinguish between different theoretical models.

Appendix A

Correlated Monte Carlo maps

A.1 Basics

Here we describe how to make Gaussian maps with a prescribed set of auto- and cross-correlation functions for use in the estimation of covariance matrices. Let us assume we have n maps, which could include temperature and various density maps at different redshifts or frequencies. Let us call these maps $\mathbf{m}_i$ where i ranges from 1 to n.

Any two maps, $\mathbf{m}_i$ and $\mathbf{m}_j$, will be correlated and these correlations will be described by a correlation function $C^{ij}(\vartheta)$ and associated multipole moments C_ℓ^{ij}. These correlations will be symmetric under interchange of the maps, $C^{ij}(\vartheta) = C^{ji}(\vartheta)$, so we have $n(n+1)/2$ correlation functions or spectra which describe the two maps.

Most map making algorithms, like `synfast` [Gorski et al., 2005], work in Fourier or spherical harmonic space. Effectively every mode is given a random amplitude ξ, which is a complex number with unit variance and zero mean: $\langle \xi \xi^* \rangle = 1$ and $\langle \xi \rangle = 0$. These are then multiplied by the square root of the power spectrum in order to ensure the proper correlation functions. (There are additional constraints to preserve the reality of the fields on the lattice, e.g. $\xi_{\mathbf{k}} = \xi^*_{-\mathbf{k}}$, but it is not necessary to go through these here).

It is sufficient to consider a single mode or harmonic amplitude of each map, as all the others will be similar but independent. Assuming we are working with spherical harmonics, we want to ensure that

$$\langle a^i_{\ell m} a^{j*}_{\ell' m'} \rangle = C_\ell^{ij} \delta_{\ell \ell'} \delta_{m m'}. \tag{A.1}$$

The δ functions follow simply from using uncorrelated random amplitudes for each harmonic mode. For a single map, the right power spectrum is ensured by simply using

$$a^i_{\ell m} = \sqrt{C_\ell^{ii}}\,\xi \tag{A.2}$$

and this is effectively the prescription used by `synfast`.

When considering more maps, it is necessary to use more random phases, building the final maps from a combination of different maps. With n maps, n different phases are required for each mode. Here, we denote the different phases with Latin letters, $a, b, c, ...$ Different phases will be assumed uncorrelated, so that $\langle \xi_a \xi^*_{a'} \rangle = \delta_{aa'}$.

The simplest example is to consider two correlated maps, $\mathbf{m}_1$ and $\mathbf{m}_2$. These are described by three spectra: C_ℓ^{11}, C_ℓ^{12} and C_ℓ^{22}. These are made using the amplitudes

$$\begin{aligned} a^1_{\ell m} &= \xi_a \sqrt{C_\ell^{11}} \\ a^2_{\ell m} &= \xi_a C_\ell^{12} / \sqrt{C_\ell^{11}} + \xi_b \sqrt{C_\ell^{22} - (C_\ell^{12})^2 / C_\ell^{11}}. \end{aligned} \tag{A.3}$$

It is simple to verify that with these amplitudes, $\langle a^1_{\ell m} a^{1*}_{\ell m} \rangle = C_\ell^{11}$, $\langle a^1_{\ell m} a^{2*}_{\ell m} \rangle = C_\ell^{12}$ and $\langle a^2_{\ell m} a^{2*}_{\ell m} \rangle = C_\ell^{22}$.

This is simple to implement with `synfast`. First create a map with power spectrum C_ℓ^{11}, and then make a second map using the *same seeds* and power spectrum $(C_\ell^{12})^2/C_\ell^{11}$. Add this second map to a third map made with a new seed and with power $C_\ell^{22} - (C_\ell^{12})^2/C_\ell^{11}$. Note that this should never require taking the square root of a negative number; however, if its very strongly correlated, numerical errors could cause problems. However, for the weak correlations considered here, this is never an issue.

The only difficulty is that this inherently produces positive correlations, as the default of the `synfast` code. This can be worked around simply. For example, if C_ℓ^{12} is always negative, one can simply flip the signs of the second map after it is produced. If instead C_ℓ^{12} changes sign, then break up the power spectrum into positive and negative pieces, making a map for each and subtracting the 'negative' map from the 'positive' map.

A.2 The general case

Next we consider an arbitrary number of maps. For simplicity, we drop the ℓ and m subscripts where the meaning is unambiguous. Effectively, the challenge is to solve for a particular set of amplitudes $\mathbf{T}$, where

$$\begin{aligned} a^1 &= \xi_a T_{1a} \\ a^2 &= \xi_a T_{2a} + \xi_b T_{2b} \\ a^3 &= \xi_a T_{3a} + \xi_b T_{3b} + \xi_c T_{3c} \\ a^4 &= \xi_a T_{4a} + \xi_b T_{4b} + \xi_c T_{4c} + \xi_d T_{4d} \end{aligned} \tag{A.4}$$

etc., subject to the constraints that $\langle a^i a^{j*} \rangle = C^{ij}$.

One thus has $n(n+1)/2$ equations with the same number of unknowns T. These begin as:

$$
\begin{aligned}
C^{11} &= T_{1a}^2 \\
C^{12} &= T_{1a}T_{2a} \\
C^{22} &= T_{2a}^2 + T_{2b}^2 \\
C^{13} &= T_{1a}T_{3a} \\
C^{23} &= T_{2a}T_{3a} + T_{2b}T_{3b} \\
C^{33} &= T_{3a}^2 + T_{3b}^2 + T_{3c}^2 \\
C^{14} &= T_{1a}T_{4a} \\
C^{24} &= T_{2a}T_{4a} + T_{2b}T_{4b} \\
C^{34} &= T_{3a}T_{4a} + T_{3b}T_{4b} + T_{3c}T_{4c} \\
C^{44} &= T_{4a}^2 + T_{4b}^2 + T_{4c}^2 + T_{4d}^2
\end{aligned}
\tag{A.5}
$$

etc. While quadratic, these can be solved in stages linearly. Solve the first for $T_{1a} = \sqrt{C^{11}}$. Use the second to show, $T_{2a} = C^{12}/\sqrt{C^{11}}$ and the third to get $T_{2b} = \sqrt{C^{22} - (C^{12})^2/C^{11}}$. This reproduces what was shown above.

After this, things continue similarly. At each point, we use the next equation to solve for the next missing variable:

$$
\begin{aligned}
T_{1a} &= \sqrt{C^{11}} \\
T_{2a} &= C^{12}/\sqrt{C^{11}} \\
T_{2b} &= \sqrt{C^{22} - (C^{12})^2/C^{11}} \\
T_{3a} &= C^{13}/\sqrt{C^{11}} \\
T_{3b} &= (C^{23} - C^{12}C^{13}/C^{11})/\sqrt{C^{22} - (C^{12})^2/C^{11}} \\
T_{3c} &= \left[C^{33} - (C^{13})^2/C^{11} - \frac{(C^{23} - C^{12}C^{13}/C^{11})^2}{C^{22} - (C^{12})^2/C^{11}}\right]^{1/2} \\
T_{4a} &= C^{14}/\sqrt{C^{11}} \\
T_{4b} &= (C^{24} - C^{12}C^{14}/C^{11})/\sqrt{C^{22} - (C^{12})^2/C^{11}}
\end{aligned}
\tag{A.6}
$$

etc. Things will take similar forms as one goes on, but getting progressively more complicated.

It can also be programmed recursively, which may be simpler to implement. By this, we mean,

$$
\begin{aligned}
T_{1a} &= \sqrt{C^{11}} \\
T_{2a} &= C^{12}/T_{1a} \\
T_{2b} &= \sqrt{C^{22} - T_{2a}^2} \\
T_{3a} &= C^{13}/T_{1a} \\
T_{3b} &= (C^{23} - T_{2a}T_{3a})/T_{2b} \\
T_{3c} &= \sqrt{C^{33} - T_{3a}^2 - T_{3b}^2} \\
T_{4a} &= C^{14}/T_{1a} \\
T_{4b} &= (C^{24} - T_{2a}T_{4a})/T_{2b} \\
T_{4c} &= (C^{34} - T_{3a}T_{4a} - T_{3b}T_{4b})/T_{3c} \\
T_{4d} &= \sqrt{C^{44} - T_{4a}^2 - T_{4b}^2 - T_{4c}^2}
\end{aligned}
\tag{A.7}
$$

etc., with each step using only variables already solved. The general recursive expression for these spectra is

$$
\begin{aligned}
T_{ij} &= \sqrt{C^{ji} - \sum_{k=1}^{j-1} T_{ik}^2}, \qquad \text{if } i = j \\
T_{ij} &= \frac{C^{ji} - \sum_{k=1}^{j-1} T_{ik}T_{jk}}{T_{jj}}, \qquad \text{if } i > j.
\end{aligned}
\tag{A.8}
$$

These amplitudes are squared for the input spectra for `synfast`, but one must beware negative cross-correlations as discussed above. A simple modification to a program like `synfast` could enable it to read in amplitudes rather than spectra, and this would be more efficient compared to reversing the sign of the maps after they are created.

Appendix B

Quasi-static nDGP solutions with curvature

In this appendix we describe how to obtain the solutions for the perturbations in the nDGP model.

B.1 Background

The projection on the brane of 5D Einstein equation for the DGP model is [Shiromizu et al., 2000, Koyama and Maartens, 2006]

$$G_{\mu\nu} = \kappa_5^2 \Pi_{\mu\nu} - E_{\mu\nu}, \tag{B.1}$$

where

$$\begin{aligned} \Pi_{\mu\nu} &= -\tfrac{1}{4}\tilde{T}_{\mu\alpha}\tilde{T}_{\nu}{}^{\alpha} + \tfrac{1}{12}\tilde{T}\tilde{T}_{\mu\nu} + \tfrac{1}{24}(3\tilde{T}_{\alpha\beta}\tilde{T}^{\alpha\beta} - \tilde{T}^2)g_{\mu\nu}, \\ \tilde{T}_{\mu\nu} &= T_{\mu\nu} - \sigma g_{\alpha\beta} - \kappa^{-1}G_{\mu\nu}, \end{aligned} \tag{B.2}$$

and $E_{\mu\nu}$ is the trace-free projection of the 5D Weyl tensor, which for the 4D Bianchi identity has the constraint

$$\nabla^{\mu} E_{\mu\nu} = (2r_c)^2 \kappa \nabla^{\mu} \Pi_{\mu\nu}\,. \tag{B.3}$$

In the background, $E_{\mu\nu} = 0$. From this formulation, one can derive the evolution of the background of Eq. (2.65).

B.2 Perturbations

In the Gaussian normal coordinates, the 5D metric is given by [Deffayet et al., 2002a]

$$ds^2 = dy^2 - n(y,t)^2 dt^2 + a(y,t)^2 \delta_{ij} dx^i dx^j, \tag{B.4}$$

where

$$\begin{aligned} a(y,t) &= a(t)\left[1-\left(H^2-\frac{\Omega_k}{a_0^2}\right)^{\frac{1}{2}} y\right], && \text{(B.5)}\\ n(y,t) &= 1-(\dot{H}+H^2)\left(H^2-\frac{\Omega_k}{a_0^2}\right)^{-\frac{1}{2}} y. && \text{(B.6)}\end{aligned}$$

The extrinsic curvature of the brane is determined by the first derivative of the metric with respect to y at the brane ($y=0$):

$$\begin{aligned} \frac{a'}{a} &= -\left(H^2-\frac{\Omega_k}{a^2}\right)^{\frac{1}{2}}, && \text{(B.7)}\\ \frac{n'}{n} &= -(\dot{H}+H^2)\left(H^2-\frac{\Omega_k}{a^2}\right)^{-\frac{1}{2}}. && \text{(B.8)}\end{aligned}$$

We pass to linear perturbations using the Newtonian gauge, where the metric is given by Eq. (2.79). We can introduce scalar perturbations on the matter energy-momentum tensor T^μ_ν as in GR:

$$\delta T^\mu_\nu = \begin{pmatrix} -\delta\rho & a\delta q_{,i} \\ -a^{-1}\delta q^{,i} & \delta P\, \delta^i_{\ j} + \delta\pi^i_j \end{pmatrix}, \tag{B.9}$$

and we also define the perturbations of the Weyl fluid as

$$\delta E^\mu_{\ \nu} = -\kappa \begin{pmatrix} -\delta\rho_E & a\delta q_{E,i} \\ a^{-1}\delta q_E^{\ ,i} & \frac{1}{3}\delta\rho_E\, \delta^i_{\ j} + \delta\pi^i_{E\,j} \end{pmatrix}. \tag{B.10}$$

We can now derive the perturbed Einstein equations which correspond to Eqq. (2.103, 2.104, 2.105, 2.106). For example, the traceless part of the space-space component gives

$$-\frac{1}{a^2}\left\{1-\frac{1}{r_c\left[(a'/a)+(n'/n)\right]}\right\}(\Phi+\Psi) = \frac{\kappa_4^2\delta\pi_E}{r_c\left[(a'/a)+(n'/n)\right]}. \tag{B.11}$$

Defining the comoving density perturbations

$$\rho\triangle = \delta\rho - 3Ha\delta q, \tag{B.12}$$

the Poisson equation is obtained as

$$\frac{k^2}{a^2}\Phi = \frac{\kappa_4^2}{2}\left[\frac{2(a'/a)r_c}{2(a'/a)r_c-1}\right]\left[\rho\triangle - \frac{\delta\rho_E-3Ha\delta q_E}{2(a'/a)r_c}\right]. \tag{B.13}$$

From the application of Eq. (B.3), the Weyl density perturbations should be determined by the constraint equations

$$\begin{aligned}
\delta\dot{\rho}_E &+ 4H\delta\rho_E - a^{-1}k^2\delta q_E = 0, &\text{(B.14)}\\
\delta\dot{q}_E &+ 4H\delta q_E + a^{-1}\left(\frac{1}{3}\delta\rho_E - \frac{2}{3}k^2\delta\pi_E\right)\\
&= -a^{-1}\frac{2}{3}r_c\left(\frac{n'}{n} - \frac{a'}{a}\right)\left\{-\frac{\rho\triangle}{2(a'/a)r_c - 1}\right.\\
&+ \frac{\delta\rho_E - 3Ha\delta q_E}{2(a'/a)r_c - 1}\\
&+ \left.\frac{1}{r_c\left[(a'/a) + (n'/n)\right] - 1}k^2\delta\pi_E\right\}. &\text{(B.15)}
\end{aligned}$$

The constraint equations are not closed and we need additional information by solving the 5D equation of motion. In the quasi-static limit, we can impose the condition on $\delta\rho_E$ and $\delta\pi_E$ from the bulk equation as [Koyama and Maartens, 2006]

$$\delta\rho_E = 2k^2\delta\pi_E. \tag{B.16}$$

Then the constraint equations give

$$\delta\rho_E = 2\left[\frac{-1 + (a'/a)r_c + (n'/n)r_c}{-3 + 4(a'/a)r_c + 2(n'/n)r_c}\right]\rho\Delta, \tag{B.17}$$

and $\delta q_E = 0$. The Poisson equation and the traceless part of Einstein equations give

$$\begin{aligned}
\frac{k^2}{a^2}\Phi &= \frac{\kappa_4^2}{2}\left[1 - \frac{1}{3\beta(t)}\right]\rho\triangle, &\text{(B.18)}\\
\frac{k^2}{a^2}\Psi &= -\frac{\kappa_4^2}{2}\left[1 + \frac{1}{3\beta(t)}\right]\rho\triangle, &\text{(B.19)}
\end{aligned}$$

where

$$\beta(t) = 1 - \frac{2}{3}\left[2\left(\frac{a'}{a}\right) + \left(\frac{n'}{n}\right)\right]r_c, \tag{B.20}$$

which can be written as

$$\beta(t) = 1 + 2H^2r_c\left(H^2 - \frac{\Omega_k}{a^2}\right)^{-1/2}\left[1 + \frac{\dot{H}}{3H^2} - \frac{2}{3}\frac{\Omega_k}{a^2H^2}\right]. \tag{B.21}$$

References

The Fifth Data Release of the Sloan Digital Sky Survey. *Astrophys. J. Suppl.*, 172:634–644, 2007.

T. Abbott et al. The dark energy survey. 2005.

Jennifer K. Adelman-McCarthy et al. The Sixth Data Release of the Sloan Digital Sky Survey. *Astrophys. J. Suppl.*, 175:297–313, 2008. doi: 10.1086/524984.

Jennifer K. Adelman-McCarthy et al. The Fourth Data Release of the Sloan Digital Sky Survey. *Astrophys. J. Suppl.*, 162:38–48, 2006. doi: 10.1086/497917.

Niayesh Afshordi. Integrated Sachs-Wolfe effect in Cross-Correlation: The Observer's Manual. *Phys. Rev.*, D70:083536, 2004. doi: 10.1103/PhysRevD.70.083536.

Niayesh Afshordi and Andrew J. Tolley. Primordial non-gaussianity, statistics of collapsed objects, and the Integrated Sachs-Wolfe effect. 2008.

Niayesh Afshordi, Yeong-Shang Loh, and Michael A. Strauss. Cross-Correlation of the Cosmic Microwave Background with the 2MASS Galaxy Survey: Signatures of Dark Energy, Hot Gas, and Point Sources. *Phys. Rev.*, D69:083524, 2004. doi: 10.1103/PhysRevD.69.083524.

Marcelo A. Alvarez, Eiichiro Komatsu, Olivier Dore, and Paul R. Shapiro. The Cosmic Reionization History as Revealed by the CMB Doppler–21-cm Correlation. *Astrophys. J.*, 647:840–852, 2006. doi: 10.1086/504888.

Luca Amendola, Radouane Gannouji, David Polarski, and Shinji Tsujikawa. Conditions for the cosmological viability of f(R) dark energy models. *Phys. Rev.*, D75:083504, 2007a. doi: 10.1103/PhysRevD.75.083504.

Luca Amendola, David Polarski, and Shinji Tsujikawa. Are f(R) dark energy models cosmologically viable ? *Phys. Rev. Lett.*, 98:131302, 2007b. doi: 10.1103/PhysRevLett.98.131302.

Nima Arkani-Hamed, Savas Dimopoulos, and G. R. Dvali. The hierarchy problem and new dimensions at a millimeter. *Phys. Lett.*, B429:263–272, 1998. doi: 10.1016/S0370-2693(98)00466-3.

C. Armendariz-Picon, Viatcheslav F. Mukhanov, and Paul J. Steinhardt. Essentials of k-essence. *Phys. Rev.*, D63:103510, 2001. doi: 10.1103/PhysRevD.63.103510.

Pierre Astier et al. The Supernova Legacy Survey: Measurement of OmegaM, OmegaLambda and w from the First Year Data Set. *Astron. Astrophys.*, 447:31–48, 2006. doi: 10.1051/0004-6361:20054185.

David J. Bacon, Alexandre R. Refregier, and Richard S. Ellis. Detection of Weak Gravitational Lensing by Large-scale Structure. *Mon. Not. Roy. Astron. Soc.*, 318:625, 2000. doi: 10.1046/j.1365-8711.2000.03851.x.

James M. Bardeen. Gauge Invariant Cosmological Perturbations. *Phys. Rev.*, D22:1882–1905, 1980. doi: 10.1103/PhysRevD.22.1882.

V. Barger, Y. Gao, and D. Marfatia. Accelerating cosmologies tested by distance measures. *Phys. Lett.*, B648:127–132, 2007. doi: 10.1016/j.physletb.2007.03.021.

Matthias Bartelmann and Peter Schneider. Weak Gravitational Lensing. *Phys. Rept.*, 340: 291–472, 2001. doi: 10.1016/S0370-1573(00)00082-X.

Rachel Bean and Olivier Dore. Probing dark energy perturbations: the dark energy equation of state and speed of sound as measured by WMAP. *Phys. Rev.*, D69:083503, 2004. doi: 10.1103/PhysRevD.69.083503.

Rachel Bean, Joanna Dunkley, and Elena Pierpaoli. Constraining Isocurvature Initial Conditions with WMAP 3- year data. *Phys. Rev.*, D74:063503, 2006. doi: 10.1103/PhysRevD.74.063503.

K. Becker, M. Becker, and J. H. Schwarz. *String theory and M-theory: A modern introduction*. 2007. Cambridge, UK: Cambridge Univ. Pr. (2007) 739 p.

C. L. Bennett et al. First Year Wilkinson Microwave Anisotropy Probe (WMAP) Observations: Preliminary Maps and Basic Results. *Astrophys. J. Suppl.*, 148:1, 2003. doi: 10.1086/377253.

B. Bertotti, L. Iess, and P. Tortora. A test of general relativity using radio links with the Cassini spacecraft. *Nature*, 425:374, 2003. doi: 10.1038/nature01997.

Edmund Bertschinger. Cosmological dynamics: Course 1. 1993.

Chris Blake, Adrian Collister, Sarah Bridle, and Ofer Lahav. Cosmological parameters from a million photometric redshifts of SDSS LRGs. 2006.

Chris A. Blake, Filipe B. Abdalla, Sarah L. Bridle, and Steve Rawlings. Cosmology with the Square Kilometre Array. *New Astron. Rev.*, 48:1063–1077, 2004. doi: 10.1016/j.newar.2004.09.045.

Alain Blanchard, Marian Douspis, Michael Rowan-Robinson, and Subir Sarkar. An alternative to the cosmological 'concordance model'. *Astron. Astrophys.*, 412:35–44, 2003. doi: 10.1051/0004-6361:20031425.

Alain Blanchard, Marian Douspis, Michael Rowan-Robinson, and Subir Sarkar. Large-scale galaxy correlations as a test for dark energy. *Astron. Astrophys.*, 449:925, 2006. doi: 10.1051/0004-6361:20054640.

Michael Blanton, Renyue Cen, Jeremiah P. Ostriker, and Michael A. Strauss. The Physical Origin of Scale Dependent Bias in Cosmological Simulations. 1998.

Elihu A. Boldt. THE COSMIC X-RAY BACKGROUND. *Phys. Rept.*, 146:215, 1987. doi: 10.1016/0370-1573(87)90108-6.

S. P. Boughn and R. G. Crittenden. Cross-Correlation of the Cosmic Microwave Background with Radio Sources: Constraints on an Accelerating Universe. *Phys. Rev. Lett.*, 88:021302, 2002. doi: 10.1103/PhysRevLett.88.021302.

S. P. Boughn, R. G. Crittenden, and N. G. Turok. Correlations between the cosmic X-ray and microwave backgrounds: Constraints on a cosmological constant. *New Astron.*, 3: 275–291, 1998. doi: 10.1016/S1384-1076(98)00009-8.

S. P. Boughn, R. G. Crittenden, and G. P. Koehrsen. The Large-Scale Structure of the X-ray Background and its Cosmological Implications. *Astrophys. J.*, 580:672–684, 2002. doi: 10.1086/343861.

Stephen Boughn and Robert Crittenden. A correlation of the cosmic microwave sky with large scale structure. *Nature*, 427:45–47, 2004a. doi: 10.1038/nature02139.

Stephen Boughn and Robert Crittenden. The large-scale bias of the hard X-ray background. *Astrophys. J.*, 612:647–651, 2004b. doi: 10.1086/422678.

Raphael Bousso and Joseph Polchinski. Quantization of four-form fluxes and dynamical neutralization of the cosmological constant. *JHEP*, 06:006, 2000.

Rebecca Bowen, Steen H. Hansen, Alessandro Melchiorri, Joseph Silk, and Roberto Trotta. The Impact of an Extra Background of Relativistic Particles on the Cosmological Parameters derived from Microwave Background Anisotropies. *Mon. Not. Roy. Astron. Soc.*, 334:760, 2002. doi: 10.1046/j.1365-8711.2002.05570.x.

A. Cabre, Enrique Gaztanaga, M. Manera, P. Fosalba, and F. Castander. Cross-correlation of WMAP 3rd year and the SDSS DR4 galaxy survey: new evidence for Dark Energy. *Mon. Not. Roy. Astron. Soc. Lett.*, 372:L23–L27, 2006.

Anna Cabre, Pablo Fosalba, Enrique Gaztanaga, and Marc Manera. Error analysis in cross-correlation of sky maps: application to the ISW detection. 2007.

R. R. Caldwell. A Phantom Menace? *Phys. Lett.*, B545:23–29, 2002. doi: 10.1016/S0370-2693(02)02589-3.

R. R. Caldwell and Eric V. Linder. The limits of quintessence. *Phys. Rev. Lett.*, 95:141301, 2005. doi: 10.1103/PhysRevLett.95.141301.

Salvatore Capozziello, Sante Carloni, and Antonio Troisi. Quintessence without scalar fields. *Recent Res. Dev. Astron. Astrophys.*, 1:625, 2003.

Antonio Cardoso, Kazuya Koyama, Sanjeev S. Seahra, and Fabio P. Silva. Cosmological perturbations in the DGP braneworld: numeric solution. 2007.

John E. Carlstrom, Gilbert P. Holder, and Erik D. Reese. Cosmology with the Sunyaev-Zel'dovich Effect. *Ann. Rev. Astron. Astrophys.*, 40:643–680, 2002. doi: 10.1146/annurev.astro.40.060401.093803.

Sean M. Carroll. The cosmological constant. *Living Rev. Rel.*, 4:1, 2001.

Sean M. Carroll, Mark Hoffman, and Mark Trodden. Can the dark energy equation-of-state parameter w be less than -1? *Phys. Rev.*, D68:023509, 2003. doi: 10.1103/PhysRevD.68.023509.

Sean M. Carroll, Vikram Duvvuri, Mark Trodden, and Michael S. Turner. Is cosmic speed-up due to new gravitational physics? *Phys. Rev.*, D70:043528, 2004. doi: 10.1103/PhysRevD.70.043528.

H. B. G. Casimir. On the Attraction Between Two Perfectly Conducting Plates. *Indag. Math.*, 10:261–263, 1948.

Renyue Cen. The Universe Was Reionized Twice. *Astrophys. J.*, 591:12–37, 2003. doi: 10.1086/375217.

Takeshi Chiba. 1/R gravity and scalar-tensor gravity. *Phys. Lett.*, B575:1–3, 2003. doi: 10.1016/j.physletb.2003.09.033.

Adrian Collister et al. MegaZ-LRG: A photometric redshift catalogue of one million SDSS Luminous Red Galaxies. *Mon. Not. Roy. Astron. Soc.*, 375:68–76, 2007. doi: 10.1111/j.1365-2966.2006.11305.x.

Asantha Cooray. Nonlinear integrated Sachs-Wolfe effect. *Phys. Rev.*, D65:083518, 2002. doi: 10.1103/PhysRevD.65.083518.

Asantha Cooray and Alessandro Melchiorri. Searching For Integrated Sachs-Wolfe Effect Beyond Temperature Anisotropies: CMB E-mode Polarization-Galaxy Cross Correlation. *JCAP*, 0601:018, 2006.

Asantha Cooray, Pier-Stefano Corasaniti, Tommaso Giannantonio, and Alessandro Melchiorri. An indirect limit on the amplitude of primordial gravitational wave background from CMB - galaxy cross correlation. *Phys. Rev.*, D72:023514, 2005. doi: 10.1103/PhysRevD.72.023514.

Asantha R. Cooray and Wayne Hu. Imprint of Reionization on the Cosmic Microwave Background Bispectrum. *Astrophys. J.*, 534:533–550, 2000. doi: 10.1086/308799.

Edmund J. Copeland. Dynamics of dark energy. *AIP Conf. Proc.*, 957:21–29, 2007. doi: 10.1063/1.2823765.

Craig J. Copi, Dragan Huterer, Dominik J. Schwarz, and Glenn D. Starkman. No large-angle correlations on the non-Galactic microwave sky. 2008.

Pier-Stefano Corasaniti, Tommaso Giannantonio, and Alessandro Melchiorri. Constraining dark energy with cross-correlated CMB and Large Scale Structure data. *Phys. Rev.*, D71:123521, 2005.

Robert Crittenden, Elisabetta Majerotto, and Federico Piazza. Measuring deviations from a cosmological constant: a field-space parameterization. *Phys. Rev. Lett.*, 98: 251301, 2007. doi: 10.1103/PhysRevLett.98.251301.

Robert G. Crittenden and Neil Turok. Looking for Λ with the Rees-Sciama Effect. *Phys. Rev. Lett.*, 76:575, 1996. doi: 10.1103/PhysRevLett.76.575.

Scott M. Croom et al. The 2dF QSO Redshift Survey - XII. The spectroscopic catalogue and luminosity function. *Mon. Not. Roy. Astron. Soc.*, 349:1397, 2004. doi: 10.1111/j.1365-2966.2004.07619.x.

Csaba Csaki, Nemanja Kaloper, and John Terning. The accelerated acceleration of the universe. *JCAP*, 0606:022, 2006.

Neal Dalal, Olivier Dore, Dragan Huterer, and Alexander Shirokov. The imprints of primordial non-gaussianities on large- scale structure: scale dependent bias and abundance of virialized objects. *Phys. Rev.*, D77:123514, 2008. doi: 10.1103/PhysRevD.77.123514.

Scott F. Daniel, Robert R. Caldwell, Asantha Cooray, and Alessandro Melchiorri. Large Scale Structure as a Probe of Gravitational Slip. *Phys. Rev.*, D77:103513, 2008. doi: 10.1103/PhysRevD.77.103513.

Simon DeDeo, R. R. Caldwell, and Paul J. Steinhardt. Effects of the sound speed of quintessence on the microwave background and large scale structure. *Phys. Rev.*, D67: 103509, 2003. doi: 10.1103/PhysRevD.67.103509.

Cedric Deffayet. Cosmology on a brane in Minkowski bulk. *Phys. Lett.*, B502:199–208, 2001.

Cedric Deffayet, G. R. Dvali, Gregory Gabadadze, and Arkady I. Vainshtein. Nonperturbative continuity in graviton mass versus perturbative discontinuity. *Phys. Rev.*, D65: 044026, 2002a.

Cedric Deffayet, Susana J. Landau, Julien Raux, Matias Zaldarriaga, and Pierre Astier. Supernovae, CMB, and gravitational leakage into extra dimensions. *Phys. Rev.*, D66: 024019, 2002b. doi: 10.1103/PhysRevD.66.024019.

James B. Dent, Sourish Dutta, and Thomas J. Weiler. A new perspective on the relation between dark energy perturbations and the late-time ISW effect. 2008.

Scott Dodelson. *Modern cosmology*. 2003. Amsterdam, Netherlands: Academic Pr. (2003) 440 p.

Scott Dodelson and Jay M. Jubas. Reionization and its imprint on the cosmic microwave background. *Astrophys. J.*, 439:503–516, 1995. doi: 10.1086/175191.

J. Dunkley et al. Five-Year Wilkinson Microwave Anisotropy Probe (WMAP) Observations: Likelihoods and Parameters from the WMAP data. 2008.

J. S. Dunlop and J. A. Peacock. The Redshift Cut-Off in the Luminosity Function of Radio Galaxies and Quasars. *Mon. Not. Roy. Astron. Soc.*, 247:19, 1990.

G. R. Dvali, Gregory Gabadadze, and Massimo Porrati. 4D gravity on a brane in 5D Minkowski space. *Phys. Lett.*, B485:208–214, 2000.

Gia Dvali, Andrei Gruzinov, and Matias Zaldarriaga. The accelerated universe and the Moon. *Phys. Rev.*, D68:024012, 2003.

Daniel J. Eisenstein et al. Detection of the Baryon Acoustic Peak in the Large-Scale Correlation Function of SDSS Luminous Red Galaxies. *Astrophys. J.*, 633:560–574, 2005. doi: 10.1086/466512.

Kari Enqvist. Lemaitre-Tolman-Bondi model and accelerating expansion. *Gen. Rel. Grav.*, 40:451–466, 2008. doi: 10.1007/s10714-007-0553-9.

Malcolm Fairbairn and Ariel Goobar. Supernova limits on brane world cosmology. *Phys. Lett.*, B642:432–435, 2006. doi: 10.1016/j.physletb.2006.07.048.

Xiaohui Fan et al. Evolution of the Ionizing Background and the Epoch of Reionization from the Spectra of z 6 Quasars. *Astron. J.*, 123:1247–1257, 2002. doi: 10.1086/339030.

Wenjuan Fang et al. Challenges to the DGP Model from Horizon-Scale Growth and Geometry. 2008.

D. J. Fixsen, E. Dwek, John C. Mather, C. L. Bennett, and R. A. Shafer. The Spectrum of the Extragalactic Far Infrared Background from the COBE Firas Observations. *Astrophys. J.*, 508:123, 1998. doi: 10.1086/306383.

Pablo Fosalba and Enrique Gaztanaga. Measurement of the gravitational potential evolution from the cross-correlation between WMAP and the APM Galaxy survey. *Mon. Not. Roy. Astron. Soc.*, 350:L37–L41, 2004.

Pablo Fosalba, Enrique Gaztanaga, and Francisco Castander. Detection of the ISW and SZ effects from the CMB-Galaxy correlation. *Astrophys. J.*, 597:L89–92, 2003.

W. L. Freedman et al. Final Results from the Hubble Space Telescope Key Project to Measure the Hubble Constant. *Astrophys. J.*, 553:47–72, 2001.

A. Friedmann. On the possibility of a world with constant negative curvature of space. *Z. Phys.*, 21:326–332, 1924. doi: 10.1007/BF01328280.

Josh Frieman et al. In preparation. 2008a.

Joshua Frieman, Michael Turner, and Dragan Huterer. Dark Energy and the Accelerating Universe. 2008b.

M. Fukugita et al. The Sloan digital sky survey photometric system. *Astron. J.*, 111:1748, 1996. doi: 10.1086/117915.

Enrique Gaztanaga, Marc Manera, and Tuomas Multamaki. New light on dark cosmos. *Mon. Not. Roy. Astron. Soc.*, 365:171–177, 2006.

Tommaso Giannantonio and Robert Crittenden. The effect of reionization on the CMB-density correlation. *Mon. Not. Roy. Astron. Soc.*, 381:819, 2007. doi: 10.1111/j.1365-2966.2007.12282.x.

Tommaso Giannantonio and Alessandro Melchiorri. Chaplygin gas in light of recent integrated Sachs-Wolfe effect data. *Class. Quant. Grav.*, 23:4125–4132, 2006.

Tommaso Giannantonio, Yong-Seon Song, and Kazuya Koyama. Detectability of a phantom-like braneworld model with the integrated Sachs-Wolfe effect. *Phys. Rev.*, D78:044017, 2008a. doi: 10.1103/PhysRevD.78.044017.

Tommaso Giannantonio et al. A high redshift detection of the integrated Sachs-Wolfe effect. *Phys. Rev.*, D74:063520, 2006. doi: 10.1103/PhysRevD.74.063520.

Tommaso Giannantonio et al. Combined analysis of the integrated Sachs-Wolfe effect and cosmological implications. 2008b.

Nickolay Y. Gnedin and Xiao-Hui Fan. Cosmic Reionization Redux. *Astrophys. J.*, 648:1, 2006. doi: 10.1086/505790.

Christopher Gordon and David Wands. The amplitude of dark energy perturbations. *Phys. Rev.*, D71:123505, 2005. doi: 10.1103/PhysRevD.71.123505.

K. M. Gorski et al. HEALPix – a Framework for High Resolution Discretization, and Fast Analysis of Data Distributed on the Sphere. *Astrophys. J.*, 622:759–771, 2005. doi: 10.1086/427976.

Benjamin R. Granett, Mark C. Neyrinck, and Istvan Szapudi. Dark Energy Detected with Supervoids and Superclusters. 2008.

J. E. Gunn et al. The Sloan digital sky survey photometric camera. *Astron. J.*, 116:3040, 1998. doi: 10.1086/300645.

James E. Gunn and Bruce A. Peterson. On the Density of Neutral Hydrogen in Intergalactic Space. *Astrophys. J.*, 142:1633, 1965.

James E. Gunn et al. The 2.5 m Telescope of the Sloan Digital Sky Survey. *Astron. J.*, 131: 2332–2359, 2006. doi: 10.1086/500975.

L. Guzzo et al. A test of the nature of cosmic acceleration using galaxy redshift distortions. *Nature*, 451:541–545, 2008. doi: 10.1038/nature06555.

Steen Hannestad. Constraints on the sound speed of dark energy. *Phys. Rev.*, D71:103519, 2005. doi: 10.1103/PhysRevD.71.103519.

G. Hinshaw et al. Three-year Wilkinson Microwave Anisotropy Probe (WMAP) observations: Temperature analysis. *Astrophys. J. Suppl.*, 170:288, 2007. doi: 10.1086/513698.

Shirley Ho, Christopher M. Hirata, Nikhil Padmanabhan, Uros Seljak, and Neta Bahcall. Correlation of CMB with large-scale structure: I. ISW Tomography and Cosmological Implications. 2008.

David W. Hogg, Douglas P. Finkbeiner, David J. Schlegel, and James E. Gunn. A photometricity and extinction monitor at the Apache Point Observatory. *Astron. J.*, 122:2129, 2001. doi: 10.1086/323103.

Wayne Hu and Scott Dodelson. Cosmic Microwave Background Anisotropies. *Ann. Rev. Astron. Astrophys.*, 40:171–216, 2002. doi: 10.1146/annurev.astro.40.060401.093926.

Wayne Hu and Ryan Scranton. Measuring Dark Energy Clustering with CMB-Galaxy Correlations. *Phys. Rev.*, D70:123002, 2004.

Wayne Hu and Naoshi Sugiyama. Small scale cosmological perturbations: An Analytic approach. *Astrophys. J.*, 471:542–570, 1996. doi: 10.1086/177989.

Wayne Hu, Douglas Scott, and Joseph Silk. Reionization and cosmic microwave background distortions: A Complete treatment of second order Compton scattering. *Phys. Rev.*, D49:648–670, 1994. doi: 10.1103/PhysRevD.49.648.

Wayne Hu, Masataka Fukugita, Matias Zaldarriaga, and Max Tegmark. CMB Observables and Their Cosmological Implications. *Astrophys. J.*, 549:669, 2001. doi: 10.1086/319449.

Wayne T. Hu. *Wandering in the background: A Cosmic microwave background explorer*. PhD thesis, 1995.

Edwin Hubble. A relation between distance and radial velocity among extra–galactic nebulae. *Proc. Nat. Acad. Sci.*, 15:168–173, 1929.

Dragan Huterer. Weak Lensing and Dark Energy. *Phys. Rev.*, D65:063001, 2002. doi: 10.1103/PhysRevD.65.063001.

Kazuhide Ichikawa and Tomo Takahashi. On the determination of neutrino masses and dark energy evolution from the cross-correlation of CMB and LSS. *JCAP*, 0802:017, 2008.

Ilian T. Iliev, Ue-Li Pen, J. Richard Bond, Garrelt Mellema, and Paul R. Shapiro. The Kinetic Sunyaev-Zel'dovich Effect from Patchy Reionization: the View from the Simulations. *New Astron. Rev.*, 50:909–917, 2006.

W. Israel. Singular hypersurfaces and thin shells in general relativity. *Nuovo Cim.*, B44S10:1, 1966.

Zeljko Ivezic et al. SDSS Data Management and Photometric Quality Assessment. *Astron. Nachr.*, 325:583–589, 2004. doi: 10.1002/asna.200410285.

T. H. Jarrett et al. 2MASS Extended Source Catalog: Overview and Algorithms. *Astron. J.*, 119:2498–2531, 2000. doi: 10.1086/301330.

Nick Kaiser, Gillian Wilson, and Gerard A. Luppino. Large-Scale Cosmic Shear Measurements. 2000.

Masahiro Kawasaki and Toyokazu Sekiguchi. Cosmological Constraints on Isocurvature and Tensor Perturbations. 2007.

Reijo Keskitalo, Hannu Kurki-Suonio, Vesa Muhonen, and Jussi Valiviita. Hints of Isocurvature Perturbations in the Cosmic Microwave Background? *JCAP*, 0709:008, 2007. doi: 10.1088/1475-7516/2007/09/008.

David Kirkman, David Tytler, Nao Suzuki, John M. O'Meara, and Dan Lubin. The cosmological baryon density from the deuterium to hydrogen ratio towards QSO absorption systems: D/H towards Q1243+3047. *Astrophys. J. Suppl.*, 149:1, 2003. doi: 10.1086/378152.

Hideo Kodama and Misao Sasaki. Cosmological Perturbation Theory. *Prog. Theor. Phys. Suppl.*, 78:1–166, 1984. doi: 10.1143/PTPS.78.1.

L. Kofman and Alexei A. Starobinsky. Effect of the cosmological constant on large scale anisotropies in the microwave backbround. *Sov. Astron. Lett.*, 11:271–274, 1985.

Edward W. Kolb and Michael S. Turner. *The Early Universe. Reprints*. 1988. Redwood City, USA: Addison-Wesley (1988) 719 P. (Frontiers in physics, 70).

Edward W. Kolb, S. Matarrese, and A. Riotto. On cosmic acceleration without dark energy. *New J. Phys.*, 8:322, 2006. doi: 10.1088/1367-2630/8/12/322.

E. Komatsu et al. Five-Year Wilkinson Microwave Anisotropy Probe (WMAP) Observations:Cosmological Interpretation. 2008.

M. Kowalski et al. Improved Cosmological Constraints from New, Old and Combined Supernova Datasets. 2008.

Kazuya Koyama. The cosmological constant and dark energy in braneworlds. *Gen. Rel. Grav.*, 40:421–450, 2008. doi: 10.1007/s10714-007-0552-x.

Kazuya Koyama. Ghosts in the self-accelerating universe. 2007.

Kazuya Koyama and Roy Maartens. Structure formation in the DGP cosmological model. *JCAP*, 0601:016, 2006.

Kazuya Koyama and Fabio P. Silva. Non-linear interactions in a cosmological background in the DGP braneworld. *Phys. Rev.*, D75:084040, 2007.

Lawrence M. Krauss and Brian Chaboyer. Age Estimates of Globular Clusters in the Milky Way: Constraints on Cosmology. *Science*, 299:65–70, 2003. doi: 10.1126/science.1075631.

Francesco Sylos Labini, Nikolay L. Vasilyev, Luciano Pietronero, and Yurij V. Baryshev. The large scale inhomogeneity of the galaxy distribution. 2008.

S. K. Lamoreaux. Demonstration of the Casimir force in the 0.6 to 6 micrometers range. *Phys. Rev. Lett.*, 78:5–7, 1997. doi: 10.1103/PhysRevLett.78.5.

Hubert Lampeitl, Tommaso Giannantonio, and et al. Combining the 1st-year SDSS-Supernova survey data with dynamical measurements from the growth of structure, the ISW effect and the BAO distance scale , In preparation. 2008.

Ruth Lazkoz and Elisabetta Majerotto. Cosmological constraints combining H(z), CMB shift and SNIa observational data. *JCAP*, 0707:015, 2007.

Ruth Lazkoz, Roy Maartens, and Elisabetta Majerotto. Observational constraints on phantom-like braneworld cosmologies. *Phys. Rev.*, D74:083510, 2006.

Julien Lesgourgues, Wessel Valkenburg, and Enrique Gaztanaga. Constraining neutrino masses with the ISW-galaxy correlation function. *Phys. Rev.*, D77:063505, 2008. doi: 10.1103/PhysRevD.77.063505.

Antony Lewis and Anthony Challinor. Weak Gravitational Lensing of the CMB. *Phys. Rept.*, 429:1–65, 2006. doi: 10.1016/j.physrep.2006.03.002.

Maxim Libanov, Valery Rubakov, Eleftherios Papantonopoulos, M. Sami, and Shinji Tsujikawa. UV stable, Lorentz-violating dark energy with transient phantom era. *JCAP*, 0708:010, 2007.

E. Lifshitz. On the Gravitational stability of the expanding universe. *J. Phys. (USSR)*, 10: 116, 1946.

Eric V. Linder. The Dynamics of Quintessence, The Quintessence of Dynamics. *Gen. Rel. Grav.*, 40:329–356, 2008. doi: 10.1007/s10714-007-0550-z.

Francisco S. N. Lobo. The dark side of gravity: Modified theories of gravity. 2008.

Marilena LoVerde, Lam Hui, and Enrique Gaztanaga. Magnification-Temperature Correlation: the Dark Side of ISW Measurements. *Phys. Rev.*, D75:043519, 2007. doi: 10.1103/PhysRevD.75.043519.

Arthur Lue. The phenomenology of Dvali-Gabadadze-Porrati cosmologies. *Phys. Rept.*, 423:1–48, 2006. doi: 10.1016/j.physrep.2005.10.007.

Arthur Lue and Glenn Starkman. Gravitational leakage into extra dimensions: Probing dark energy using local gravity. *Phys. Rev.*, D67:064002, 2003.

Arthur Lue and Glenn D. Starkman. How a brane cosmological constant can trick us into thinking that W < -1. *Phys. Rev.*, D70:101501, 2004.

Arthur Lue, Roman Scoccimarro, and Glenn Starkman. Differentiating between Modified Gravity and Dark Energy. *Phys. Rev.*, D69:044005, 2004. doi: 10.1103/PhysRevD.69.044005.

Robert Lupton, James E. Gunn, and Alex Szalay. A Modified Magnitude System that Produces Well-Behaved Magnitudes, Colors, and Errors Even for Low Signal-to-Noise Ratio Measurements. *Astron. J.*, 118:1406, 1999. doi: 10.1086/301004.

Chung-Pei Ma and Edmund Bertschinger. Cosmological perturbation theory in the synchronous and conformal Newtonian gauges. *Astrophys. J.*, 455:7–25, 1995. doi: 10.1086/176550.

Roy Maartens. Brane-world gravity. *Living Rev. Rel.*, 7:7, 2004.

Roy Maartens and Elisabetta Majerotto. Observational constraints on self-accelerating cosmology. *Phys. Rev.*, D74:023004, 2006. doi: 10.1103/PhysRevD.74.023004.

Enrique Martinez-Gonzalez, Jose L. Sanz, and Joseph Silk. Imprints of galaxy clustering evolution on Delta T/T. 1994.

J. D. McEwen, Y. Wiaux, M. P. Hobson, P. Vandergheynst, and A. N. Lasenby. Probing dark energy with steerable wavelets through correlation of WMAP and NVSS local morphological measures. 2007a.

Jason D. McEwen, P. Vielva, M. P. Hobson, E. Martinez-Gonzalez, and A. N. Lasenby. Detection of the ISW effect and corresponding dark energy constraints made with directional spherical wavelets. *Mon. Not. Roy. Astron. Soc.*, 373:1211–1226, 2007b. doi: 10.1111/j.1365-2966.2007.11505.x.

Matthew McQuinn, Steven R. Furlanetto, Lars Hernquist, Oliver Zahn, and Matias Zaldarriaga. The Kinetic Sunyaev-Zel'dovich Effect from Reionization. *Astrophys. J.*, 630: 643–656, 2005. doi: 10.1086/432049.

Viatcheslav F. Mukhanov, H. A. Feldman, and Robert H. Brandenberger. Theory of cosmological perturbations. Part 1. Classical perturbations. Part 2. Quantum theory of perturbations. Part 3. Extensions. *Phys. Rept.*, 215:203–333, 1992. doi: 10.1016/0370-1573(92)90044-Z.

D. Munshi, P. Valageas, Ludovic Van Waerbeke, and A. Heavens. Cosmology with Weak Lensing Surveys. *Phys. Rept.*, 462:67–121, 2008. doi: 10.1016/j.physrep.2008.02.003.

Adam D. Myers et al. First Measurement of the Clustering Evolution of Photometrically-Classified Quasars. *Astrophys. J.*, 638:622–634, 2006. doi: 10.1086/499093.

S. Nesseris and Leandros Perivolaropoulos. Testing LCDM with the Growth Function delta(a): Current Constraints. *Phys. Rev.*, D77:023504, 2008. doi: 10.1103/PhysRevD.77.023504.

Shin'ichi Nojiri and Sergei D. Odintsov. Modified gravity with negative and positive powers of the curvature: Unification of the inflation and of the cosmic acceleration. *Phys. Rev.*, D68:123512, 2003. doi: 10.1103/PhysRevD.68.123512.

Shin'ichi Nojiri and Sergei D. Odintsov. Dark energy, inflation and dark matter from modified F(R) gravity. 2008.

M. R. Nolta et al. Five-Year Wilkinson Microwave Anisotropy Probe (WMAP) Observations: Angular Power Spectra. 2008.

Michael R. Nolta et al. First Year Wilkinson Microwave Anisotropy Probe (WMAP) Observations: Dark Energy Induced Correlation with Radio Sources. *Astrophys. J.*, 608: 10–15, 2004. doi: 10.1086/386536.

V. K. Onemli and R. P. Woodard. Super-acceleration from massless, minimally coupled phi**4. *Class. Quant. Grav.*, 19:4607, 2002.

V. K. Onemli and R. P. Woodard. Quantum effects can render w < -1 on cosmological scales. *Phys. Rev.*, D70:107301, 2004.

J. P. Ostriker and E. T. Vishniac. Generation of microwave background fluctuations from nonlinear perturbations at the ERA of galaxy formation. *"Astrophys. J. Lett."*, 306:L51–L54, July 1986. doi: 10.1086/184704.

Nikhil Padmanabhan et al. Correlating the CMB with Luminous Red Galaxies : The Integrated Sachs-Wolfe Effect. *Phys. Rev.*, D72:043525, 2005. doi: 10.1103/PhysRevD.72.043525.

Nikhil Padmanabhan et al. The Clustering of Luminous Red Galaxies in the Sloan Digital Sky Survey Imaging Data. *Mon. Not. Roy. Astron. Soc.*, 378:852–872, 2007. doi: 10.1111/j.1365-2966.2007.11593.x.

L. Page et al. Three year Wilkinson Microwave Anisotropy Probe (WMAP) observations: Polarization analysis. *Astrophys. J. Suppl.*, 170:335, 2007. doi: 10.1086/513699.

J. A. Peacock. *Cosmological physics*. 1999. Cambridge, UK: Univ. Pr. (1999) 682 p.

P. J. E. Peebles. *Principles of physical cosmology*. 1994. Princeton, USA: Univ. Pr. (1993) 718 p.

P. J. E. Peebles and Bharat Ratra. The cosmological constant and dark energy. *Rev. Mod. Phys.*, 75:559–606, 2003. doi: 10.1103/RevModPhys.75.559.

Hiranya V. Peiris and David N. Spergel. Cross-correlating the Sloan Digital Sky Survey with the Microwave Sky. *Astrophys. J.*, 540:605, 2000. doi: 10.1086/309373.

Will J. Percival et al. The shape of the SDSS DR5 galaxy power spectrum. *Astrophys. J.*, 657:645–663, 2007a. doi: 10.1086/510615.

Will J. Percival et al. Measuring the Baryon Acoustic Oscillation scale using the SDSS and 2dFGRS. *Mon. Not. Roy. Astron. Soc.*, 381:1053–1066, 2007b.

S. Perlmutter et al. Measurements of Omega and Lambda from 42 High-Redshift Supernovae. *Astrophys. J.*, 517:565–586, 1999. doi: 10.1086/307221.

M. M. Phillips. The absolute magnitudes of Type IA supernovae. *Astrophys. J.*, 413: L105–L108, 1993.

Jeffrey R. Pier et al. Astrometric Calibration of the Sloan Digital Sky Survey. *Astron. J.*, 125:1559, 2003. doi: 10.1086/346138.

Davide Pietrobon, Amedeo Balbi, and Domenico Marinucci. Integrated Sachs-Wolfe effect from the cross-correlation of WMAP 3 year and NVSS: new results and constraints on dark energy. *Phys. Rev.*, D74:043524, 2006. doi: 10.1103/PhysRevD.74.043524.

Levon Pogosian. Evolving dark energy equation of state and CMB/LSS cross- correlation. *JCAP*, 0504:015, 2005.

Levon Pogosian, Pier Stefano Corasaniti, Christian Stephan-Otto, Robert Crittenden, and Robert Nichol. Tracking Dark Energy with the ISW effect: short and long- term predictions. *Phys. Rev.*, D72:103519, 2005. doi: 10.1103/PhysRevD.72.103519.

Cristiano Porciani, Manuela Magliocchetti, and Peder Norberg. Cosmic Evolution of Quasar Clustering: Implications for the Host Haloes. 2004.

N. Puchades, M. J. Fullana, J. V. Arnau, and Diego Saez. On the Rees-Sciama effect: maps and statistics. *Mon. Not. Roy. Astron. Soc.*, 370:1849–1858, 2006.

Lisa Randall and Raman Sundrum. A large mass hierarchy from a small extra dimension. *Phys. Rev. Lett.*, 83:3370–3373, 1999a. doi: 10.1103/PhysRevLett.83.3370.

Lisa Randall and Raman Sundrum. An alternative to compactification. *Phys. Rev. Lett.*, 83:4690–4693, 1999b. doi: 10.1103/PhysRevLett.83.4690.

Anais Rassat, Kate Land, Ofer Lahav, and Filipe B. Abdalla. Cross-correlation of 2MASS and WMAP3: Implications for the Integrated Sachs-Wolfe effect. *Mon. Not. Roy. Astron. Soc.*, 377:1085–1094, 2007. doi: 10.1111/j.1365-2966.2007.11538.x.

Bharat Ratra and P. J. E. Peebles. Cosmological Consequences of a Rolling Homogeneous Scalar Field. *Phys. Rev.*, D37:3406, 1988. doi: 10.1103/PhysRevD.37.3406.

M. J. Rees and D. W. Sciama. Large scale Density Inhomogeneities in the Universe. *Nature*, 217:511–516, 1968.

Y. Rephaeli. Comptonization of the cosmic microwave background: the sunyaev-zeldovich effect. *Ann. Rev. Astron. Astrophys.*, 33:541–579, 1995. doi: 10.1146/annurev.aa.33.090195.002545.

Yoel Rephaeli and Sharon Sadeh. S-Z Power Spectra. 2008.

Gordon T. Richards et al. Efficient Photometric Selection of Quasars from the Sloan Digital Sky Survey: 100,000 z<3 Quasars from Data Release One. *Astrophys. J. Suppl.*, 155:257–269, 2004. doi: 10.1086/425356.

Gordon T. Richards et al.

Adam G. Riess et al. Observational Evidence from Supernovae for an Accelerating Universe and a Cosmological Constant. *Astron. J.*, 116:1009–1038, 1998. doi: 10.1086/300499.

Adam G. Riess et al. Type ia supernova discoveries at z>1 from the hubble space telescope: Evidence for past deceleration and constraints on dark energy evolution. *Astrophys. J.*, 607:665–687, 2004.

Huub J. A. . Rottgering et al. LOFAR - Opening up a new window on the Universe. 2006.

Sara Rydbeck, Malcolm Fairbairn, and Ariel Goobar. Testing the DGP model with ESSENCE. *JCAP*, 0705:003, 2007.

R. K. Sachs and A. M. Wolfe. Perturbations of a cosmological model and angular variations of the microwave background. *Astrophys. J.*, 147:73–90, 1967.

Varun Sahni and Yuri Shtanov. Braneworld models of dark energy. *JCAP*, 0311:014, 2003.

Varun Sahni and Alexei Starobinsky. Reconstructing dark energy. *Int. J. Mod. Phys.*, D15: 2105–2132, 2006. doi: 10.1142/S0218271806009704.

R. Salvaterra and A. Ferrara. The Imprint of the Cosmic Dark Ages on the Near Infrared Background. *Mon. Not. Roy. Astron. Soc.*, 339:973, 2003. doi: 10.1046/j.1365-8711.2003.06244.x.

Michael R. Santos, Volker Bromm, and Marc Kamionkowski. The Contribution of the First Stars to the Cosmic Infrared Background. *Mon. Not. Roy. Astron. Soc.*, 336:1082, 2002. doi: 10.1046/j.1365-8711.2002.05895.x.

Ignacy Sawicki, Yong-Seon Song, and Wayne Hu. Near-horizon solution for DGP perturbations. *Phys. Rev.*, D75:064002, 2007.

Bjoern Malte Schaefer. The integrated Sachs-Wolfe effect in cosmologies with coupled dark matter and dark energy. 2008a.

Bjoern Malte Schaefer. Mixed three-point correlation functions of the nonlinear integrated Sachs-Wolfe effect and their detectability. 2008b.

Bjoern Malte Schaefer and Matthias Bartelmann. Weak lensing in the second post-Newtonian approximation: Gravitomagnetic potentials and the integrated Sachs-Wolfe effect. *Mon. Not. Roy. Astron. Soc.*, 369:425–440, 2006.

Bjoern Malte Schafer, Christoph Pfrommer, Matthias Bartelmann, Volker Springel, and Lars Hernquist. Detecting Sunyaev-Zel'dovich clusters with PLANCK: I. Construction of all-sky thermal and kinetic SZ-maps. *Mon. Not. Roy. Astron. Soc.*, 370:1309–1323, 2006.

David J. Schlegel, Douglas P. Finkbeiner, and Marc Davis. Maps of Dust IR Emission for Use in Estimation of Reddening and CMBR Foregrounds. *Astrophys. J.*, 500:525, 1998. doi: 10.1086/305772.

Peter Schneider. Weak Gravitational Lensing. 2005.

Ryan Scranton et al. Physical Evidence for Dark Energy. 2003. doi: OSTI/15011774.

Uros Seljak. Rees-Sciama effect in a CDM universe. 1995.

Uros Seljak. Gravitational lensing effect on cosmic microwave background anisotropies: A Power spectrum approach. *Astrophys. J.*, 463:1, 1996. doi: 10.1086/177218.

Uros Seljak and Matias Zaldarriaga. A Line of Sight Approach to Cosmic Microwave Background Anisotropies. *Astrophys. J.*, 469:437–444, 1996. doi: 10.1086/177793.

Tetsuya Shiromizu, Kei-ichi Maeda, and Misao Sasaki. The Einstein equations on the 3-brane world. *Phys. Rev.*, D62:024012, 2000. doi: 10.1103/PhysRevD.62.024012.

Michael Shull and Aparna Venkatesan. Optical Depth of the Cosmic Microwave Background and Reionization of the Intergalactic Medium. 2007.

Joseph Silk. Cosmic black body radiation and galaxy formation. *Astrophys. J.*, 151:459–471, 1968.

Anze Slosar, Asantha Cooray, and Joseph Silk. Cross-correlation studies as a probe of reionization physics. *Mon. Not. Roy. Astron. Soc.*, 377:168–178, 2007. doi: 10.1111/j.1365-2966.2007.11584.x.

Anze Slosar, Christopher Hirata, Uros Seljak, Shirley Ho, and Nikhil Padmanabhan. Constraints on local primordial non-Gaussianity from large scale structure. 2008.

J Allyn Smith et al. The u′g′r′i′z′ Standard star system. *Astron. J.*, 123:2121–2144, 2002. doi: 10.1086/339311.

George F. Smoot. Nobel Lecture: Cosmic microwave background radiation anisotropies: Their discovery and utilization. *Rev. Mod. Phys.*, 79:1349–1379, 2007. doi: 10.1103/RevModPhys.79.1349.

Yong-Seon Song. Large Scale Structure Formation of normal branch in DGP brane world model. 2007.

Yong-Seon Song, Ignacy Sawicki, and Wayne Hu. Large-scale tests of the DGP model. *Phys. Rev.*, D75:064003, 2007.

Thomas P. Sotiriou. Modified Actions for Gravity: Theory and Phenomenology. 2007.

Thomas P. Sotiriou and Valerio Faraoni. f(R) Theories Of Gravity. 2008.

D. N. Spergel et al. Wilkinson Microwave Anisotropy Probe (WMAP) three year results: Implications for cosmology. *Astrophys. J. Suppl.*, 170:377, 2007. doi: 10.1086/513700.

D. N. Spergel et al. First year wilkinson microwave anisotropy probe (wmap) observations: Determination of cosmological parameters. *Astrophys. J. Suppl.*, 148:175, 2003.

Volker Springel and Lars Hernquist. Cosmological SPH simulations: The entropy equation. *Mon. Not. Roy. Astron. Soc.*, 333:649, 2002. doi: 10.1046/j.1365-8711.2002.05445.x.

Alexei A. Starobinsky. A new type of isotropic cosmological models without singularity. *Phys. Lett.*, B91:99–102, 1980. doi: 10.1016/0370-2693(80)90670-X.

Albert Stebbins. Measuring velocites using the CMB & LSS. *New Astron. Rev.*, 50:918–924, 2006.

Chris Stoughton et al. The Sloan Digital Sky Survey: Early data release. *Astron. J.*, 123: 485–548, 2002. doi: 10.1086/324741.

Naoshi Sugiyama, Joseph Silk, and Nicola Vittorio. Reionization and cosmic microwave anisotropies. 1993.

R. A. Sunyaev and Ya. B. Zeldovich. Small scale fluctuations of relic radiation. *Astrophys. Space Sci.*, 7:3–19, 1970.

R. A. Sunyaev and Ya. B. Zeldovich. The Velocity of clusters of galaxies relative to the microwave background. The Possibility of its measurement. *Mon. Not. Roy. Astron. Soc.*, 190:413–420, 1980.

Leonard Susskind. The anthropic landscape of string theory. 2003.

Max Tegmark. Doppler peaks and all that: CMB anisotropies and what they can tell us. 1995.

A. Torres-Rodriguez and C. M. Cress. Constraining the Nature of Dark Energy using the SKA. *Mon. Not. Roy. Astron. Soc.*, 376:1831–1837, 2007. doi: 10.1111/j.1365-2966.2007. 11565.x.

Robin Tuluie, Pablo Laguna, and Peter Anninos. Cosmic Microwave Background Anisotropies from the Rees- Sciama Effect in $\Omega_0 \leq 1$ Universes. *Astrophys. J.*, 463: 15, 1996. doi: 10.1086/177220.

J. Anthony Tyson. Precision studies of dark energy with LSST. *AIP Conf. Proc.*, 870:44–52, 2006.

Jussi Valiviita. *The Nature of Primordial Perturbations in the Light of CMB Observations*. PhD thesis, Helsinki Institute of Physics, 2005.

Ludovic van Waerbeke et al. Detection of correlated galaxy ellipticities on CFHT data: first evidence for gravitational lensing by large-scale structures. *Astron. Astrophys.*, 358:30–44, 2000.

Patricio Vielva, E. Martinez-Gonzalez, and M. Tucci. WMAP and NVSS cross-correlation in wavelet space: ISW detection and dark energy constraints. 2004.

Robert M. Wald. *General Relativity*. 1984. Chicago, Usa: Univ. Pr. (1984) 491p.

Yun Wang and Pia Mukherjee. Robust Dark Energy Constraints from Supernovae, Galaxy Clustering, and Three-Year Wilkinson Microwave Anisotropy Probe Observations. *Astrophys. J.*, 650:1, 2006. doi: 10.1086/507091.

Steven Weinberg. Anthropic Bound on the Cosmological Constant. *Phys. Rev. Lett.*, 59: 2607, 1987. doi: 10.1103/PhysRevLett.59.2607.

Steven Weinberg. The cosmological constant problem. *Rev. Mod. Phys.*, 61:1–23, 1989. doi: 10.1103/RevModPhys.61.1.

Steven Weinberg. *Cosmology*. 2008. Oxford, UK: Univ. Pr. (2008) 612 p.

Jochen Weller and A. M. Lewis. Large Scale Cosmic Microwave Background Anisotropies and Dark Energy. *Mon. Not. Roy. Astron. Soc.*, 346:987–993, 2003. doi: 10.1111/j.1365-2966.2003.07144.x.

C. Wetterich. Cosmology and the Fate of Dilatation Symmetry. *Nucl. Phys.*, B302:668, 1988. doi: 10.1016/0550-3213(88)90193-9.

Richard L. White, Robert H. Becker, Xiao-Hui Fan, and Michael A. Strauss. Probing the Ionization State of the Universe at z>6. *Astron. J.*, 126:1, 2003. doi: 10.1086/375547.

David M. Wittman, J. Anthony Tyson, David Kirkman, Ian Dell'Antonio, and Gary Bernstein. Detection of weak gravitational lensing distortions of distant galaxies by cosmic dark matter at large scales. *Nature*, 405:143–149, 2000. doi: 10.1038/35012001.

Kelvin K. S. Wu, Ofer Lahav, and Martin J. Rees. How smooth is the universe on large scales? 1998.

Jaswant Yadav, Somnath Bharadwaj, Biswajit Pandey, and T. R. Seshadri. Testing homogeneity on large scales in the Sloan Digital Sky Survey Data Release One. *Mon. Not. Roy. Astron. Soc.*, 364:601–606, 2005.

Donald G. York et al. The Sloan Digital Sky Survey: technical summary. *Astron. J.*, 120: 1579–1587, 2000. doi: 10.1086/301513.

Ivaylo Zlatev, Li-Min Wang, and Paul J. Steinhardt. Quintessence, Cosmic Coincidence, and the Cosmological Constant. *Phys. Rev. Lett.*, 82:896–899, 1999. doi: 10.1103/PhysRevLett.82.896.

Bruno Zumino. Supersymmetry and the Vacuum. *Nucl. Phys.*, B89:535, 1975. doi: 10.1016/0550-3213(75)90194-7.